Development of mid-infrared materials and light emitting diodes

Philip William Bond

MPhys AFHEA

This thesis is submitted for the degree of

Doctor of Philosophy in Engineering

Lancaster University

School of Engineering

April 2025

Development of mid-infrared materials and light emitting diodes

Philip William Bond

Abstract

Light Emitting Diodes (LEDs) operating in the technologically important mid-infrared (MIR) spectral range (2 – 5 µm) are important for a variety of applications including environmental gas sensing, non-invasive medical diagnosis, and tunable IR spectroscopy. However, MIR LED efficiency at room temperature is still low due to the prevalence of non-radiative recombination. The research presented here is aimed at developing material systems which increase the efficiency of these LEDs, as well creating bright, wavelength specific devices.

Furthermore, a novel application for the MIR spectral range was investigated, in detecting plastics based on their spectral fingerprint around 3 µm. This is an important application as black plastics are currently unrecyclable due to their inability to be detected by current optical sorting technologies in plastic recovery facilities (PRFs). Using an analysis of the life cycle of plastics, and black plastics, a discussion is had regarding the necessity of them to remain in the economy and how recycling technologies can be used to increase economic circularity – leading to a more sustainable use of resources.

To target the 3 µm region, the InGaAsSb/AlGaAsSb type-I quantum well material system was studied. Samples were grown by MBE on n-GaSb substrates, characterised by x-ray diffraction (XRD) and photoluminescence (PL) spectroscopy to find structural and bandgap characteristics. The samples grown showed emission from 2.1 – 3.4 µm using various quantum well structures. When integrated into an LED, room temperature emission was obtained at ~ 2.8 µm.

Due to their Auger quenching mechanisms and reduction in SRH recombination, InAs/$InAs_{1-x}Sb_x$ superlattices strain balanced to GaSb were studied. These structures were also grown via MBE and characterised using XRD and PL, showing emission ~ 4 µm at 4 K. These superlattices were integrated into LEDs, which showed bright emission ~ 3.9 µm at low temperature, with emission increasing up to 4.5 µm at room temperature.

Outputs:

Publication:

[1] P. W. Bond, M. Bentley, L. Hanks, A. P. Craig, Q. Zhuang, A. R. J. Marshall, P. J. Carrington. (2025). A study of InAs/$InAs_{1-x}Sb_x$ ($x < 0.13$) strain balanced superlattices and their integration into mid-infrared light emitting diodes. [In preparation].

Conferences:

[1] P. W. Bond, M. Bentley, L. Hanks, S. Davis, A. P. Craig, Q. Zhuang, A. R. J. Marshall, P. J. Carrington. Growth of strain balanced InAs/$InAs_{1-x}Sb_x$ type-II strained layer superlattice (SLS) LEDs on GaSb. United Kingdom Molecular Beam Epitaxy Conference 2025. Warwick, UK. Oral presentation.

[2] P. W. Bond, M. Bentley, L. Hanks, A. R. J. Marshall, P. J. Carrington. Type-II InAs/InAsSb strain balanced superlattice mid-infrared light emitting diodes grown on GaSb. United Kingdom Semiconductors conference 2024. Sheffield, UK. Poster.

[3] P. W. Bond. Using mid-infrared (2 – 5 μm) light emitting diodes to identify black plastics. Lancaster University School of Engineering Post-graduate Conference 2024. Lancaster, UK. Oral presentation and poster.

[4] P. W. Bond. Using mid-infrared (2 – 5 μm) light emitting diodes to identify black plastics. Lancaster University School of Engineering Post-graduate Conference 2023. Lancaster, UK. Oral presentation. [Second prize].

[5] P. W. Bond. Using mid-infrared (2 – 5 μm) light emitting diodes to identify black plastics. Lancaster University School of Engineering Post-graduate Conference 2022. Lancaster, UK. Oral presentation [First prize for talks].

Contents

List of figures:

List of tables:

Acknowledgements

I would first like to acknowledge the invaluable supervision which has been provided to me over the last three years by Dr. Peter Carrington. Without who's guidance this journey would have been much more treacherous.

I would also like to thank Dr. Andrew Marshall and Dr. Qiandong Zhuang for all of their advice and support in helping me understand and analyse my data. Moreover, I would like to thank Dr. Alison Stowell for her guidance regarding the analysis of plastic policy. Furthermore, the help that Dr. Matthew Bentley gave me on all of the practical work that has been undertaken during this project has been essential; I could not have done it without your knowledge and patience.

I also give my gratitude to: Dr. Adam Craig, Dr. Laura Hanks, George Segar, Josh Fletcher and Sam Davis, for the help you have given me both practically, and theoretically. As well as all of the technical staff in the Physics Department and School of Engineering, without whom, the practical work required would not be possible.

I further acknowledge the assistance of Prof. Richard Harper and Prof. Rob Short for their running of the Material Social Futures programme, which along with the Leverhulme Foundation funded this PhD project.

I would finally like to thank my long-suffering family and friends, who have supported me in a plethora of ways since the beginning of this project.

Author's declaration

I declare that this thesis, titled 'Development of mid-infrared materials and light emitting diodes' is my own work and has not been submitted in substantially or the same form for the award or a higher degree elsewhere. Where published work of others was consulted, it is referenced in the text and shown in the bibliography. The research was carried out at Lancaster University's School of Engineering under the supervision of: Dr. Peter Carrington, Dr. Andrew Marshall, Dr. Qiandong Zhuang and Dr. Alison Stowell; between October 2021 and October 2024.

1. Introduction

1.1. Overview

There are many applications for the technologically important mid-infrared (MIR) region of the electromagnetic spectrum (2 – 5µm), these include but are not limited to: gas sensing, medical diagnostics, infrared imaging and defence [1-3]. When considering gas sensing, there are a plethora of industrial and greenhouse gasses with absorption spectra which lie in this wavelength range, including: methane (CH_4: 3.3 µm), carbon dioxide (CO_2: 4.2 µm), carbon monoxide (CO: 4.5 µm) and nitric oxide (NO: 5.2 µm) [4]. This is due to the rotational bond energies of many molecules lying in this range, allowing them to be detected, the gasses and their corresponding absorbance bands can be seen in Figure 1.1. Although there is a great deal of technology established employing mid-infrared emitters for the aforementioned applications, there are constantly novel uses being discovered.

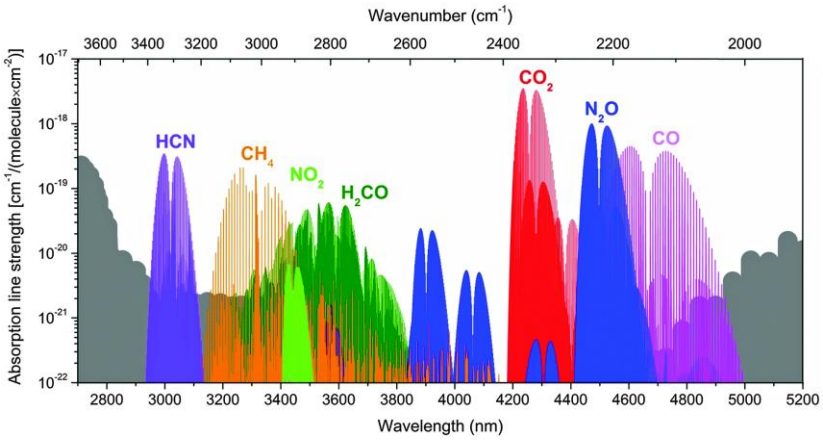

Figure 1.1: the gas absorption spectra from 2.8 - 5.2 µm, showing the absorption strength of each gas at various wavelengths [5].

One potential novel application of the MIR spectrum is in the identification of plastics, this is an extremely important process, especially in plastic sorting facilities which recycle plastic. One factor which limits the efficiency of plastic recycling is the non-detectability plastics which are dyed black using carbon-black pigment by current technologies. This is due to the wavelength of light – Near Infrared (NIR) – used in current optical sorting technology in plastic recovery facilities (PRFs) being completely absorbed by the carbon black pigment. Several solutions have been proposed for this. One, is the creation of black pigments which can be detected using NIR radiation, however, this new pigment does not have the benefits of carbon-black pigment as will be discussed in section 5.4. Another laser-based technology which detects the plastics using a plethora of mechanisms, often incorporating artificial intelligence methodologies; this has the

drawback of being extremely energy intensive and non-portable. However, some success has been realised in the detection of carbon-black plastics using the MIR spectrum [6-8]. Using MIR radiation, it could be possible to detect black plastics using an array of LEDs, which would reduce power consumption and allow for the miniaturisation of the technology. To explore this, FTIR scans were conducted on samples of non-black and black commonly recycled plastics to see what energies corresponding to the 2 – 5 μm wavelength range show reflection peaks. The results show that for polyethylene, polypropylene and polyvinylchloride, there are distinguishable spectral fingerprints between 3.3 – 3.6 μm. This wavelength range was used as it is the MIR region in which room temperature operational LEDs can be successfully created.

III-V alloys have shown great promise in creating high quality semiconducting optical devices operating in the MIR range, including: light emitting diodes (LEDs) [9, 10], lasers [11, 12] and photodetectors [13, 14]. The reason this material system can be used to make devices emitting in this wavelength range is due to the alloys having bandgaps which correspond to these wavelengths at room temperature. Moreover, the similarities in lattice constants of the alloys allow complex heterostructures, including alloys comprised of three or more different elements, to be grown which can be further used to tailor bandgap, emission spectra and external efficiency. Moreover, growing thin film heterostructures allows the use of quantum confinement to improve emission quality and further tailor alloy bandgaps. Since their discovery for use in optical semiconductors around half a century ago, a great deal of research and development has been conducted on this material system, leading to great advances in the field. The development of growth methods such as Molecular Beam Epitaxy (MBE), Metalorganic Vapour-Phase Epitaxy (MOVPE) and Liquid Phase Epitaxy (LPE) have furthered the ability to grow complex, thin film structures.

Despite their promise as room temperature emitters and detectors, there are several factors which limit the performance of these devices, especially for LEDs and lasers. This includes non-radiative recombination and poor light extraction (internal and external efficiency). These are caused by mechanisms of charge carrier recombination not resulting in the production of a photon and the difference in refractive indices between semiconductor and air. There have been several solutions proposed to these problems, for non-radiative recombination, the growth of strained epitaxial layers and tuning the bandgap. The use of Distributed Bragg Reflectors (DBR) mirrors has shown the ability to improve light extraction from the semiconductor system.

This research was conducted with the Centre for Material Social Futures (MSF) [15] at Lancaster University. The aim of MSF, funded by the Leverhulme trust, is to bridge the gap between research undertaken by social and physical sciences. Because of this, as well as the research

conducted in optoelectronics and spectroscopy relating to black plastics, this research also includes: a review of plastics, the problems they cause and how this relates to governments, non-governmental organisations and individuals are given. This is important because, the societal problems caused by plastic is widespread, being largely known by the public all over the world. Plastics came into wide-scale production after WWII, before which it had been widely used in the military but not entered the commercial space. Since then, an estimated 8.3×10^9 metric tons (Mt) of virgin plastics have been created with annual production going from 2Mt in 1950 to 380Mt in 2015 with an average growth rate of 8.4% annually [16]. Despite the fact that in the natural environment, it can take a minimum of around 20 years and a maximum of around 200 years or more for plastics to decompose [17]. When plastics were first produced, they were just discarded, since then, plastic recycling has increased by ~0.4% each year to the current rate of 18% [16]. This is largely caused by the linear economy that they exist in, with plastics being produced, used, then discarded. Causing a build-up of plastics in land-fill sites due to them not breaking down naturally. The relatively common process of plastic recycling has gone someway in alleviating this problem; however, the process is not currently extensive enough.

Based on the FTIR scans conducted and literature around the absorption spectra of plastics/polymers, strained, type-I $In_xGa_{1-x}As_{1-y}Sb_y/Al_zGa_{1-z}As_{1-w}Sb_w$ quantum wells were developed for emission around 3 µm. This utilised strained quantum wells to reduce non-Auger recombination and the large wavefunction overlap to increase the rate of radiative recombination. The active regions were grown and characterised to see their performance and were then integrated into LED structures, giving room temperature emissions. This culminated in developing the system with GaSb barriers, i.e. z = 0 and w = 1, which creates a less complex growth due to Al cells of the MBE not being required and allowed for longer wavelengths to be realised, it also allowed for longer wavelengths to be realised.

As well as this, type-II InAs/InAsSb structures were investigated. This is in attempt to further see if the Ga-free system reduces non-radiative SRH recombination and the type-II bandgap alignment reduces Auger recombination, both of which are severe limiting factors in the performance of MIR optical devices. Samples were grown and characterised at low temperatures (4 K), then integrated into LEDs based on this calibration. These LEDs showed emission from 4K up to room temperature. Modelling was also conducted using Nextnano to find the charge carrier recombination path causing the resultant emission spectrum.

1.2. Aims and overview of thesis

The aim of the research is to develop highly efficient, bright, LEDs emitting in the MIR region for use in the detection of recyclable plastics as well as other molecules. This will be done using novel structures, some of which can be integrated into more complex devices in future research.

Chapter 2: Theory. This chapter aims to provide a comprehensive explanation of the theoretical concepts which are necessary in explaining and understanding the research which has been undertaken.

Chapter 3: Experimental procedures. This chapter lays out an explanation of the experimental methods used in the growth, fabrication, characterisation and analysis of samples and devices discussed in this thesis. Moreover, and explanation of FTIR spectroscopy is given for the analysis of the MIR absorption spectra of black plastics.

Chapter 4: Literature review. This chapter provides an overview of the development of LEDs from their initial conception to the present. Providing details on the material systems used with their benefits and drawbacks. It also discusses the technologies used, such as inter-band cascading structures and integrated distributed Bragg reflectors (DBRs).

Chapter 5: A material social outlook on plastics at the current end of their life. This chapter provides a review of the development of plastic from its conception as an experimental material to its widespread use today. It delves into how plastic is treated in society, and what happens to it at the end of its life. Moreover, an analysis of the implications of the current method of plastic "waste" management on the environment is given. Finally, the FTIR reflection spectra of commonly recycled plastics is taken so that the devices/material systems could be tailored for the purposes of recycling.

Chapter 6: Developing type-I InGaAsSb based active regions for room temperature emission around 3.3 µm. This chapter discusses the development of type-I active regions based on $In_xGa_{1-x}As_{1-y}Sb_y$ type-I quantum wells in an $Al_wGa_{1-w}As_{1-z}Sb_z$ barrier system. In this, simulations are carried out to provide information on the bandgaps and critical layer thickness of the system. Then the development of the active regions, as well as their implementation into LEDs are discussed and an analysis of their performance is given.

Chapter 7: Type-II InAs/InAsSb Strain Balanced Superlattices. This chapter discusses the development of low Sb InAs/InAsSb strain balanced superlattices. Band structure simulations and material system simulations were carried out to see how the bandgap changes with varying layer thicknesses and Sb content. Moreover, simulations to see the strain balancing

characteristics of the system were also carried out. Both active region analysis and integration of the active region into LED structures is discussed.

Chapter 8: Conclusion. A summary of the results will be given to finalise the thesis and a discussion of where they fit into the existing literature. A brief discussion of where this research could lead will also be given.

2. Theoretical concepts

2.1. Semiconductor physics

2.1.1. Energy bands of semiconductors

When considering a single atom, the electrons surrounding the nucleus form discrete energy levels, based on the Schrödinger equation – which defines the energy of an electron in the presence of a certain potential energy. The Pauli exclusion principle – which states that no two electrons can occupy the same quantum mechanical state [18] also affects the discrete energy level that electrons can take. However, when atoms are spaced closely together, the coulomb interaction between outer electrons, as well as the Pauli exclusion principles, causes the discrete energy levels to distort into quasi-continuous energy bands [18]. Energy bands are a quasi-continuous range of energies which an electron in a given band can take. As well as creating energy bands, due to wavefunction overlap the electrons in the outermost full energy band (the valence band) become delocalised and can move between different atoms in the space surrounding them, this causes atomic bonds between atoms. It is only in higher energy levels, where there are more electrons that the quasi-continuous energy bands are formed.

When lots of atoms are held together in a structure, usually via covalent bonds, i.e. when valence electrons from each atom are “shared” between atoms. This gives a situation in which electrons in the valence bands are sufficiently close together that energy levels coalesce and form energy bands. In a crystal structure, such as a quarter of a two-inch wafer which will be discussed throughout this thesis, the number of atoms is generally of the order of Avogadro’s constant (10^{23}). This means that there are many valence electrons in proximity, so many wavefunctions are overlapping. Causing energy bands to form, especially in the valence band as previously discussed. As well as a valence band, there is also an available state of energies above this, known as the conduction band. The conduction band is the band in which electrons are free to move around the lattice. It is less populated than the valence band and charge carriers are more loosely contained by the electrostatic force from the nucleus. The position of the conduction band relative to the valence determines if the material is: conductive, insulating or a semiconductor.

If there is an overlap between the conduction and valence bands, this makes the material a conductor. This is because in its equilibrium state, there are always electrons in the conduction band, so if an electrical bias is applied this type of material, the electrons in the conduction band will flow. A layout of the valence and conduction band of a conductor can be seen in Figure 2.1 (a). A semiconductor and insulator are different from a conductor in that they both

have an energy gap between the conduction and valence bands. These are energy states within the material that the charge carriers cannot occupy. Semiconductors and insulators are different to one another in that the gap between the conduction and valence band in a semiconductor is much smaller than that of an insulator. Examples of these bandgaps are displayed in Figure 2.1 with (b) being a semiconductor and (c) being an insulator, the bandgaps, E_g and E_i are the respective bandgaps characterised by $E_g << E_i$. In a semiconductor, it is possible to cause charge carriers to move from the valence to the conduction bands given sufficient energy, whereas this is not possible in an insulator.

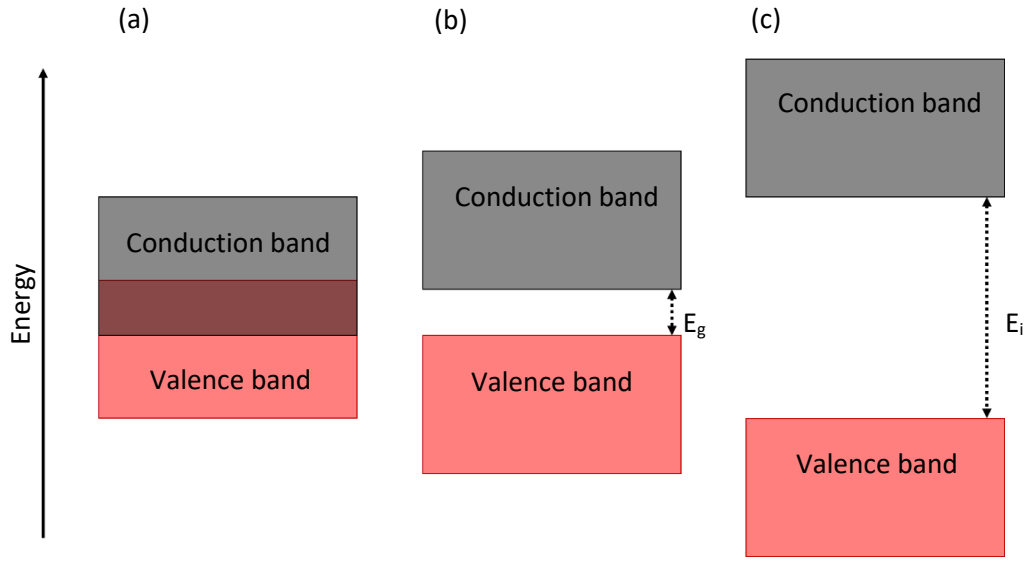

Figure 2.1: Diagram displaying the valence and conduction band position in: (a) conductors, (b) semiconductors (bandgap E_g) and (c) insulators (bandgap E_i).

At 0 K, because there is no thermal energy in any charge carriers, they remain in the valence band for a semiconductor or insulator. In a conductor, they will be able to enter the conduction band no matter what the temperature due to overlapping bands. However, when the temperature is increased, the charge carriers will obtain thermal energy. In a semiconductor, this thermal energy is sufficient to move the carriers from the valence band to the conduction band. As the temperature increases, the charge carriers have more thermal energy which causes more of them to move into the conduction band, this is done according to the Fermi distribution. In an insulator, because the energy gap between the conduction and valence band is so large, there is a negligible amount of charge carriers which will move to the conduction band, even at room temperature (~300K). Semiconductors which have no excess charge carriers are known as intrinsic charge carriers, those with an excess of electrons are known as n-type semiconductors and those with a deficit of electrons (excess of holes) are known as p-type semiconductors.

As well as the energy bands splitting into conduction and valence, due to degeneracy caused by the angular momentum of particles in the band. This splits the valence band into three sub bands: heavy-hole, light-hole and spin orbital, this split is caused by different values of angular momentum and the spin values of the charged particles in the valence band [19].

2.1.2. Bandgap temperature dependence

As mentioned in section 2.1.1, there are various effects that temperature has on the filling of various bands with charge carriers. However, it also has an effect on the energy of the charge carriers and the band they occupy. Temperature also influences the size of the bandgap. This is because as the temperature changes, the position of the conduction and valence band varies; this change in position is caused by multiple factors. As temperature changes, the distance between atoms in the lattice will change, this usually follows a linear relationship with temperature. However, at very low temperatures this relationship can be nonlinear. If the spacing between the lattice changes, the difference in proximity of the electrons to other atoms in the lattice also change, this varies the force binding electrons to the atom [20]. Another factor is the lattice-electron interaction, which can change greatly with temperature. This change is due to electrons being less tightly bound to the atoms in the lattice as temperature increases, and vice versa. Weaker bound electrons require less energy to move into higher energy bands, this means that as temperature increases, the bandgap decreases. The bandgap as a function of temperature can be modelled using the Varshni equation, shown in equation 2.1 [20].

$$E_g = E_g(0) - \frac{\alpha T^2}{T + \beta} \qquad 2.1$$

In this equation, $E_g(0)$ is the bandgap at 0 K; α and β are both physical constants which have no precise definition, however, β is related to the Debye temperature of the material. The material parameters are generally found experimentally; this has been documented extensively for the III-V material system in “Band parameters for III-V compound semiconductors and their alloys” by Vurgaftman et. al. [21].

The Varshni equation is very effective at modelling bandgaps at higher temperatures. Although, at lower temperatures, localisation and exciton effects causes the emission spectrum to be red shifted relative to the Varshni fit. Models such as the Vina and Passler equation seek to remedy these effects by adding extra parameters to the equations, terms accounting for exciton localisation [22]. These parameters are difficult to predict based on the structure and alloy of

the device, so they are good at finding electron localisation effects based on the bandgap but are not as effective at predicting the low temperature bandgap behaviour of a material.

2.1.3. Doping and bandgap alignment

As previously mentioned, charge carriers can be excited into the conduction band via thermal energy, in intrinsic semiconductors, this occurs as temperatures exceed 0K [23]. It is also possible to change the predominant charge carriers in the material by adding “donor” or “acceptor” atoms/molecules to the intrinsic semiconductor, this process is known as doping and the materials used are dopants. Donors are molecules which have one more electron in their outer energy-band than the molecule they are being added to. Accepters have one fewer electron in their outer energy band in comparison to the molecule they are being added to. When donors are added to an intrinsic semiconductor, there are excess electrons in the conduction band and the material is referred to as an n-type semiconductor. When acceptors are added to an intrinsic semiconductor, there is a deficit of electrons (a surplus of holes in the valence band) and the material is known as a p-type semiconductor. This has the effect of making the predominant carrier type “holes”, or missing electrons in the valence band. These holes can be modelled as an electron with a greater relative mass and positive charge [23]. Because the Fermi-level denotes the equilibrium point between the charge carrier distribution in the conduction and valence bands. In an intrinsic semiconductor, it lies in the centre of the bandgap. If a donor atom is added to the material, there is an excess of electrons in the conduction band, so the equilibrium point is closer to the conduction band edge, meaning the Fermi-level is closer to the conduction band. The inverse is true for a p-type semiconductor, as acceptor atoms are added, there are more charge carriers in the valence band, so the Fermi level is closer to the valence band. This effect can be seen in Figure 2.2 (a), where the band-edges are of the same energy, but the Fermi level has changed. Adding donors to a material is known as “n-type” doping, and adding acceptors to a material is known as “p-type” doping.

When two semiconductors meet at a continuous point, it is known as a semiconductor-semiconductor junction. Junctions are defined as a heterojunction or a homojunction depending on if the semiconductors at either side are made of the same material or not. A junction of a material where one side is p-doped and the other is n-doped is referred to as a p-n junction. If a p-type and n-type semiconductor are bought together, electrons from the n-type side and holes from the p-type side will flow into the oppositely doped side due to diffusion. This diffusion current then causes a build-up of electrons in the p-type region and a build-up of holes in the n-type region either side of the junction. Eventually, this local build-up of charge causes a potential

barrier which stops more charge carriers diffusing across, this section where charge carriers have diffused across is known as the depletion region. Because of the new distribution of holes and electrons throughout the material, the relative energy levels of the p-doped regions and n-doped regions to shift relative to one another. This new distribution throughout the structure causes the Fermi level to become constant, as opposed to the p-type and n-type regions in isolation. A visual representation of this can be seen in Figure 2.2 (a) and (b).

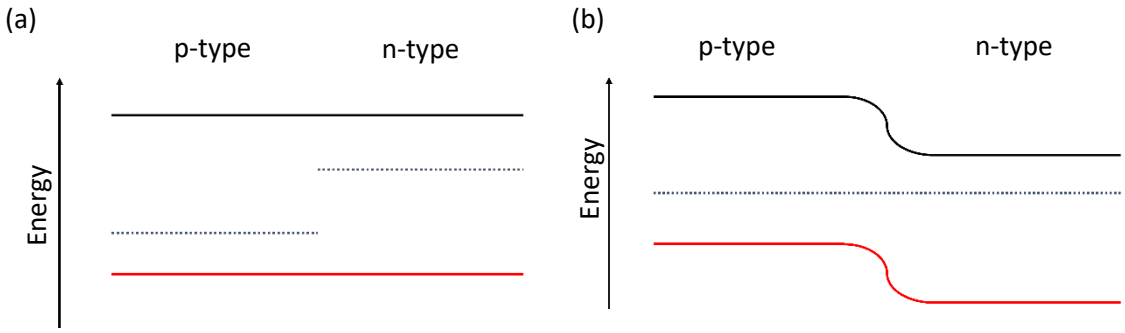

Figure 2.2: Band-edge diagrams showing the relative band edge positions: black, conduction band; red, valence band; grey dotted, Fermi level. (a) Before charge carriers settle to equilibrium, (b) at equilibrium point.

With the n-doped and p-doped regions on either side, this causes a potential difference across the depletion region, given by equation 2.2 [23], where N_a is the concentration of acceptors, N_d is the concentration of donors and n_i is the intrinsic charge carrier concentration of the material.

$$V_0 = \frac{kT}{e} ln\left(\frac{N_a N_d}{n_i^2}\right) \qquad 2.2$$

The depletion region also has a finite width. This is defined by how far charge carriers travel into where they create this equilibrium region – i.e. where the material is intrinsic. The width is based on the bias applied across the junction, because this effect the equilibrium of charge carriers. This width is given in equation 2.3, where ε_0 is the permittivity of free space, ε_r is the relative permittivity of the material and V is the bias applied over the junction.

$$W = \sqrt{\frac{2\varepsilon_0 \varepsilon_r}{e}(V_0 - V)\left(\frac{1}{N_A} + \frac{1}{N_D}\right)} \qquad 2.3$$

Whereas in a homojunction, two of the same materials with the same bandgap form a junction; in a heterojunction, two different materials come together to form a junction. In heterojunction structures, there are three different ways in which bandgaps can be aligned based on where their conduction and valence bands lie relative to the other material in the junction. These are: type-I, type-II and broken gap alignments. In type-I junctions, one of the materials will have a

higher conduction band-edge and lower valence band-edge than the other material. In type-II junctions, one material will have both a higher conduction band-edge and the same material will have a higher valence band-edge than the other material. In broken gap junctions, the valence band-edge of one material band-edge is higher than the conduction band-edge of the other material. These junction alignments can be seen in Figure 2.3 (a), (b) and (c) [23].

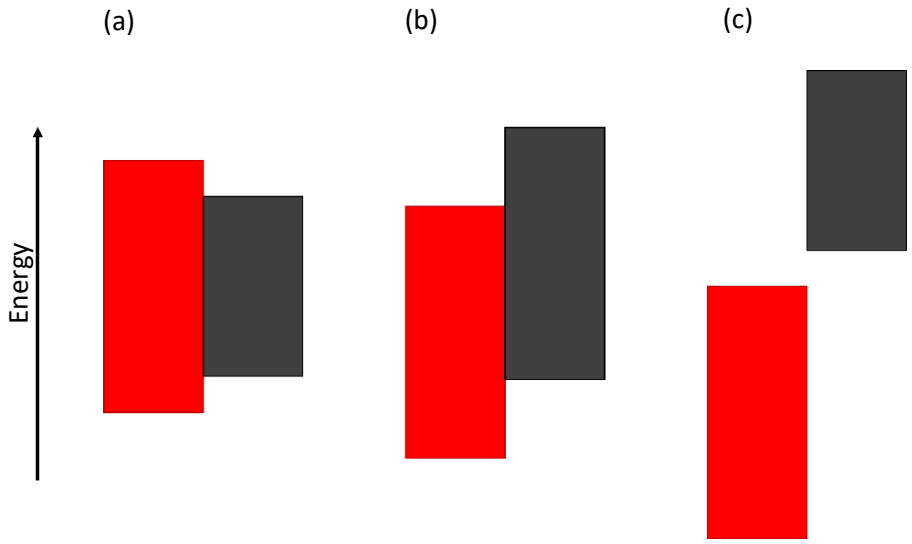

Figure 2.3: the bandgap alignments for: (a) type-I, (b) type-II and (c) broken-gap junctions. Red signifies material 1, grey signifies material 2.

2.1.4. Quantum confinement in semiconductors

When charge carriers move through a bulk semiconductor, they are unconfined; they can move unrestrained in the x, y, and z coordinate system. It is possible to build heterostructures which confine the freedom of movement of electrons to less than three dimensions. Using quantum wells, it is possible to achieve two-dimensional confinement; quantum wires give one-dimensional confinement, and quantum dots give zero-dimensional confinement. Zero-dimensional confinement is where the electron is completely spatially confined. These structures are created using heterojunctions, where a potential well can be created, it is in this well that the charge carrier will be confined. In order to cause confinement, the dimensions of the confinement has to be on the scale of the De Broglie wavelength of the charge carrier it is confining. The De Broglie wavelength is described in equation 2.4 where λ is the De Broglie wavelength, h is Planck's constant and p is the momentum of the electron [24], this is generally ~10 nm or smaller.

$$\lambda = \frac{h}{p} \qquad 2.4$$

If the confining space is of this order of magnitude, then the charged particle will be spatially confined, as it acts as a wave between two potential barriers which it cannot fully tunnel through. In a bulk structure, the electron can have any energy if it lies within the corresponding band. In a quantum confined structure, the particle acts in a quantum manner, so its energy will be discrete with respect to the confinement. The energy level of the surrounding bands should be such that it creates a potential barrier at either side the confining region. Confinement has two types, in type-I confinement, the electrons and holes are both confined in the same space, this would be both charge carriers in the same material in Figure 2.3 (a). In type-II confinement, the charge carriers are confined in different spaces, i.e., the electrons would be in one material and the holes confined in another, as shown in Figure 2.3 (b) and (c). Because being in a quantum well causes the charge carriers to have discrete energy level in their respective band, it changes the energy that charge carriers occupy in the well respective to the band edge. In a system where there is quantum confinement, the bandgap is defined as the difference in energy from the electron energy level to the hole energy level. Thus, the bandgap of the system can be changed by changing the confinement conditions, such as well width and confinement energy.

2.1.5. Density of states

The density of states (DoS) in a semiconductor is a measure of how many available states there are at a given energy. This is an important part of analysing how a device or sample will perform, based on how many charge carriers will be present between two giving energies. In bulk semiconductors (no quantum confinement), the density of states of charge carriers is given by the density-energy relationship shown in equation 2.5. This shows that the density of states is a continuous function of energy.

$$Z(E) = \frac{4\pi}{h^3}(2m_e^*)^{\frac{3}{2}}E^{\frac{1}{2}} \qquad 2.5$$

Here, $Z(E)$ is the density of states, *h* is Planck's constant, m_e^* is the effective mass of the charge carrier and E is the relative energy from the lowest point of the energy band. If convolved with the Fermi-Dirac distribution function, this shows the number of electrons of a given energy at any point in the energy band [23].

When considering a two-dimensional quantum well, the density of states is given by the formula shown in equation 2.6, where *n* is a positive integer greater than 1, and $\hbar$ is the reduced Planck's constant, i.e., $h/2\pi$.

$$Z(E) = \frac{nm_e^*}{\pi\hbar^2} \quad 2.6$$

This two-dimensional density of states is independent of energy, the density in each quantum state is solely defined by equation 2.6 [23]. This means that the density of states is dependent on the order of the energy level based on the quantum state, creating a "step" function of density of states, rather than the continuous bulk model.

2.2. Carrier transport and recombination

2.2.1. Charge carrier injection

When applying a potential difference across a semiconductor, a current will flow if there is an excess of charge carriers in the conduction or the valence band, where the charge carriers less bound to the atom and can move somewhat between multiple atoms. The flow of current will be dependent on the direction of the applied potential difference, as well as if the charge carriers are in the conduction or valence bands. When considering a p-n junction, the direction in which the potential difference is applied is known as a bias. If the positive potential terminal is connected to the p-type doped region and the negative connected to the n-type doped region then the bias is referred to as "forward bias". When the positive terminal is connected to the n-type doped region and the negative terminal connected to the p-type region, this is referred to as "reverse bias". Examples of a forward and reverse bias being applied across a p-n junction can be seen in Figure 2.4 (a) and (b) respectively.

(a) (b)

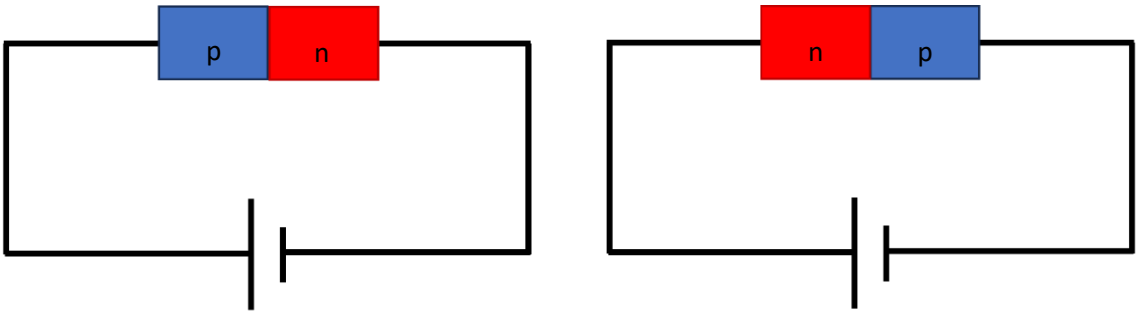

Figure 2.4: potential difference applied across a semiconductor junction for (a) forward bias and (b) reverse bias.

When a forward bias is applied across the p-n junction, this causes a reduction in the potential barrier between the two regions. Because of this, the diffusion current is increased, which causes electrons from the n-type region and holes from the p-type region to enter the depletion region. The carriers are then replaced by the driving source [23]. As charge carriers are injected into the depletion region, they recombine releasing energy equal to the bandgap that they cross.

As the forward bias across the junction is increased, the potential that the charge carriers cross is lower meaning more enter the intrinsic region, thus increasing the current passing through the device. The opposite to the reverse bias, i.e. having the positive terminal connected to the n-type region and the negative terminal connected to the p-type region. The causes holes in the p-type region to move towards the positive terminal and vice versa for electrons in the n-type region. This causes the width of the depletion region to increase as more electrons flow into the p-type and holes flow into the n-type [23]. The different effects of bias on the junction creates the effect of current flowing easily one-way (forward bias) and not flowing in the other direction (reverse bias), this creates devices which do this are known as diodes. The current that a forward bias causes in an ideal diode is given by the Shockley equation, shown in equation 2.7. This describes the current of a diode with cross sectional area A, hole and electron diffusion constants D_p and D_n respectively; electron and hole charge carrier lifetimes of τ_n and τ_p respectively; intrinsic carrier density of n_i and donor and acceptor carrier densities of N_D and N_A respectively.

$$I = eA\left(\sqrt{\frac{D_p}{\tau_p}}\frac{n_i^2}{N_D} + \sqrt{\frac{D_n}{\tau_n}}\frac{n_i^2}{N_A}\right)\left(e^{\frac{eV}{kT}} - 1\right) \qquad 2.7$$

This is how an ideal diode would operate; however, physical devices do not operate in this manner, however, different types of resistances limit the performance of the device in different ways. Series resistance (R_S) occurs due to resistance of the intrinsic region as it has fewer free charge carriers, as well as resistance coming from the contacts. Parallel resistance (R_P) occurs when current bypasses the junction, by mechanisms such as surface currents. This causes the current of a real diode to be described by equation 2.8, n_{ideal} is the ideality factor of the diode, this should be around 1 to 2. Series resistance causes an increase in the resistance of charge carriers under forward bias, parallel resistance causes a lowering of resistance under reverse bias. An ideal diode would have an infinite parallel resistance so that no current bypasses the junction. This equation also considers how temperature will affect the system.

$$I - \frac{v - IR_s}{R_P} = eA\left(\sqrt{\frac{D_p}{\tau_p}}\frac{n_i^2}{N_D} + \sqrt{\frac{D_n}{\tau_n}}\frac{n_i^2}{N_A}\right)e^{e(V-IR_s)/n_{ideal}kT} \quad 2.8$$

2.2.2. Recombination processes

When charge carriers are injected into the intrinsic region of a semiconductor under forward bias, they will be forced to cross the bandgap. This occurs at the same rate for electrons and holes. This causes the electrons and holes to recombine with one another, creating energy equal to that of the bandgap. This energy can either be converted into a photon – a process known as radiative recombination; alternatively, it could move charge carriers into different energy bands, i.e. Auger recombination, or emit the energy as lattice vibrations (phonons), i.e. Shockley-Read-Hall (SRH) recombination [23]. For the purposes of light emitting diodes, radiative recombination is the desired process, as photons of a predictable wavelength are generated. Non-radiative recombination processes are undesirable, because they do not convert charge carriers into photons, thus reducing the efficiency of the device.

There are several ways to cause charge carrier recombinations in semiconductor materials. One method is using electrical pumping of a p-n junction as described in section 2.2.1, alternatively pumping via a laser emitting photons with a higher energy than the bandgap of the material being pumped. The spectrum of light created via electrical pumping is known as electroluminescence and via photon pumping is known as photoluminescence. Whereas in electrical pumping, charge carriers are pumped into the intrinsic region by applying a bias. For photon pumping, carriers in the valence band are given sufficient energy to cross into the conduction band when they absorb a high-energy photon from a laser. They will then de-excite, losing that energy and travel back down into the valence band emitting a photon with energy equal to the bandgap.

2.2.2.1 Radiative recombination

Radiative recombination occurs when charge carriers from one band, recombine with charge carriers from another band, causing the release of energy in the form of a photon. Because it is free charge carriers which are injected into the intrinsic region, the rate of recombination (R) is given by equation 2.9. This gives a direct proportionality to the electron and hole densities.

$$R = Bnp \tag{2.9}$$

In equation 2.9, n is the electron concentration and p is the hole concentration. B is a proportionality constant known as the Bimolecular recombination coefficient [25]. As dopants are added to a semiconductor, it increases the concentration of one charge carrier type whilst decreasing the other. Because of this, the product of the of the n-type and p-type dopant concentration is equal to the square of the intrinsic charge carrier concentration, i.e. $np = n_i^2$.

The transition from the conduction to valence band of a charge carrier can also be described using the transfer matrix, shown in equation 2.10, $W_{i\to j}$ is the recombination from state i to state j.

$$W_{i\to j} = \frac{2\pi}{\hbar}\left|H'_{ji}\right|\rho\left(E = E_g + \hbar\omega\right) \tag{2.10}$$

ρ is the density of states at a given energy and $\left|H'_{ji}\right|$ is the transitional matrix element. When considering a non-time-dependant transitional matrix element, the matrix element is given by the formula in equation 2.11. ψ_i is the wavefunction of the charge carrier in state *i*, $\psi_j{}^*$is the complex conjugate of the wavefunction of the charge carrier in state *j*, this is then integrated over the space it is contained in [25]. The space it is confined in is technically infinite, but the wavefunction will go almost to zero outside of the quantum well and barrier system.

$$\left|H'_{ji}\right| = \int_{-\infty}^{\infty} \psi_i(x)\psi_j{}^*(x)\,dx \tag{2.11}$$

The transitional matrix element is also known as the wavefunction overlap; it shows that charge carriers which are spatially confined around one another are more likely to recombine. In bulk semiconductors, the transitional matrix element is given by equation 2.12, where m_e^* is the effective mass of the electron and Δ is the spin orbital splitting. This is derived using the four band Kane model.

$$\left|H'_{ji}\right| = \frac{m_e^2 E_g\left(E_g + \Delta\right)}{12 m_e^*\left(E_g + \frac{2}{3}\Delta\right)} \qquad 2.12$$

In quantum structures, if the wavefunctions of the electrons and holes are known, which can be done through modelling of the quantum structures. The wavefunction overlap can be calculated numerically using equation 2.11. Wavefunction overlap is a normalised constant which varies between 1, for wavefunctions which are completely overlapping, and 0, for wavefunctions which are completely spatially separated.

Due to the energetic states available to charge carriers, when recombination occurs, there is a distribution of energies that photons can take. The intensity of this emission spectra for a bulk semiconductor, as a function of energy - *I(E)* – is given by the distribution shown in equation 2.13. This means that the minimum energy photons emitted are equal to the bandgap energy.

$$I(E) = \sqrt{E - E_g}\, e^{-\frac{E}{kT}} \qquad 2.13$$

The maximum intensity of this emission spectra is equal to $E_g + \frac{kT}{2}$, and the linewidth is equal to $1.8kT$. However, when considering quantum well structures, although the maximum intensity remains the same, the distribution is Gaussian and the linewidth is reduced to $\ln(2)\, kT$ [26].

2.2.2.2 Shockley-Read-Hall (SRH) recombination

Shockley-Read-Hall recombination is a non-radiative recombination process. It occurs when a charge carrier moves from an energy band to an energy trap state rather than to another band. Trap states occur in a bandgap due to non-uniformities in the lattice structure. This can include: non-native atoms in the structure; dislocations, defects and non-uniform alloy structure [27]. Trap states can trap both electrons and holes; their effectiveness at trapping charge carriers is determined by their energy relative to the Fermi level and the lifetime of the trap state. The lifetime of a carrier in a trap state is given in equation 2.14; N_T is the trap concentration, v_i is the charge carrier velocity σ_i is the capture cross sections of the traps for the charge carriers.

$$\frac{1}{\tau_i} = N_T v_i \sigma_i \qquad 2.14$$

The rate of SRH recombination in a system is given by the formula in equation 2.15. Where p_0 and n_0 are the intrinsic hole and electron concentrations; Δn and Δp are the electron and hole

doping densities, p_1 and $n_1$are the concentrations of holes and electrons respectively near the Fermi level.

$$R_{SR} = \frac{p_0 \Delta n + n_0 \Delta p + \Delta n \Delta p}{\left(N_T v_p \sigma_p\right)^{-1}(n_0 n_1 \Delta n) + (N_T v_e \sigma_e)^{-1}(p_0 p_1 \Delta p)} \quad 2.15$$

When the material is approximately intrinsic, the lifetime of the carriers is given by equation 2.16.

$$\tau = \tau_{n_0}\left[1 + \cosh\left(\frac{E_T - E_F}{kT}\right)\right] \quad 2.16$$

From equation 2.15, the rate of SRH recombination is inversely proportional to the carrier lifetime, thus, the rate is lower when the carrier lifetime is larger. Equation 2.16 shows trap states that are close to the Fermi level will decrease the lifetime. Also, at lower temperatures, the cosh function will be lower, so the lifetime will also be lower. SRH recombination rates are highest when the trap states in the material are near the Fermi level – which is generally around the middle of the bandgap in the intrinsic region. At high temperatures, the carrier lifetime is decreased, meaning at higher temperatures SRH recombinations will increase, thus decreasing the efficiency of any device [27]. Because SRH recombination is only dependent on one charge carrier, as it is an electron or a hole moving into a trap state and releasing energy as a phonon, the rate of SRH recombination has a linear proportionality to the number of charge carriers.

2.2.2.3 Auger recombination

Auger recombination is another non-radiative recombination process which takes place between three charge carriers. It occurs when an electron and a hole recombine. The energy from this recombination then causes a charge carrier in another band to move to a higher state in that band, or to move up into a higher energy band. There are four ways in which this can occur. One is, Conduction – heavy-hole, light-hole – heavy-hole (CHLH), this is when a recombination from the conduction band to the heavy-hole band causes a hole to move from the light-hole band to the heavy-hole band. Another is, Conduction – heavy-hole, conduction – conduction (CHCC), this is when recombination causes an electron in the conduction band, to move to a higher state in the conduction band. Moreover, conduction – heavy-hole, heavy-hole - heavy-hole (CHHH), is when a recombination causes a hole in the heavy-hole band to move to a higher state in that band. Finally, conduction – heavy-hole, spin orbital – light-hole (CHSL) when a recombination causes a charge carrier from the spin orbital to enter the light-hole band. These recombination processes can be seen in Figure 2.5 (a), (b), (c) and (d).

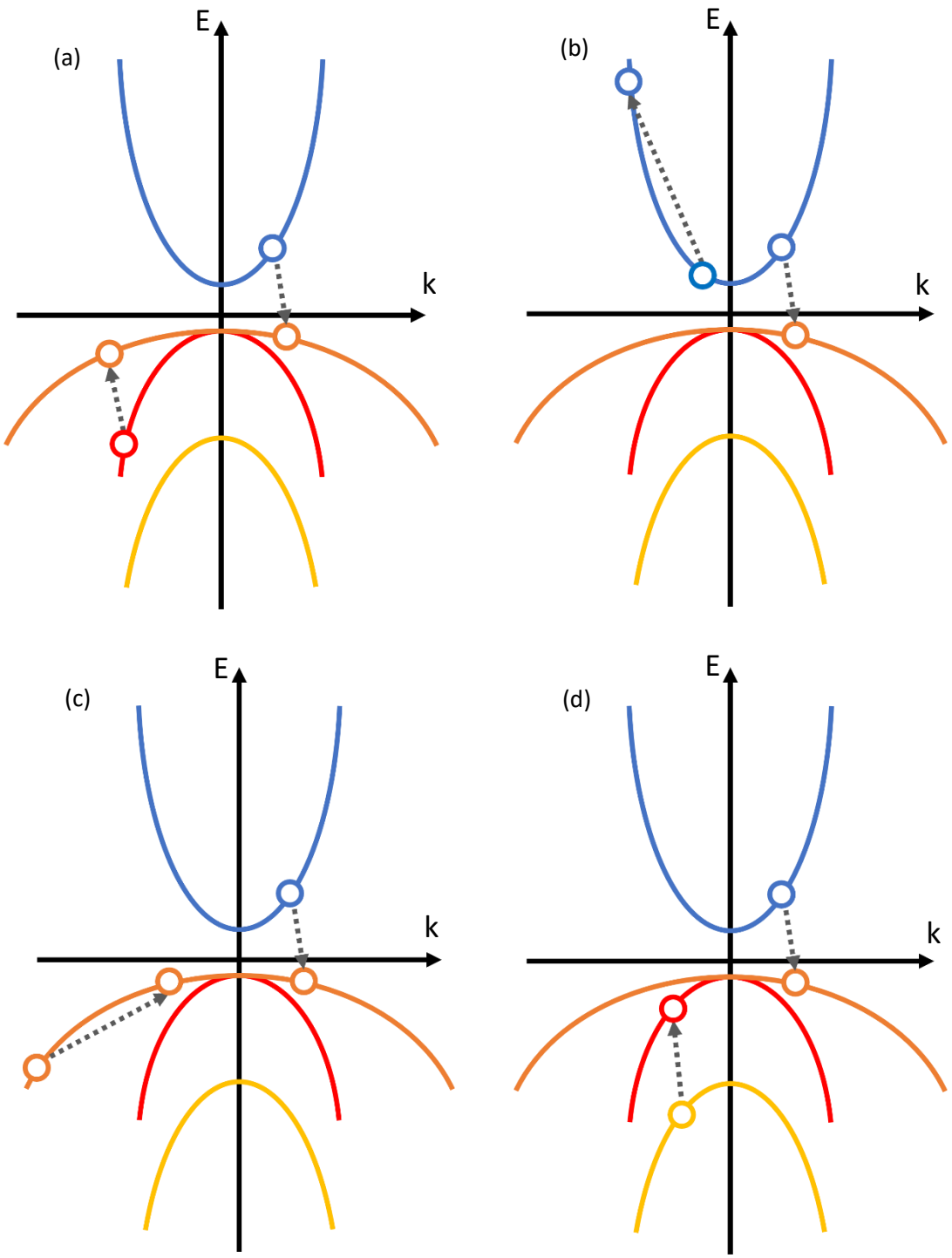

Figure 2.5: Energy (E), wavevector (k) diagrams showing the Auger recombination processes for (a) CHLH, (b) (CHCC), (c) CHHH and (d) CHSL. The blue line represents the conduction band, orange the heavy-hole, red the light hole, and yellow the spin-orbital.

Radiative recombination is proportional to the square the charge carrier concentration, due to it being caused by two charge carriers and SRH has a linear relationship as aforementioned. There are three charge carriers which partake in Auger recombination, so the Auger rate follows a cubic relationship, this is shown in equation 2.17. This is assuming that the electron and hole carrier concentration are equal.

$$R = C_0 e^{-\frac{E_a}{kT}} n^3 \tag{2.17}$$

In this case, C_0 is a proportionality constant which is different for specific materials, E_a is the activation energy of the specific process. The CHCC and CHSL activation energies are shown in equation 2.18 and 2.19 respectively.

$$E_a^{CHCC} = \frac{m_c}{m_c + m_{HH}} E_g \tag{2.18}$$

$$E_a^{CHSH} = \frac{2m_c + m_{SO}}{2m_{HH} + m_c - m_{SO}} \left| E_g - \Delta \right| \tag{2.19}$$

Because the Auger recombination rate is dependent on band energy parameters and relative mass of charge carriers, it is possible to use bandgap engineering techniques to quench Auger recombination. However, because activation energies for Auger recombination are directly proportional to the size of the bandgap, as wavelength increases the Auger activation energy decreases. This means that Auger recombination is very prevalent in longer wavelength devices [28]. There is also a strong temperature dependence of the Auger recombination rate, this is shown in equation 2.20.

$$R \propto e^{-\frac{E_a}{kT}} T^3 \tag{2.20}$$

The cubic dependence of temperature for the Auger recombination rate shows that as temperature increase, the Auger recombination rate will increase. This is because the cubic term dominates at room temperature whereas a negative inverse exponential term plateaus. This leads to it being the dominant recombination type at room temperature in low-bandgap III-V semiconductors [29].

2.2.3. Recombination current

The current passing through a p-n junction is prortional to the rate of recombination. This is because for current to flow in the device, it must pass the bandgap, causing the charge carriers to recombine via the mechanisms discussed in section 2.2.2. It is possible to work out the rate at which each different type of recombination mechanism is occurring in a device. The current running through a device is given by equation 2.21, where A, B and C correspond to the contribution to current from: SRH, radiative and Auger recombinations respectively [30].

$$I \propto An + Bn^2 + Cn^3 \tag{2.21}$$

The coefficient for B is proportional to the integrated emission, i.e. the area under the luminescence peak, should then be proportional to n^2. Because of this, if the driving current or input laser power over the square root of the integrated emission is plotted as a function of integrated emission (L), the graph that is essentially plotted is equation 2.22.

$$\frac{I}{\sqrt{L}} \propto A + Bn + Cn^2 \tag{2.22}$$

Plotting software can then be used to find the coefficients of A, B and C, giving the contributions of the different types of recombination mechanisms [30]. This can then be used to determine what proportion of the current in the device is due to different recombination mechanisms. This is important when analysing the efficiency of a device. Alternatively, the relation in 2.23 can be used [31].

$$I \propto \left(\sqrt{L}\right)^z \tag{2.23}$$

By plotting the natural logarithm of input current as a function of the natural logarithm of the square root of the integrated emission the coefficient Z can be found. The Z value will show the dominant recombination mechanism, with 1, 2 or 3 being SRH, radiative or Auger respectively.

The internal efficiency can also be measured using the output power of the device, using the formula shown in equation 2.24. Where P is the output power of the device and η_{opt} is the optical extraction efficiency, given by equation 2.25, where n is the refractive index of the semiconductor material [32].

$$\eta = \frac{Pe}{h\nu I \eta_{opt}} \quad 2.24$$

$$\eta_{opt} = \frac{1}{n(n+1)^2} \quad 2.25$$

2.3. III-V material system

III-V materials are molecules made of atoms from a combination of group-III and group-V atoms. Group-III atoms are: Boron, Aluminium, Gallium, Indium and Thallium; group-V atoms are: Nitrogen, Phosphorous, Arsenic, Antimony and Bismuth.

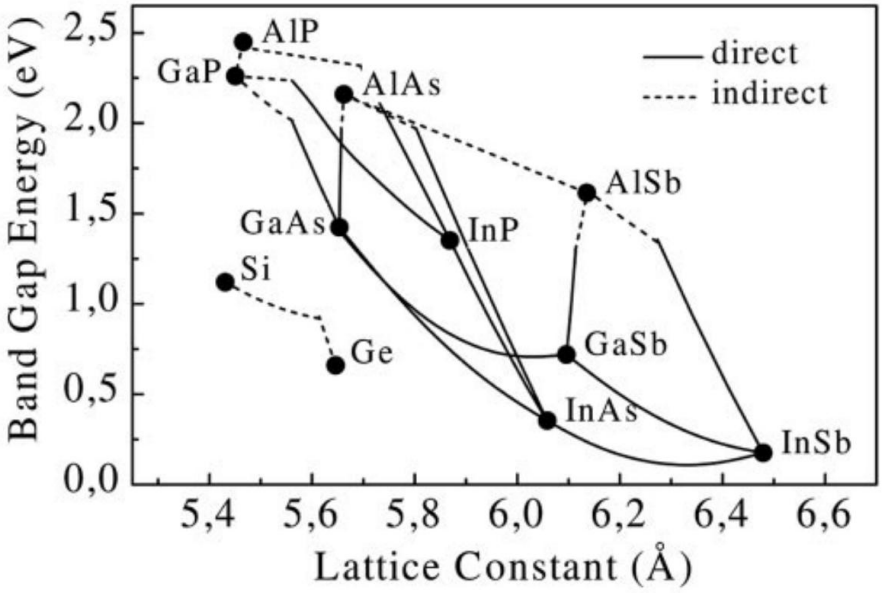

Figure 2.6: bandgap energy vs lattice constant diagram of III-V material system for binary systems created by Bett et. al. [33], the lines connecting binary points show the ternary systems.

When one group-III atom and one group-V atom form a molecule, it has a bandgap with an energy such that the material is classed as a semiconductor, this is known as a binary III-V molecule. Moreover, multiple of these molecules can bond together to form large crystal lattice structures. A selection of binary III-V materials are shown in Figure 2.6, with their bandgap energy plotted as a function of their lattice constant.

2.3.1. Alloys

An alloy is a mixture of two or more binary materials which form a new compound, made of three or more atoms. Ternary compounds are shown in Figure 2.6, in the dotted or dashed line, depending on if the material bandgap is direct or indirect. The lines connecting show the bandgap and lattice constant of ternary alloys. As well as ternary alloys, four or five different atoms can be mixed to create an alloy, these are known as quaternaries and quintenary

respectively. To ensure that covalent bonds form, there has to be equal parts group-III and group-V atoms in the system.

When alloys are created, the bandgap and lattice constant of the alloy is an interpolation of the bandgap and lattice constant of the constituent binary materials. For example, when ternaries are created, out of the binaries AB and AC, if the proportion of binary AB in the ternary is *x* then the lattice constant of AB_xC_{1-x} is given by equation 2.26 [34]. This is known as Vegard's law and the principle can be applied to higher order alloys to find their lattice constants.

$$a_{ABC} = xa_{AB} + (1-x)a_{AC} \tag{2.26}$$

When considering quaternaries, there are two different forms they can take, depending on the portion of group-III and group-V atoms. Two group-III atoms and two group-V atoms (taking the form $A_xB_{1-x}C_yD_{1-y}$); three group-III and one group-V or three group-V and one group-III, (which take the form $AB_xC_yD_{1-x-y}$). The formulae to find each of these respective lattice constants are given in equations 2.27 and 2.28.

$$a_{ABCD} = xya_{AB} + x(1-y)a_{AD} + (1-x)ya_{BC} + (1-x)(1-y)a_{BD} \tag{2.27}$$

$$a_{ABCD} = xa_{AB} + ya_{AC} + (1-x-y)a_{AD} \tag{2.28}$$

The interpolation of the lattice constants for alloy materials follows a linear scheme based on the composition of the alloy. The bandgap of the materials does not follow a linear scheme though. For ternary alloys, there is a constant known as the "bowing parameter", which makes the bandgap interpolation non-linear. The bandgap of the alloy AB_xC_{1-x} is given in equation 2.29 [35]. In this equation, C_{ABC} is the bowing parameter of the alloy, each different ternary alloy will have its own bowing parameter.

$$E_{ABC} = xE_{AB} + (1 \to c)E_{AC} + x(1-x)C_{ABC} \tag{2.29}$$

Likewise, when there is a quaternary system $A_xB_{1-x}C_yD_{1-y}$, the bandgap is given by the formula in equation 2.30. There is no bowing constant for quaternaries specifically but there is a nonlinear mix of the bowing parameters for the ternaries ABC, ABD, BCD and ACD [35].

$$E_{ABCD} = \frac{x(1-x)[yE_{ABC} + (1-y)E_{ABD}] + y(1-y)[xE_{ACD} + (1-x)E_{BCD}]}{x(1-x) + y(1-y)} \tag{2.30}$$

2.3.2. Strained systems

As mentioned in sections 2.1.3 and 2.1.4, in the creation of hetero-junction, semiconductor materials with different bandgaps are bought together. In practice, this is done by growing different III-V materials via various processes on-top of one another. This creates one continuous crystal with abrupt junctions (interfaces) where the alloy turns from one type to another. As discussed in section 2.3.1, different alloys have different bandgaps and lattice constants. Because of this, when different alloys are grown on-top of one another, it causes the lattice constant to change [35]. This change in lattice constant is based on the lattice constant of the substrate that the structure is grown on, the epitaxial layers grown will deform to the lattice constant of the substrate. This is because the substrate is so much large than the epitaxial layers being grown, so it exerts a greater force on the epitaxial layer which is only a few monolayers thick.

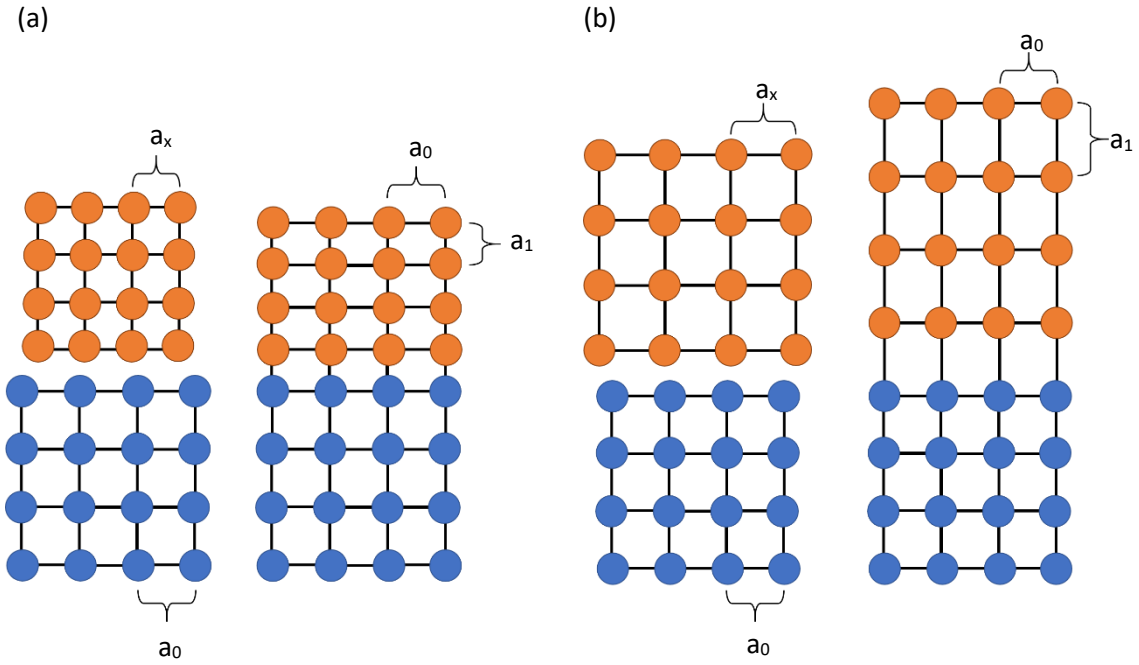

Figure 2.7: Diagrams showing the effect of (a) tensile strain, and (b) compressive strain on the structure of the epitaxial material before (left) and after (right) growth.

Figure 2.7 shows how the epilayer deforms along the surface of the substrate structure under the two different types of strain. These are: tensile strain, which occurs when the epitaxial layer has a smaller lattice constant than that of the substrate; and compressive strain, when the epitaxial layer has a larger lattice constant than that of the substrate. As seen in Figure 2.7, strain causes the epitaxial material to deform, so that it has the same in plane lattice constant as the

substrate, subsequently causing the out of plane constant to change. Tensile strain occurs under the condition, $a_1 < a_x$ and for compressive strain $a_1 > a_x$.

The stress of a system is defined by the ratio of the lattice constant of the substrate over the relaxed epitaxial layers, shown in equation 2.31. This defines the stress parallel to the growth surface, and the stress perpendicular to it – which is the stress in the growth direction. To find the stress in each direction, different lattice constants are used, equations 2.32 and 2.33 show the lattice constants which should be used when calculating each component of strain.

$$\varepsilon_{\parallel,\perp} = \frac{a_{\parallel,\perp}}{a_x} - 1 \tag{2.31}$$

$$a_{\parallel} = a_0 \tag{2.32}$$

$$a_{\perp} = a_x \left[1 - D\left(\frac{a_{\parallel}}{a_x} - 1\right)\right] \tag{2.33}$$

The parameter D in equation 2.33 is a material dependant parameter which can be calculated based on the elastic constants of the epitaxial material [35]. For a 001-crystal structure – those which are exclusively used in this research, D is given by equation 2.34. The parameters c_{12} and c_{11} are the elastic constants in different directions in the plane of the substrate of the epitaxial material.

$$D = 2\frac{c_{12}}{c_{11}} \tag{2.34}$$

2.3.2.1 Effect on energy bands

Strain affects the positions of the valence band edges: heavy-hole, light hole and spin orbital, as well as the position of the conduction band. The change in band positions are given by equations 2.35 and 2.36 for the valence average and conduction band respectively; a_v and a_c are the hydrostatic deformation potential of the respective bands.

$$\Delta E_{v,av} = a_v(2\varepsilon_{\parallel} + \varepsilon_{\perp}) \tag{2.35}$$

$$\Delta E_c = a_c(2\varepsilon_{\parallel} + \varepsilon_{\perp}) \tag{2.36}$$

Along with band-edge position change, the sub-bands which make up the valence band shift with respect to one another due to sheer stress. These shifts are described by equations 2.37, 2.38 and 2.39 for the heavy-hole, light-hole and spin orbital respectively. Δ_0 is the spin-orbital position before it is perturbed by strain.

$$\Delta E_{HH}^{sh} = -\frac{1}{2}\delta E^{sh} \tag{2.37}$$

$$\Delta E_{LH}^{sh} = -\frac{1}{2}\Delta_0 + \frac{1}{4}\delta E^{sh} + \frac{1}{2}\left[\Delta_0^2 + \Delta_0 \delta E^{sh} + \frac{9}{4}\left(\delta E^{sh}\right)^2\right]^{\frac{1}{2}} \tag{2.38}$$

$$\Delta E_{SO}^{sh} = -\frac{1}{2}\Delta_0 + \frac{1}{4}\delta E^{sh} - \frac{1}{2}\left[\Delta_0^2 + \Delta_0 \delta E^{sh} + \frac{9}{4}\left(\delta E^{sh}\right)^2\right]^{\frac{1}{2}} \tag{2.39}$$

The value of δE^{sh} is determined by the orientation of the surface interface, for 001-interfaces, it is given by equation 2.40, where b is the tetragonal deformation potential.

$$\delta E^{sh} = 2b(\varepsilon_{\perp} - \varepsilon_{\parallel}) \tag{2.40}$$

These perturbations due to strain mean that the band edges of the valence and conduction band are given by equations 2.41 and 2.42 [35].

$$E_v = E_{v,av} + \frac{\Delta_0}{3} + E_{HH}^{hy} + max\left(E_{HH}^{sh}, E_{LH}^{sh}\right) \tag{2.41}$$

$$E_v = E_{v,av} + \frac{\Delta_0}{3} + E_G + \Delta E_c \tag{2.42}$$

Equation 2.41 shows that there are two valence bands – heavy hole (HH) and light hole (LH) which charge carriers can reside in. However, it is the higher energy of the two which the charge carrier will be in due to it having the lowest energy relative to the conduction band.

The effect of strain on the valence band is that it splits, as can be seen in equations 2.37, 2.38 and 2.39. The different valence sub-bands split at different rates, as well as this, the dispersion relationship is made anisotropic [36].

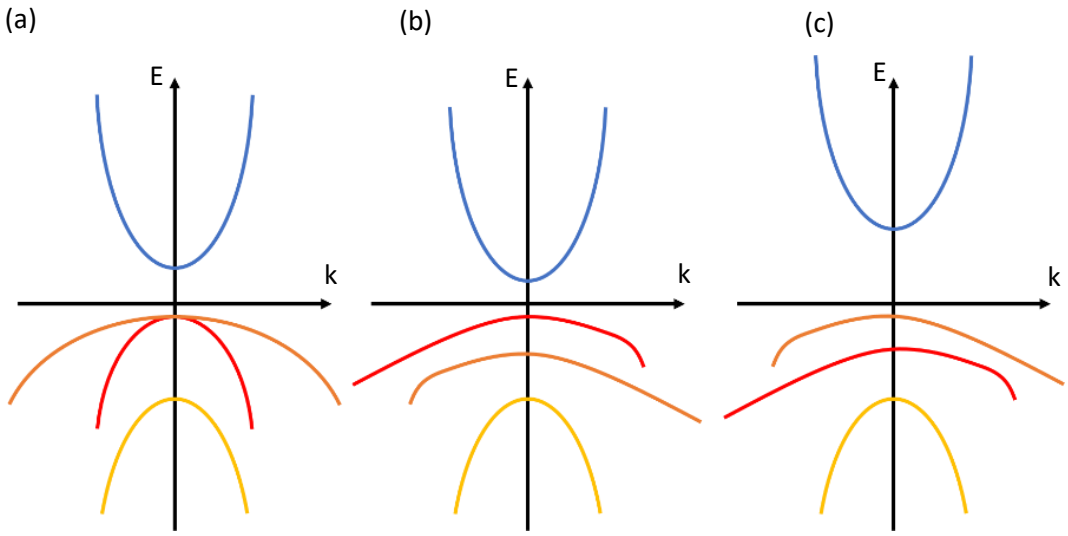

Figure 2.8: effects on the valence and conductions bands for (a) unstrained, (b) tensile strain, (c) compressive strain. The conductions bands are blue, conduction; orange, heavy-hole; red, light-hole and yellow, spin-orbital.

The effect of this strain on the conduction and valence bands can be seen in Figure 2.8, the biaxial component of strain changes the size of the bandgap, and the hydrostatic component causes the splitting of the valence band. This band splitting makes energy level engineering via quantum effects in the valence band possible. As well as changing the bandgap, this allows for other engineering techniques which can decrease the amount of non-radiative recombinations which occur.

As mentioned in section 2.2.2.3, Auger recombination is dependent on the difference in energies of various energy bands due to the recombination method being caused by charge carriers moving between bands. Because strain can be used to move the position of the band, strain engineering can be used to reduce the amount of Auger recombination which occurs in a system. This is because the band-splitting makes it more difficult for charge carriers in the valence band to go from one sub-band to another (i.e. from HH to LH), this reduces the likelihood of the CHLH Auger recombination mechanism [37]. Furthermore, the increase in strain, increase the activation energy of the Auger process, which in turn increases the Auger lifetime, making the process occur less than radiative recombination. This has been documented well in quantum well systems [38].

2.3.2.2 Critical layer thickness

The strain caused by growing lattice-mismatched epilayers on-top of one another can have a negative effect on the crystalline structure of the system. To maintain the in-plan lattice constant, non-lattice matched epilayers are under a force which allows them to deform to maintain the in-plane lattice constant of the substrate, rather than its equilibrium lattice constant. If a sufficiently large non-lattice matched epilayer is grown on a substrate then dislocations can start to form. This is due to dislocation nucleation being the energetically favourable state for the crystal to form as opposed to a regular lattice crystal [39]. I.e. the force that the lattice is exerting on itself is too great, and it causes a 'slip' in the structure to relieve the force. Defects in a lattice structure are optically and electronically detrimental to a semiconductor. They increase the resistance for charge carriers and create trap states, which increases the rate of non-radiative recombinations, specifically SRH recombination, as discussed in section 2.2.2.2.

Although strain in a system can cause lattice defects, occurring when a system of a certain strain exceeds a certain thickness, known as the critical layer thickness (h_c). Before this, a lattice mismatched layer can be grown with no adverse effects on the crystalline structure. The critical layer thickness is the thickest a strained epilayer can be grown before lattice defects start occurring. One way to calculate this parameter is given in equation 2.43 as proposed by Matthews and Blakeslee. Where b is the strength of the dislocation; f is the strain; ν is Poison's ratio, described in equation 2.44; α is the angle between the dislocation lines and the Burges vector and λ is the angle between slip direction and the perpendicular line of intersection in the slip plane and the interface [39].

$$h_c = \frac{b}{2\pi f}\frac{(1-\nu\cos^2\alpha)}{(1+\nu)\cos\lambda}\left(ln\left(\frac{h_c}{b}\right)+1\right) \quad 2.43$$

$$\nu = \frac{c_{12}}{c_{11}-c_{12}} \quad 2.44$$

The Matthews and Blakeslee model of critical thickness considers the mechanical properties of a dislocation and when this would cause defects to form. However, a model proposed by People and Bean considers the energy density in the material due to strain. Giving a relationship between the energy density and misfit dislocations, this model is shown in equation 2.45 [40].

$$h_c \approx \left(\frac{1-\nu}{1-\nu}\right)\left(\frac{1}{16\sqrt{2}}\right)\left(\frac{b^2}{a(x)}\right)\left[\frac{1}{f^2}ln\left(\frac{h_c}{b}\right)\right] \quad 2.45$$

Both equations 2.43 and 2.45 make their assumptions based on the strain due to one strained epitaxial layer being grown on a substrate. When this is extended to how the strain acts upon multiple epitaxial layers, the critical thickness is given by equation 2.46. Where θ is angle between dislocation line and the Burgers vector. The previous models assume that upon reaching the critical layer thickness, the strain causes a sudden "avalanche" of dislocations to occur. Whereas after the critical layer thickness is surpassed, there is a dislocation density which increases the larger the layer is than the critical layer thickness. Equation 2.47 describes the dislocation density, where h is the thickness of the layer, this is only applicable when $h > h_c$ [41].

$$h_c = \frac{b}{8\pi f}\left[\frac{1-\nu\, cos^2\,\theta}{(1+\nu)\, cos\,\lambda}\right]\left(ln\left(\frac{h_c}{b}\right)+1\right) \qquad 2.46$$

$$\rho = \frac{f}{b\sin\theta\cos\phi}\left(1-\frac{h_c}{h}\right) \qquad 2.47$$

2.4. Fourier-transform infrared spectroscopy

Molecular spectroscopy uses the interaction of electro-magnetic radiation with chemical bonds in matter to deduce information about their structure and identify their bond types. Using the types of bonds present in a structure, the chemical composition of a sample can be deduced. Due to its ability to identify certain bonds between atoms in a molecule, molecular spectroscopy is extensively used across many fields, including foodstuff analysis, biomedicine and bio sample analysis [42]. Electromagnetic radiation interacts with different types of bonds differently. These can be: electron transitions, bond vibrations, molecular rotations, electron spins and nuclear spins. Corresponding with: UV/visible; infrared; microwave and radio waves [43]. The infrared part of this spectrum is concerned with observing the vibrational energy transitions, this is in the range of 4000 cm^{-1} - 625 cm^{-1} [44]. The way that these vibrations occur in the molecules can be seen in Figure 2.9.

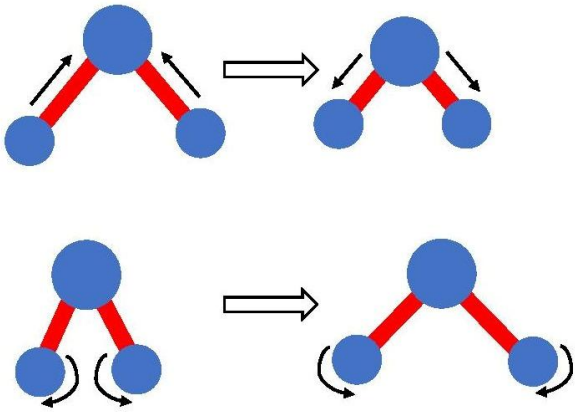

Figure 2.9: the movement of bonds that contribute to absorption of infrared light.

The frequency corresponding to the rotational bond is like that of a mass on a spring, it can be approximated using the formula shown in equation 2.48.

$$\nu = \sqrt{\frac{k}{m}} \qquad 2.48$$

Here, *m* is the equivalent mass of the two atoms which are vibrating, this can be calculated using equation 2.49. *k* is the equivalent of the sprint constant, proportional to the strength of the bond, meaning that single bonds will have a lower frequency than double bonds and so on for higher order bonds[44].

$$\frac{1}{m} = \frac{1}{m_1} + \frac{1}{m_2} \qquad 2.49$$

The factor which distinguishes the intensity of individual rotational bonds, is the population of their lower energy level in comparison to the one it is being excited to. The distribution of molecules in the energy levels is given by equation 2.50 [43].

$$\frac{n_u}{n_l} = \frac{g_u}{g_l} exp\left(\frac{-\Delta E}{k_B T}\right) \qquad 2.50$$

Here, n is the number of molecules in the upper *(u)* and lower (*l)* energy levels; g is the degeneracy of the energy levels, ΔE is the quantised energy of the transition, k_b is Boltzmann constant, and T is the absolute temperature of the system. This shows how the intensity is dependent upon the degeneracy of the energy levels as well as the temperature of the system.

Because of the discrete energies of the vibrational modes that are measured in FTIR spectroscopy, these modes absorb infrared light of a certain frequency. If the amount of light absorbed or reflected can be calculated. This will cause peaks/troughs in intensity corresponding to the energy of the bonds in the system, showing that those bonds between those elements exist [43].

2.5. Bandgap modelling

For the band-edges and wavefunction modelling in this project, Nextnano was used, this is an electronic and optoelectronic nanodevice simulator [45]. The software allows the user to create a model semiconductor sample with the layer thicknesses and alloy types being programable. The software calculates the band-edges of the device using the Krijn model, explained in section 2.3. This includes the alloy bandgap calculation which uses the Varshni model to see find bandedges at a specific temperature, as explained in section 2.1.2. The software allows all of the relevant material parameters to be changed, most of these values are obtained from the paper published by Vurgaftman et al [21], these can also be programmed to have whatever value the user defines. Using band-edges, the Nextnano software can then calculate what the charge carrier wavefunctions in various parts of the device would be as well as the band edges. This is extremely useful when modelling low dimensional devices – such as quantum wells and superlattices in the case of this project. The energy levels in quantum wells as well as the wavefunction overlap of charge carriers can be calculated using this method. There are several

ways that this can be done: using a classical, single-band method; a k·p 6-band approximation; or a k·p 8-band approximation.

Although the Schrödinger model can be used to find wavefunctions, a complete model of the potential energies for the electron and holes are required for this. The Schrödinger solution also requires a great deal of calculations. However, for an electron or hole in a structure, the majority of the carriers are within meV of the band-edge. Because of this, k·p-perturbation can be carried out allowing the rest of the dispersion relationship to be calculated [46], this is a much less intense calculation. In k·p perturbation, for however many bands are involved, a Bloch potential is used to describe the band edges. Then the formula in equation 2.51, where $c_{m,l}$ are constants of normalisation for the different wavefunctions in the equation, is implemented to give the energy levels ($E_n(\vec{k})$).

$$c_l\left[E_n(\vec{k}) - E_l(0) - \frac{\hbar^2}{2m_0}k^2\right] - \sum c_m \frac{\hbar}{m_0}\left(\bar{k}\cdot\vec{p}_{lm}\right) = 0 \qquad 2.51$$

For the single band application of the k·p model, a non-spinor charged particle is considered in the potential field and it is assumed that it does not interact with any other particles, this is the classical model. However, the k·p 8-band simulation assumes that there are four bands which are occupied by charged particles: conduction, heavy-hole, light-hole and spin orbital. Then, in accordance with the Pauli exclusion principle, there are two charged particles in each band with opposite spins.

The basic principle of the Nextnano simulation – as stated above – is defining the band structure. To do this, a substrate that the structure will be grown on is selected then define the rest of the layers – buffer region, active region, et cetera. When doing this it is possible to define the thickness of each layer, as well as the alloy contents of any alloys that contain more than two elements. Once this is done, the band approximation is chosen. As described above, it uses the calculated band-edges to find the wavefunction of charge carriers in each respective band, the data from the calculations can then be saved for further analysis. As well as the information that can be obtained from the Nextnano file produced, such as: energy of certain levels, wavefunction amplitudes and probabilities. It is also possible to calculate wavefunction overlap using the amplitude wavefunctions.

3. Experimental procedures

This chapter will outline: sample growth, pre-fabrication characterisation of structure and emission; device fabrication techniques and post-fabrication characterisation. There will be an outline of all the equipment used, as well as the principles behind any measurements that were performed.

3.1. Molecular beam epitaxy (MBE)

Molecular beam epitaxy (MBE) is a method of growing semiconductors using monolayer deposition of materials from heated sources onto a substrate under ultra-high vacuum conditions [47]. III-V alloys can be created using fluxes of different group-III and group-V atoms, which form a lattice together on a substrate, different alloys can be created by controlling the fluxes. Thermal effusion K-cells are used to create group-III matrix fluxes: Indium (In), Gallium (Ga), Aluminium (Al). Also, for the dopants: Beryllium (Be) (p-type) and Gallium Telluride (GaTe) (n-type). Group-V matrix fluxes are created using cracker cells; these include Arsenic (As) and Antimony (Sb). The growth rate of the alloys is controlled by the flux of the group-III materials, and the composition is determined by ratio of all different atoms in the process. The rate at which thermal effusion K-cells create a gas matrix is controlled by temperature. This is controlled by a heater on both the base and tip of the cell, which are set 100 °C apart. Group-V materials are kept in cracker cells, which are kept at a constant temperature (bulk), the rate at which they create a matrix is controlled by the valve position. The group-V materials must keep a constant pressure on the sample whilst growing for lattice incorporation, else group-V evaporation will take place, decreasing the quality of the sample.

3.1.1. General use

Whilst growing, the environment must be kept at high vacuum, if this requirement is not met it can cause a decrease in the mean free path of the gas fluxes such that they may not reach the substrate. As well as this, residual gasses in the air such as Carbon-monoxide (CO), Carbon-dioxide (CO_2) and other carbon-based contaminants, can cause carbon to be incorporated into the epilayers during deposition, this would decrease the quality of the lattice. In air, at atmospheric pressure, incorporation of carbon into the lattice from these residual gasses is sufficient such that it does not allow the formation of a III-V lattice. If the pressure of the growth camber is reduced to 10^{-10} mbar, this incorporation rate is reduced to 10^{-4} ML/s, which is negligible in comparison to the rate at which the alloy lattice will be grown, which is around 1 ML/s. Using the correct growth conditions, due to the mono-layer deposition nature of MBE,

it is possible to precisely grow heterojunction structures with abrupt interfaces and structures on the scale of nanometres – or single monolayers.

Using high vacuum conditions also has the benefit of allowing for reflection high-energy electron diffraction (RHEED) to be used. This is a method of characterising surface morphology of a crystalline structure growing on a surface [47], used to characterise if material is growing on a substrate, and the rate at which it is growing. To achieve this, an electron "gun", fires electrons with energies of around 10 keV at angle of around 5° to the surface of the substrate. These electrons then experience Bragg diffraction, caused by interference of the high energy electrons being reflected from epilayers within the structure, i.e. the surface and layers which penetrate the surface of the substrate. This causes them to interfere with one another, creating a diffraction pattern.

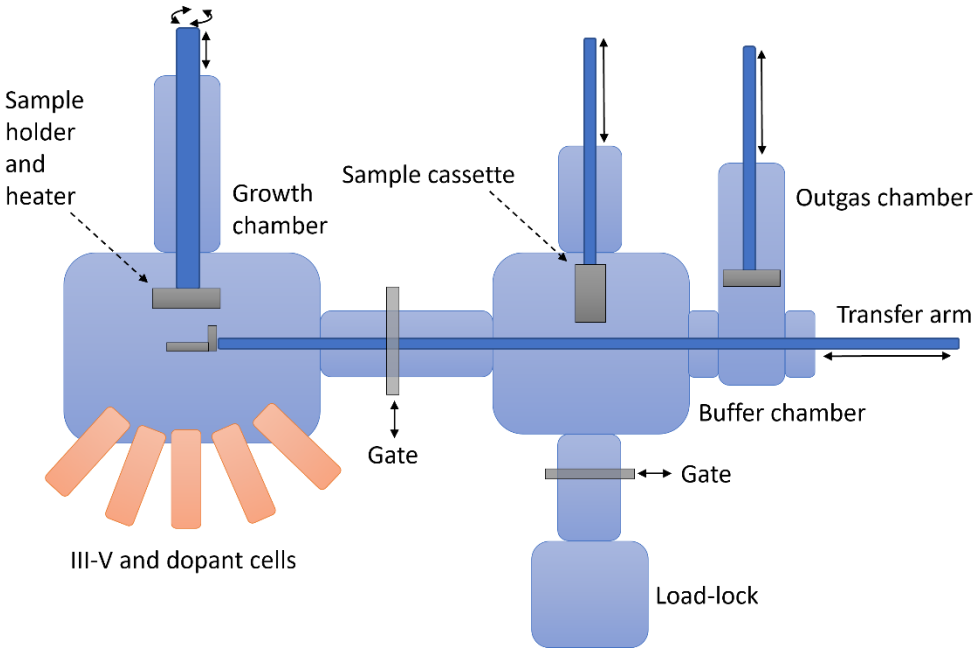

Figure 3.1. A simplified diagram showing the basic operating principles of the VEECO GENxplor MBE system used in this work. Solid black lines show the direction of motion of the corresponding parts.

This can then be seen using a photomultiplier usually attached to a camera which allows the pattern to be viewed. For GaSb, when electrons are diffracted from a heated surface with no material growing, a dotted pattern (1×3) can be seen. A (2×5) pattern can also be observed, but this occurs when the conditions for growth are not ideal [48]. Other materials show different surface recombinations, but they will not be discussed as it is outside the scope of this thesis. When group-III materials are incorporated, starting material growth, the dotted pattern turns into a streaky pattern. The dotted pattern is indicative of a three-dimensional morphology of the surface, which occurs when growth is not occurring. The streaky pattern occurs when there

is two-dimensional morphology of the surface, generally indicative that material is growing two dimensionally, as would be expected with high quality epitaxial growth. Practically, the streaky pattern is used to indicate that material growth is successfully occurring.

RHEED is also used to calibrate the growth rate of certain alloys. This is done before the growth of samples to ensure that the alloys are growing at the correct rate. It is done by observing oscillations in the intensity of the RHEED's "streaky" pattern. From one intensity maxima to another indicates the growth of one monolayer of material. This is because the morphology changes from a 2D plane, to a 3D morphology, back to 2D when a new layer has been formed. Which can be used to find the average growth rate using a set substrate temperature and group-III cell tip temperature. This is done by taking the number of maxima and minima observed during a certain time period to find the rate. For example, if ten maxima are observed in ten seconds, then the growth rate of that material is 1 ML s^{-1}.

The MBE reactor used at Lancaster is a VEECO GENxplor, a simplified diagram showing the different parts of the machine used in the growths can be seen in Figure 3.1. There are three chambers in this MBE machine: load-lock, buffer chamber and the growth chamber. The load lock is the smallest of the chambers, and it is where the substrate is loaded from and the grown sample unloaded from. It is only connected directly to the buffer chamber and can have its pressure isolated by a gate between the two chambers. The purpose of this chamber is to be able to go from atmospheric pressure to around 10^{-7} bar relatively quickly so that the samples can be taken out without having atmospheric pressure outside of the growth camber. This is for loading and unloading of samples before and after growth, the chamber can be bought from atmospheric pressure to 10^{-7} bar using a turbo pump system. The buffer chamber is connected to both the load-lock and the growth chamber via two different gates, ensuring the load lock is not directly connected to the growth chamber. This is where substrates are stored before being placed into the growth chamber or being outgassed, it is kept at around 10^{-8} bar. The outgas chamber is connected to the buffer chamber but not through a gate, this is the chamber in which substrates will be "outgassed". Outgassing is a process by which the substrate is heated to remove any surface contaminants from the substrate before it is loaded into the growth chamber. The growth chamber is the chamber kept at the highest vacuum and is where the growth process occurs. It is connected to the buffer chamber so that substrates can be loaded in; it can be isolated from all of the other cambers by closing the gate between it and the buffer chamber. Two different pumps are used to keep the buffer chamber and the growth chamber, these are: ion sputter/pump and a cryopump.

The process of loading a substrate into the growth chamber is as such:

- Using the liquid nitrogen controller, set the temperature of the growth chamber to –140 °C.
- Move the cassette holder from the buffer chamber into the load-lock, close the gate, then bring the load-lock to atmospheric pressure, so that it can be unloaded.
- Load the substrate into a sample holder, this project grew on a quarter of a 2-inch GaSb wafer for each growth.
- Put the sample, in the holder, into the load lock and pump the chamber.
- Once the load-lock is at a pressure of 5.7×10^{-7} mbar, open the gate between the load-lock and the buffer chamber, move the cassette with the sample into the buffer chamber, close the gate between the load-lock and the buffer chamber.
- Using the transfer arm, move the sample from the buffer chamber into the outgas chamber, then, move it up in the sample holder of the outgas chamber and set the relevant outgas recipe to run.
- Once the outgas recipe is complete, move the sample back into the buffer chamber.
- Ensuring that the difference in pressure between the growth chamber and the buffer chamber is around one order of magnitude, open the gate between growth chamber and the buffer chamber.
- Using the transfer arm, move the sample from the buffer chamber into the growth chamber, put it on the sample holder, remove the transfer arm from the growth chamber and close the gate.
- Start the sample spinning counterclockwise.
- Start the growth recipe.
- Once the recipe is complete, open the gate between the growth chamber and buffer chamber, move the sample into the transfer cassette, then close the gate.
- Ensuring the pressure difference is correct between the buffer chamber and load-lock, open the gate between the buffer chamber and the load-lock and move the sample in the cassette into the load-lock, close the gate from the buffer chamber to the load-lock.
- Bring the load-lock to atmospheric pressure and unload the sample.

3.1.2. Set point calibration

During many of the growth which will be discussed in this thesis, ternary and quaternary alloys will be grown on GaSb substrates. The optimal structure for some of these samples occurs when the alloys are grown lattice matched to the substrate – for example, $Al_xGa_{1-x}As_{1-y}Sb_y$. When calculating the cell temperatures to grow a specific ternary alloy containing two group-III elements and one group-V, for example $In_xGa_{1-x}Sb$, an extrapolation of the ternary elements is done based on the constituent binary growth rates. However, when finding cell temperatures for a ternary or higher order alloy which has more than one group-V element, for example $InAs_{1-x}Sb_x$ or $Al_xGa_{1-x}As_{1-y}Sb_y$, a calibration growth is required. This is due to the volatility of group-V elements from the cracker cells, often using the same bulk temperature and valve position does not yield the same group-V integration into the alloy. This is also due to the integration of group-V elements into the alloy being more dependent on the substrate temperature in comparison to group-IIIs. Because of this, it is not possible to directly calculate the alloy content that will be obtained from a mixture of group-V fluxes based solely on bulk temperature and valve position. Each time a growth is done with a particular ternary or quaternary (both with two group-Vs), a calibration must be done with set bulk temperatures to find out group-V incorporation based on valve position. To do this calibration, if there are two or more group-III elements in the alloy, their cell temperatures are calculated based on their growth rates, which will remain fixed. To find the group-V valve position for the element with lower concentration in the alloy, a constant bulk temperature is chosen, normally a lower temperature as it is the element with a lower content in the alloy which will have the cell valve position changed. Three valve positions of the group-V will be chosen, which will create three epitaxial layers with fixed group-III incorporation and slightly varied group-V, each of which will be grown around 300 nm thick so that they are visible on a XRD scan, but not so thick that they exceed the critical thickness, causing relaxations in the lattice. Because the three different alloys will have different lattice constants, on the XRD scan, there will be three peaks corresponding with each layer, XRD modelling software can be used to find the alloy content corresponding with each peak. The amount that the valve position is varied will be relatively small, the difference in alloy content is also relatively small, normally within 10 %. Because of this, if a plot of group-V content as a function of valve position is made, it gives an approximately linear relationship. This plot can then be used to find the valve position which will give the desired group-V flux for the desired incorporation in the alloy using the linear interpolation of the data. This can be used to find the valve position which coincides with the alloy being lattice matched to the substrate, or to find a specific alloy based on bandgap engineering or strain balancing.

3.2. X-ray diffraction (XRD)

X-ray diffraction is a method of characterising the thickness of epilayers and their alloy content. Because the thickness of layers for different materials can be determined, this method can show the alloy content the growth conditions give. This is critical when trying to obtain a certain thicknesses and alloy contents in heterojunction structures. It can be used to identify the grown structure, allowing relevant changes to the growth to be made to create the desired structure.

Because the layer separation of atoms in III-V lattice is of the same order of magnitude as the wavelength of an x-ray, the principle of Bragg reflection can be applied. This means at certain angles, some of the reflected rays from different epilayers in the structure will interfere constructively, so the magnitude of the x-ray intensity will increase. The condition for constructive interference is given in equation 3.1 [49].

$$n\lambda = 2d\sin\theta \qquad 3.1$$

In equation 3.1, n is an integer, λ is the wavelength of the incident x-rays, d is the vertical separation of epilayers (the out of plane lattice constant) and θ is the angle of incidence of the ray – also equal to the angle of reflection. When the reflection of light on the surface of the sample is such as shown in Figure 3.2, and the conditions of equation 3.1 are met, constructive interference will occur.

To practically obtain an XRD scan, an ω-2θ scan is conducted. To do this, the experiment as shown in Figure 3.3 is set-up. The main components required are: an x-ray source, beam collimator, goniometer/sample holder, slit and detector. The x-ray source is an evacuated tube, in which electrons produced by thermionic emission from a tungsten cathode collide with a metal target. This causes photons in the x-ray region to be emitted. A collimator is used to ensure that the beam is parallel when it hits the target, if the beam were diffuse upon hitting the target, the reflected x-rays would scatter and be more difficult to detect. The goniometer is used to set the angle between the source and the detector so that the angles can be changed throughout the experiment. This is also used to hold the sample in place via vacuum. The slit in-between the detector and the sample, which should be the same distance away from the sample as the x-ray source is, is used in order to improve the resolution of the scan [50].

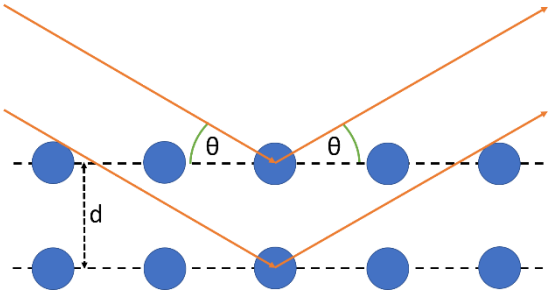

Figure 3.2: how light is reflected from individual monolayers when it is incident on a regularly spaced lattice. The orange arrows indicate incoming light, the blue dots are the atoms in the lattice.

This allows intensity to be plotted as a function of ω, which can then be modelled to determine layer thickness and alloy content. To do this, the value of ω and 2θ must be found for the substrate peak – the peak with highest intensity as the substrate is the thickest layer by several orders of magnitude. Once the values of ω and 2θ have been found for the given sample, a scan of ω-2θ is taken, this is done from ω_{SUB} ± 2°, this can be altered based on where the satellite peaks lie. An angle of 2° either side of the substrate peak is sufficient to gather enough data for the XRD modelling software to accurately model the alloy contents of the epitaxial layers. This is further due to the range of peaks which are measured, most of which have their principle peak within two degrees of the GaSb substrate peak. If all of the satellite peaks are not included in the scan, the model of the XRD scan will be less accurate, leading to an incorrect assumption of what the grown material is.

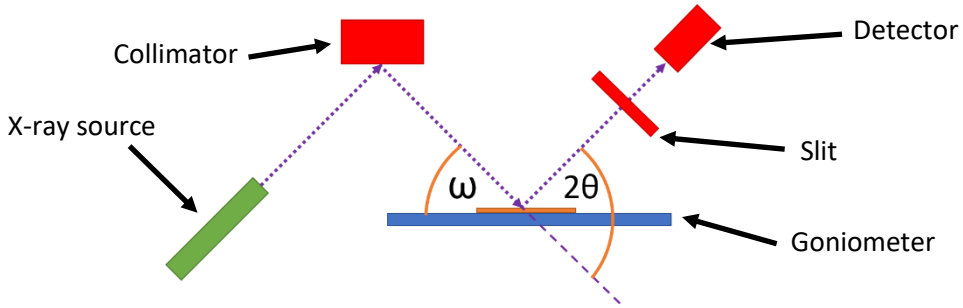

Figure 3.3: basic diagram of the path of the x-ray from the source to detector as well as the other parts that allow an ω-2ϑ scan to be conducted.

3.3. Photoluminescence (PL)

Photoluminescence is an important part in the growth procedure for calibrating the active region of a device. It is also key in showing many physical properties of emissions, which can give further information in the quality and structure of a growth. In this project, a PL setup was used that allowed emission spectra readings to be taken from 4 – 300 K, the experimental setup used to do this can be seen in Figure 3.4. In this setup, a CW red laser was used to excite emission; controlled by software on a PC so that its output power could be set from 50 –

140 mW. There are two planar mirrors which are used to aim the laser beam to hit the sample at an angle as it is contained in a cryostat. The path from the laser to the first mirror in uninterrupted. The path from the first mirror to the second mirror has a chopper placed in the way to vary the modulation of the laser beam in order for the signal to be picked up by the lock-in amplifier. The path from the second mirror to the sample in the cryostat is uninterrupted and the second mirror is used to position the beam on the sample. The path between the cryostat and the monochromator is the path in which the sample will emit light once it has been excited by the laser. There are two planoconvex lenses that the emission will pass through. The first of these is used to collimate the light, to reduce radial loss between the sample and the monochromator. Then the second lens refocus the light into the front opening of the monochromator. There is a red-light filter between the cryostat and monochromator to stop red light from the laser entering the monochromator, this would be detrimental in aligning the lenses such that they maximise the signal from the PL entering the monochromator as the laser power is on the order of 100mW, whereas the PL signal of the device is several orders of magnitude weaker. This means that the PL signal would be insignificant compared to that of the laser, such that moving the position of the sample would have no noticeable effect on the reading of the lock-in amplifier. Whereas if the sample is moved and the laser light blocked, the difference is noticeable and can be maximised by moving the sample in the plane perpendicular to the direction of the PL signal.

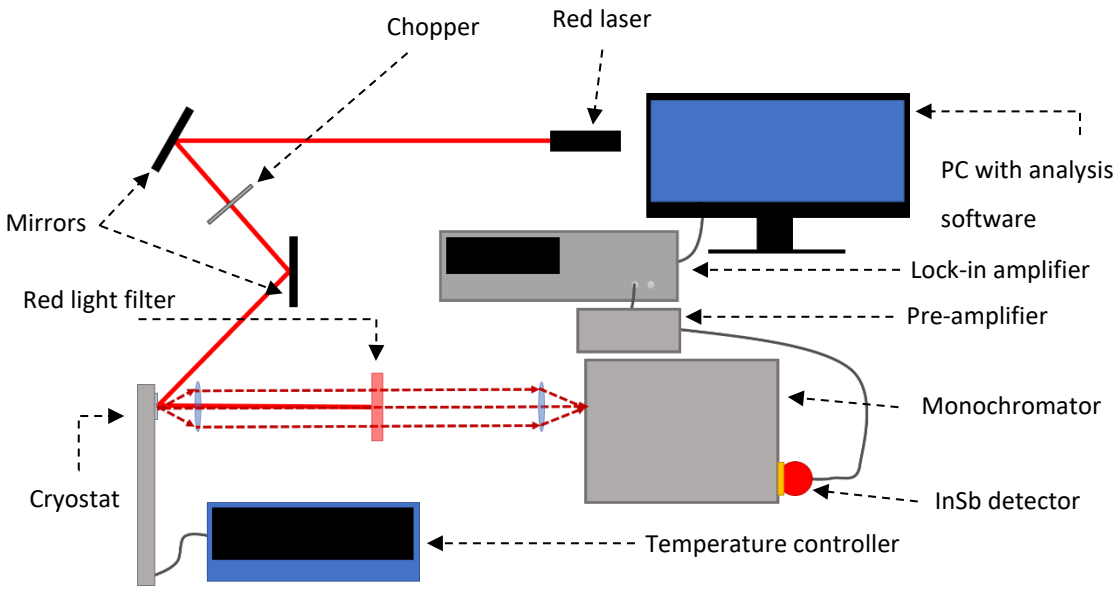

Figure 3.4: The experimental setup to measure PL spectra of samples, for room temperature and low temperature.

Because PL shows the intensity of a specific wavelength relative to the other wavelengths in the spectrum, before going to the detector, a monochromator is used to split the emission spectrum into its constituent wavelengths. It does this via a system of two planar mirrors, two concave mirrors and a diffraction grating. Light enters through a slit on one side of the monochromator (the opening), it is reflected into the system using a planar mirror, then collimated using a concave mirror. Once collimated, the light will be reflected off a diffraction grating; this causes the polychromatic light to have its constituent wavelengths diffracted at different angles. The angle of diffraction is based on the wavelength of incoming light, as well as the distance between slits in the grating [51], the distance between slits in the grating is kept constant. The light will then be uncollimated by another concave mirror and reflected into the InSb detector by a planar mirror. The angle of the diffraction grating can be used to select the wavelength of light entering the detector by changing the angle, as light of different wavelengths will be reflected at different angles. Once the signal from the monochromator has been detected, it goes through a pre-amplifier, then to a lock-in amplifier, the lock-in amplifier sends the intensity of the signal to software on a PC. A spectrum can be plotted by plotting software based on the signal from the lock-in amplifier at various wavelengths.

To perform temperature dependant measurements from 4 – 300 K, a continuous flow liquid helium cryostat was used. This works by loading the sample into a vacuum chamber with a pressure of ~ 10^{-2} mbar. Liquid helium can then be pumped around this chamber, thus reducing the temperature. The flow of liquid helium is controlled by a gas flow pump, once the helium has been pumped around the chamber, it is pumped out, being replaced and is sent to a helium recovery system. This takes the chamber from 300 K to 4 K in ~ 30 minutes. Once its temperature has reached an equilibrium point, it can be controlled using a heater and a reduction in the flow of liquid helium to be bought back up to room temperature.

3.4. Device fabrication

In order to create a device out of a piece of a sample, several steps are required which allow relevant contacts and performance enhancing features to be added so that a current can be put through it and light extracted. The processes which were used to do this in this project will be discussed in the following section. All of which was carried out in a cleanroom laboratory in the Quantum Technology Centre (QTC) in Lancaster University physics department.

3.4.1. Photolithography

Photolithography is the process by which a mask can be put onto a sample, so that a contact can be evaporated onto some parts, but not others; also, so that it can under-go wet-etching, so the etchant will only affect certain parts of the sample. To do this, a photopositive resist is put on the sample that once exposed to UV light and developed, the parts exposed to UV light will dissolve and the rest of the resist will form a non-photosensitive covering of the sample. To obtain a uniform layer of resist on the sample, once the liquid resist has been put on top of the sample via pipette, it is spun in SUSS LabSpin6 spinner at a speed of the order of magnitude ~10^3 min^{-1}, it is then baked on a hotplate to set the resist – the exact speed, resist type and baking information used can be found in Table 3.1.

Resist name	**Spin time /s**	**Spin speed /min^{-1}**	**Bake time /min**	**Bake temperature /°C**	**Used for**
LOR3A	30	3000	5	180	Thermal evaporation, wet-etching
S1813	30	6000	2	115	Wet-etching

Table 3.1: The resists used in device fabrication during this work, as well as the speed and bake time which they require and which process each of them are used in.

Once the resists have been applied and baked for the correct time, photolithography can be done. To do this, a SUSS MJB4 Laboratory Mask Aligner is used. This allows the user to place chrome masks in front of the sample, and align it as required, so that some parts are exposed to the UV light, and others are not.

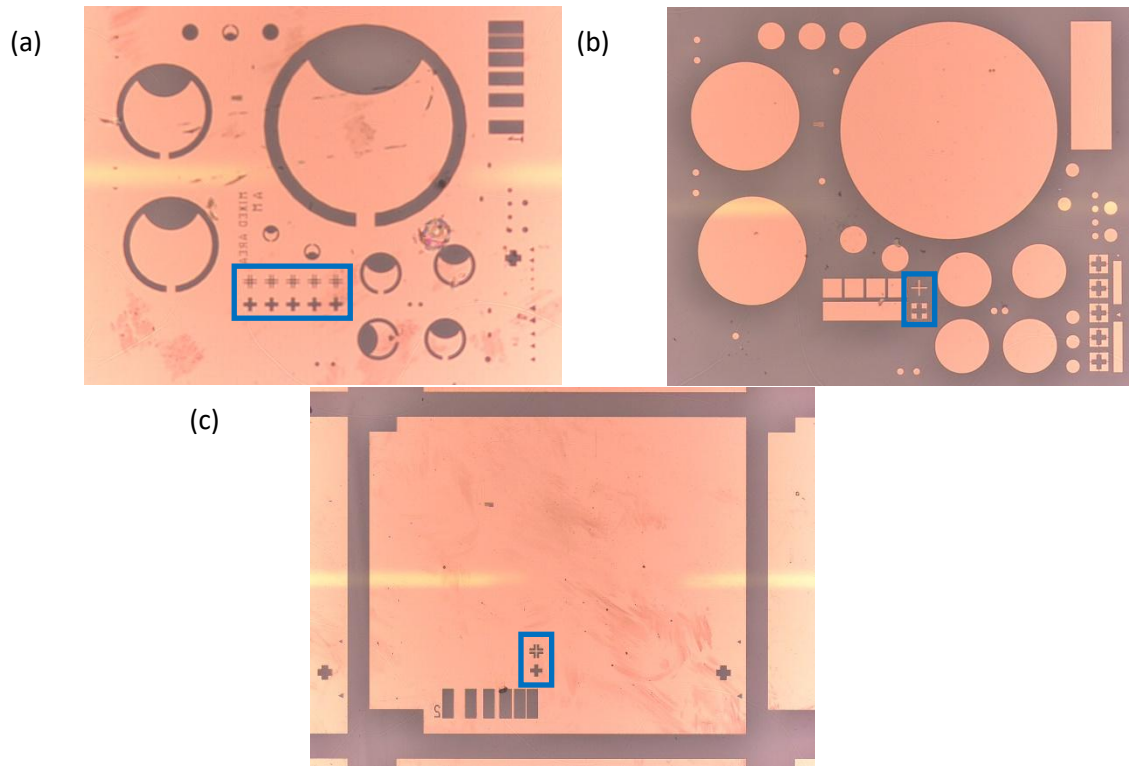

Figure 3.5: chrome masks used for (a) top-contact, (b) etching mesa, (c) grid contact, using photopositive resists. Parts highlighted with blue squares are the alignment markers.

The mask aligner has a built in UV lamp which will expose the sample for a given amount of time, for resists in this work, the exposure time was 2.5 seconds. There are three different masks used in this work, these are: top contact, MESA and grid contact, these masks can be seen in Figure 3.5 (a), (b) and (c) respectively.

To ensure proper contact alignment and accurate etching around the contact, the masks must be aligned to one another, if they are not, this could cause parts of the circuit to short as the current would not pass through the active region. To do this, there are alignment marks on each of the masks, which have a piece of gold evaporated onto them during the evaporation process, these can be seen highlighted in blue boxes in Figure 3.5. Once these are lined up with one another, all of the proper alignment has been completed, and the masks will be where they should be after lithography. Once the UV exposure has been completed, the sample must be developed to make the mask non-photosensitive. This is done by placing the exposed sample in Microposit™ MF-CD-26 developer for 80 seconds, rinsing it in de-ionised (DI) water and drying it using compressed N_2 gas.

3.4.2. Thermal evaporation

Thermal evaporation is a process by which metal contacts are put onto a sample, this is completed under high vacuum, around 10^{-6} mbar, to ensure that pollutants do not get onto the surface of the sample or into the contact material as this can decrease the quality of the contact. This is done by super-heating specific metals via running a high current through them until they turn gaseous and evaporate onto the surface of the sample. They are then deposit onto the sample, creating a layer of metal, this process can be used to create contacts with thicknesses of 10s, up to 100s of nanometres. For this project, Titanium/Gold (Ti/Au) contacts were used, usually aiming for 20 nm of Ti and 200 nm of Au.

Material	**Sublimation current /A**	**Deposition rate /Å s^{-1}**
Ti	58	0.3
Au	28	3.0

Table 3.2: the current which must be put through respective crucibles to cause thermal evaporation to occur, as well as the approximate deposition rate that this causes.

To do this, a Moorfield Thin Film Deposition Thermal Evaporator was used. This is made up of: a vacuum chamber, a sample holder and four crucibles which hold the metals which will be deposited – for this project, only two were used. Once the samples are in the sample holder and it is in the vacuum chamber, facing the metal crucibles, the camber can then be pumped down to an adequate pressure, < 10^{-6} mbar. The crucibles heat up the metal by driving a current through them, which is controlled externally by a current controller, the approximate current and subsequent evaporation rates for Ti and Au are shown in Table 3.2. At the appropriate current, sublimation will occur – the material going from solid to gas – and then the gaseous metal will deposit on the surface of the sample once it comes into contact. The shutter can stop the process by closing between the crucible and the sample, this is also used to stop deposition on the sample from metal that sublimates before the sublimation temperature. Figure 3.6 shows the layout of the thermal evaporator as well as the constituent parts which control the evaporation.

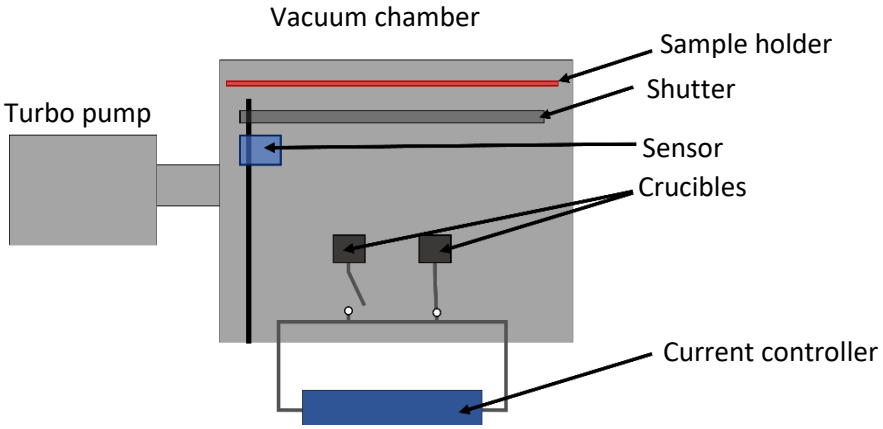

Figure 3.6: the layout of the thermal evaporator and all the constituent parts.

Thermal evaporation is used to evaporate on: top contact, grid contact and back contact. As discussed in section 3.4 the top contact and grid contact – which would both be on the same side of the sample have a mask on them. After the evaporation the sample will be soaked in acetone which causes the parts with resist on to come off taking the evaporated metal on top of it with it, leaving a contact only on the parts of the sample which did not have resist on them. The back contact – applied when the substrate and all buffer layers are correctly doped does not require a mask as it just needs to cover all of the back/substrate side of the sample.

3.4.3. Wet-etching

Wet-etching is the process of creating a mesa structure on a device, these structures increase the likelihood that light will escape from the device, this is due to the side wall reflection from the semiconductor-air interface and light directionality due to total internal reflection affects. It has a further effect of decreasing current crowding in the device and the increase in surface area allows for greater cooling, decreasing the negative impact of Joule heating [52]. Moreover, allowing a grid contact to be put on the device in section that is relevantly doped, required if current cannot be passed through the substrate, for example if it is undoped or will contain a lot of defects. This is done by having a mask of S1813 resist over the top of the contact structures which will be the top of the mesa and then putting the structure into an acid/peroxide solution. This will cause the part of the device not covered by resist to be etched away by the acid, creating different levels. Different acids etch through different materials at different rates, so sometimes multiple etchants are required to etch all the way through to the required level of specific devices which are made of two or more materials which cannot be etched by the same etchant. The information for the etchant used for each different device from this project can be seen in Table 3.3.

Device	Etchant	Ratio	Approximate etch rate/ nm min^{-1}
InGaAsSb/AlGaAsSb type-I LED	H_3PO_4:$C_6H_8O_7$:H_2O_2:H_2O	2:10:10:20	75
InAs/InAsSb type-II LED	H_3PO_4:$C_6H_8O_7$:H_2O_2:H_2O	2:10:10:20	80
InGaAsSb/GaSb type-I LED	H_3PO_4:$C_6H_8O_7$:H_2O_2:H_2O	2:10:10:20	25

Table 3.3: the etchants used on different layers of different devices, as well as their ratios and approximate etch rates.

The mesa structure of a LED generally has a height of around 1000 nm, to measure the height of the mesa after a certain amount of time in the etchant, a Bruker Dektak XT Profiler is used. This allows one to measure the depth from the top of the structure – including the mask on top – to the base where the etch has stopped. This can be used to initially take an etch rate to give an estimate of how long the total etch will take, although the same etchant goes through different layers at different speeds so the etch should be checked in more regular intervals. The etch will stop once the desired height for the mesa has been reached, considering the resist on top, which is usually around 1500 nm thick. Once the etch has reached the desired depth, the resist can be removed by leaving it in acetone for several hours, then rinsing it with MF-CD-26 developer, IPA and then DI water. This leaves the desired mesa structure, with the contacting layer on-to with the respective electrode and a mesa structure extending down into the buffer region, encompassing the active region of the device.

3.4.4. Scribing

Scribing allows a processed sample which is approximately a third of a quarter 2-inch wafer which will contain between twenty and fifty mesa structures on it to be cut out into individual pieces which can be mounted and bonded to create a useable device.

To do this, a SUSS RA 120M Scriber is used. This device is used to create a continuous scribe, whereby the sample is held in place, and using a diamond pointed scribing tool, a straight, continuous line will be scribed into the sample, around 150 nm deep. This can be set to be done repeatedly with the tool moving a set distance across the sample each time, meaning that the scribe lines are between the repeating top contact pattern which allows individual devices to be

separated. This can be done in both the x and y axis by moving the sample holder by 90° and repeating the scribe. If pressure is applied to the sample on two points on opposite sides of a scribe, a full break will occur along the scribe edge. A clean break will occur if the scribe lines line-up with the direction of the crystal, this means that initially, the device contacts should be lined up so that they are in line with the direction of the crystal.

3.4.5. Wire-bonding

Wire bonding is how the contacts which have been put on the device are connected to the contacts on the mount, so that the device can be plugged into a power supply. Once the sample has been scribed into individual device pieces. The type of TO header used will depend upon if the device needs to be top-top or top-bottom contacted; in a top-top contact the top contact and grid contact are bonded to separate legs. In a top-bottom contact, the top contact goes to a leg which is electrically insulated from the rest of the TO header. The device is glued to the face of the TO header using an electrically conducting two-part silver epoxy, the face of the TO header is connected to one of the legs, allowing it to act as an electrode, allowing current to be pumped through the substrate via the base of the header. Once the device is on the header with the bonding agent, it is cured for around 12 hours on a hotplate at 80°C. This bonds the bottom contact to the header, allowing current to be put in from the base, through the substrate, for a top-bottom contact. The top contacts have to be connected to the TO header legs via a gold wire. To do this, a tpt HB05 wire bonder is used. The gold wire is super-heated at one end so that a ball forms, this allows the user to more effectively bond to one of the gold contacts. The bond is most effective when the first bond is from the top contact of the device, there is a pre-set force and contact time programmed into the wire-bonder which will occur when it touches one of the places it is bonding wire to. A set amount of wire will then be fed through by the machine, and the wire will be bonded to the second contact point, the machine will apply a certain force to this, which will cause the gold to bond onto this second contact point.

3.4.6. Summary

There are several processes which have to be carried out in order to turn a doped wafer into a light-emitting diode. The processes up to cleaving are shown in Figure 3.7, mounting and wire bonding are then used in order to finalise the device so that it can be tested.

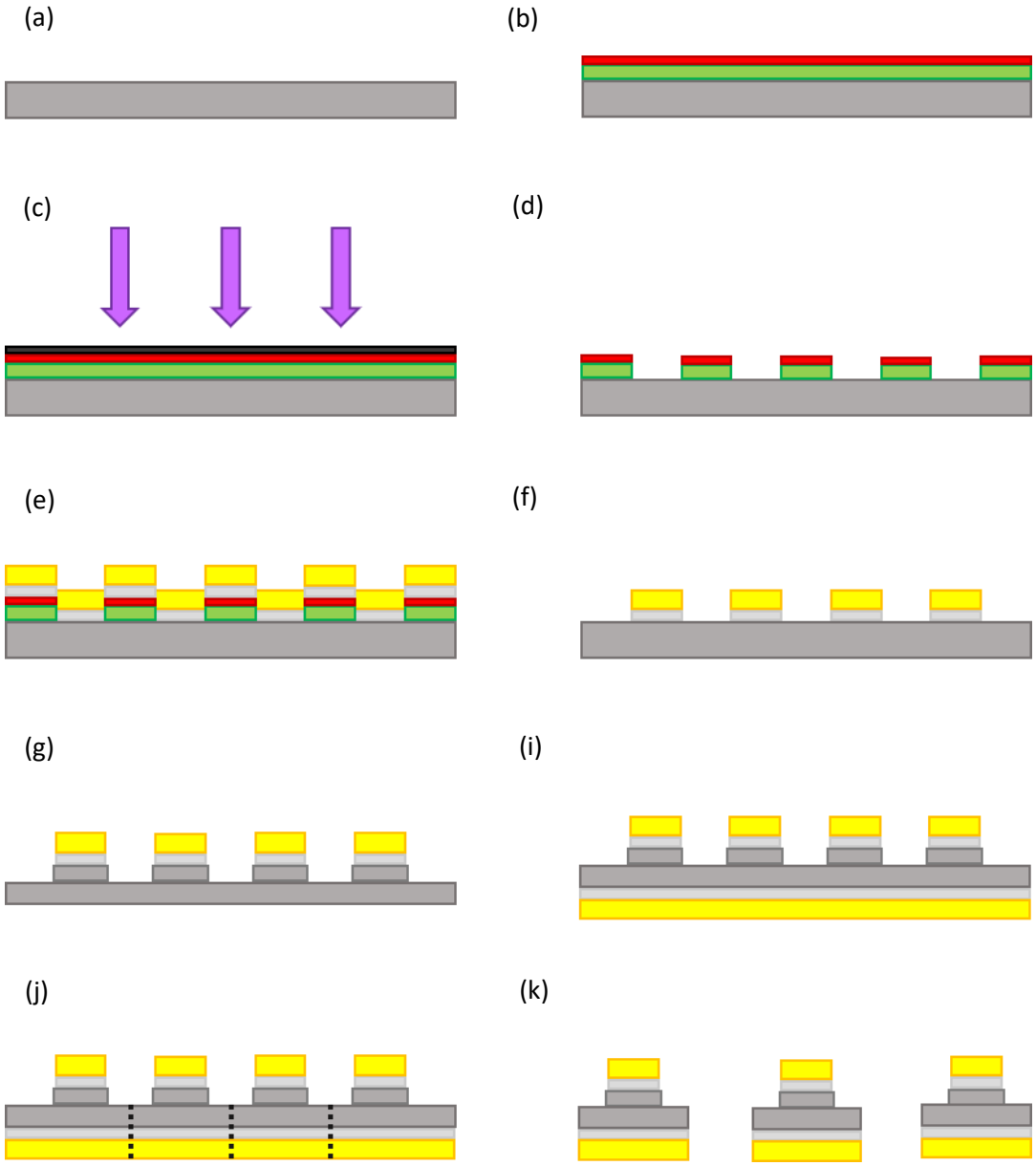

Figure 3.7: a flow chart of the fabrication processes from wafer to pre-bonded device. These are: (a) an unprocessed sample; (b) a sample with LOR-3A and S1813 resist layered on top (c) a mask placed on-top of the resist, with UV light incoming to pattern the resist; (d) remaining resist which has been developed, leaving resist in some places whereas it is washed away in others; (e) Ti/Au evaporated on to the surface of the sample, some coating the sample, and some coating the resist which is on top of it; (f) sample once resist with metal on top has been removed, leaving only the metal contacts where they are desired; (g) mesa structures being etched, leaving a mesa with contacts on top; (i) bottom contact evaporated onto the rear of the substrate (j) sample cleaved; (k) sample broken along cleaved lines, leaving individual mesa device structures which can then be mounted.

3.5. Electrical characterisation

Electrical characterisation is important for devices as it shows how they perform as an electrical component. If a device has too high a resistance it will not work as efficiently at converting electrons into photons. It can also be used to find the power supplied to a device at a certain bias. Electrical characterisation can be done as soon as the adequate contacts have been put onto a device – via probing, and after the device has been fully fabricated – by regular I-V characterisation with a mount.

3.5.1. Current-voltage (I-V) characteristics

When measuring the I-V characteristics of a device, or part of a device, a potential difference is applied across the two contacts, the absolute value of the corresponding current is then saved and the potential difference is changed. In this project, this was done by connecting the device to a Keithly source meter, which is in turn, connected to a computer which uses LabView software to change the potential difference and record voltage and absolute current at each corresponding value. The generic setup used to take I-V measurements can be seen in Figure 3.8, the device is connected to the Keithly source meter via a coaxial cable. There are two different ways in which I-V characteristics are measured, one after all contacts are applied, but before scribing and wire bonding takes place (probing), then I-V measurements are taken of the fully bonded device Figure 3.8 (b).

3.5.1.1 Probing

Probing is measuring the current-voltage characteristics of a sample in different locations of the sample before the sample is cleaved, mounted and bonded. This is used to see if the devices work as they should, i.e. give diode like characteristics. Because the sample is not bonded when probing is done, the current is passed through the sample by connecting probes, which are in turn connected to a power source meter, to the contacts. If it the sample is top-top contacted, then one of the probes will be connected to the grid contact, and the other to the top contact; if the sample is top-bottom contacted, the sample will be placed on a glass slide with a thin gold film coating, one probe is then connected to the top contact, and the other is placed on the gold coated slide, allowing current to be passed through the bottom contact. The contacting for probes can be seen in Figure 3.8 (a).

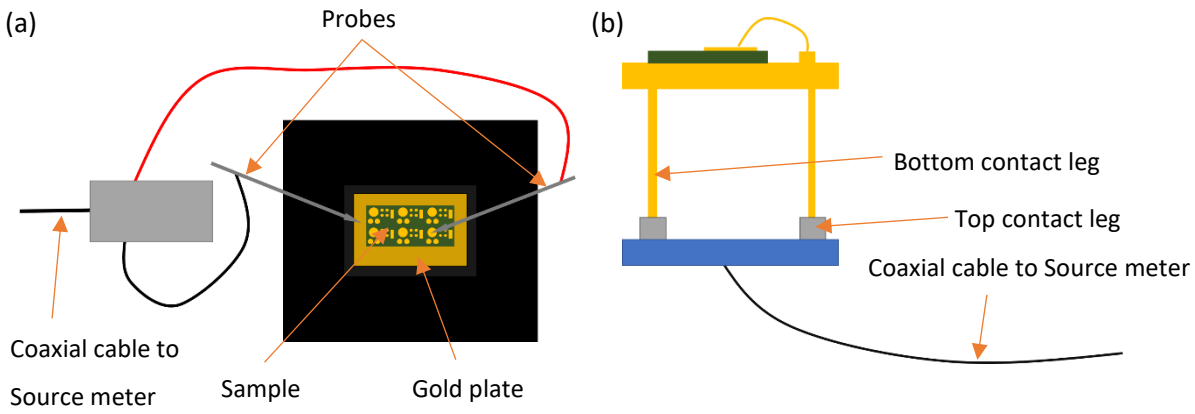

Figure 3.8: the setup for taking I-V characteristics for (a) probing and (b) for a mounted and bonded device.

Probing can also show how the current moves around the mesa structure and active region. The top-contact mask has three different diameter contacts: 800 µm, 400 µm and 200 µm, all of which have mesa structures. Because probes can be moved around and are not bonded to the contacts, it can be used to take the I-V characteristics of each of the different sizes of mesa. If this is done for a sufficient number of mesas around the sample, they can be plotted, each mesa size should approximately group with the others of the same diameter. The I-V curves can then be normalised with either mesa perimeter or area; if the I-V curves all group together when normalised for area, it shows that the current flows through the area of the mesa. However, if the grouping occurs when normalising for perimeter, it shows that current is largely flowing around the surface of the mesa rather than through it, which can be a sign of high surface current which is undesirable for recombination in the active region.

3.5.1.2 Mounted and bonded device

One a device has been mounted, the setup for taking the I-V curve can be seen in Figure 3.8 (b), this then goes, via a coaxial cable, to be analysed as explained in section 3.5.1. This has to be done again as bonding should create a better contact than probing so the current should be higher for the same potential difference. This shows if the bonding has been successful and also allows the resistance at different forward biases to be calculated. If the resistance is significantly higher for a bonded device in comparison to the probed devices, it can imply that something has gone wrong with the bonding process and can indicate poor contact quality.

3.5.2. Total effective resistance

The total effective resistance of an I-V curve can be calculated by taking the inverse of the differential of the I-V curve, showing the resistance of the device at each potential difference measurements were taken at. This was done by importing the data saved by the LabView software and exporting it into a Python 3 script. Using the NumPy Python library differentiation function [53], it is possible to find the gradient of the graph at each corresponding point, and using simple, inbuilt mathematical functions, taking the inverse of these points. This made it possible to find the series resistance at each potential difference and see how it changes, for this purpose, the resistance is only considered under forward bias, as that is what the devices will be operating under.

3.6. Electroluminescence

Electroluminescence (EL) is the emission spectrum which comes from the electrical pumping of a device. To measure the EL spectra of a device, it must be fully fabricated as explained in section 3.4, this is so that it can be electrically pumped from an external source. In this project, the driving current was provided by an alternating current (AC) power source, this had the option to operate in pulses with a duty cycle of which could be varied from 0 – 100%, this would be selected based on the device that was being tested and how much it would heat up whilst having current put through. Devices were tested at ~10 – 20% duty cycle to avoid the effects of Joule heating, allowing for higher driving currents to be tested without heating occurring. The frequency of the AC was set to 1kHz, this is a standard AC frequency and allowed the signal to be picked up by the lock-in amplifier.

EL was tested from 4 – 300 K during this project, to do this, the device is mounted inside a cryostat, in a holder which once inside the cryostat is aligned so that it emits straight, relative to the translucent window of the cryostat. When the device is being driven, it emits radially, which means that if the rays are left uninterrupted most of the light will not reach the detector. To compensate for this, a system of two planoconvex lenses is used, one lens is placed as close to the window of the cryostat as possible, with the convex face of the lens facing the incoming light, the purpose of this lens is to take radial light, and collimate it, so that the beams are as close to parallel as they can be. The second lens is used to un-collimate the light so that it can be focused into the slit; this is done by having the planar face of the lens face the incident light. This lens set up can be seen in

Figure 3.9, there are seven degrees of freedom between the two lenses, these are used to align the device so that the maximum amount of light possible enters the detector. A monochromator

is used to separate the EL emission into its constituent wavelengths, this is the same technique used in the PL in this project and the experimental setup of this described in section 3.3.

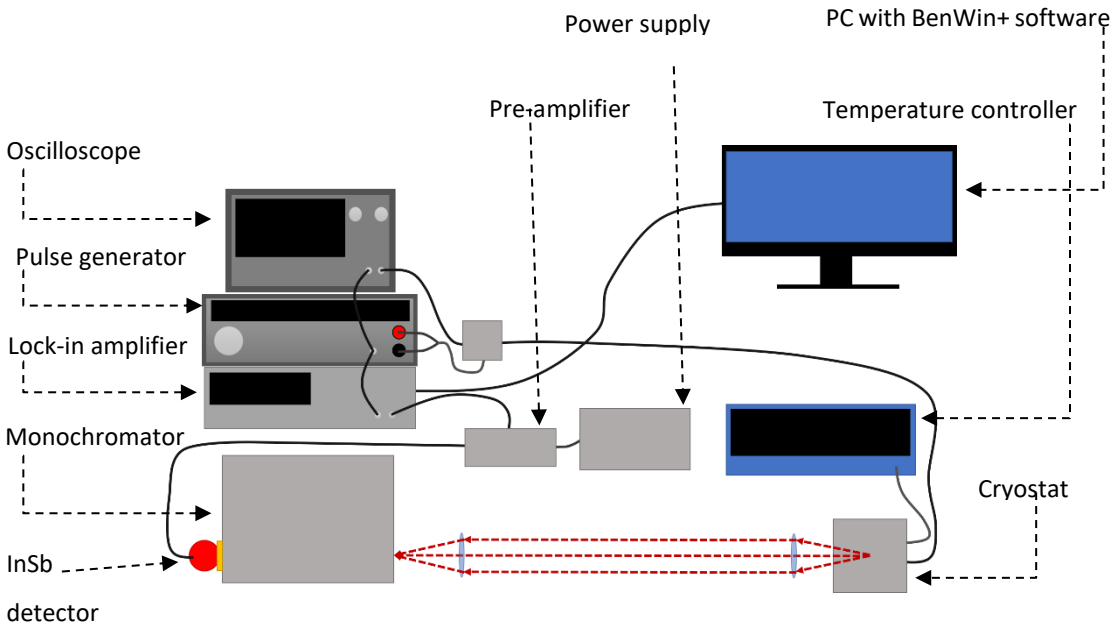

Figure 3.9: The setup used to electrically pump a device and then measure the emission spectra, this can be used for room temperature, and low temperature measurements.

To obtain spectra at different temperatures, the device chamber in the cryostat is pumped down to 10^{-2} mbar. The cryostat used for taking EL measurements is a cryo-free cryostat, meaning that no exchange gasses are needed to reduce the temperature to 4 K. Instead, a mechanical cooler is used operating using a Gifford-McMahon coolers. Using an internal heater controlled by a controller in the cryostat, it is possible to control the temperature in the cryostat from 4 – 300 K. This is used to take EL measurements in this temperature range, used to see how the emission spectrum changes as a function of temperature for bandgap analysis. This is in comparison to a liquid helium cooled cryostat, which uses cryogenics to reduce the temperature down to 4 K.

The main features that are found at any given temperature are: peak wavelength/emission energy, integrated emission and the amplitude of the emission spectrum. The line-width (or full-width half-maximum (FWHM)) of a spectrum is found by finding the difference of the corresponding wavelengths at half of the amplitude of the emission spectrum.

3.7. Power measurements

Power measurements are required to see both the output power of the device, which allows its brightness to be compared to other devices, but also so that the external efficiency of the device can be calculated.

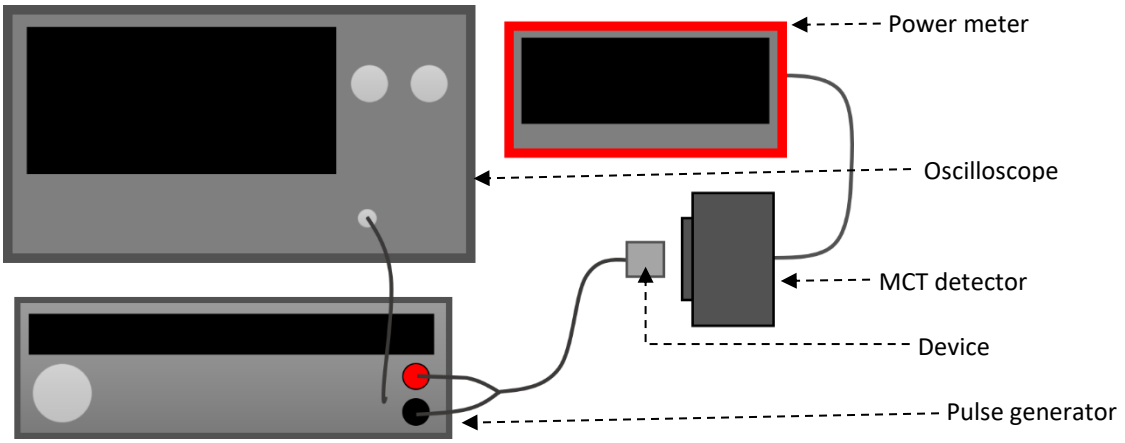

Figure 3.10: Setup to measure the power output of devices.

To measure the output power of a device, the equipment is set up as shown in Figure 3.10. In this, the device is driven by an alternating current, power source meter at 1 kHz with a duty cycle of ~20%, to prevent Joule heating. Heating effects can decrease the output power of the device, thus, increasing the contribution of noise, making the power reading less accurate. To detect the output power of a given device, a Thorlabs S180C Mercury Cadmium Telluride (HgCdTe/MCT) photodiode is connected to a Thorlabs PM100D power meter console; the peak wavelength of the device can be programmed into the power meter so that the power calibration can be competed.

Once the device has been turned on, it should be placed in close proximity to the detector so that as much of the produced light as possible enters. At first, the output power of the device will not be consistent, a real time measurement is given on the power meter and before taking an average, the power should be oscillating a small amount around an equilibrium point. After this, an average power reading over a thirty second period should be taken, the power meter will give an average reading, as well as an uncertainty, this is recorded manually. Power readings are from taken from a driving current of 40 mA, which is the lowest driving current provided by the source meter, up to around 200 mA, which is the highest that the device can safely be driven at. This should be recorded, along with the current going into the device, as well as the voltage across it, to calculate the input power.

3.8. Fourier-transform infrared (FTIR) spectroscopy

FTIR spectroscopy is the experimental method used to identify the energy of certain chemical bonds, in the infrared spectrum; generally, from 4000 – 400 cm^{-1} (2.5 – 25 µm), the theory behind which is explained in section 2.4. Because photons corresponding to these bond energies are absorbed, if the sample has a polychromatic light source shone on it, some of the

corresponding to the energy of chemical bonds will be absorbed, and the rest will be transmitted or reflected.

To measure transmittance, absorption and/or reflection of a sample, a Michelson interferometer is used with a broadband laser source. The Michelson interferometer consists of a light source, a beam splitter, a fixed mirror, a moveable mirror and a detector. The layout of a Michelson interferometer can be seen in the FTIR spectrometer diagram in Figure 3.11. In the Michelson interferometer, the light source (after passing through the sample in the case of an FTIR spectrometer), hits the beam splitter; 50% of the light is reflected, hitting the stationary mirror, the other 50% passes through, hitting the moveable mirror. Both are then reflected, upon hitting the beam splitter again, 50% of the light reflected from the stationary mirror will be transmitted through the beam splitter; 50% of light reflected from the moveable mirror will be reflected such that it enters the detector.

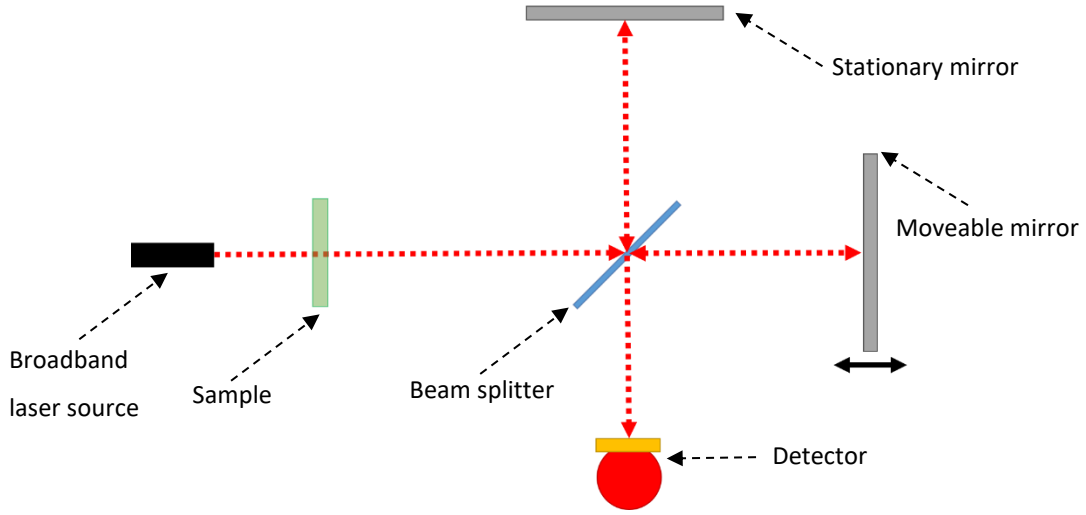

Figure 3.11: The workings of an FTIR spectrometer, including sample setup for measuring absorption or transmittance. The solid black arrow on the moveable mirror indicates the direction in which it can be displaced.

Because the beams travelling from the beam splitter to the detector have the same beam path, they interfere with one another. The detected signal will show the interference pattern of the broadband source, this pattern is dependent upon the position of the moveable mirror. When the stationary and moveable mirror are the same distance from the beam splitter, there is no path difference, all of the wavelengths will interfere constructively. However, as the moveable mirror moves backwards, the detected signal will have some constructive, and some destructive interference, because constructive interference patterns occur when the path difference is a factor of nλ and destructive interference occurs when the path difference is a factor of $\frac{(2n+1)\lambda}{2}$, where $n \in \mathbb{Z}^+$. A Fourier transform is conducted at each mirror position as each interference

pattern is a summation of many cosine waves of different wavelengths and amplitudes. After a sufficient number of mirror positions, analysis software can be used to plot the amplitude of different wavelengths measured by the detector [54].

In practice, to use a Michelson interferometer to find the absorption/reflection spectra of a sample; first, the number of scans and resolution of the scan (in cm^{-1}) is defined in the software which controls the spectrometer. Then, a background scan must be done with the corresponding resolution, as some absorption will happen due to atmospheric gasses which if not accounted for, would create incorrect data. Then, the scan is defined for the sample, and the software will automatically make the spectrometer complete the scans and corresponding Fourier transforms. This will give the user a spectrum of intensities at different wavelengths, standard formatting is that the infrared light is measured by wavenumber and the intensity is a base ten logarithmic scale.

4. Literature review

In this chapter, an overview of the development of and current leading technology in light emitting diodes (LEDs) operating in the technologically important mid-infrared (MIR) spectral region (2 – 5 µm) reported in the literature will be given. A range of material alloy systems and bandgap alignments will be considered and compared. The enhancement of emission through active regions being placed in resonant cavities and the use of inter-band cascading through charge carrier injection shall also be discussed.

4.1. Bulk LEDs

Bulk homojunction LEDs were the first material systems to be fabricated into devices. The first reported device emitted in the near-infrared (NIR) spectral range, with ~ 800 nm emission from a GaAs based p-n junction by Hall and Fenner in 1962 [55]. Mid-infrared devices were then created in 1966 by Melngailis and Rediker using electrical injection of carriers in an InAs based p-n junction. This emitted at 3.7 µm at room temperature [56]. Electroluminescence from a GaSb p-n homojunctions was first reported by Blom et al in 1971 [57], this was from a device grown via Liquid Phase Epitaxy (LPE). This device emitted at room temperature with two peaks, one at 1.7 and one at 1.6 µm. This due to two acceptor states near the valence band-edge creating two possible recombination sites for the charge carriers. Due to advances in epitaxial growth techniques such as molecular beam epitaxy (MBE), liquid phase epitaxy (LPE), and metal-organic chemical vapor deposition (MOCVD) it became possible to grow other III-V binaries, ternaries and higher-order alloys for bulk structures. This was beneficial as it allowed a wider range of bandgaps to be realised which could be grown on standard substrates due to lattice matching.

4.1.1. InAsSb

Dobbelaere et al. (1993) used MBE to grow an $InAs_{1-x}Sb_x$ p-n structure on both GaAs and Si substrates [58], three different devices with Sb contents of: x = 0, 0.06 and 0.15 were grown. The resultant spectra can be seen in Figure 4.1 (a) with peaks around 3.3, 3.5 and 4.2 µm corresponding to x = 0, 0.06 and 0.15 respectively. There is a slight distortion in the spectra around 4.2 µm which is due to CO_2 atmospheric absorption, demonstrating this materials suitability for gas detection. It also showed that the addition of Sb in the alloy increases the brightness of the spectra several times. They further showed that as temperature increases, the external efficiency of the device decreases, this can be seen in Figure 4.1 (b). The efficiency decreases by a factor of 10 from 77 K to room temperature due to an increase in the prevalence of non-radiative recombination mechanisms.

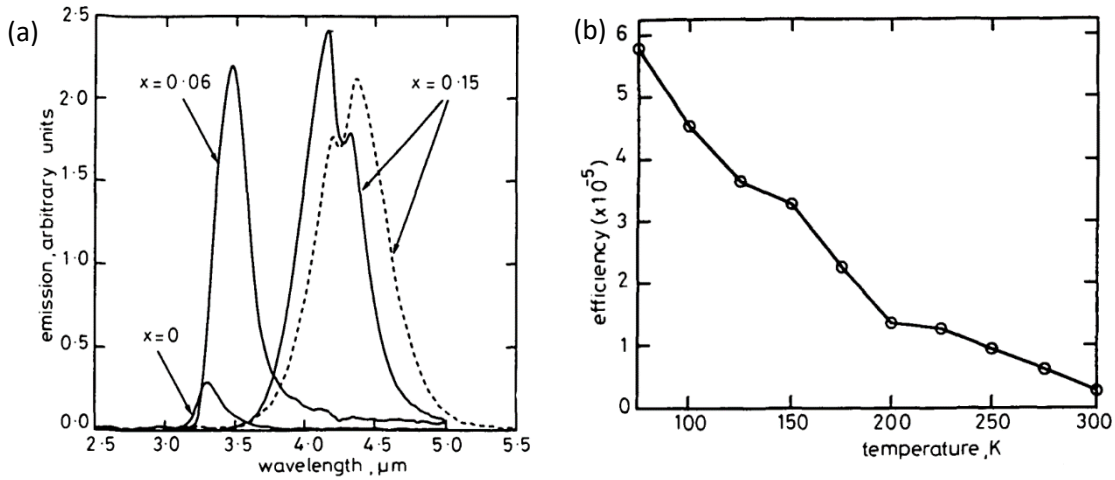

Figure 4.1: (a) electroluminescence of InAsSb devices reported by Dobbelaere [58], the solid line shows results for devices on GaAs and the dotted Si and (b) a plot of the external efficiency for the InAsSb light emitting diode reported by Dobbelaere

Zotova et al (1992) reported a quaternary InAsSbP LED grown using LPE onto InAs substrate which gave emission at 4.7 μm [59]. Quaternaries have the advantage of a wider range of alloy compositions which can be grown lattice matched, or having a particular amount of strain, on a particular substrate due to the extra degree of freedom in the alloy in comparison to ternaries. A wider range of alloy compositions also allows for a wider range of possible bandgaps, allowing for the tailoring of emission.

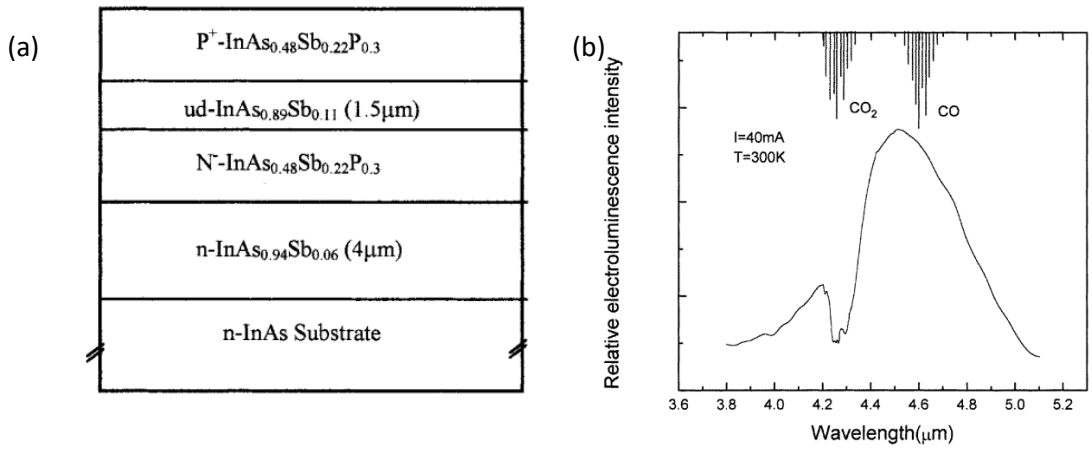

Figure 4.2: (a) the structure of the heterojunction device reported by Gao [60] and (b) the room temperature electroluminescent spectra from that device, showing the CO_2 absorption band around 4 200 nm.

$InAs_{0.89}Sb_{0.11}/InAs_{0.48}Sb_{0.22}P_{0.3}$ heterostructure were reported by Gao et al (1999) [60] which was grown via LPE onto an n-InAs substrate. An $InAs_{0.94}Sb_{0.06}$ buffer was added to account for the lattice mismatch of the InAsSb in the heterostructure with the substrate, reducing the likelihood that defects would occur in the lattice structure. This buffer can be seen in the schematic in Figure 4.2 (a) as well as the layout of the rest of the heterostructure. This device had an

electroluminescence peak at room temperature of 4.5 µm, as can be seen in Figure 4.2 (b), with a maximum output power of 50 µW.

At Lancaster University, MBE was used to grow an $InAs_{0.06}Sb_{0.94}$ LED integrated onto Silicon via a GaSb buffer layer as reported by Delli et al (2019) [9]. III-V integration onto silicon is important as it allows for on-chip light sources compatible with current technology to be utilised. This gave room temperature emission at around 4.5 µm with a 6 µW output power and external efficiency of 0.011 %.

4.1.2. InGa(As)Sb

The quaternary InGaAsSb has the aforementioned benefits of having multiple degrees of freedom, allowing for lattice matching to a plethora of substrates whilst being able to engineer the bandgap. However, the growth of this material system faces an alloy metastability challenge. With certain alloys, the material does not form homogeneously, instead, segregated regions of InAs and GaSb, which gives non-uniform optical and adverse electrical properties [61]. This is generally considered to be with In contents of over 20 % and arsenic contents over 20 %, a more in depth discussion of the miscibility gap is had in sections 6.1.1 and 6.1.2. The development of MBE has made growing in the so called “miscibility gap” easier, but the material quality is much harder to preserve and the substrate temperature must be tailored specifically for the material system.

Zotova et al reported in 1992 a ternary bulk system of $In_{0.94}Ga_{0.06}As$ grown using LPE onto an InAs substrate. The bulk structure was lattice matched to the substrate and gave room temperature emission at 3.3 µm [59]. Heterojunction structures have also been utilised in creating devices operating in the mid-infrared region. Popov et al (1997) reported a N-AlGaAsSb/n-GaInAsSb/P-AlGaAsSb lattice matched double heterostructure grown via LPE onto n-GaSb substrates [62]. This gave a room temperature electroluminescence peak at 1.94 µm, with a maximum output power of 3.7 mW and quantum efficiency of 5.5%.

In 2007, Krier et al reported a quintenary GaInAsSbP device grown via LPE, lattice matched to n-GaSb substrate [63]. Quintenary alloys have a further advantage from quaternary as they have an additional degree of freedom, in the same way that a quaternary has an extra degree of freedom over ternaries. This means an even wider range of lattice matched alloys can be grown on a given substrate, giving more band-edge configurations for a larger range of emission spectra. This device gave high intensity electroluminescence from 77 K up to room temperature, with a RT peak around 4.3 µm.

An InGaAsSb/AlGaAsSb heterostructure grown via LPE onto n-GaSb substrate was reported by Petukhov et al (2013) [64]. Two peaks were observed here, one at 0.64 eV (1.94 µm) and another at 0.284 eV (4.37 µm), these are from the GaSb substrate and InGaAsSb regions respectively. The power of the InGaAsSb peak, at room temperature (294 K), had an output power of ~1 µW being driven at 1.0 A. A maximum output power of ~20 µW was obtained by the device at 383 K whilst being driven at 2.5 A.

4.1.3. AlInSb

The AlInSb material system has been extensively researched due to it showing better charge carrier mobility compared to other III-V materials, leading to improved electrical characteristics, as reported by Meriggi et al (2015) [66]. Moreover, because the alloy contains only one group-V material (Sb), it is much easier to control the alloy content, making it easier to grow specific alloys in comparison to ternaries with two group-Vs such as InAsSb. Ying et al (2014) demonstrated an $Al_{0.05}In_{0.95}Sb$ structure grown on GaAs substrate with a GaSb buffer layer via MBE [67]. Growing on GaAs is beneficial because it is less expensive than GaSb, however, it presents the challenge of having a different lattice constant, this is why buffer regions are required. Moreover, it is semi-insulating, so more complex fabrication is required to properly contact it in comparison to growing on GaSb. Due to the difference in lattice constant of the binary GaSb, AlSb and InSb alloys – AlSb and InSb both have a larger lattice constant than GaSb, it is not possible to grow the $Al_xIn_{1-x}Sb$ lattice matched to GaSb. However, growing on GaSb is still beneficial as its lattice constant is closer than that of GaAs, meaning that thicker layers can be grown without relaxation occurring. Room temperature electroluminescence was reported around 4.2 µm for this device. It was further demonstrated that the n-i-p structure is superior in comparison to the p-i-n structure here due to the electrical characteristics of the n-doped material in comparison to p-doped.

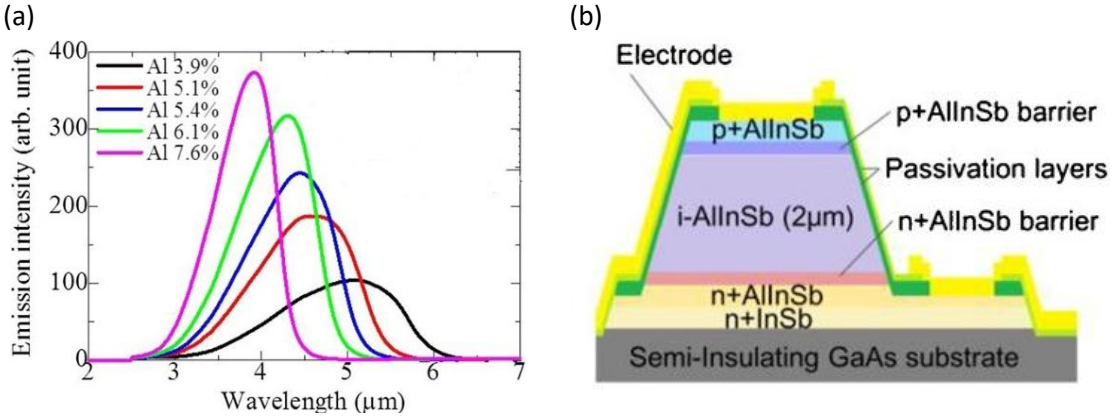

Figure 4.3: (a) room temperature EL of AlxIn1-xSb devices reported by Fujita [65] and (b) schematic of that device, showing the substrate and buffer regions.

Fujita et al (2018) reported an $Al_xIn_{1-x}Sb$ based device grown via MBE onto a GaAs substrate with x = 3.9 – 7.6 % [65]. These devices gave room temperature EL spectra with peaks from ~4 – 5 µm with decreasing Al content increasing the wavelength, as seen in Figure 4.3 (a). This displays an advantage of this material system in comparison to InGaAsSb; it can be engineered to have a smaller bandgap, thus emit at a longer wavelength. The buffer region and n-i-p structure of the device can be seen in Figure 4.3 (b). This had the highest power conversion efficiency of any reported LED around 4 µm at the time of publication at ~ 1 %.

4.2. Quantum wells

Quantum wells (QWs), single and multiple, have been utilised in a multitude of different material systems to specifically tailor emission wavelength, improve radiative recombination rates and supressing non-radiative ones. The mechanisms by which this occurs are discussed in section 2.1.4. Type-I and type-II structures as well as different alloys have been utilised to further tailor the bandgap for emission and non-radiative recombination quenching. The use of quantum wells has also allowed for strained structures to be grown due to the thickness of a quantum well being lower than the critical layer thickness for strains of around 1 – 2 %.

4.2.1. Single quantum wells (SQWs)

Molecular beam epitaxy has been used to grow single quantum well structures. Baranov et al (1996) reported a $Ga_{1-x}In_xSb$/GaSb type-I strained quantum well on GaSb substrates. These devices had well widths with thicknesses from 7 – 10 nm and Indium contents (x) of 0.26 and 0.35 [68]. These devices gave room temperature electroluminescence in the range of 1.9 – 2.2 µm. Furthermore, Tang et al (1998) reported a type-II InAs/$InAs_{1-x}Sb_x$ structures grown on p-InAs substrate via MBE [69]. Devices were grown with Sb contents (x) of 0.16 and 0.26, emitting at 5 and 8 µm with output powers of 50 and 24 µW respectively, this was done with a driving current of 1 A. InGaSb/AlGaAsSb type-I structures grown on GaAs substrates via MBE utilising a GaSb buffer layer were reported by Yu et al (2011) [70]. This sample showed photoluminescence of 1.94 µm at room temperature. Mikhailova et al (2019) reported GaSb/InAs type-II quantum wells grown on n-GaSb substrates via metalorganic vapor-phase epitaxy (MOVPE) [71]. These samples displayed room temperature electroluminescence at 3.3 µm and 77 K electroluminescence at 3.2 µm, with additional peaks at 3.5 and 4.6 µm corresponding to transitions from the first electron energy level to various other hole states in the structure.

Although several single quantum well devices have been grown and fabricated and have shown room temperature EL. It has been shown through multiple studies that using more quantum wells achieves more luminescence – for both electrically and optically pumped systems. An

example of this can be seen in Figure 4.4 (a), where the spectral purity of the device is increased by having multiple quantum wells, as will be discussed in section 4.2.2.

4.2.2. Multiple quantum wells (MQW)

4.2.2.1 Type- I InGaAsSb/AlGaAsSb

The InGaAsSb well with AlGaAsSb barrier material system is very versatile, with a wide range of tailorable bandgaps based on alloy content of each alloy in the well and barrier. Research into the InGaAsSb/AlGaAsSb material systems show that it can be turned into high quality type-I devices. An example of the band structure of these devices can be seen in Figure 4.4 (b) [72], showing the large conduction band and valence band offset for charge carrier confinement.

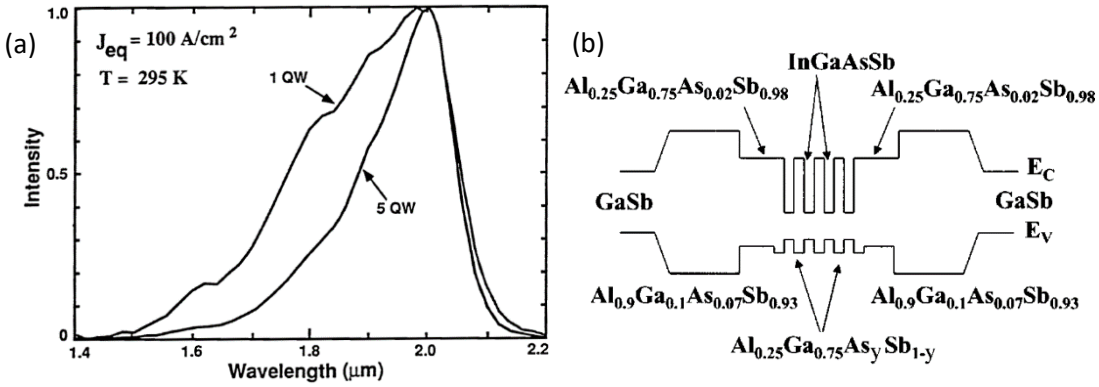

Figure 4.4: (a) single quantum well vs multiple quantum well EL spectra at RT for the InGaAsSb/AlGaAsSb device reported by Garbuzov [73] . The band structure of a laser device with an Al0.25GaAsSb/InGaAsSb active region used for emission in the 2.0 – 3.0 μm range [72].

The AlGaAsSb/InGaAsSb system has been effectively utilised to create devices which emit in the 2 – 2.5 μm wavelength range. This uses active regions with Indium contents ranging from ~ 10 – 40 %, Arsenic contents ranging from ~ 2 – 20 % and well widths of ~ 10 nm [74, 75]. It is also possible to change the strain in the quantum well by varying the Indium and Arsenic contents. Strain has been used to engineer the bandgap structure and to supress Auger recombination, this is further discussed in section 2.3.2.1.

This system has also been used to create devices with wavelengths of 2.8 μm, reported by Li et al (2004) [72], grown via MBE on GaSb substrates. In this system, a type-I quantum well with an Indium content of 40% and an arsenic content of 14 % was utilised with $Al_{0.25}$GaAsSb lattice matched barriers, this gave room temperature emission with good electrical performance. Lin et al (2004) also reported type- I InGaAsSb/AlGaAsSb devices grown via MBE onto n-GaSb substrates [76], with indium contents of 30%, arsenic 9.6% and well widths of 10 nm, room temperature electroluminescence was achieved at 2.24 μm. They also grew devices with active

regions containing indium contents of 50%, arsenic 23 % and 20 nm wells to achieve emission at 3.04 µm. The strain in these quantum wells ranged from 1.19 % for lower indium and arsenic contents to 1.50 % for higher indium and arsenic. Most of the samples discussed here were grown on GaSb substrates and fabricated as Fabry-Perot laser by including cladding layers or as light emitting diode. However, Qi et al (2019) reported this material system with $In_{0.17}GaAsSb$ type-I active regions and lattice matched barriers [77] grown on GaAs substrates with GaSb buffer regions via MBE. Devices had strains of 1.1% and well widths of ~10 nm, this produced an emission of 2.4 µm at room temperature.

As the bandgap of InGaAsSb decreases through the addition of In and As into the alloy, the absolute position of the valence band decreases, whereas the barrier valence position stays the same. This poses a problem in the material system because as the valence band confinement decreases, the hole confinement decreases. Lower hole confinement can decrease the wavefunction overlap of the charge carriers, leading to a lower rate of recombination, thus quenched radiative recombination. It can also allow for charge carriers to be forced out of the well due to the thermal energy of the system. However, the barriers can have Indium incorporated to create the quintenary $Al_xGa_wIn_{1-x-w}As_{1-y}Sb_y$, this is a requirement to obtain longer wavelengths from GaSb based type-I quantum wells. This is due to a deeper valence bandedge, giving greater confinement potentials for the holes in the device as the valence bandedge of the well has a lower energy. This is useful as the amount of As in the alloy increases, it decreases the position of the valence bandedge, in a quaternary barrier system with no In, this will decrease the hole-confinement potential. However, the quintenary alloy, with its lower valence band edge allows for greater hole confinement of these high As well alloys. Because of this greater hole confinement, more indium and arsenic can also be incorporated into the well. Jung et al (2010), from the world leading research group in Stony Brook, has reported a dual wavelength light emitting diode grown on n-GaSb via MBE which incorporated type-I InGaAsSb wells with both quaternary and quintenary barriers [78]. The structure used in this device was similar to that shown in Figure 4.4 (b), with type-I wells and graded cladding. However, rather than $Al_xGa_{1-x}As_{1-y}Sb_y$ barriers, there are $Al_xGa_wIn_{1-x-w}As_{1-y}Sb_y$ barriers grown lattice matched to GaSb. This produced room temperature emissions of 2 µm and 3 µm with output powers of 2.8 mW and 0.14 mW from the quaternary and quintenary barriers respectively. Suchalkin et al (2008), also of Stony Brook, further reported InGaAsSb in quintenary barriers, grown on n-GaSb substrates via MBE [79]. The room temperature emission of $In_{0.55}GaAs_{0.22}Sb$ wells in quaternary and quintenary barriers can be seen in Figure 4.5 (a), with emission peaks ranging from 3.0 µm up to 3.5 µm. The maximum room temperature output power of these devices was reported to

be 0.7 mW. The effect of using quaternary and quintenary barriers can be seen in Figure 4.5 (b), showing that using quintenary barriers produced devices with higher output power capabilities.

Similarly, Ding et al (2016) reported a $Ga_{0.177}InSb$/AlGaInSb type-I structure grown on GaAs substrate, similar to the quintenary structure previously discussed, but with arsenic free wells and barriers [80]. Arsenic free structures provide the benefits of single group-V growth as previously mentioned, it is much easier to create high quality material with the intended alloy content. This structure gave room temperature EL with a peak of around 4.4 µm which was more than twice as bright as a bulk reference sample for the same driving current. However, this device suffered from not having graded cladding layers, restricting the sample to surface emitting spontaneous emission rather than being able to lase through stimulated emission. Graded layers in the cladding allow for easier injection of charge carriers into the active region of a laser and also decrease the turn on voltage of the device, allowing it to operate at lower input powers [81].

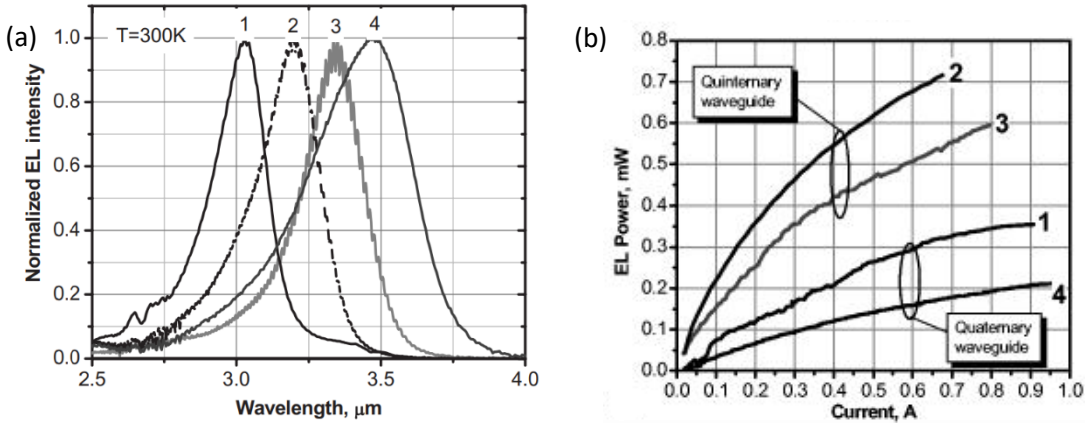

Figure 4.5: (a) the normalised room temperature electroluminescence spectra of InGaAsSb/Al(In)GaAsSb devices reported by Suchalkin [79] and (b) the corresponding output powers as a function of driving current of the devices who's spectra are shown in (a).

Jung et al (2011) further developed the quintenary barrier quantum well system, using the same device structure reported by Suchalkin, with InGaAsSb active region with quintenary barriers [82]. These were used to create 512 x 512 LED arrays emitting at 3.66 µm at room temperature, with each LED having a radiance of 1.3 W cm^{-2}.

Another structure which has been utilised to create longer emission with type-I bandgap alignment is InGaAsSb wells with GaSb barriers. Although this can also be used to create type-II devices, with sufficiently low arsenic contents, a type-I bandgap is achievable. An example of the valence band offset of the system is provided in Figure 4.6 (a), showing how the valence band offset increase as the strain increases (decrease in As content). This requires the InGaAsSb to have a sufficiently small bandgap so that it can be well contained in the GaSb bandedges.

Sifferman et al (2015) reported type-I $In_{0.55}GaAsSb/GaSb$ grown on n-GaSb substrate via MBE, samples of various As contents were grown to see the effect of strain on the system [83]. This device employed 10 nm InGaAsSb quantum wells with 20 nm GaSb barriers. It was also reported in this paper that the emission intensity is increased when the substrate temperature during the QW growth process is lower, with devices being grown at 350 and 410 °C. This is partially due to the varying Arsenic contents across the different quantum wells discussed in the paper, which is especially prevalent when substrate temperature is changed. The difference in the PL intensity cannot be solely attributed to the difference in substrate temperature during growth. But the variable PL intensity due to growing with different substrate temperatures is also a result of the quality of alloy formation when growing close to this miscibility gap. Because the alloy is Indium rich, it requires a lower growth temperature to properly form epilayers, this will vary depending on the alloy mixture. This simultaneously allows for structures with higher strains to be grown due to an increase in As incorporation, the effect of substrate temperature and strain on PL intensity can be seen in Figure 4.6 (b). The PL samples gave room temperature emission around 3.4 µm. These active regions were also placed into samples which were fabricated into lasers, giving emissions around 3.4 µm.

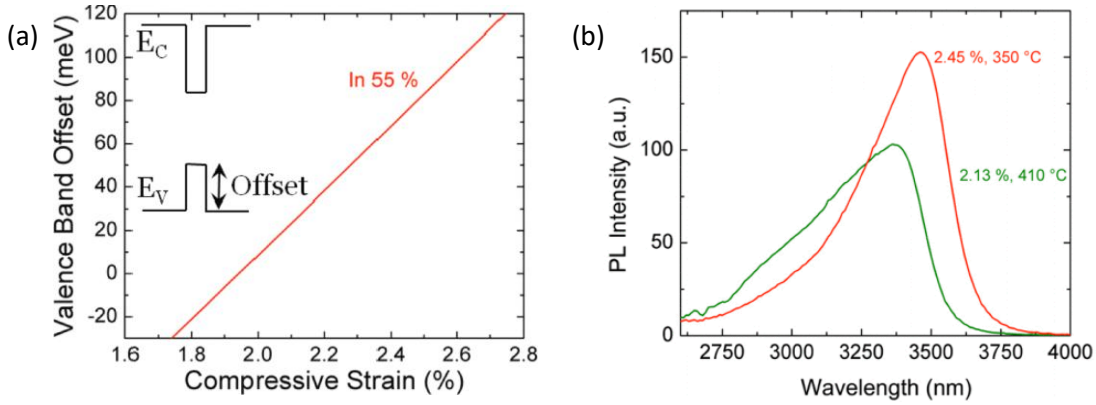

Figure 4.6: achievable valence band offsets of the $In_{0.55}Ga_{0.45}As_{1-y}Sb_y$ system as the strain of the active region is increased and (b) comparison of PL from two InGaAsSb/GaSb samples grown at 350 and 410 (red and green respectively) with their respective strains shown. Both were reported by Sifferman et al [83].

4.2.2.2 Type – I (In)(Ga)AsSb/InAlAs

Grietens et al (1996) reported an Sb free InGaAs/InAlAs type-I device grown via MOVPE and lattice matched on GaAs [84]. This contained 20 nm $In_{0.8}Al_{0.2}As$ barriers with 10 nm 0.68% compressively strain $In_{0.9}Ga_{0.1}As$ wells which gave room temperature emission of 2.4 µm with an output power of 1.85 µW. These however had a low efficiency of 0.0064% due to high SRH and Auger recombination.

Gallium free $InAs_{0.915}Sb/Al_{0.12}InAs$ type-I wells integrated onto undoped GaAs and Si have been reported by Altayar et al (2022) at Lancaster University [10]. These devices were grown via MBE with various buffer layers to account for the lattice mismatch between Si/GaAs and GaSb based growth. Devices on both GaAs and Si gave low temperature EL with a peak at around 2.9 µm at 20 K. The room temperature EL peaked at around 3.4 µm, with output powers of 63 and 80 µW for the sample on GaAs and Si were obtained respectively on a 1% duty cycle.

4.2.3. Type-II MQWs and Strained layer superlattices (SLSs)

Type-II bandgap alignment can be used to tailor the bandgap of devices more easily and access smaller bandgaps in comparison to type-I alignment due to the electrons and holes being confined separately. They also have extra Auger quenching mechanisms which cannot be achieved in type-I devices. The in-plane Auger process is diminished because of the specially separate charge carrier confinement, making the transition less probable [85], this is further supressed by the removal of hole resonance states with the spin orbital [86]. Due to the positioning of bandedges in type-II devices, they have shown good performance in the > 3 µm wavelength range, from mid to long-wave infrared. Superlattices have the extra benefit of low-charge carrier confinement in the wells. This causes a more de-localised wavefunction in comparison to type-I and type-II MQW systems to form, known as a mini-band. Minibands have the benefit over type-II MQWs in that they have a higher wavefunction overlap and over type-I MQWs in that they have spatially separate confinement functions. However, they have well confined hole states due to the deeper valence band offsets in most materials. This causes well localised hole wavefunctions which is beneficial as it reduces the temperature dependence of Auger recombinations [87]. W-QWs, first developed by Meyer and Hoffman in 1995 [88] utilising both the separate special confinement of type-II band alignment and the benefits which come with high wavefunction overlap.

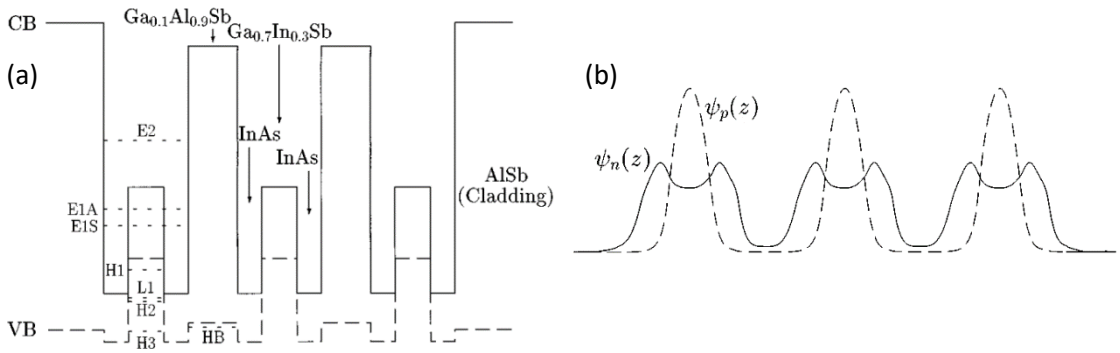

Figure 4.7: (a) the bandstructure of an InAs/GaInSb W-QW in AlSb cladding and (b) the resultant wavefunction of electrons ψ_n and holes ψ_p [88].

This technology uses InAs/GaInSb type-II wells contained in AlSb barriers which gives a type-II bandgap alignment as can be seen in Figure 4.7 (a). This confines electrons within the InAs and holes in the GaInSb. Wavefunction overlaps of up to 70 % have been demonstrated using W-QWs, the resultant wavefunctions can be seen in Figure 4.7 (b). The delocalised electron wavefunction has a relatively broad probability function where the central peak of the hole wavefunction is, hence the larger than normal wavefunction overlap for type-II confinement. Emissions of around 3 µm have been realised using this system, which is utilised in the brightest and highest output power device. Much research in W-QWs has focused on their utilisation in laser structures; where for superlattices research has focused on their application into photodetectors, however, both superlattices and W-QWs have been utilised in LEDs.

4.2.3.1 Strained layer superlattices

The InAs/GaSb system has been utilised to create light emitting diodes, first reported in 1998 by Moiseev et al [89]. InAs/GaSb superlattices were grown on InAs substrate via MBE. Two different devices were created, one with 5nm/5nm InAs/GaSb wells, and the other with 50nm/100nm InAs/GaSb wells. The device with equal an InAs/GaSb period structure is shown in Figure 4.8 (a) including the doping type and AlSb electron blocking barriers. The change in period of the superlattice region in turn changes the position of the energy level and in turn, the bandgap. These both gave emission at 77 K in the 3 – 4 µm region. However, the emission spectra peaks do not only come from the superlattice region. The EL of one of the superlattice devices can be seen in Figure 4.8 (b), the three peaks are due to recombination from: A, e-hh_1; B, e-hh_2; and C, e_2-hh_1. Hoffman et al (1995) reported an InAs/GaSb superlattice light emitting diode grown on undoped GaSb [90]. At 77 K, this showed emission in the mid-infrared (4.6 µm) and long-wave-infrared (10.8 µm) using two different superlattice structures. Most of the work since this has been completed on detectors, with cut-off wavelengths from 3 – 30 µm [91] and cascading devices – these will be discussed later.

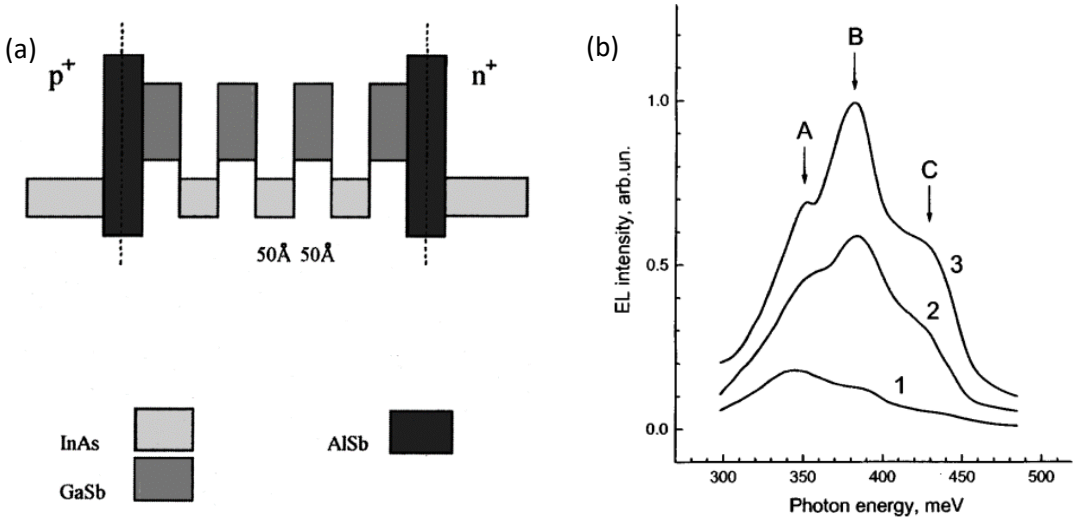

Figure 4.8: (a) the schematic of the active region for the InAs/GaSb device reported by Moiseev [89] and (b) the EL spectra at 77 K of the device described in (a) with driving currents of: (1) 50 mA, (2) 100 mA, and (3) 200 mA; A, B and C describe three separate peaks.

An alternative material system that has been used to create type-II superlattices and MQW systems is InAs/InAsSb. This has an advantage over InAs/GaSb systems in that it is Ga-free, which means that it is less likely to undergo SRH recombination due to the native defects in the bandgap caused by Gallium. Moreover, the system is much easier to grow as it only requires three valves, two of which are always open, whereas InAs/GaSb requires four valves in which are always being switched. Much like for the InAs/GaSb system, most of the research has been focused on detectors, which have shown cut-off wavelengths from 5 to 15 µm [92, 93]. Pullin et al (1999) reported an InAs/InAsSb superlattice system with an AlSb electron blocking layer, grown via MBE on InAs substrate, Sb contents were ~ 8 % [94]. This gave an emission of 4.2 µm with an output power of 100 µW at room temperature. The internal quantum efficiency of the device was ~ 30% at low temperatures, this then dropped to ~ 2 % at room temperature. The active region in this device was ~ 60 nm thick, around the maximum that could be grown before relaxation of the material. This is due to the inherent stress caused by growing lattice mismatched InAsSb onto InAs.

4.2.3.2 Type-II multiple quantum wells

Lancaster University has completed a significant amount of research in developing the InAs/InAsSb material system, including integration onto different substrates, as well as creating strained and strain balanced systems. Krier et al. (2006) reported an InAs/InAsSb MQW system with Sb ~ 0.13 grown on p-InAs substrates via MBE [95]. This device gave room temperature EL with several peaks, from the bulk InAs; electron level from the quantum well to hh_1 and the electron level to lh_1. Room temperature emission was 4.0 µm with an output power of 1.4 µW.

This work was developed on by Carrington et al (2009), who grew the same MQW structure but using Sb ~ 8 % [32]. This was grown on n-InAs substrate via MBE, with a lattice matched AlGaAsSb electron blocking layer. The devices gave room temperature EL with an output power of 12 µW and external efficiency of 0.04 %. There were three EL peaks at room temperature, corresponding to 2.95 µm, 3.35 µm and 3.76 µm for bulk InAs, e-hh_1 and e-lh_1 respectively. The different transitions can be seen in Figure 4.9 (a), this agrees with the results from Krier as well. The room temperature EL, with these peaks can be seen in Figure 4.9 (b), the type-II transitions are more current dependant than the bulk InAs transition which dominates at higher driving current.

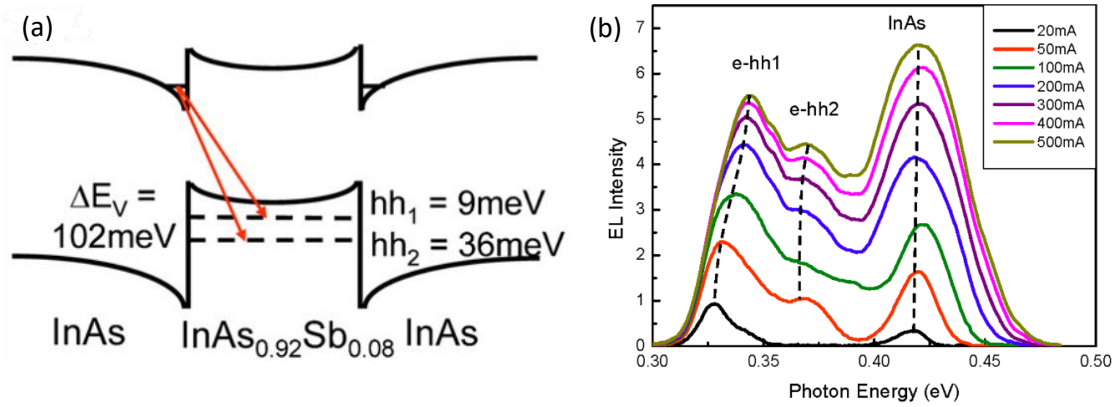

Figure 4.9: (a) the bandgap diagram of InAs/InAsSb type-II quantum well as reported by Carrington [32], shown are the electron level, as well as heavy hole and light hole energy levels in the valence bands and (b) room temperature EL of InAs/InAsSb MQWs reported by Carrington, given as a function of driving current, this is for the device who's bandedges are shown in (a).

Furthermore, Keen et al (2018) reported InAs/InAsSb MQW devices grown by MBE on InAs substrates with Sb ~ 6 and 8 % [96]. These devices gave room temperature emissions of 4.4 µm and 4.7 µm, with output powers of 8.2 ad 3.3 µW respectively. Delli et al (2020) reported the integration of this MQW system onto Silicon [97], obtaining room temperature PL. This was dominated by the e-hh_2 recombination mechanism at around 3.76 µm, however, at lower temperatures, the e-hh_1 recombination mechanism is dominant.

4.2.4. Interband cascading light emitting diodes

Interband cascading devices have been well developed in the past few decades since they were first reported by Yang et al in 1994 [98]. The reason they have been a focus of development is due to their ability to "recycle" charge carriers. I.e. once a charge carrier has been injected, it can partake in multiple bandgap transitions, thus increasing the efficiency of devices. This is done using an electron injection region and a hole injection region, operating using InAs/GaSb broken gap junctions. When a forward bias is applied, the bandedges move, as shown in Figure

4.10 (a), causing charge carriers move, allowing for the 'injection' to occur. If electron and hole injectors are placed next to one-another and active regions either side of this, it allows for electrons and holes to be injected in a more uniform way than in a conventional MQW system [99]. A bandedge diagram incorporating an electron and hole injection region as well as W-QWs is shown in Figure 4.10 (b), further showing how once a charge carrier recombination occurs, this allows for the recycling mechanism of ICLEDs to occur. This is important in creating devices with high wall plug efficiency and high output power.

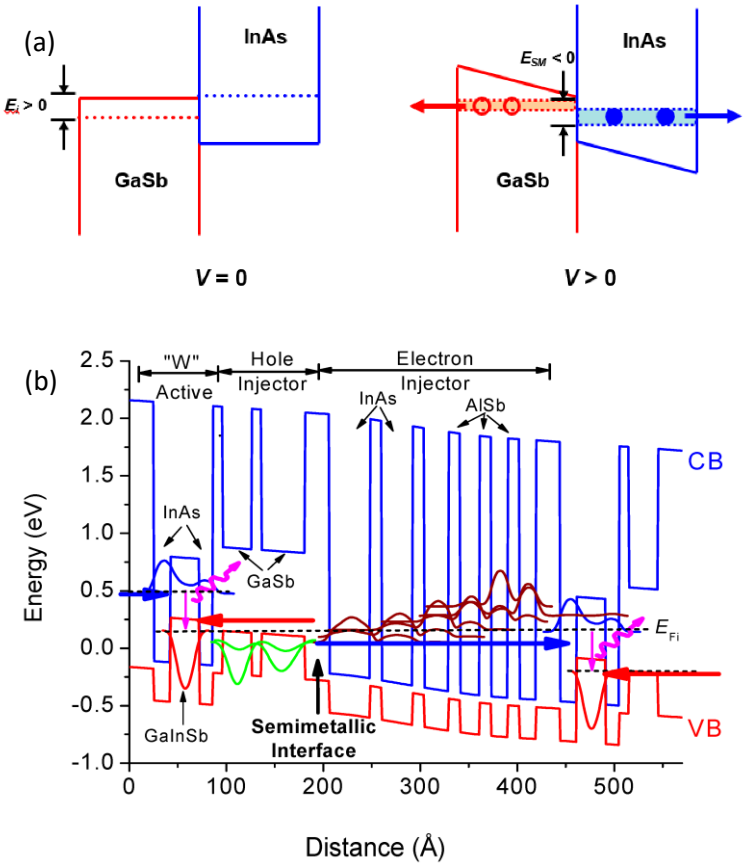

Figure 4.10: (a) the operating principle of the interband cascading system and (b) how this is integrated into a device, utilising W-QWs [99].

This initial structure contained selectively doped InAs/GaSb superlattices with AlSb barriers which could recycle charge carriers once they had undergone one recombination. Koerperick et al (2008) reported an ICLED device based on InAs/GaSb superlattices grown via MBE onto n-GaSb substrate [100]. They grew several devices with different numbers of cascading stages: 1, 4, 8 and 16. The devices emitted around 4 µm for all of the different stages, with a maximum output power of 0.9 mW. It was shown that increasing the number of cascading stages increased the external quantum efficiency from a minimum of 0.36 % with 1 region, to 9.8 % with 16 cascading regions. Similarly, Koerperick et al also reported a device with a similar design, but

different active region which emitted at 8.6 µm with a maximum output power of 0.6 mW [101]. This device had 16 stages of repeating active regions.

ICLED devices utilising InAs/GaSb active regions have also been reported by Ricker et al (2015) who grew a duel wavelength device on n-GaSb substrate via MBE [102]. This device emitted at 3.81 and 4.72 µm with radiances of 5.5 and 2.7 W cm^{-2} sr respectively. The device employed 12 and 16 stage cascading region for the short and long wavelength active regions respectively. Zhou et al (2019) also reported an InAs/GaSb active region device grown via MBE on n-InAs substrate [103]. Two different devices with two and five cascading regions were grown, schematics of which can be seen in Figure 4.11 (a). These emitted around 4.3 µm at room temperature with a maximum output power of 3.65 mW at 80 K and a wall-plug efficiency of 0.2 %, these spectra can be seen in Figure 4.11 (b).

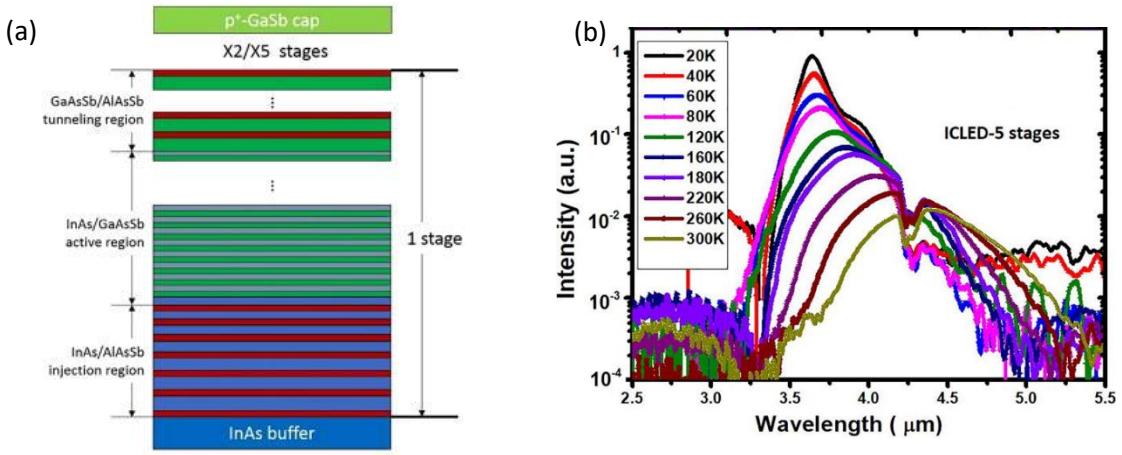

Figure 4.11: (a) schematic of the InAs/GaAsSb ICLED reported by Zhou [103] and (b) the EL spectra for the 5-stage LED who's composition was shown in (a).

Incorporating both resonant cavity enhancement (as will be discussed in section 4.3) as well as interband cascading active regions, Díaz-Thomas et al (2020) reported an interband cascading device based on InAs/GaInSb type-II W-QW structures grown on n-GaSb via MBE [104]. This utilised a 3λ, with lambda being the maximum emission wavelength, optical cavity with a seven-stage cascading region, with a semiconductor GaSb/AlAsSb bottom distributed Bragg reflector (DBR) mirror and a dielectric ZnS/Ge top DBR. This device gave room temperature emission at 3.3 µm with an output power of 60 µW, the spectra purity of the room temperature emission was greatly increased by the resonant cavity. Díaz-Thomas et al (2025) have also reported an interband cascading device in a resonant cavity which has been integrated onto silicon, emitting around 3.4 µm [105]. Showing the possibility for high performance III-V interband cascading devices to be integrated onto Silicon. W-QWs have further been utilised in the creation of ICLEDs by Kim et al (2018) [106] at the Naval Research Laboratory. In this, a 22-stage device was created,

which emitted light at 3.1 µm with an output power of 2.9 mW and WPE of 0.4 %. This is an improvement on the group's previous iterations of the ICLED, such as Abell et al. who reported a similar structure with 15-stages which emitted light at 3.3 µm with a continuous output power of 1.6 mW. The work on ICLEDs is largely built on the research which has come out of the Naval Research Laboratory in the US – partially discussed above – who pioneered the interband-cascade laser. They first reported room temperature operation of a device grown on n-GaSb in 2006, making use of W-QWs to obtain a device emitting between 3.3 – 3.6 µm [107].

4.3. Resonant cavity LEDs

RCLEDs were first reported by Schubert et al (1992), who grew a near infrared device on n-GaAs substrate via MBE [108]. This device consisted of an AlAs/AlGaAs 99% reflectance bottom DBR mirror, with a λ cavity consisting of n and p doped AlGaAs and a metallic semi-transparent top contact used as a top-mirror. This device gave room temperature emission of 862 nm with an output power of ~ 200 µW. The practical benefits of resonant cavity devices were also outlined. These are: enhanced spontaneous emission, including decreased spontaneous lifetime for carriers; improved light extraction due to a higher proportion being emitted through the top of the device; and an improvement in the spectral purity of the emission. The enhancement of spontaneous emission is described by the transfer matrix method (TMM) [109], this utilises the semi-transparent DBRs to cause constructive interference throughout the cavity. An example of how this occurs when the DBR layers and active region cavity are designed correctly can be seen in Figure 4.12, whereby having a 12.5 pairs and 4 pairs of GaSb/AlAsSb mirrors on the bottom and top respectively can lead to an enhancement factor of ~12.5 in the cavity. A mid-infrared RCLED was then reported by Green et al (2004), grown via MBE on n-GaAs substrate [110]. This contained an InAs/InAsSb MQW active region with p-i-n doping, which itself acted as a 3λ/2 cavity. The top contact acted as a 95 % reflectivity mirror, an epitaxial DBR mirror was grown below the active region with a GaAs/AlAs R < 95 % to act as a lower reflectivity mirror. This meant that the device emitted light through the substrate. This device gave room temperature emissions of 3.96 µm, the output power was reported to be ~2.2 times larger than that of a LED not in a cavity.

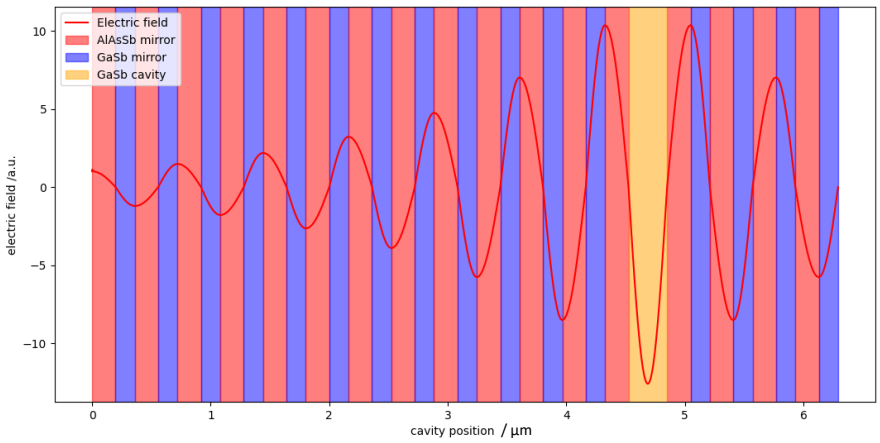

Figure 4.12: A diagram showing how a λ/2 cavity with λ /4 GaSb/AlAsSb mirrors can be utilised to amplify the electric field passing through them via constructive interference, as described by the transfer matrix method (TMM).

Ducanchez et al (2008), from the research group in Montpellier, France, reported an RCLED device based on a type-I InGaAsSb/AlGaAsSb active region grown via MBE onto GaSb substrate [111]. This device used epitaxially grown lattice matched GaSb/AlAsSb$_{0.93}$ DBR mirrors for both the top and bottom mirrors. The bottom mirror had five periods and the top three, creating a surface emitting device, the structure of which can be seen in Figure 4.13 (a). The active region contained 4 QWs placed at the antinode points of a 3λ/2 cavity. This device gave a room temperature emission of 2.3 µm, the spectra of which can be seen in Figure 4.13 (b). An output power of 0.4 mW was measured with an injection current of 800 mA. A tunnel junction was also employed in the structure, meaning the entire device could be n-doped, which gave better electrical performance than having a p-doped top mirror.

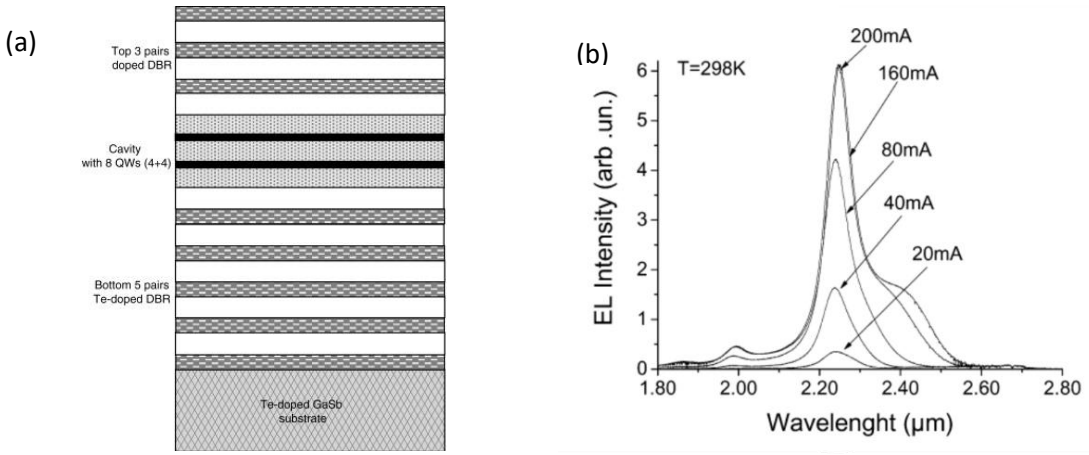

Figure 4.13: (a) a schematic of the substrate emitting MIR-RCLED reported by Ducanchez [111] and (b) current dependant EL spectra from the device at room temperature.

Meriggi et al (2015) reported a RCLED grown on GaAs substrate with a GaSb buffer region via MBE with a AlInSb bulk active region [112]. The AlInSb active region doubled as a cavity, with a 5 pair AlSb/GaSb DBR below the active region, giving a reflectivity of 65 %, the top mirror was the semiconductor-air interface. This device emitted at 4.2 µm with EL three times brighter than a control device which was not in a cavity.

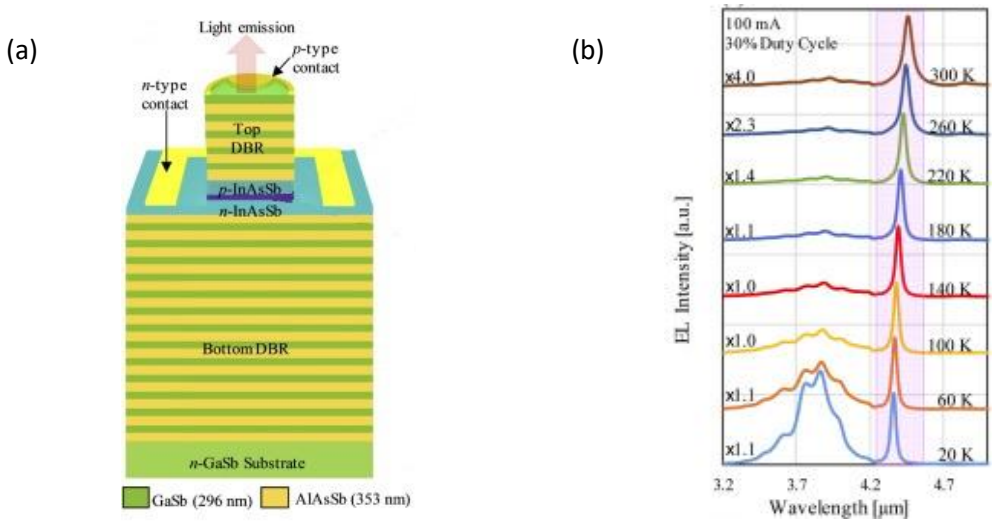

Figure 4.14: (a) the structure of the RCLED device grown on GaSb reported by Al-Saymari [113] and (b) the temperature dependant EL spectra of that RCLED.

Also in this wavelength range, at Lancaster University, Al-Saymari et al (2020) reported a RCLED emitting at 4.5 µm utilising lattice matched GaSb/AlAsSb DBR mirrors and an InAsSb cavity grown via MBE on GaSb substrate [113]. This device had ~ 1 % strained type-I InAsSb wells, in lattice matched AlInAs barriers. An AlSb electron blocking barrier was also utilised to prevent charge carrier leakage. Because the mirrors were grown lattice matched to the substrate, more could be grown than on previous RCLED devices without relaxation occurring, meaning a higher spectral purity. The doping profile of this device was n-type bottom InAsSb cavity with an undoped active region, then a p-doped top half of the cavity which is followed by a p-doped top DBR. This is so that electrons don't have to be pushed through the many repeats of the bottom DBR which would result in adverse electrical characteristics. This leads to a top-top contact configuration being used, part of the bottom half of the cavity is used as a bonding pad, and the top DBR is used as the mesa structure which is then contacted. The bottom DBR contained 13.5 pairs of mirrors and the top 4.5 pairs, this can be seen in Figure 4.14 (a). This resulted in the room temperature output power being 13 times higher than that of an LED which was not in a resonant cavity. The temperature dependant EL for this device can be seen in Figure 4.14 (b). Al-Saymari et al (2023) also reported a RCLED grown via MBE onto InAs substrate with AlAsSb/GaAsSb DBR mirrors [114]. This device had an InAs/GaAsSb SLS active region with an

AlSb/GaSb SLS electron barrier contained in an InAs cavity. The bottom DBR consisted of 13.5 pairs and the top, 5 pairs, this led to a spectrally pure EL emission at room temperature with a peak at 4.6 μm.

4.4. Summary and outlook

In this chapter, different structures used to create mid-infrared LEDs in the 2 – 5 µm wavelength range have been discussed, the devices and their emission output power can be seen in Table 9.1 in section 9.1. The devices are displayed in graphical form in Figure 4.15, comparing wavelength and output power for different types of devices. From this, it is clear that generally, as the emission wavelength of the device is increased, the output power falls. With the difference between a 2 µm and a 5 µm device being ~ 100. This is due to an increase in non-radiative recombination processes for devices with smaller bandgaps, however, this can be supressed using various band-structural engineering techniques. However, comparing the output power of structures can be futile. Various technologies have been utilised which significantly increase the output power of longer wavelength devices, such as the W-QW ICLED developed by Kim et al. at the Naval Research Laboratory in the United States of America, emitting at 3.1 µm as seen in Figure 4.15. Moreover, this does not consider the internal or external efficiencies of the device, or the spectra purity. There is a plethora of characteristics which make for a high-performance LED, which can decrease the output power of a device, but give it a specific use characteristic.

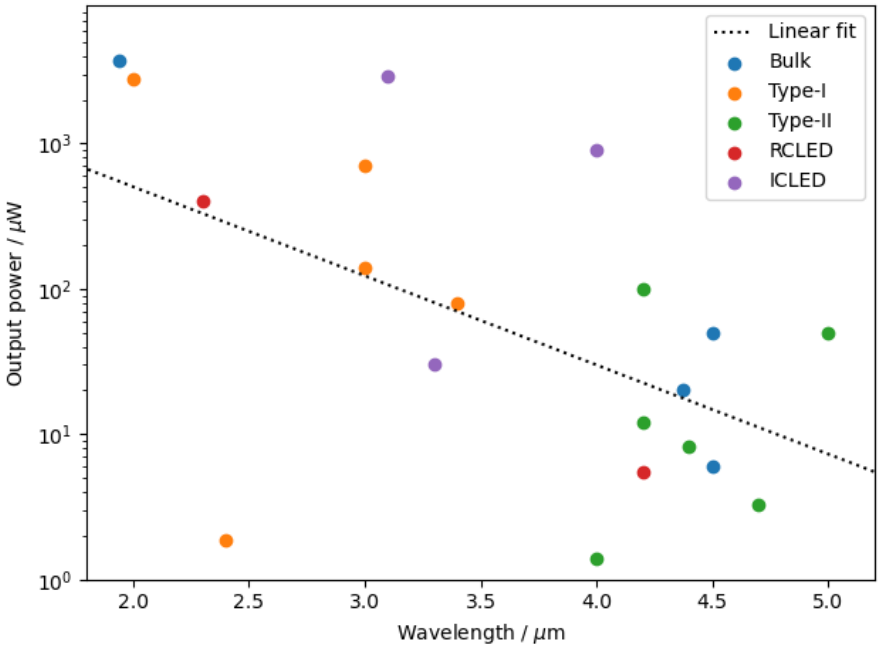

Figure 4.15: graph showing the output power of the devices discussed in this chapter as a function of the peak EL wavelength with. The data is displayed in Table 9.1 showed in section 9.1, where all of the devices which have value in the output power column are included in the graph above. A linear regression fit is also shown, giving a general trend of output power as a function of wavelength.

To achieve emission of < 3.5 µm, a type-I device should be used, this is clear from Figure 4.15. Section 4.2.2, showed that AlGaAsSb/In_xGaAs_ySb with x = 0.15 – 0.4 and y = 0.05 – 0.2 can be used to achieve emissions < 3 µm. To get emission > 3 µm, quintenary barriers can be used or high In wells with GaSb barriers. In these type-I devices, strained active regions are used to supress Auger recombination due to the degeneration of valence band states. For emission > 3.5 µm, type-II devices have to be employed, InAs/GaSb and InAs/InAsSb devices have both been shown to give emission in this range, going as high as 8 µm. The type-II configuration is also beneficial in that it reduces non-radiative Auger recombination due to elimination of certain processes due to spatially separate charge carrier confinement. Moreover, Ga-free InAs/InAsSb also have been shown to reduce non-radiative SRH recombination due to the removal of native defects around the Fermi level.

RCLEDs have been utilised to improve the spectral purity of LEDs, as well as the extraction efficiency of the devices. Different active regions can be incorporated into a RCLED to tailor the emission; the emission profile can be changed by varying the number of DBR repeats on the top and bottom mirrors. They have been demonstrated over a wide range of emissions, from 2 up to 5 µm.

Interband cascading has also been utilised to improve the performance of devices, largely using type-II InAs/GaSb based active regions. It was shown that by increasing the number of stages in an ICLED the output power can be increased for the same driving current. It is possible to create ICLED devices which have a much higher output power than non-cascading devices as shown in Figure 4.15.

III-V materials have been shown to produce high quality LEDs with high output powers across the mid-infrared spectrum; the best performing devices are represented by W-QW based ICLEDs and InGaAsSb type-I QWs. This is an extremely competitive field with lots of high-quality research being constantly published, however, there are still many challenges that are yet to be overcome. Although complex structures which create higher output and efficiencies are being created, more complex structures are more difficult to grow, requiring longer growth processes and costing significantly more. This gives ample room for developing methods to simplify this growth process whilst still increasing the performance of devices.

The development of these is crucial for many well-established applications such as greenhouse and/or industrial gas sensing as well as chemical sensing for compounds such as glucose. Novel applications for mid-infrared radiation are constantly being found, an example being the sensing of black plastics as will be discussed in section 5. Research into glucose sensing [115] has been

conducted and photodiode arrays based on GaSb alloys have been created in this spectral region [116]. Detection of C-H bonds in non-polymer based molecules [109] has further been realised using this material system. Furthermore, a Lithuanian company, Brolis, have utilised MIR sensing in the monitoring of dairy products with their Herdline range [117]. This has also been used in the monitoring of dairy products in published work [118, 119]. Moreover, research into growth on Silicon is crucial for the development of integrated MIR photonics; resonant cavity devices and plasmonics [120] also show great promise.

5. A material social outlook on plastic and the current end of its life

5.1. Lexicon

In this chapter, several terms will be used which are specific to the framing of the work. They are defined as follows.

Embodied energy: the amount of energy required to create an object from a raw material. The starting point of where this quantity is measured from is subjective, i.e. the researcher could choose any point in time to begin their energy analysis of the material. None-the-less, it can be set at a point which can be useful when comparing different processes to make the same object or comparing different objects which do the same thing – i.e. internal combustion vs. electric vehicles.

Energy loss: the amount of energy inputted into a process, but which does not contribute to the final outcome. For example, energy lost to noise when boiling water.

Waste: a period defined by a prolonged state of un-use of an object; for example, objects in landfill. This is a liminal space in which an item may degrade to varying extents but can also be bought out of that space to be made use of again.

Biproduct diversion: when a product of a production process which is not included in the final product is used in a way such that it is not in a state of "waste".

Cradle-to-cradle analysis: the analysis of a material which is continually used – not necessarily always in the same product.

Dirigability: a state of steerability – commonly used in terms of boats. However, in this chapter, it will be thought of in terms of energy - i.e. how it can be transferred. In the context of products – the different ways in which they can be used, both during and after their "life".

PESTLE analysis: analysing systems in terms of: political, economic, social, technological, legal and environmental implications.

5.2. An overview of plastics

Long chains of identical monomers – molecules based on carbon and hydrogen with other elements depending on the specific monomer – known as polymers are the main constituents of plastics. Additives known as "plasticisers" are often added to the polymer, these plasticisers give the plastics certain properties which are generally beneficial to their use cases [121]. The polymer with the addition of plasticisers is what is commonly known as a plastic. Some natural plastics exist, such as rubber [122]; however, the in the modern conception and in common

parlance, the term plastics are generally used to refer to synthetic plastics. Plastics were first synthesised in 1862 by Alexander Parkes, it was marketed as an alternative to ivory and horn for decoration, as well as shellac for waterproofing [123]. The material developed steadily over the next century; the advent of the Second World War accelerated the rate of research into the material. In the 1950s, the market for materials such as: polyester, polypropylene, high-density polyethylene and polystyrene grew significantly due to the realisation of their utility [123]. Since then, the production of plastic has increased by ~8.3% every year from 1.7 Mega tonnes (Mt) in 1950, to 348 Mt in 2017. It is estimated that in this time, around 9.2 billion tonnes of plastics have been produced [16]. Since 2017, this trend has continued; however, the rate of production increase in 2020 was lower due to the changing requirements of production due to the coronavirus pandemic. Even during that time the amount of plastic produced still increased from previous years – in 2021 390.7 Mt of plastics were produced [124].

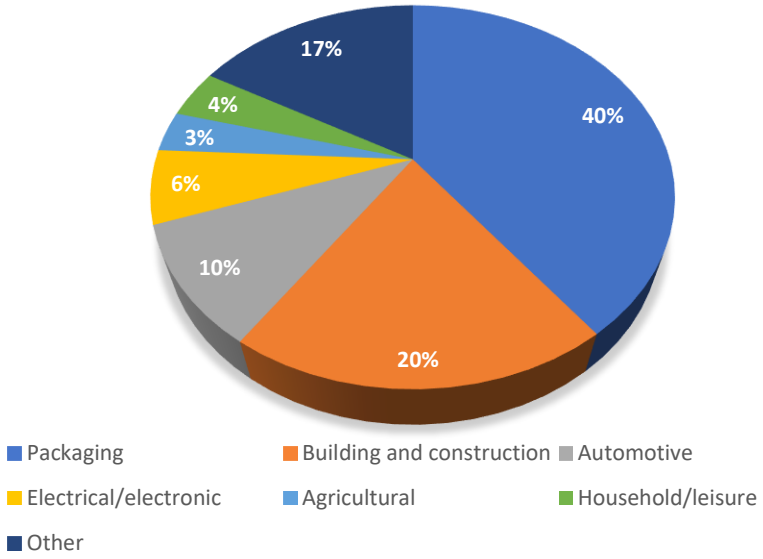

Figure 5.1: Pie chart showing the portion of plastic which is used for different purposes as of 2020 [125].

Plastics are used in the creation of a plethora of different types of commodities in a wide range of sectors; generally, most commodities will have a variant that is made from plastics, ranging from coffee cups, to fishing line, to building material [124]. Plastics have replaced many materials in a variety of different fields since their mainstreaming. In medicine, almost all tools contain plastics, this is due to them being highly malleable; easily sterilised and cheaper to produce than other types of materials [126]. In packaging, their low weight and durability have resulted in them becoming the main type of packaging material. In farming, the use of plastic mulch films – although having unknown long term effects to the environment and soil – has led to higher crop yields, earlier harvests, improved fruit quality and decreased water consumption in the sector [127]. Plastics are also now used in a number of other industries [128]. The share

of different sectors' use of plastic can be seen in Figure 5.1, primarily showing that 40 % of all plastic produced is used in packaging.

Different commodities made of plastic take different amounts of time to decompose based on the specific plastic/polymer used and the structure of the commodity. Plastic bags and coffee cups take around twenty and thirty years respectively, whereas plastic bottles and coffee pods can take four-hundred and five-hundred years respectively [129]. Despite this, the average amount of time that most plastic packaging is used – including coffee cup lids and plastic bottles – is under a year. With some single-use items often being discarded within minutes of the goods being purchased. Electronic goods are used for between five and fifteen years and building material between twenty-five and fifty years. From this, it is clear that there is a large discrepancy between how long plastic materials are used for, and how long it takes them to break down [16]. Due to this longevity of the material, plastics must either be reused until the polymer material system breaks down; recycled so that the material can be used to create a new commodity, or discarded, entering a state of waste as the material still has the potential to be used. These three fates plastics can have will be discussed in this chapter, including their larger ramifications, what is currently being done about this, and what can be done to mitigate negative effects in the future. In turn, to understand this, it is important to holistically understand the broader life that plastic takes.

5.3. The life of plastic

When considering the life of plastic, three elements will be considered. These are: the material itself; the energy which goes into making it and the energy contained within the plastic. When considering the material, it is useful to use the framework of cradle-to-cradle [130], this is a philosophy which states that all material should go back into the production process. Seeing what was once categorised as "waste", as material for new production, giving an opposing viewpoint to how most current production works. When considering energy, there are two things to consider, the energy that went into creating the material through the production process and the energy which can be extracted, or the available/transferrable energy. Also, this is energy that can be transferred from the material into another form (kinetic, thermal, etc.). The energy used to create the material can be defined by processes such as polymerisation, transportation etc. This would be referred to as the embodied energy which cannot be extracted from the material. Because plastic is such a unique material system, the transferrable energy which is physically contained within it is dirigible – i.e. it can be directed in different ways based on how it is treated at various points in its life cycle. However, the embodied energy of the

plastic is non-dirigible, it is an energy investment into a material, and how that material is treated outlines how useful that investment will prove. At different points in the life-cycle of plastic, each of these view points of the material are considered [131]. How plastics are acted upon during the different stages of their life gives a large view of different political, economic, environmental and philosophical outlooks on society at large. The material systems life will be divided up into three general stages: birth, life and end-of-life, these will be discussed.

5.3.1. Birth

For a plastic to be created, it must be processed from crude oil – the initial constituent raw material. Crude oil is naturally produced liquid petroleum, which accumulates in porous rocks in the earth's crust [132]. It is made up of a plethora of hydrocarbons – monomers of different lengths which have a variety of different uses, from long-chain with uses as bitumen for surfacing roads, all the way up to short-chain refinery gas. These different types of hydrocarbons are separated by distillation, a process of separating material by molecular weight.

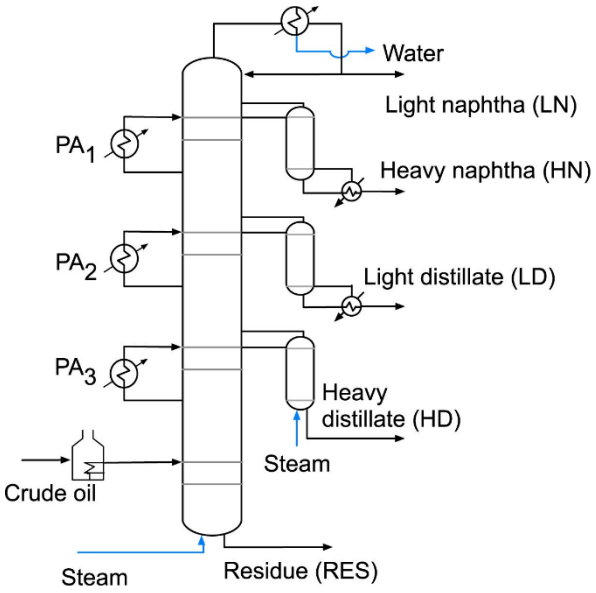

Figure 5.2: a diagram showing the distillation of crude oil into its constituent parts, with the temperature of each part of the distillation chamber being show[133].

A diagram showing this process is given in Figure 5.2, this outlines how distillation can be used to sort the constituents of crude oil, as lighter elements distil further up, and heavier ones stay near the bottom of the vat. One of the products of distillation is naphtha, this is the raw material which is used to create plastic. Naphtha then goes through a process known as polymerisation, a process by which shorter length hydrocarbon monomers are re-arranged by various different processes to create long, repeating chains of hydrocarbons, known as polymers [134]. Through

different processes and adding in different chemicals, it is possible to create any polymer via this process.

Polymers are then transformed into plastics by adding various compounds, this gives them different properties, such as flame retardance, elasticity, toughness etc. This is done by various processes with various compounds which are too numerous to list here but can be found in the polymer application database [135]. This list is however incomplete, new additions are constantly being added due to vast amounts of research and development in the field, much of which is beyond the scope of this project. However, at the end of the plasticisation process, plastics are formed into small pieces – known as pellets or nurdles – usually no more than a few cubic millimetres. These pellets are then shipped from the plastic producer, to companies/state entities which creates commodities out of plastic, different production techniques such as injection moulding are used in this process [136]. As of 2020, 90% of all plastic being produced were virgin plastic, accounting for 6% of global oil consumption, furthermore, the production process accounts for most Anthropocene greenhouse gas emissions [137].

5.3.2. Life

Here, the life of a plastic commodity is defined as the time period from when the commodity starts being used by a user, users or larger population, to when the user(s) ceases using it with no intension of re-use, or in the case of industrial/infrastructural plastics, they have to be replaced or are no longer usable. The ceasing of use by a user(s) is normally categorised by the commodity being placed in some sort of waste disposal system, such as general waste bin or recycling bin/collection site of some sort.

Because of the variety of different plastics which are present in the modern economy with different uses – as discussed earlier in the chapter – the form which the life of the plastics take can be vastly different, from plastic packaging to building materials. It is in this phase, that the use value of the plastics is realised, i.e. the value obtained from using the plastic item over not using it, this can come in many forms, such as promoting higher yields in agricultural practice or making foods have a longer shelf life [138]. This value is somewhat arbitrary and difficult to quantify, however, the fact that they are used, implies that they have a high use value over other commodities. How plastics are used is not relevant to this this discussion, as it is concerned with how plastics are treated at the end of their life and how to extend this period of life.

5.3.3. End-of-life

The end-of-life of a plastic is defined as the time period after the plastics' life; this would generally be when it stops being used due to breaking or for its purpose having been fulfilled. Especially in the case of single use, not using it anymore – such as plastic packaging for food once the food has been used. How plastic is treated at this point determines how much extra economic utility can be extracted from the material than was intended when the commodity was originally made. At the end of life of a plastic, they are commonly categorised as waste; here, waste will not be framed as a state in which something automatically becomes, but a temporary state which something can be bought out of.

Although not specific to plastic, this concept is fleshed out in "Cradle-to-cradle: re-making the way we make things" by Braungart and McDonough [130]. Here, the ideas of "nutrient cycles" are explored, with this cycle containing a "nutrient" feed and "metabolism" mechanism. The simplest way of understanding this is by the natural cycles, the example used in the text is a cherry blossom tree, the process of the tree growing a cherry creates blossom, which is not part of the cherry itself. In one way, the blossom is a waste product, however, once it has served its purpose, it will fall to the ground, decompose and then become fertiliser for new plants – even the cherry tree itself. As a part of the natural world, humans came from this biological cycle, with early hunter-gatherer era humans producing things which could be directly discarded in the environment and break down as nutrients for that environment. However, as human society developed into an agricultural one and through many various stages into an industrial one, the level of anthropogenic manipulation of the environment increased. It is now largely accepted that we live in what would be described as the Anthropocene era, marked by large scale human manipulation of the natural environment. This is seen to largely have started at the advent of the industrial revolution [139], however, there is debate on when this definition would have started, with some sources claiming it could be defined earlier. This was to account for a larger number of people living closer together in one permanent settlement. In the current agricultural sector, most of the nutrients in the soil come from artificial fertilisers which have many adverse environmental effects, including: increase in soil erosion and draining of the natural nutrients from the soil over time. Some of this is due to a divergence from the natural cycle of crop rotation which used to be common in pre-industrial agriculture, a process which naturally replenishes soil nutrients. This is an example of humans diverging from reaping what can be accessed by us from the "natural" world, into one where we collectively morph said natural world so that it provides for us. But the morphing requires the use of concentrated chemicals which otherwise would not occur in nature. This outlines the idea of biological and technical

nutrient cycles. Biological nutrient cycles are those which occur in nature – without anthropogenic influence – as outlined by the cherry blossom example. Technical nutrients are those which are anthropogenic and used to make technical commodities. The earliest example of a technical commodity is metal, which does not naturally decompose and has to be created via an arduous process – not just shaped as in the case of stone.

When separated, it is easy to dispose of biological and technical nutrients. Biological nutrients naturally decompose back into biological cycles. Technical nutrients are more complex to bring back into a cyclical process, but it is possible – recycling of plastics or paper is an example of this. In cradle-to-cradle, it is exemplified how many processes which are currently viewed as producing "waste", are only such because of the difficulty in separating the constituent parts. Human excrement (a biological product which can be used as fertiliser) becomes waste because it is treated with chemicals which sanitise most of it but mix biological and technical nutrients. This is further exemplified by the mixture of technical nutrients, when a car or television comes to the end of its life and they are scrapped, all of the materials are separated by type (i.e. metal, plastic, etc). However, this greatly reduces the ability to create high quality material from these "nutrients" because of the difficulty in separating the different materials. This chapter of the book suggests a design side solution to this problem, whereby technical items can be more easily separated into "type", i.e. steel and copper rather than just metal.

This shows that waste is currently a categorisation of post-use – commodities are thrown away when the use that they are framed for is finished. This is different for various commodities but generally plastic is expected to have a finite use-life, whereby after, it can be discarded. This is incorporating the ideas of Thompson in his book "Rubbish theory" [140], outlining the idea of value as a mutable social relation which is not inherent to the object itself. Further incorporating the notion that the greater labour, which is exacted on a commodity, the greater its value will be. To extend this idea, plastics go into the liminal state of waste because their use-value has been fully extracted. However, when viewing waste as a period of unuse, where given the correct tools and facilities, the material categorised as waste, can be bought back into use at various levels. These two different ways of viewing plastics at the end of their life, are analogous to death and rebirth, categorising a linear and circular economy respectively. This links back to the ideas outlined in cradle-to-cradle, as this is bringing material back out of a transient state of waste, and into one of use. This is one of the fundamental principles of all circular economic theories.

5.3.3.1 Death – linear economy

The linear economy is definition of a type of economy in which commodities are produced, used and then put into permanent un-use, this can be through various mechanisms, but the material does not re-enter the economy in a way in which it could have a positive impact. As mentioned previously, over time, plastics break down becoming smaller polymer chains and eventually microplastics. Microplastics have been found all over the environment, from oceans to the tops of mountains, and most recently, in the human body [141]. This is not surprising as up to 3% of plastics produced every year end up in the ocean [125] where when they break down, it is easy for the biproducts to be spread worldwide. Moreover, those which are disposed of by official means – i.e. waste collection services – end up in landfill or being incinerated, commonly known as a take-make-waste economic model [142]. This comes from the idea of "taking" virgin resources, producing commodities from them – i.e. "making" and then "wasting" them, as they are discarded, not to be used again. It is called linear as the life of plastic in this sense can be plotted linearly on a timeline, this can be seen in Figure 5.3, whereby each stage proceeds the other with a clear start and finish point.

Figure 5.3: flow chart showing how the linear economy works. Showing the different stages of production, use and un-use going linearly from one to another.

The final section in the flowchart in Figure 5.3, un-use, can encompass a variety of different fates. For example, the majority of plastics are sent to landfill [16], this is certainly classed as un-use as the material is still there, it is just not being used by anyone. Incineration would also be classified as this, although this is usually used as energy recovery, i.e. using the plastic as fuel for a power station. It still ends up with the material being used once more and is then unable to be used again – as it has been incinerated. This gives a finite life on the energy "investment" made by creating the plastic in the first place, which is then either not used or destroyed. Therefore, the linear economy is one which requires constant production from virgin material – crude oil in this case – if it wants to continue creating new commodities. Although certain open loop processes occur, i.e. the current form of recycling, a linear economy does not rely on this for its general production. The open loop process of recycling is one whereby some materials are put

back into the economy but then follow the same linear use pattern and are often discarded at the end of this re-entering. From when plastics were first industrially created, until around the 1980s, they were disposed of in a completely linear manner with commodities going to land-fill sites after their use, in 2019 around 57% of plastics went to landfill sites [143]. Aside from the environmental problem of burning or discarding plastics in landfill, crude oil is a finite resource which takes millions of years to form from organic matter. Because of this, using it at such a rate puts serious strain on the quantity of crude-oil supply that there is in the natural world. As more is used, supply has to be taken from more ecologically sensitive areas through more geologically harmful methods.

5.3.3.2 Rebirth – circular economy

The circular economy is defined in opposition to the linear economy, so whereas the linear economy has a clear start and end point; in a circular economy after the start point, materials are kept in the economy via a plethora of different processes. Although there is always loss in any system, in a circular economy one principle is that this should be minimised. One definition of the circular economy is: “A systems solution framework that tackles global challenges like climate change, biodiversity loss, waste and pollution. It is based on three principles, driven by design: eliminate waste and pollution, circulate products and materials (at their highest value) and regenerate nature.” [144].

Although other schools of thought do exist which critique this exact definition and use their own. In other literature, it is defined as “An industrial society that is restorative by intention and design which utilises ecosystem cycles in economic cycles by respecting their natural reproduction rates” [145]. In order to achieve the goals of a circular economy, there are a multitude of material cascading mechanisms which take materials after they have been used or bi-products of certain industrial processes and re-purposes them so that they can be put back into the supply chain, this is outlined in Figure 5.4.

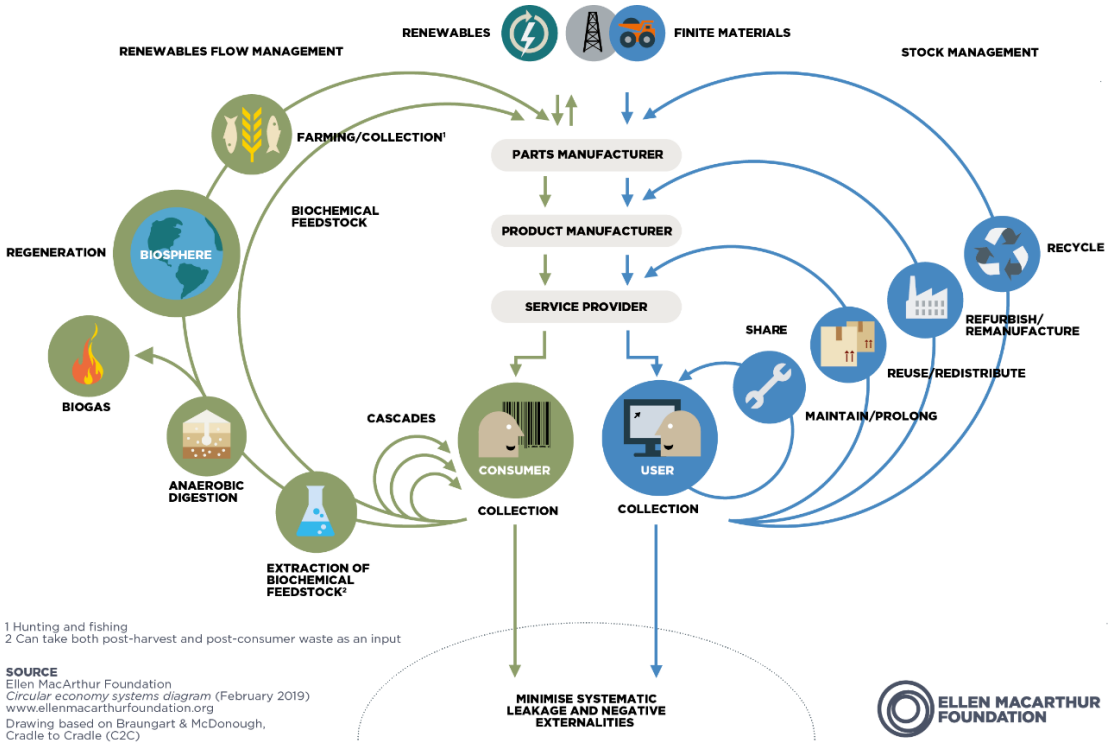

Figure 5.4: the so-called "butterfly diagram" showing the mechanisms by which materials can be cascaded from consumer or user back up the supply as to be used again. The leakage mechanisms are also outlined [144].

This is particularly important for plastics from petroleum-based sources, as the replenishment rate of petroleum is millions of years, so any resource which are extracted should be used as much as possible, a practically infinite number of times. This is because it maximises the embodied energy in the system as well as minimising the virgin material used. It is clear that the circular economy is an inversion of the linear economy, this is because the linear economy has a clear – and permanent – state of un-use. Whereas in the circular economy, as much of the material produced as possible, once in a state of un-use, will be put back into the production chain.

The term “reduce, reuse, recycle” has often been used to describe the individual outlook that we ought to have with plastics [146]. This continues to define our attitude in how the problem should be tackled. Although individuals can only do so much to help with the economy as a whole, the good attitude of individuals within a larger system which itself works towards the goals of circular economy is vital in its creation. The first term, reduce, is a critical one for individual habits; however, as a systematic approach, it is less so. In general, plastics should be eliminated where possible, this is because even with a reduction in the amount of plastic which goes into a design, there will always be some leakage into the environment and their creation is a carbon positive process. The use of plastics in industries such as: farming, construction and medicine – as discussed earlier in this chapter – rely greatly on plastics. The removal of plastics

from such industries would have some predictable catastrophic effects and many unforeseen consequences, society as it currently exists would have to be completely redesigned to accommodate this. Therefore, as a systematic approach, reducing cannot be applied to fix the problems caused by plastics currently, despite it being able to alleviate some of the worse effects. The idea of reusing is trivial, rather than discarding objects after their useful or intended lifetime has come to an end, they should be re-used to do the same task or repurposed to do a different one. This can be seen from the UK government putting a tax on the sale of single-use plastic bags – whereas before they could be given out for free. From when the tax came in, the use of single-use plastic bags dropped by a factor of 6, with the highest reduction of the bags annually being 59% [147]. This shows the efficacy of re-using on reducing the amount of problematic plastics which caused a large amount of pollution [148]. Despite these reductions in single use plastic bags, the UK ban as well as various countries around the world who have implemented similar bans have found that there are several unexpected and unintended consequences. These include: companies using non-plastic, single use bags which are more energy demanding to produce; the prevalence of thicker reusable bags being used in the same manner as single use plastic bags; black markets appearing in several countries, and more [149].

The third, and final term of the phrase, recycle, is one which is much more complex compared to the others, and has an abundance of technical, political and social issues surrounding it. The specific of recycling as a mechanism for reusing polymer materials will be discussed in section 5.3.5. Recycling is defined as a process of recovery and reprocessing of materials for the creation of new material/ commodities [150]. Although recycling is not a solution which will itself bring about a circular economy, it is an important component in a larger system which would constitute a circular economy. This can be seen in Figure 5.4, with recycling being the mechanism by which material that has been collected can be placed back into the production process – in the initial manufacturing stage.

5.3.4. Comparison of linear vs. circular economic methods

In the case of plastic, after an item has been used and the user has no need for it anymore, once it has been discarded, it is generally referred to – and shall be here – as waste. There are three broad categories of how plastic waste can be dealt with, these are: discarding, recycling and incineration. Discarding is defined as when plastic is sent away – usually to landfill – where there are no reclamation efforts, recycling is defined as when plastic waste is re-processed so that it can be used again. Incineration is when plastic is burned, this is sometimes referred to as “energy recovery” and can be used to create electricity, however, it creates toxic fumes which include

heavy metals [151]. Because the toxic fumes which are produced in this process are let out into the environment, this can have serious negative effects, such as acid rain and an increase in heavy-metals in the ground. Before the 1980s, plastic waste was generally just discarded; but since then, there has been a great effort to increase the amount of material recycled, along with incineration [16]. In 2017, recycling rates in different countries varied from 30% - 40% to as low as 9% in the United States of America (USA), overall recycling rates worldwide were 18%, it has been projected that by 2050, the global recycling rate will be 27% [16].

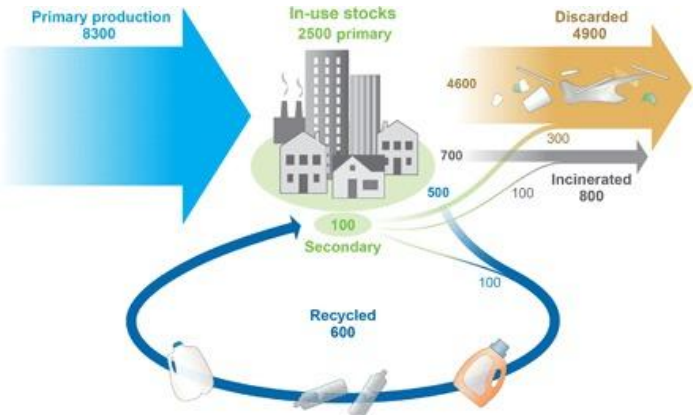

Figure 5.5: a flow diagram showing what currently happens to plastic at the end of their life by Geyer et. al. [16]. This also shows that although a loop can be created via recycling, the material does eventually leave that loop and get discarded or incinerated.

Because of this, if a diagram were made of the current mode of production, recycling and discarding, a great proportion of the input would end up in the systematic leakage section due to the discarding and incinerating of plastic materials, a non-circular solution to the waste. A visual representation of this can be seen in Figure 5.5, where most the primary production ends up discarded or incinerated and an open loop is visible.

The non-circular nature of the treatment of the majority of plastic waste, as well as the open loop recycling model which largely exists, shows that the current economy of plastics worldwide is one of linearity. Polymers and plastics always leave the economy at some point, and are not bought back in, with new material having to be produced from virgin sources constantly.

From Figure 5.5, it is also clear that although recycling helps in keeping material in use for longer, eventually, it does get discarded or incinerated – thus exiting use, entering a permanent state of waste. This is generally due to a process known as downcycling, downcycling is a term which describes a recycling process, generally of plastic, whereby the product made of the recycled material is of lower quality than the original product [152]. A widely used example of this, is recovered plastic being turned into fleece to create jackets, which are then recycled to make short term building materials, i.e. ones which are not used in permanent structures. This is an

example of downcycling because each subsequent item is expected to last longer, and serves a less valuable role than what it was created from [152]. Although this is useful in some respects, in the long-run, it does not help reducing waste, only prolongs the inevitability of plastics going to waste. Downcycling could also be described as an open-loop recycling process, this is because although it creates a circular mechanism, the material does eventually break out and become waste.

The reason downcycling has become a prevalent way of repurposing a lot of material is because the quality of recycled plastic is less than that of virgin plastics. This is due to the purity of feedstock which is used to create recycled plastic. When plastics are sorted in plastic recovery facilities (PRFs), as the process is not 100% accurate, the feedstock (pellets/nurdles) created is not pure – it can contain plastics of other polymer types than the one intended. In general, PRFs create material with less than 5% impurities [153], however, some specific high quality sorting facilities can create recycled material with impurities as low as 0.2% [154]. Although this is a relatively low percentage of the plastic being an impurity, it does affect the performance of the plastic. Recycled plastic is generally less clear, less malleable and is less strong – as well as a plethora of other negative characteristics compared with plastics made from virgin material [152]. These can be contaminants from other plastics, for poly-ethylene based plastics (HDPE/LDPE), the inclusion of PVC, PET or PP can create inhomogeneities which significantly decreases the quality of the final recycled product [155]. Being able to more effectively identify, and sort plastics is one way in which the quality of material can be improved, as well as create pure streams of plastics for materials which currently are not sorted due to the cost of doing so but end up as contaminants in other plastic streams. An example of this is curb side recycling, whereby all different types of plastics are gathered together to be eventually put in the same material stream to be sorted, rather than being sorted by specific type initially. Higher purity recycling material streams lead to more recycled material being used for higher economic purposes, generally referred to by the terms recycling or upcycling. This creates a closed loop-system where material stays inside the production and use processes rather than being discarded due to a decrease in quality.

Not only is the current treatment of plastic waste such that it could not be defined as circular; but the current treatment leads to widespread pollution. Even if the plastics are placed in a seemingly controlled environment at the end of their lives, there are many mechanisms by which they can leak into the surrounding area. Plastics of various shapes and sizes, from macro to micro and seemingly nano have been observed in: remote ocean surfaces; water columns, deep sea environments; soils, the bodies of animals of all shapes and sizes and in various other

locations [156]. The full extent of the effects of plastics in the environment has not been fully realised, however, some have been noted as: toxicological risks to environments; changes to the carbon cycle and physical damage to megafauna due to entanglement or ingestion of macroplastics [156].

When comparing the linear and circular economies, it is useful to look at the materials and energy at each point in the production process. Work is constantly being done on the material system, increasing its embodied energy, as it is originally produced – which requires energy to get the raw materials on-top of the manufacturing process, then transported to the destination in which it will spend its useful life. At the end of its life, if the material is discarded, all of the energy is wasted, i.e. both the energy stored in the material (chemically), and also the embodied energy. If the material is incinerated, the chemical energy is used – given that it is in an energy recovery facility – however, the embodied energy still goes to waste, all of the transportation and manufacturing has to be done again for new material. However, if the material is recycled, almost all of the energy is saved. Although energy is required to convert it into a form by which it can be reprocessed into new material; creating one-tonne of plastic from recycled material saves 5774 kWh (20.79 billion Joules) of energy - this is a saving of 34 %; 3 114L of oil, 25 cubic metres of landfill space and 3 000L of water [157]. On-top of this, the use of recycled material negates the need to obtain new crude oil. This has also been confirmed in a case for the specific case of polypropylene, with recycled material saving 37.4 % of the energy required to make the equivalent amount of virgin material [158]. These cases have taken into account the International Organization for Standardization (ISO) Environmental management – lifecycle assessment – principles and framework [159], where the process begins with the extraction of raw material. This is the most beneficial way to analyse life-cycles and the associated embodied energy of the material from an economic and environmental point of view, as extraction of raw resources for polymer production is where the cycle starts. Calculating the energy that it takes to create crude oil would not be necessary in this analysis. This shows that not only does recycling keep material in the production cycle, but it also saves other resources which would otherwise have had to be used.

5.3.5. The role of recycling in a circular economy

Recycling can take many forms due to its vague definition. However, when it comes to recycling on an industrial scale, there are generally two different types: mechanical and chemical. Mechanical recycling is a process which takes plastic feed – sorted into polymer type – and then performs a process known as extrusion, by which the feedstock is heated up and passed through

a screwing system. This is then used to create plastic nurdles, which are used as a feedstock for creating new plastic items. The process is outlined in Figure 5.6 (a) from initial insertion of plastic pellets in the feed section, through the screw and to the final metering section, where the final product is produced. Mechanical recycling is highly compatible with: polyethylene-terephthalate; high-density polyethylene; low-density polyethylene and polypropylene [160], but with repeated recycling, the quality of the polymer chains does degrade due to many chemical mechanisms leading to decreased quality of the plastic. Although it can be used on these polymer types, it is less effective when applied to polyvinyl-chloride and polystyrene.

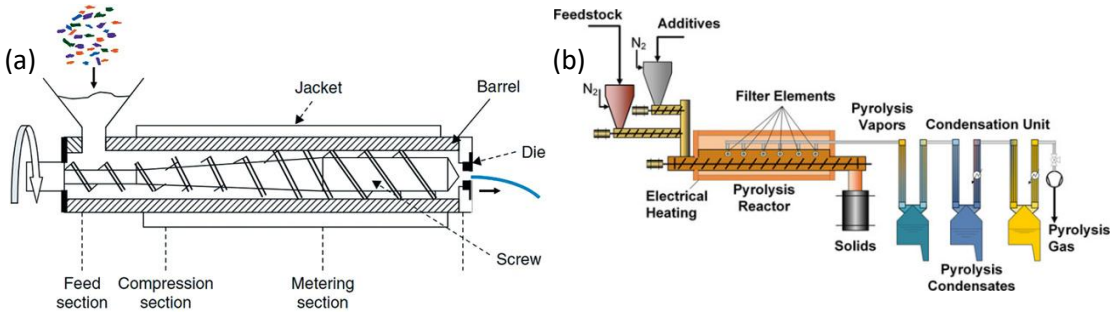

Figure 5.6: (a) a diagram showing the extrusion process used in mechanical recycling [160] and (b) a diagram showing the process of pyrolysis for chemical recycling [161].

Chemical recycling is a method which depolymerises plastics rather than converting them straight into a new feedstock material. This is usually done via “pyrolysis”, the final product of this are monomers which can then be re-polymerised. The process of chemical recycling is much more complex than that of mechanical recycling, the diagram in Figure 5.6 (b) shows the process of pyrolysis. This creates a superior end product than that of mechanical recycling, closer to the quality of virgin plastic. But it is a much more intensive procedure, with many more complicated steps to reach a final recycled product [162]. Furthermore, current chemical recycling technologies produce less greenhouse gasses than incineration, but still more than mechanical recycling. Moreover, compared to incineration, neither process produces as many ozone depleting bi-product, or ones which result in acidification of the environment [163]. Although technologies are continually being improved, and new methods being created, mechanical recycling is currently the only recycling method which is economically viable [125]. When considering the role of recycling, the efficiency of the process should be considered. Here, there should be two factors which are considered. One, is how much of the plastic feedstock is converted into useable nurdles; the second, is the energy efficiency, i.e. does making a unit weight of recycled material use less energy than a unit weight of virgin plastic? Using this framework, it is clear that mechanical recycling is slightly lacking in material efficiency, but very

good in terms of energy efficiency. As it is a relatively low energy consumptive process, however the material it produces is not excellent. Whereas chemical recycling is very good in material efficiency, but poor in energy efficiency. As it produces high quality plastics but is highly energy and time intensive.

For each of the recycling types, the required feedstock is sorted plastics, i.e. plastics of only one polymer type. Plastics which are collected by local councils, equivalent government bodies or any other plastic collection schemes are sent to plastic/material recovery facilities (PRF/MRFs), here, a plethora of sorting techniques are applied. Some of these sorting techniques include: density separation (sink-float); manual sorting; visible spectroscopy; near-infrared (NIR) spectroscopy; hyperspectral imaging; x-ray fluorescence laser induced breakdown spectroscopy and many more [164]. Although a multitude of techniques exist for the sorting of plastics, the main one which is used is NIR spectroscopy [165].

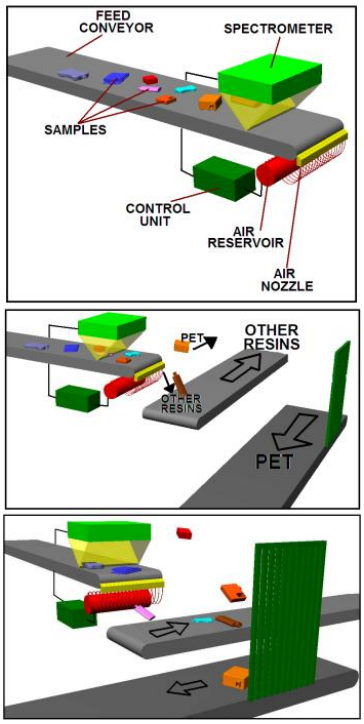

Figure 5.7: a diagram showing how plastics are sorted at PRFs, from the scanning via a spectrometer to the air blast sorting into different streams [166].

At PRFs, the initial feedstock is a mixed plastic bail, this is a large, bound amalgamation of mixed waste, mostly made up of plastic; there are also many contaminants initially, including: metals (such as aluminium foil), fats from food products, paper, and many others [167]. At the start of the process, a basic cleaning process is applied to the waste; then the bails will be optically sorted into constituent plastic types on the large scale, these different flows of plastic are then sorted based on colour – this is generally into clear and coloured plastic. After this, plastic labels

are removed from the products and the remaining plastic is shredded into small fragments. Other sorting processes such as density sorting can be applied at this point – this is generally to sort PE/PP from PET, another optical sorting process will be applied, and then mechanical recycling techniques are used to create the nurdles. The optical selection processes are based on positive selection, meaning that if an item is identified as a certain type of plastic, it is removed from the general flow, into a separate flow, at the end of the selection process, anything that is left in the general flow is viewed as waste and goes to landfill or is incinerated [125]. The process of optical sorting and then segregation into different material streams is outlined in Figure 5.7.

Plastic incineration and landfill usage has been shown to be detrimental in many ways – some of which are outlined in this chapter. Because of this, the reduction in the quantity of this general waste flow at the end of the selection process could be realised by improving the efficiency of recycling facilities, as well as limiting the amount of material being incinerated. This can be linked to the idea of waste being a liminal state, the stream of plastic that is discarded/incinerated can be reduced, it just depends on the technical ability of the sorting facility. One mechanism by which the amount of waste can be reduced, is by having a sorting system which can identify the polymer type of plastics containing the carbon-black pigment – this is a pigment commonly used to colour plastics black. The near-infrared detection systems commonly used for optical detection cannot identify these plastics, this is due to the pigment absorbing the wavelength of light used for this type of detection [7, 8], this is still effective on other colours of plastic, as long as they do not contain this pigment.

5.4. Black plastics

As mentioned in the previous section, black plastics are a cause of inefficiency in plastic sorting facilities, taking material out of an economic loop which could otherwise contribute to a circular economy. It has been noted in several publications that black plastics cannot be recycled due to them not being able to be optically sorted by current NIR technology [168-171]. The reason for this, is that the pigment used to dye the plastic – known as carbon black – absorbs almost all NIR radiation [172], and example of this can be seen in Figure 5.8 showing a comparison of white PVC and PVC which contains carbon-black pigment. This shows that there are discernible spectral characteristics in the NIR reflectance spectrum, however in the same spectrum for the carbon-black pigmented plastics there are no discernible characteristics. In order to make recycling more material efficient there are different approaches when considering this limitation. One, would be to eliminate black plastics through reduced consumer/industrial use

or by government policy. Another would be to find a way to make black plastic that is able to be optically sorted using existing industrial sorting technologies. Finally, a technological solution through an optical sorting system which could identify current black plastics would resolve the issue.

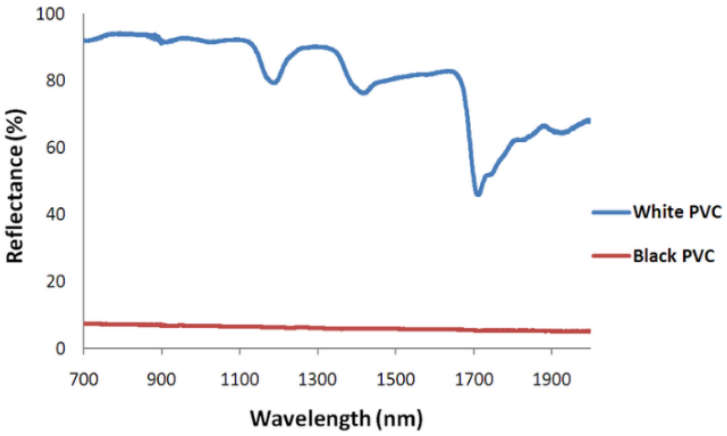

Figure 5.8: A comparison of the NIR spectra of a white sample of PVC and one containing the carbon black pigment from research conducted by Masoumi et. al [165].

Because black plastics are not current detectable using existing technologies, they go into the waste steam in PRFs; it has been outlined earlier in this chapter why this is an environmentally damaging and fundamentally opposed to the circular economy. Both of these factors have been shown to have a plethora of negative consequences. However, black plastics pose a particular problem if they go to landfill or are incinerated; this is because they contain between 3 – 5 % toxic materials, such as antimony, which is to make them flame and heat retardant. When these are incinerated or left in landfill, the toxic heavy metals will be carried away through exhaust fumes or leak into the ground respectively [173]. This shows that black plastic poses a particularly large problem when they enter the waste stream, and it is vitally important to be able to have black plastics as part of a circular economy.

Although there are several ways in which black plastics are being phased out, they have continued to be used because they give polymers specific properties which are highly beneficial to becoming plastics. These include: colour stability, solvent resistance, ultra-violet light resistance and many more [173]. Black plastics span a wide range of polymer types and are used to create goods for: food-contact, storage/construction, clothing, electronics and many more [173]. As well as black plastics being useful as a virgin plastic, plastic which has been made from recycled feed-stock can have its material properties improved by the addition of carbon-black pigment [125]. This means that carbon-black pigment can be used to increase the durability of recycled plastics, which could in turn lead to a reduction of down-cycling due to deteriorating

material quality. Although most plastics containing carbon black are currently not recycled, there has been great success in recycling vehicle tires without reduction in material quality [174]. This is done through chemical recycling, tires have been an effective commodity to recycle because waste is not put into a mixed system, therefore sorting is not required [175]. Companies such as Lawrence industries and others are hoping to capitalise on this and offer services in recovering carbon black from other commodities [176]. This further shows that it is only the sorting of commodities which prevents them from being recycled, once the sorting process has taken place, they can be recycled mechanically or chemically, the same as any other plastic.

5.4.1. Government policy

The government of the United Kingdom does acknowledge the non-recyclability of black plastics due to optical absorption as well as why they are currently used for food packaging, as stated in PostNote number 605 [177]. According to the Twenty-five Year Environment Plan, published by the United Kingdom Government in 2018 [178], the government plan to have eliminated avoidable plastic waste by 2042 and eliminate all waste by 2050. They outline that to do this, the pace at which the proportion of plastics which are re-usable and recyclable is increased as well as working with NGOs to reduce the amount of plastic used. However, the idea of dealing with waste using energy recovery is also present in this document, as well as in the 2020 waste management plan for England [179]. Thus, this remains another reason that the efficiency of recycling facilities should be increased. In the governments net zero plan, as well as their delivery plan 2022 – 2025 [180, 181], black plastics are not mentioned, most of the discussion is around plastic packaging and how this should be cut back. Despite this, both of these policy documents discuss the requirement for plastics to become reusable and recyclable. However, this is severely lacking many aspects of the plastic economy which currently make it so linear. The only document stating black plastics and their problem in the broader scope of waste is the Resources and Waste Strategy for England, published in 2018 [182], this states the problem of black plastics and their un-recyclability.

Currently, in the UK, government policy is largely concerned with eliminating single-use plastics, often citing the 5p plastic bag tax as an effective way of combatting this. This is a worthy topic for the government to focus their efforts on in terms of plastic pollution, but even in its success, it will not provide a holistic solution for the problem of plastic pollution. Furthermore, much of what the government is doing is passing the buck down the line to NGOs who are having responsibility put on them to find solutions to problems, this was largely done with respect to consumer black plastic. Moreover, as previously discussed, the banning of plastic bags has had

a plethora of unintended negative consequences which were largely unforeseen, this could be seen as a cautionary tale in creating further legislation.

5.4.2. Non-government organisations

Analysis of black plastic usage, market trends, and possible solutions to the problems of black plastics have been carried out by non-governmental organisations (NGOs). Two NGOs who have carried out a broad scope of research on different solutions as well as what producers are doing to stop this problem, are WRAP and RECOUP. RECOUP is a charity which aims at to achieve a more sustainable use of plastics, increased recycling and change legislation so that plastic waste has less of a negative impact. WRAP is an organisation fighting to alleviate climate change, one way in which it does this is by looking at how plastics can be made more sustainable, from how they are produced, consumed, and disposed of. The action that these NGOs have taken can be broken down into two major parts, and one speculative. The two major areas of research and application have been replacing black plastic packaging with clear or lighter coloured plastics and using NIR detectable colourants. RECOUP briefly discusses the use of artificial intelligence (AI) for non-NIR sorting machines in its 2020 report [172], however, they do not go into how widely this has been applied or its efficacy. As well as RECOUP doing work to get brands to move away from black plastic packaging, Greenpeace – an environmental justice action/pressure group – have been largely credited with major supermarkets banning black plastics in December 2019 [183-185].

Another solution proposed is to use detectable black pigment. Detectable black pigment is a different type of pigment to carbon black, but it still colours the plastic black. However, it comes with the benefit of not absorbing NIR radiation, hence, being detectable by current technologies. There is academic research showing that Calcium Manganese Oxides can be utilised for this. Research has shown that near infrared light can be reflected off plastics coloured with this pigment in various different forms [186]. Several companies have implemented this in their packaging, these are displayed in Table 5.1, this has been done for common packaging material such as PET and PP. A report by WRAP did show that there is no drop in the efficacy of recycling when NIR detectable black plastics are mixed in with non-carbon black pigmented plastic packaging [187]. There is also a plethora of companies which now make non-carbon black pigment for use in plastics, these include: Ampacet, COTREP and kpKapture, showing that this is a solution which is preferable for manufacturers.

	Company	Advocacy group
Replacing black plastic packaging	• Quorn • Co-operative • Spar • Aldi • Morrisons • Tesco	• RECOUP • Green peace
Using detectable black pigment	• The Collective Dairy • Unilever • Berry M&H	• RECOUP • WRAP

Table 5.1: Companies using the various solutions proposed by advocacy groups to reduce the amount of black plastic in the economy.

Although detectable black pigment allows companies to pack their products in black packaging again, this is a purely aesthetic solution. Strength testing of plastics which have been coloured using non-carbon black pigment show that they are no stronger than regular coloured plastic, so the material benefits of carbon-black are not held. This means that it cannot be used as a replacement of carbon black pigment, as it has none of the same properties bar aesthetic that the carbon black pigment adds [188]. Moreover, this solution only applies to new black plastics, there is plenty of legacy black plastic in the economy – for example DVD/VHS cases which can still not be sorted.

5.4.3. Optical solutions for carbon black pigment

Whereas government policy is largely trying to legislate away black plastics, so that no new black plastic is created, as well as passing the buck to NGOs to do the research, there are several points which are missed in their analysis. First, there is already a lot of black plastic currently circulating in the supply chain, which at some point, will need to be sorted to be recycled or incinerated. Second, there are a plethora of reasons why carbon black pigment should remain in use in plastics for practical purposes. If it were completely banned this could have many negative consequences due to many materials not having the properties which they previously had because of the carbon black pigment, as will be discussed in section 5.4. Finally, even if there is a UK ban on black plastics via government policy, this does not consider the fact that this ban will not take affect everywhere, other places will still produce black plastics. The world is so interconnected, as previously mentioned, plastic pollution originating in one place can have effects on faraway places around the globe. Moreover, although NIR detectable black pigment allows plastics to be coloured black, and detected by NIR systems, it is not a replacement for

carbon black. This is because carbon black provides a plethora of uses other than just as a colourant, which are not replicated by NIR detectable pigment.

When considering plastics containing carbon black pigment, although this is not detectable using near-infrared detection technology, there have been several ways in which it has been possible to detect plastics coloured with carbon-black pigment using optical technologies. There are multiple companies who have made industrial scale plastic sorting machines which use various technologies to sort black plastics which are in a waste stream. These include Steinert's UniSort Black [189], which uses hyperspectral imaging (HSI) technology in addition to standard NIR spectroscopy technology to create an additional black plastic waste stream. Pellenc [190] uses a mixture of NIR and visible spectroscopy, which is supported with convolutional neural networks (CNNs) to sort the different types of plastics. Tomra [191] use LAISER technology along with AI assisted analysis of NIR spectra to detect black plastics in their systems.

There are several methods of detecting black plastics which have been mentioned in literature, one is using Laser Induced Breakdown Spectroscopy (LIBS). A spectroscopic method for solid materials, in which a high-power laser is focused onto a target surface, causing ablation. The fluorescence caused by this is then analysed by a spectrometer around the visible spectrum (200 – 900 nm) [192]. It has been shown that this spectroscopic method can be used to detect black plastics by polymer type [193, 194]. This works for black plastics because it can tell the fraction of carbon and hydrogen in a sample by molecular weight, which is then used to determine the polymer type. Because of the high energy of the laser light, ablation occurs rather than just absorption, which is why the carbon-black pigment is not a problem, unlike in NIR spectroscopy. Another method used to identify black plastics has been mid-infrared spectroscopy, it was shown by Signoret et al. that it was possible to obtain clear spectra in the mid-infrared range (4000 – 400 cm^{-1}) [195]. This methodology works by comparing the spectra to the expected absorption lines, based on the energy transitions of bonds in the material. These bonds change based on the molecular structure, which is why it is possible to discriminate between various different types of plastics/polymers. Other groups have shown that using mid-infrared spectroscopy and a mixture of artificial intelligence methods, plastics containing carbon black pigment can be identified based on the mid-infrared spectrum [6, 170, 196]. This uses the same methodology, but the AI powered identification allows for quicker and more accurate analysis on the system. This is particularly useful when considering commercialising the technology.

5.4.3.1 Optical solution in the mid-infrared (2 – 5 µm) region

As discussed, various research groups have shown that black plastics can be identified using various methods of analysis on their mid-infrared spectrum. However, this is a process which requires a laser with frequencies spanning the mid-infrared range as well as analysis software which can complete a Fourier transform. All of this results in this method being energy and time intensive. If there is sufficient spectral information in the 2 – 5 µm range however, it is possible that this process could be simplified. Reflection minima/maxima can be detected using LEDs with specific output frequencies, coupled with detectors which are also specifically tuned for operation in the region of interest. FTIR scan in this range (3 – 4 µm) have been conducted on black and non-black plastics of polymer type: polyethylene, polypropylene and polyvinyl-chloride, these scans can be seen in Figure 5.9 (a) – (c). From this, it is clear that both black and non-black plastics have discernible spectral fingerprints in this region, with the only difference being that black plastics have a lower reflection – apart from PVC.

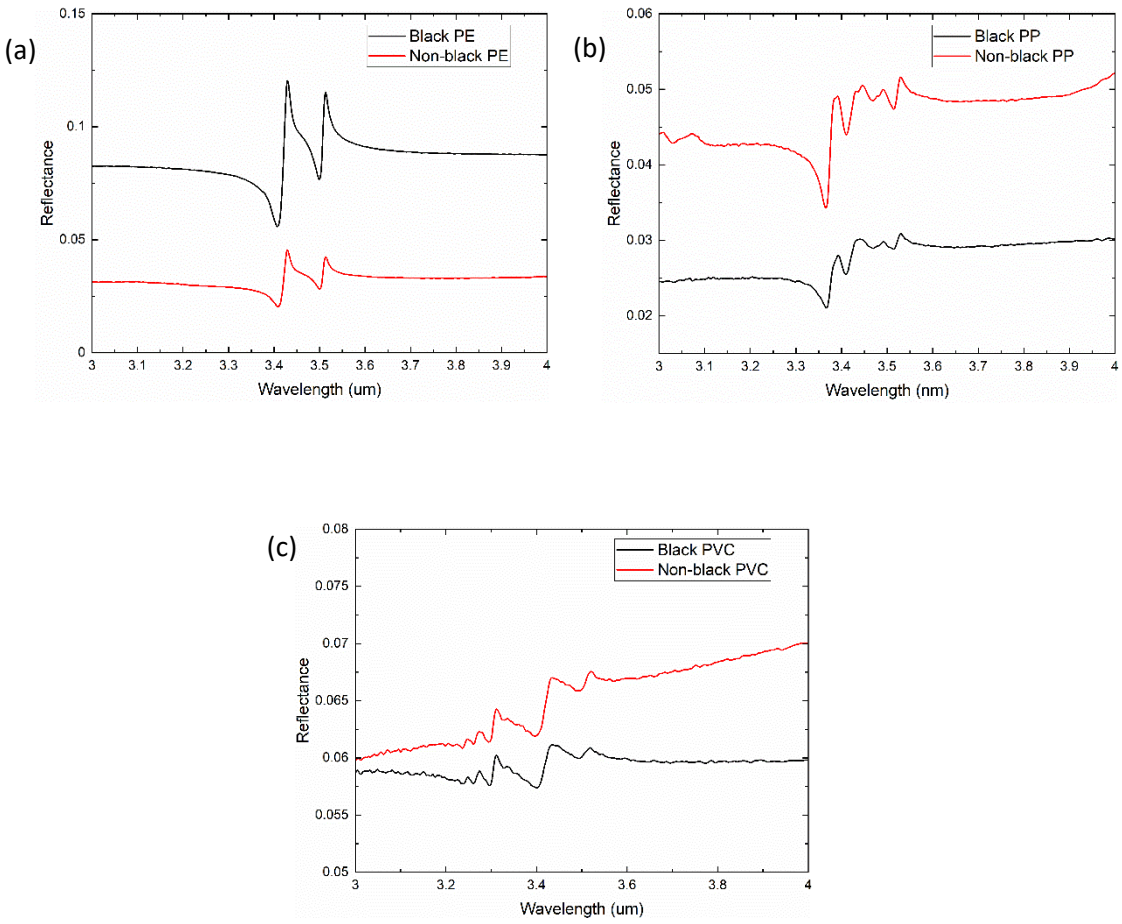

Figure 5.9: FTIR spectra comparison of black and non-black plastics between 3 – 4 µm for (a) polyethylene, (b) poly propylene and (c) polyvinyl-chloride.

The reflection minima of the spectrum are due to the absorption in the plastic, this is caused by the stretching of bonds – as discussed in section 2.4. These reflection minima (absorption maxima) are displayed with their corresponding wavelength in Table 5.2, where the bond causing the absorption is also shown. It can be seen that for the same bonds certain plastics have different absorption minima, this is due to the different molecular weights of the molecules causing different energies of stretching.

Plastic	**Absorption / µm**			
PE	-	3.407	-	3.499
PP	3.365	3.411	3.470	3.515
PVC	-	3.402	-	3.496
Causal bond	CH_3 asymmetric stretch	CH_2 asymmetric stretch	CH_3 symmetric stretch	CH_2 symmetric stretch

Table 5.2: the absorption in (µm) of the three different polymers shown in Figure 5.9. The bonds which cause the reflection minima/absorption peak are also shown [197-199].

From this, it is shown that there are spectral characteristics in this range. Because of this, it should be possible to discern these using LEDs with corresponding detectors, this has been shown practically in the detection of gasses and other compounds, as discussed in section 4.4.

5.5. The future of black plastics as part of a circular economy

As stated in this chapter, carbon-black pigment is currently a non-replaceable component in the manufacturing process of many plastics, giving them functionality such as: added strength, flame retardance, conductivity, UV protection and many more. However, they pose a unique problem as part of a circular economy due to them not being currently recyclable; because of their inability to be sorted by current NIR spectroscopic technologies. Once sorted by polymer type, there is no reason that black plastics, through the means of chemical or mechanical recycling, cannot be turned into recycled feedstock for the creation of new commodities. This is important in taking what is currently categorised as “waste” and turning it into a technical nutrient as discussed in section 5.3.3.2, which can be remade into new, useful commodities. This has wide ranging positive effects from being able to create plastic feedstock in a more energy effective manner; reducing the amount of raw materials which have to be extracted and stopping technical nutrients from entering biological cycles – which can have acute ramifications.

Several companies have created technologies which can sort black plastics by polymer type via a plethora of different methods. However, these are all industrial level sorters, some of which incorporate lasers, making them highly energy intensive. It has been shown in literature that it is possible to obtain the MIR spectra via infrared spectroscopy for polymers and commercial plastics containing carbon black pigment. Hence, technologies using MIR spectroscopy are a novel and largely untested method of creating sensors for black plastics. As these spectra are easier to obtain than NIR ones, it may be possible to use less energy intensive methods, such as light emitting diodes (LEDs) to identify these plastics using selected absorption peaks in the wavelength range. It was shown that there is a strong spectral fingerprint for: polypropylene, polyethylene and polyvinylchloride in the 3 – 4 µm wavelength range. The development of emitters (LEDs) and detectors in this wavelength range, specifically around the reflection minima and maxima is vital in being able to create the technology which could detect these materials. The development of LEDs in the discussed wavelength range will be a vital starting point in seeing if this is in-fact a possible solution, this is one of the aims of this thesis.

The work of the UK government regarding black plastics has been discussed, showing that their long-term goal is to stand for their removal. They seem to use NGOs to implement this, with their work mainly being focused on plastic packaging and the general reduction of the use of non-recyclable plastics. This work discussed the short-sightedness of this strategy, due to it overlooking the benefits of carbon-black pigment not only during the lifetime of plastics, but as a means of more effectively recycling them.

Detection of these black plastics does not only mean that they can be used to create black plastic feedstock from recycled material, which is a more energy and material efficient way of creating plastic. It will also mean that black plastics of various types will be able to be extracted from other plastic streams in PRFs more easily, this will lead to less contaminants in the recycling process, creating better quality recycled plastic feedstock which can be used to create commodities of higher use value. Creating commodities from recycled material of high use value is extremely important in a circular economy as it puts material back into the economy via corresponding cascading mechanisms. Furthermore, if the technology used to detect black plastics uses less energy, then the energy efficiency of the plastic creation process is increased as the embodied energy of the feedstock is lower.

In summary, it is not currently possible for black plastics to be part of a circular economy due to the inability of existing technologies to sort them, hence, not they cannot be recycled. However, via the creation of various technologies, it may be possible to include this plastic with important properties into the economy at large whilst still maintaining a sustainable, circular mode of

production. This would allow for the closing of a material loop in the circular economy. Although by itself this is not a holistic solution to the linear economy, it is an important part of several material cascading mechanisms which could contribute to a reduction in the amount of material which is permanently taken out of the economy.

6. Developing type-I InGaAsSb based active regions for room temperature emission around 3.3 µm

Type-I strained $In_xGa_{1-x}As_{1-y}Sb_y$ quantum well based active regions have been shown to have strong emission from 1.6 µm up to around 3 µm, as discussed in section 4.2.2 in both LEDs and lasers. For the purpose of sensing black plastics in the mid-infrared range, the results in section 5.4.3.1 show that there is a strong spectral fingerprint for commonly recycled plastics at 3.3 – 3.6 µm. Because of the wavelength range of this spectral fingerprint, in order to create a sensing device for different polymer types, LEDs emitting in this range have to be developed. Around 3 µm is the upper limit of where type-I devices have been shown to operate and is the lower limit of where type-II devices have been shown to operate at room temperature. Both bandgap types are highly tailorable in this region so each could be used in the creation of a device. However, the use of the InGaAsSb material system previously to create highly luminescent LEDs and lasers emitting < 3 µm can be built upon. Moreover, the extra degree of freedom in the quaternary alloy rather than ternary allows for a wider range of alloy contents with engineered bandgaps and strain characteristics. Being able to control the strain and bandgap with an extra degree of freedom allows for higher strain at all wavelengths to become available in comparison to ternary $In_xGa_{1-x}Sb$ system. This strain tailoring is beneficial due to the reduction in non-radiative Auger recombinations caused by band-splitting of hole states it causes. Furthermore, two-dimensional quantum confinement as discussed in 2.1.4, allows for additional tunability of the output wavelength and an increase in spectral purity due to quantum confinement effects. Moreover, by placing the QWs in resonant cavity it is possible to further engineer the spectral characteristics of the output which is vital for sensing applications. This device is referred to as a resonant cavity LED or RCLED and is discussed in section 4.3. These devices have been successful in creating LEDs which have their emission tailored to coincide with that of the absorption spectra of gasses such as NO_2 and NO. State of the art research was conducted by Al-Saymari et al at Lancaster University in the creation of spectrally pure RCLEDs based on InAsSb QW active regions and epitaxially grown DBRs emitting > 4 µm [200]. Type-I InGaAsSb based active regions grown on GaSb substrates have also been grown epitaxially for resonant cavity enhanced emission at ~ 2.5 µm. However, the use of type-I InGaAsSb QWs requires the growth of lattice match AlGaAsSb barriers which are integrated into the cavity. This provides additional challenges in tuning the resonant frequency of the structure due to the addition of a material with different refractive index to the rest of the cavity. Moreover, to achieve lattice matched AlGaAsSb, calibration growths are required to obtain valve positions for

the group-V elements, adding to the number of growths required to create the desired structure as described in section 3.1.2.

A solution to this, is to base the barriers for the QW on the cavity material, this would require fewer group-V valve and bulk temperature changes meaning growth is easier and less likely to result in defects. In order to do this, InGaAsSb type-I QWs with GaSb barriers must be developed so that they can be implemented into resonant cavities for enhancement. There are certain challenges associated with this material system; due to the bandgap of GaSb in comparison to InGaAsSb, there is a small valence band offset, this can lead to poor hole confinement or the creation of type-II QWs. Moreover, to obtain emission in the > 3 µm range, the corresponding alloy contents of InGaAsSb which must be grown are close to the miscibility gap, this can lead to the creation of poor-quality material and inconsistent alloy content.

6.1. InGaAsSb/AlGaAsSb type-I structures

6.1.1. Design

6.1.1.1 Critical layer thickness

When considering the design of the structure, one thing that must be considered is the strain in the QWs, caused by growing an InGaAsSb alloy lattice mismatched onto GaSb. Figure 6.1 (a) shows the lattice constants of various $In_xGa_{1-x}As_{1-y}Sb_y$ alloys with $0.05 < x < 0.60$ and $0.65 < y < 1.00$, where GaSb has a lattice constant of 6.0959 Å.

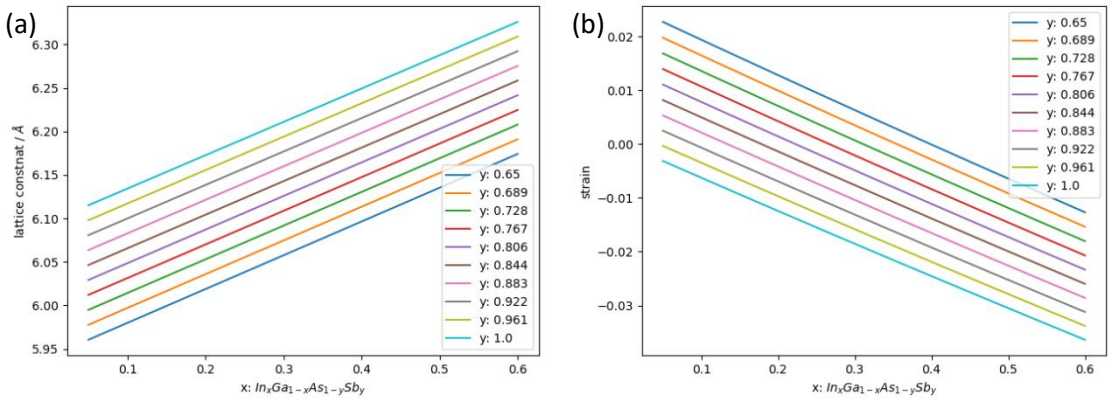

Figure 6.1: (a) the lattice constant of $In_xGa_{1-x}As_{1-y}Sb_y$ for varying alloy contents and (b) the strain of that system grown on GaSb.

Figure 6.1 (b) then shows the corresponding strain of the alloy when grown on a GaSb substrate, a strain of 0.00 corresponds to the alloy being lattice matched. Positive strain corresponds to alloy having a smaller lattice constant than GaSb, which exhibits tensile strain. Negative strain

corresponding to the alloy having a larger lattice constant than GaSb, exhibiting compressive strain, this is calculated in accordance with equations 2.43 and 2.45 as discussed in section 2.3.2.

When growing type-I QWs, it is beneficial for the system to be under compressive strain. As discussed in section 2.3.2.1, compressive strain causes the energy of the heavy-hole band to raise and the light-hole band to fall. The splitting of the light and heavy-hole bands under compressive strain creates opportunities for Auger recombinations to be reduced as discussed in section 2.2.2.3. Under tensile strain, there is an overlap between the light and heavy hole bands in k-space, this makes it more likely that non-radiative recombination mechanisms will occur.

Although strain is beneficial to optical performance of the system, the growth of lattice mismatched layers can cause defects to occur in the epitaxial layer, as discussed in section 2.3.2.2. The maximum thickness of an epitaxial layer that can be grown is known as the critical layer thickness. Two of the different models describing this are that presented by Matthews and Blakeslee, and by People and Bean. The differences between these two equations, 2.43 and 2.45, are discussed in the aforementioned chapter. These two equations were modelled in Python 3.0, the code for which is available in a GitHub repository in section 9.3. The critical layer thicknesses were calculated for the same alloy contents shown in Figure 6.1. The critical layer thicknesses this corresponds to are displayed in Figure 6.2 (a) and (b) for Matthews-Blakeslee and People-Bean equations respectively for the InGaAsSb alloy.

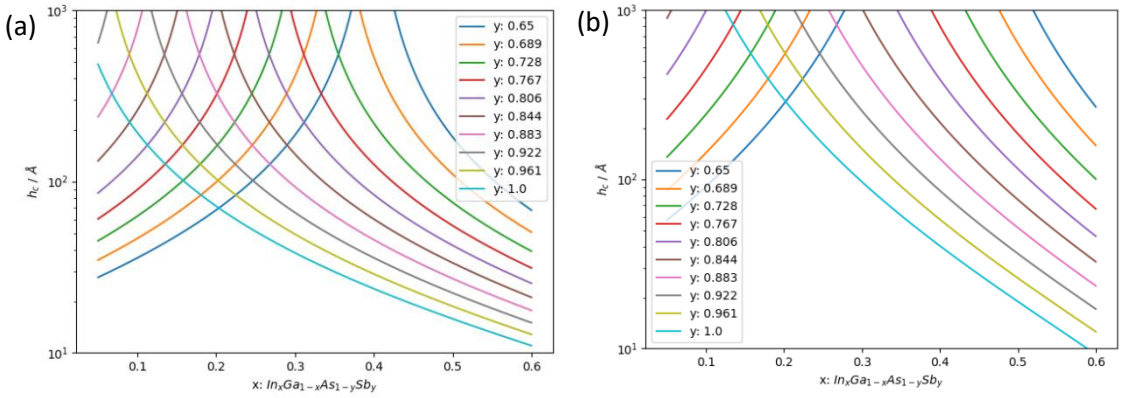

Figure 6.2: the critical layer thickness of $In_xGa_{1-x}As_{1-y}Sb_y$ layers as a function of x and y according to (a) Matthews-Blakeslee equation and (b) People-Bean equation.

The graph in Figure 6.2 (a) shows that when accounting for the mechanical properties of the epitaxial layer (Matthews-Blakeslee model), the critical layer thickness is smaller than when accounting for the energy in the system (People-Bean model, Figure 6.2 (b)). Both of the models show that for this range of alloy contents, InGaAsSb can be grown with thicknesses from

~ 1 – 100 nm. $In_xGa_{1-x}Sb$, which is shown by the pale blue line corresponding to y = 1 (no arsenic incorporation), shows that as indium incorporation is increased, the critical layer thickness of the alloy goes from ~ 100 nm at x = 0.05 to ~ 1 nm at x = 0.60. It is possible to increase the critical layer thickness of the of the epilayers by adding As to the alloy, this can be seen in in both models displayed in Figure 6.2, whereby as the Sb content decreases, the critical layer thickness of the epilayer increases.

As well as the InGaAsSb QW, it is important to consider the critical layer thicknesses of the $Al_xGa_{1-x}As_{1-y}Sb_y$ barriers. In order to confine the charge carrier wavefunctions in the respective bandedges, barriers of around 20 nm are required, with 0.25 < x < 0.35. Figure 6.3 (a) and (b) show the critical layer thickness of this alloy according to the Matthew-Blakeslee and People-Bean equations respectively. From this, the alloys are lattice matched with 0.96 < y < 0.99, for the given range of x, this can be seen from the asymptotes of the graphs which correspond to lattice matched points. The dotted line on each graph indicates a layer thickness of 20 nm. Figure 6.3 (a) shows that with y > 0.9, the barriers will be grown within their critical layer thicknesses, Figure 6.3 (b) indicates that for y > 0.85 the critical layer thickness will not be exceeded.

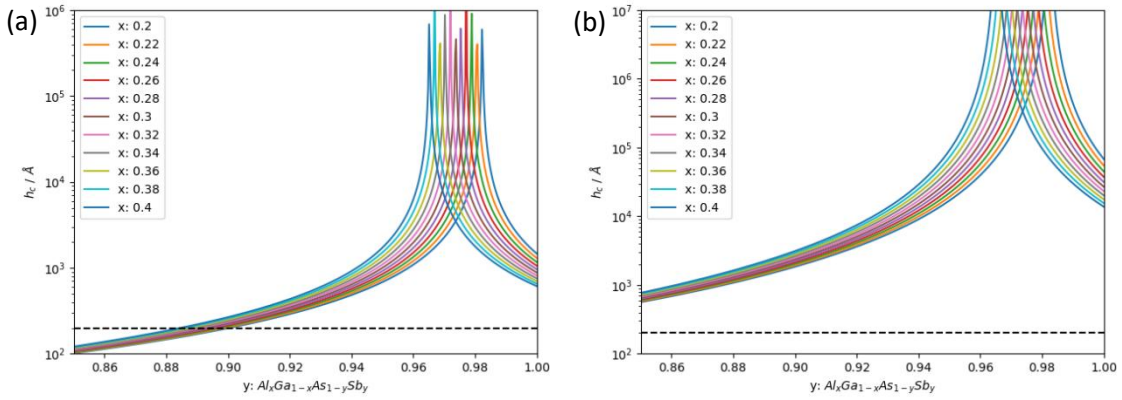

Figure 6.3: The critical layer thickness of $Al_xGa_{1-x}As_{1-y}Sb_y$ based on (a) Matthews Blakeslee and (b) People Bean equations.

Although there is a relatively wide range of group-V incorporation which allows 20 nm of AlGaAsSb to be grown within the critical layer thickness. Because in an active region, up to six barriers will be grown, with strained InGaAsSb layers between them, it is better to grow as close to lattice matched as possible as this allows for greater strain to be achieved in the QWs without material relaxation occurring.

6.1.1.2 Alloy bandgaps

As well as accounting for the critical layer thickness which can be grown for various alloys. When designing an active region, it is important to consider the bandgap of the alloy, as this will determine the wavelength that the sample emits at. The main factor which effects this is the alloy content of the QW (InGaAsSb), as this will change the position of the conduction and valence bandedges based on the specific alloy content and strain. Furthermore, the width of the InGaAsSb QW will affect the bandgap due to it affecting the energy at which charge carriers are held because of the two-dimensional quantum confinement. In order to quantify how alloy content affects the bandgap of this system, k·p 8-band room temperature simulations were carried out in Nextnano, as described in section 2.5.

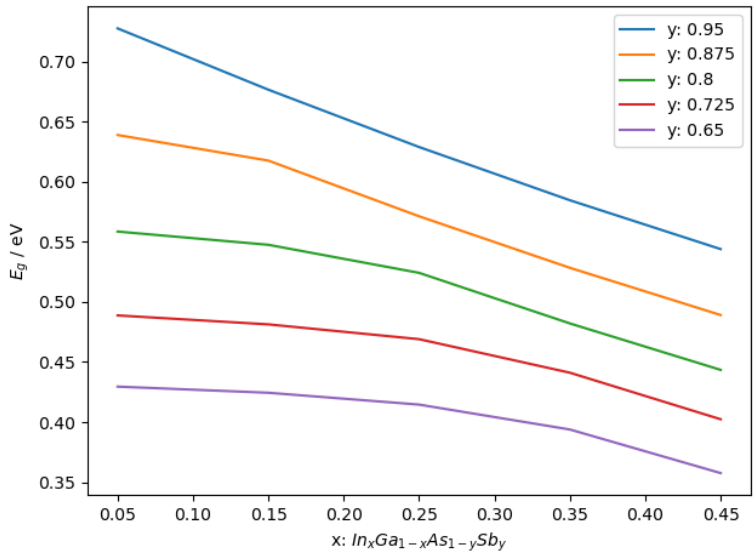

Figure 6.4: The available bandgaps from the type-I QW $In_xGa_{1-x}As_{1-y}Sb_y$ material system with a 10 nm QW for 0.05 < x < 0.45 and 0.65 < y < 0.95. Simulated using the k·p 8-band approximation in Nextnano.

The results of the Nextnano simulation can be seen in Figure 6.4, this was done for a single 10 nm QW inside 20 nm barriers. For type-I QWs, a single QW will have the same bandgap as MQWs because of the wavefunction isolation. Because of this, to save on computational power, the simulations were carried out on single QWs. The results show that in the specified alloy range, the bandgap varies from ~ 0.7 eV to ~ 0.35 eV, or emissions of 1.74 µm < λ < 3.42 µm. As the indium in the active region is increased, this decreases the bandgap of the material. As arsenic is increased, this will further decrease the bandgap. However, with the addition of arsenic, this bandgap decrease happens to a lesser extent than the addition of Indium to the alloy. As previously mentioned, the addition of arsenic and indium into the system can cause difficulties during epitaxial growth due to the miscibility gap of the alloy with higher arsenic and

indium. For the miscibility gap of $In_xGa_{1-x}As_ySb_{1-y}$, the miscibility gap $0.15 < y < 0.60$ and $x > 0.60$. However, the miscibility is dependent on the incorporation of each alloy [201]. This means that not all of the bandgaps simulated are feasible to grow.

6.1.2. Active region

Based on the constraints of the critical layer thickness of the $In_xGa_{1-x}As_{1-y}Sb_y$ alloy and the range of available bandgaps based on the Nextnano model, type-I $In_xGa_{1-x}As_{1-y}Sb_y$/ $Al_{0.35}Ga_{0.65}As_{0.034}Sb_{0.966}$ QWs were grown with thicknesses of ~ 10 nm QWs and 20 nm barriers. These samples were grown on n-GaSb substrates, structurally characterised via XRD and optically characterised by photoluminescence. Photoluminescence at room temperature is particularly important because it shows that the active regions is of good quality and can be put in an LED structure giving bright electroluminescence spectra. The Indium content of the QW alloys was aimed to be ~ 0.35, with each different growth, the As content of the QWs would be varied by increasing the valve position of the cell whilst the bulk temperature was kept constant and relatively low. This was so that the effect of increasing the arsenic content of the alloy could be observed whilst other variables were held constant. Increased arsenic and indium in the alloy can lead to growing in the "miscibility gap", whereby the structure does not properly form, with high levels of indium in certain places and low indium in others. During these growths, the alloy contents were tailored such that they were outside of this miscibility gap, ensuring good quality formation of the material. This was further confirmed using XRD and optical emission analysis – material in the miscibility gap shows poor optical emission properties and poor QW formation can be observed in the XRD scan via broad satellite peaks.

6.1.2.1 Growth

The multi quantum well (MQW) samples were grown via MBE on n-GaSb substrates as outlined in section 3.1. Before epitaxy is started, the substrate is outgassed, then once in the growth chamber, a deoxidation process is completed, whereby the GaSb substrate is heated to 600 °C under Sb flux to remove oxides from the surface. Once this process is complete, the substrate temperature is reduced to 430 °C, at which GaSb and GaSb based alloys can be grown. Then 400 nm of GaSb buffer is grown at a rate of 1 µm $hour^{-1}$, followed by 500 nm of lattice matched $Al_{0.35}Ga_{0.65}As_{0.034}Sb_{0.966}$ – this is the same alloy that is used for the QW barrier. Once this buffer region has been grown, the growth of the active region begins. This begins by growing the 10 nm InGaAsSb QW, once this is done, the system is kept under Sb flux whilst the Ga cell cools down to allow for the AlGaAsSb growth, cooling the Gallium cell takes around two minutes to reach the desired temperature and for it to be stable. Then, 20 nm of barrier is grown, once this

is complete, the system is kept under Sb flux whilst the Ga cell heats up to allow for the growth of the next InGaAsSb QW. Then a 20 nm AlGaAsSb barrier is grown, once this process is complete the beginning of the process starts again so that the next layer of InGaAsSb can be grown.

Sample	**$In_xGa_{1-x}As_ySb_{1-y}$**		**QW width / nm**	**Barrier width / nm**
	x	**y**		
SAMPLE 6.1	0.34	0.032	9.3	18.2
SAMPLE 6.2	0.34	0.039	9.3	18.2
SAMPLE 6.3	0.34	0.055	9.3	18.2
SAMPLE 6.4	0.34	0.112	9.3	18.2
SAMPLE 6.5	0.34	0.124	14.5	18.1

Table 6.1: the alloy content and QW widths of the samples shown in Figure 6.5, for all samples the desired QW width was 10nm with 20nm barriers aside from SAMPLE 6.5 which had 15nm QW width and 20nm barriers.

Five repeats of this QW were grown, totalling ~ 170 nm. In the $In_xGa_{1-x}As_{1-y}Sb_y$ QW, four samples were grown with x = 0.34 with y ranging from 0.888 – 0.948, then one sample was grown with x = 0.41 and y = 0.124. The varying arsenic contents was achieved by varying the valve position with a constant bulk temperature. This structure is finally capped with 100 nm of $Al_{0.35}Ga_{0.65}As_{0.034}Sb_{0.966}$ then 20 nm of GaSb to prevent surface oxidation. The structure of these samples can be seen in Figure 6.6.

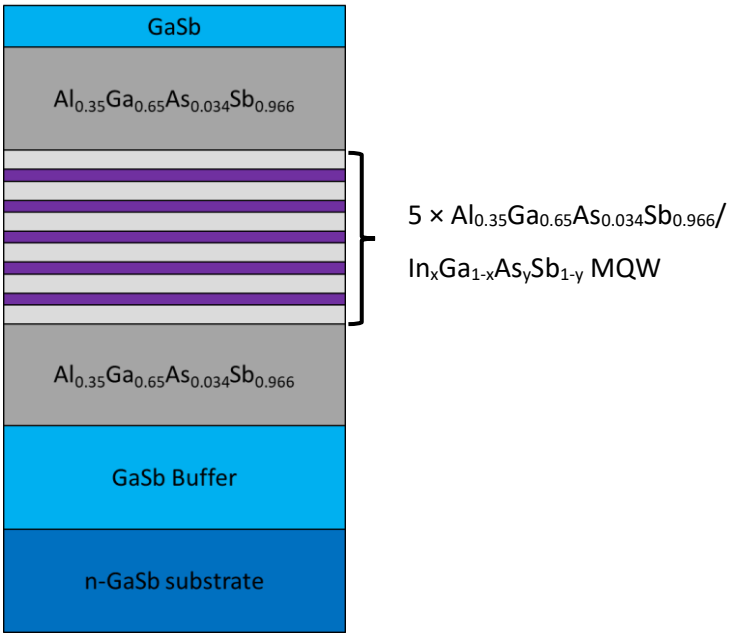

Figure 6.6: the structure of the AlGaAsSb/InGaAsSb MQW samples.

6.1.2.2 Structural characterisation

The samples were characterised using x-ray diffraction, the process of which is outlined in section 3.2, in order to determine the thickness and alloy content of the layers. Once the ω - 2θ scan has been completed, a simulation was conducted. The simulation allows the alloy content and layer thicknesses of the structure to be found by modelling the peaks of the XRD scan. The XRD scans and corresponding models of the type-I QWs can be seen in Figure 6.7 (a) – (e), the structures extrapolated from the model can be seen in Table 6.1. The clear satellite peaks in Figure 6.7 (a) – (d) suggest good QW formation with abrupt interfaces, essential for high quality active regions. Figure 6.7 (e) however, shows satellite peaks which are not as clearly defined, suggesting poorer quality QW, although, the presence of satellite peaks suggests that the QWs did form. The decrease in quality could be due to the higher indium and arsenic incorporation, pushing the alloy closer to the miscibility gap, causing a less uniform structure of the InGaAsSb alloy as discussed in section 6.1.1.2. The scans also suggest that the QW barriers were grown lattice matched to the substrate, suggesting there will be no relaxation in these alloys.

There are certain challenges in modelling the $In_xGa_{1-x}As_ySb_{1-y}$ alloy due to it being a quaternary, giving it four degrees of freedom in the simulation: x, y, QW width and barrier width. This degree of freedom means that it is possible to fit an XRD scan with models which each have different alloy contents and QW widths. It is assumed that when grown with the same group-III temperatures, that the Indium and Gallium contents are constant – based on growth rates done by the MBE users – across all samples along with QW width. This leaves the group-Vs as the

variable that will be the most uncertain at the beginning and that can be predicted to change throughout. It is important to take this into consideration when modelling the XRD scans of quaternary alloys as it can cause misleading results.

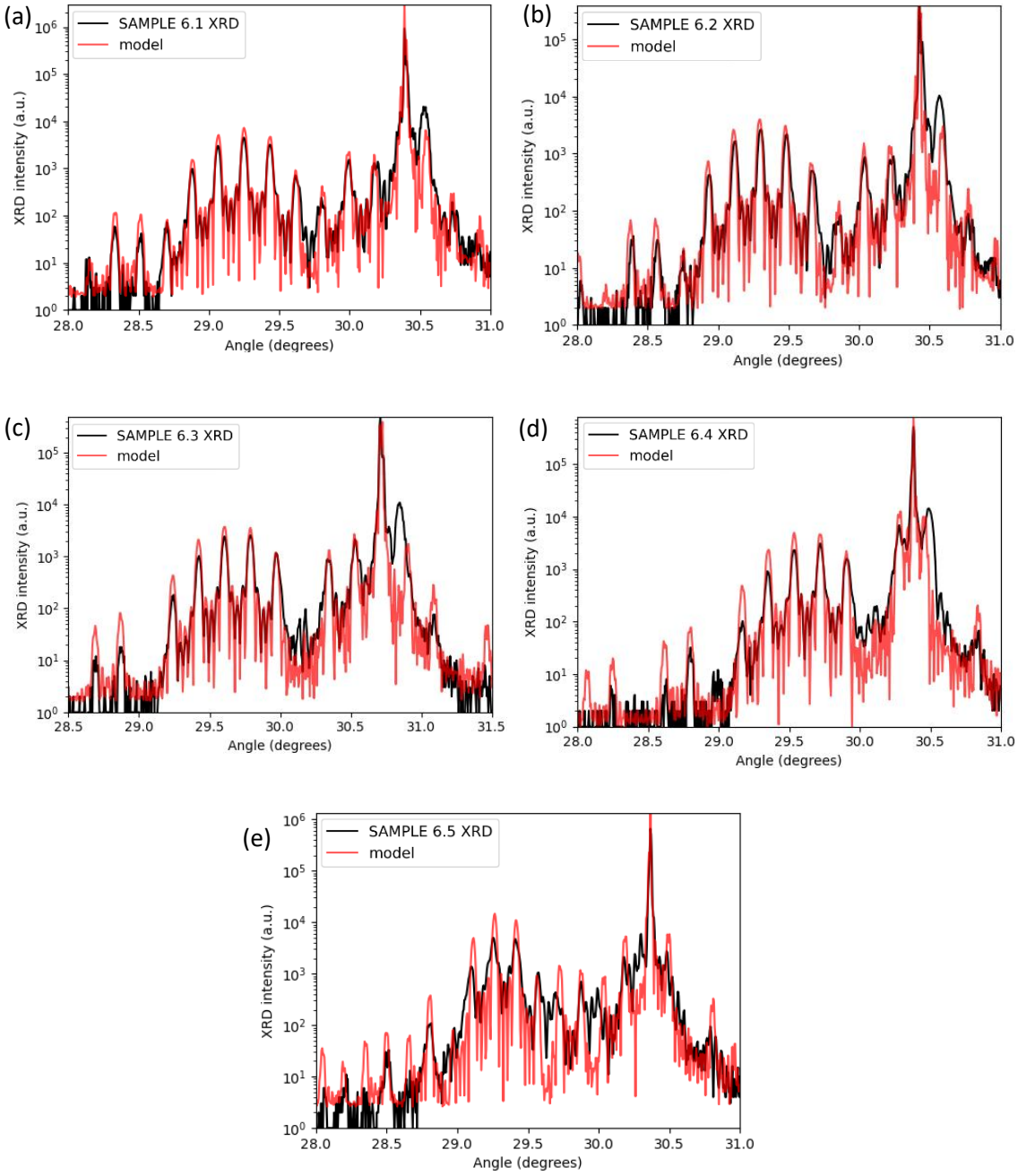

Figure 6.7: XRD scans of $Al_{0.35}Ga_{0.65}As_{0.034}Sb_{0.966}/In_xGa_{1-x}As_ySb_{1-y}$ type-I QW samples: (a) SAMPLE 6.1, (b) SAMPLE 6.2, (c) SAMPLE 6.3 , (d) SAMPLE 6.4 and (e) SAMPLE 6.5.

In an attempt to further increase the wavelength output of these type-I QWs, samples were grown with increased Indium and Arsenic whilst decreasing the Aluminium contents in the barriers. Higher Indium and arsenic decrease the bandedges of InGaAsSb conduction and valence band relative to one another, meaning that the quantum energy levels will be closer together. Moreover, the QW width was increased as this further decrease the bandgap. The

aluminium in the barriers was decreased because it gives a slightly lower charge carrier confinement potential, although this has the effect of decreasing the wavefunction overlap, it will also decrease the bandgap. The new barrier alloy is $Al_{0.25}Ga_{0.75}As_{0.02}Sb_{0.98}$ which is lattice matched to GaSb.

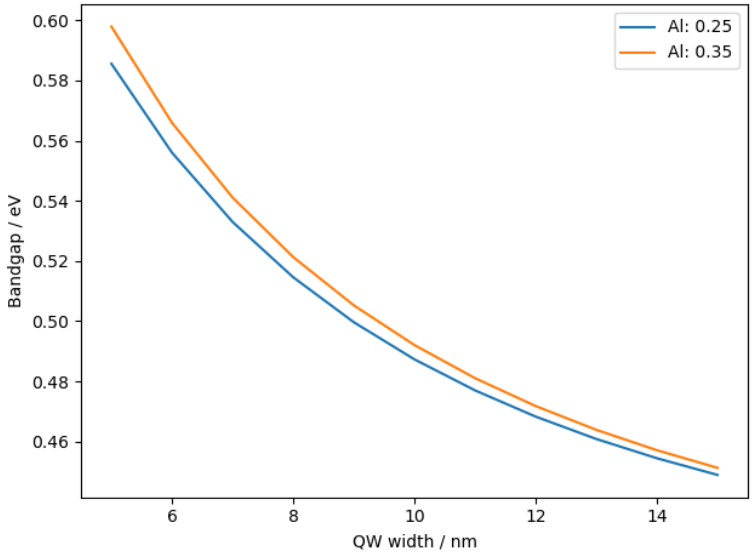

Figure 6.8: The bandgap of an $In_{0.4}Ga_{0.6}As_{0.15}Sb_{0.85}$ type-I QW in lattice matched $Al_xGa_{1-x}As_{1-y}Sb_y$ barriers with the QW width varying from 5 - 15 nm for x = 0.25 and x = 0.35.

The effect of decreased Al in the barriers and varying QW widths can be seen in Figure 6.8. Whereby Nextnano simulations show that the bandgap of the system can be decreased significantly – by around 15 meV – by increasing in the QW width from 5 nm to 15 nm. The decrease in Al incorporation in the barrier alloy has less of an effect but it still works to decrease the bandgap by several meV.

These samples were grown using the same methodology outlined in section 6.1.2.1, but with different cell temperatures for the barrier region due to the reduction in Aluminium content of the alloy. Two samples were grown using the same barrier configuration but varying the alloy content of the QWs. The XRD scans and model of the two MQW samples grown with $Al_{0.25}Ga_{0.75}As_{0.02}Sb_{0.98}$ can be seen in Figure 6.9 (a) and (b) with the corresponding alloy contents shown in Figure 6.9.

The XRD scans shown in Figure 6.9 show well defined satellite peaks throughout the scan, implying the formation of well defined, good quality QWs. Furthermore, there appears to be no peak indicating that the barriers are not lattice matched, so relaxation due to barrier mismatch will not occur. The alloy contents are displayed in Table 6.2. This shows that there was difficulty

in altering the As incorporation into the InGaAsSb alloy – despite the As valve position being altered for both of them.

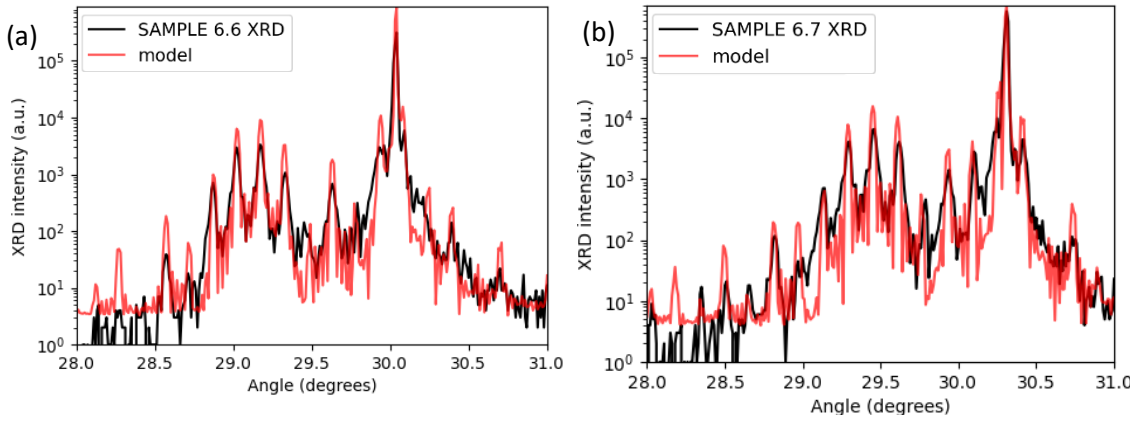

Figure 6.9: XRD scan of the $Al_{0.25}Ga_{0.75}As_{0.034}Sb_{0.966}/In_xGa_{1-x}As_ySb_{1-y}$ type-I MQW samples: (a) SAMPLE 6.6 and (b) SAMPEL 6.7.

The limiting factor in As incorporation is likely to be the flux produced by the cell during the growth of the well. There is low As flux as the bulk temperature has to be kept low to create the correct conditions for the lattice matched barriers which requires very low amounts of As. Moreover, the arsenic incorporation may be limited by the presence of Sb during growth – possibly saturating the environment. Both of these factors seem to limit the As incorporation to around 0.15. When the InGaAsSb alloy is growing, the As valve is open to its maximum extent, creating the maximum flux for the bulk temperature, and is then closed slightly for when the AlGaAsSb alloy is being grown. If the As incorporation of the QWs were to be increased, it would require a higher bulk As temperature, which may not work on the cladding and barrier layers.

Sample	**$In_xGa_{1-x}As_ySb_{1-y}$**		**QW width / nm**
	x	**y**	
SAMPLE 6.6	0.40	0.15	14.5
SAMPLE 6.7	0.38	0.15	14.0

Table 6.2: the alloy content and quantum well widths of the samples shown in the XRD scans in Figure 6.9 with the data being extrapolated from these scans.

During one growth, it could be detrimental to vary the bulk temperature of the As cell as it can cause large fluctuations in the flux it produces, causing non-uniform QW structures. Moreover, this would greatly increase the time taken for the active region growth due to the addition of heating and cooling the cell.

6.1.2.3 Photoluminescence

Once the device has been structurally characterised, optical testing began, this required measuring the photoluminescence of each sample. The samples were tested at room temperature using the methodology outlined in section 3.3. The normalised spectra for the samples displayed in Table 6.1 are shown in Figure 6.10 (a). These spectra imply that samples: SAMPLE 6.1, SAMPLE 6.2, SAMPLE 6.3 and SAMPLE 6.4 have high quality, Gaussian like peaks, indicating good material quality. Also showing the potential for this active region to be integrated into high quality devices. However, although SAMPLE 6.5 gives room temperature PL, the spectrum does not display a Gaussian like characteristics, and has a non-Gaussian, wide spectrum, possibly consisting of two radiative recombination mechanisms or indium segregation in the alloy. This indicates poorer material quality in comparison to the other samples which could be due to the higher arsenic content in the QW, in addition to being grown thicker. The poorer material quality is indicted by the XRD scan shown in Figure 6.7 (e) which has less well-defined peaks than the rest of the samples. SAMPLE 6.5 had a QW width which exceeded the critical layer thickness using the Matthews-Blakeslee equation (h_c = 6.12 nm), but did not exceed the critical layer thickness using the People-Bean equation (h_c = 24.9 nm). Therefore, it is possible that there is some form of relaxation which occurred during the formation of the QW.

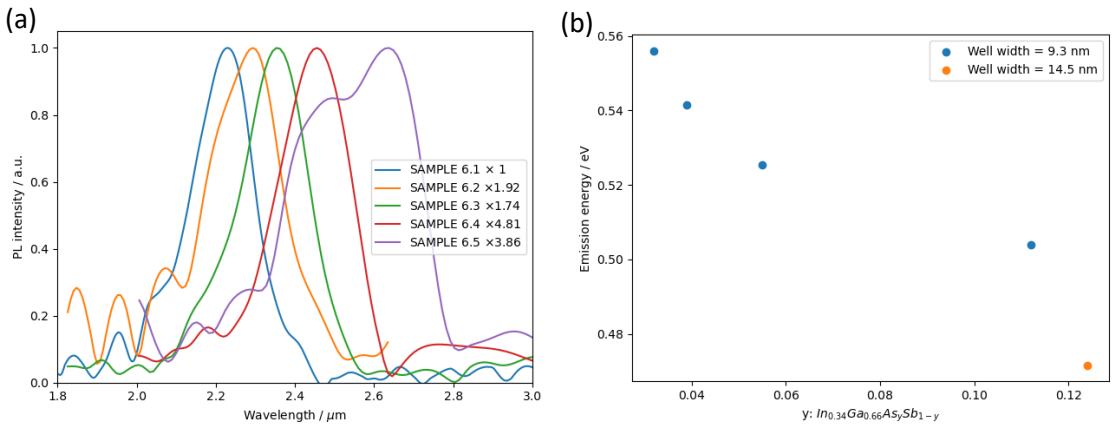

Figure 6.10: (a) normalised room temperature PL spectra for the $In_xGa_{1-x}As_ySb_{1-y}/Al_{0.35}Ga_{0.65}As_{0.034}Sb_{0.066}$ type-I QWs summarised in Table 6.1 and (b) the peak energy of the emission of these spectra as a function of arsenic incorporation (y).

The peak energy of emission is plotted as a function of As incorporation in the QW and the resultant relationship can be seen in Figure 6.10 (b). This shows that from the samples which were grown with constant indium, increasing the arsenic in the alloy decreases the bandgap – increasing the emission wavelength. Moreover, as the QW width is increased, a further decrease in the bandgap is seen. This is apparent from the difference between the two samples in Figure 6.10 (b) with As ~ 0.11 whereby a QW width increase from 9.3 nm to 14.5 nm causes a decrease

in the bandgap by > 20 meV. These results are in-line with the trends shown in the simulations in Figure 6.4 and Figure 6.8.

Samples SAMPLE 6.6 and SAMPLE 6.7 were optically tested in the manner as SAMPLE 6.2 – SAMPLE 6.5, using the same equipment and experimental setup at room temperature. These samples were sufficiently bright that they could also be tested using different laser powers at room temperature. The results of this can be seen in Figure 6.11 (a) and (b) for SAMPLE 6.6 and SAMPLE 6.7 respectively.

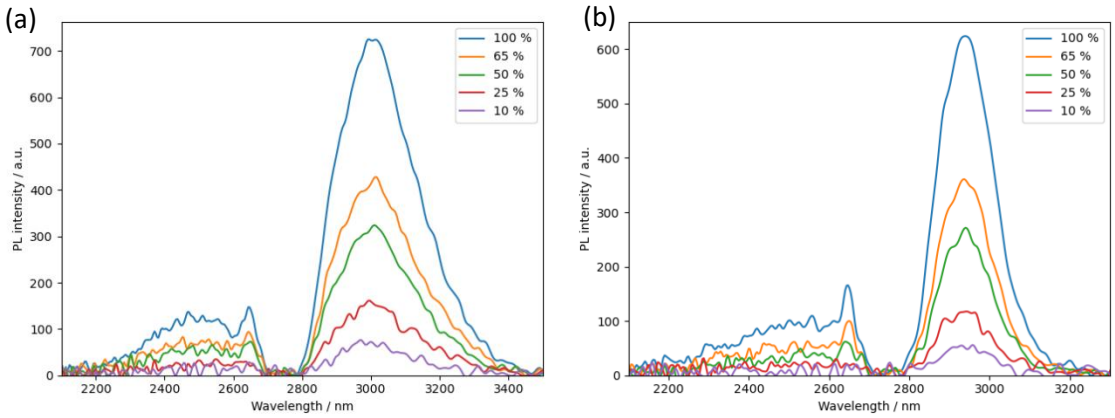

Figure 6.11: Room temperature (293 K) photoluminescence spectra of (a) SAMPLE 6.6 and (b) SAMPLE 6.7 with the laser power being decreased from 100 % - 10 % using filters.

From the PL spectra, SAMPLE 6.6 has a peak at 3010 nm and SAMPLE 6.7 at 2940 nm. These correspond to room temperature bandgaps of 0.399 and 0.408 eV respectively. Although the spectra are clear, with well-defined peaks corresponding to the specified bandgaps, both spectra are obfuscated. This obfuscation occurs slightly ~2600 nm resulting in a slight dip in intensity, and from ~ 2700 – 2800 nm with a full obfuscation of the spectrum, this is caused by a mixture of water and CO_2 absorption bands at the correspondent energy. These absorption bands cannot be avoided due to their strength and the fact that there is not a purge gas system available for this setup. SAMPLE 6.7 having a slightly shorter wavelength than SAMPLE 6.6 is also expected because of the lower Indium incorporation in the QW, on-top of the QW being slightly thinner. Both lower Indium and thinner QWs have both been shown in simulation to increase the bandgap and therefore decrease the emission wavelength.

Power dependant measurements were done to find the dominant recombination mechanisms as laid out in section 2.2.2. The integrated intensity of the spectra is lower than it would be without the absorption features, however, because the proportion of data removed from each spectrum is the same, this should not affect the relationship between integrated intensity. Figure 6.12 shows the $\log_{10}$ of the square root of the integrated emission as a function of the

$\log_{10}$ of the input laser power. The red line on both plots shows linear interpolation of the five data points from laser powers: 100 %, 65%, 50 %, 25 % and 10 %. The gradient of the linear interpolations for each set of data are 2.06 and 1.48 for SAMPLE 6.6 and SAMPLE 6.7 respectively. This shows that radiative recombination is the dominant mechanism for SAMPLE 6.6, minimal amounts of Auger recombination occurring as Z > 2. The proportion of radiative recombination is worse in SAMPLE 6.7 with a Z value of ~1.5, implying an approximately equal amount of SRH and radiative recombination. However, it should be noted that these tests were only done over one order of magnitude of laser input power, this is lower than that which would often be expected of a measurement of Z-value.

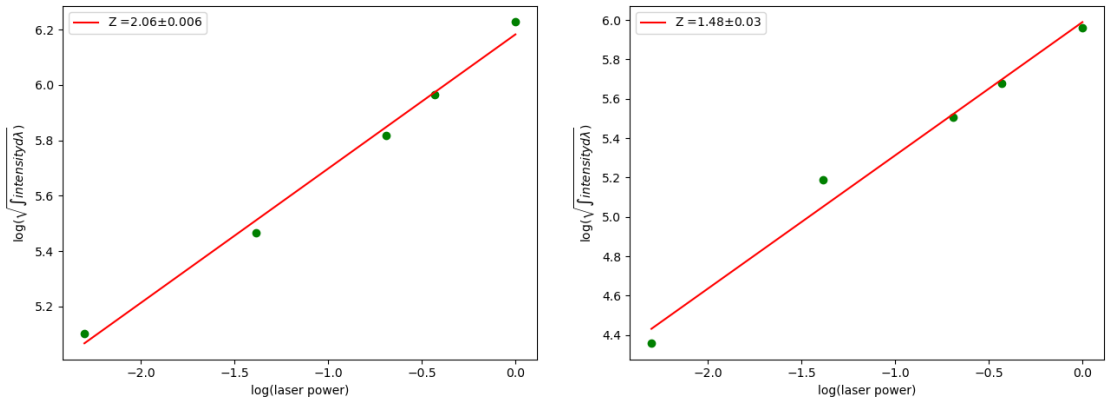

Figure 6.12: The linear fit of $\log_{10}$ of the integrated emission spectra as a function of the $\log_{10}$ of the laser power of (a) SAMPLE 6.6 and (b) SAMPLE 6.7, the inverse gradient of the linear fit is shown in the legend as Z.

These results imply that the InGaAsSb/AlGaAsSb type-I MQW system has high levels of radiative recombination at room temperature. Furthermore, it shows that the decreasing of Aluminium in the barrier region does not decrease the quality of emission, with levels of 0.25 and 0.35 in the barrier both resulting in bright room temperature emission. This makes the material system an ideal candidate for integration into an LED structure.

6.1.3. Light emitting diode

To create a device emitting at the same wavelength as the PL samples SAMPLE 6.6 and SAMPLE 6.7, the set points from the sample growth were used for the active region of an LED. This active region was placed inside a waveguide with graded, doped, lattice matched, AlGaAsSb on either side. The graded layers went from $Al_{0.1}Ga_{0.9}AsSb_{0.991}$ to $Al_{0.9}Ga_{0.1}As_{0.076}Sb_{0.924}$ for the layers which require the injection of electrons (n-doping) and vice versa for the injection of holes. This is required due to the large energy level discrepancy between the conduction and valence bands of the AlGaAsSb alloy and GaSb. The graded layers are added so that charge carriers can be

injected into the active region with greater ease. Moreover, the graded layers are grown lattice matched to GaSb such that they don't exceed their critical layer thicknesses and cause defects in the system. A schematic of the layout and doping of the LED structure can be seen in Figure 6.13.

6.1.3.1 Growth

The devices based on the schematic in Figure 6.13 were grown on n-GaSb substrates via MBE using the method discussed in section 3.1. Before being moved into the growth chamber, the substrates are outgassed to remove volatile contaminants. Once in the chamber, an additional in-situ deoxidation process is completed wherein the substrate is heated to 600 °C under Sb flux to remove any additional oxides from the surface without causing group-V evaporation. This process is further described in section 3.1. Once the substrate has been deoxidised, a 100 nm Te doped n-GaSb buffer layer is grown using a substrate temperature of 550 °C.

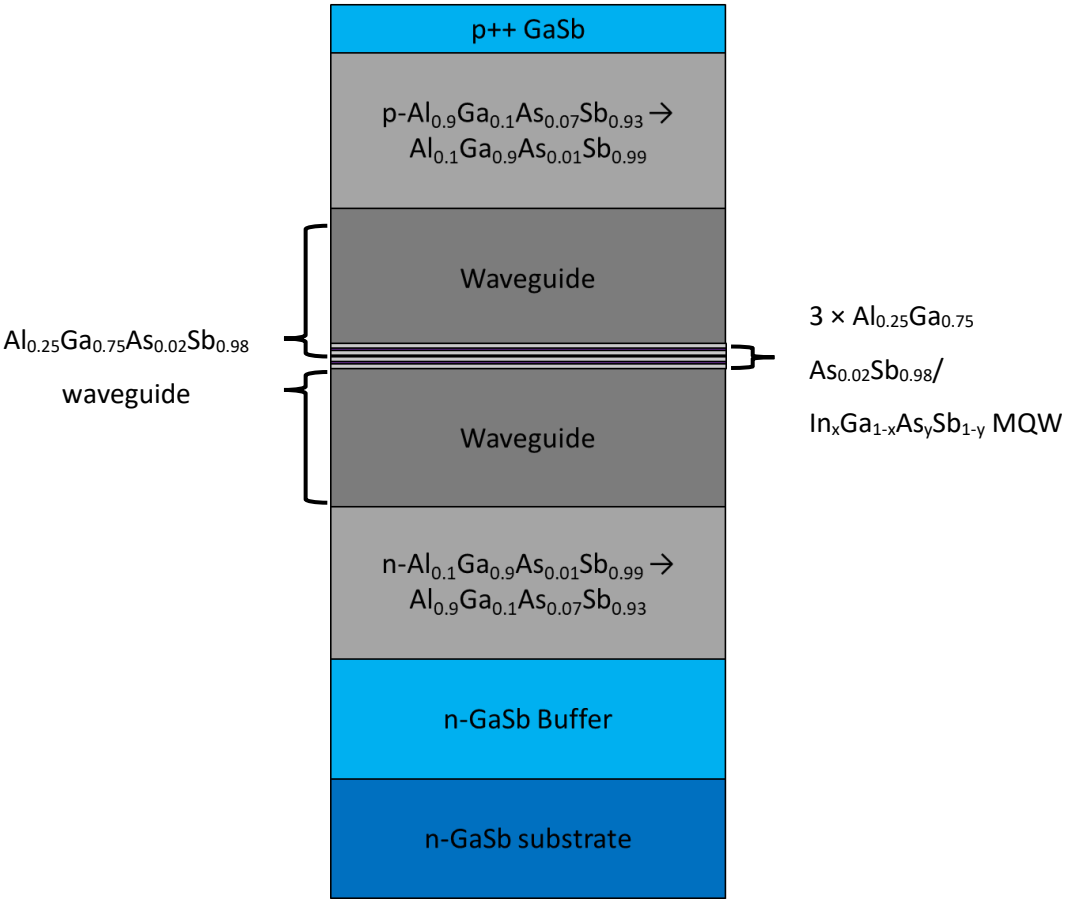

Figure 6.13: the schematic of the AlGaAsSb/InGaAsSb MQW LED including the buffer layer, cladding, waveguide and active region. The dopant of each level is shown too.

After this has been grown, the first stage of the n-AlGaAsSb graded cladding layer is grown, in this process, first, $Al_{0.1}Ga_{0.9}As_{0.009}Sb_{0.991}$ is grown. The As valve position and the Aluminium and

Gallium cell temperatures are then set such that $Al_{0.9}Ga_{0.1}As_{0.076}Sb_{0.924}$ is grown, this is done based on triple layer calibrations described in section 3.1.2. As the Gallium and Aluminium cells cool and warm respectively, the Arsenic valve is gradually opened, allowing a greater flux thus greater incorporation. The Ga and Al cooling and warming respectively over this time would be expected to create an approximately linear grading from $Al_{0.1}Ga_{0.9}AsSb$ to $Al_{0.9}Ga_{0.1}AsSb$, the increased As flux also increases approximately linearly along with the group-IIIs, allowing for a graded, lattice matched layer to be grown. The As flux increases as the As incorporation in the alloy to create lattice matched conditions to GaSb increases as the Al in the system is increased. This occurs over a period of 6 minutes, creating a 100 nm of grading. Allowing charge carriers to be injected from the GaSb substrate into the cladding more easily than using a stepped system with discontinuous energy levels. Once the cladding alloy is $Al_{0.9}Ga_{0.1}As_{0.076}Sb_{0.924}$ an additional 300 nm is grown. After this, the Gallium and Aluminium cells are set to grow an $Al_{0.25}Ga_{0.75}As_{0.02}Sb_{0.98}$ alloy along with the corresponding As valve set point. This is used to create a 500 nm waveguide before the MQW system is grown, as described in section 6.1.2.1. Following the active region, an additional 500 nm of $Al_{0.25}Ga_{0.75}As_{0.02}Sb_{0.98}$ waveguide is grown before the p-cladding is grown, doped with Be. This is done in the reverse manner to the n-cladding and at a substrate temperature of 530 °C. Following this, a 300 nm p++-GaSb contacting layer is grown at the same substrate temperature which is the final layer of the growth. To achieve this, the temperature of the Be cell is raised by ~ 7 °C, this temperature change of the Be cell was calculated based on dopant incorporation growths.

6.1.3.2 Structural characterisation

The device samples had their structures characterised using x-ray diffraction, with ω-2θ scans. These scans and their corresponding models can be seen in Figure 6.14 (a) and (b) for LED 6.1 and LED 6.2 respectively. The alloy composition of each device – as extrapolated from the model – can be seen in Table 6.3. This shows that Indium incorporation into the alloy was ~0.41 for both samples, with the Arsenic varying slightly between the two growths. Moreover, for LED 6.1, the single peak around that expected of the substrate implies that all of the material is lattice matched, there is some peak broadening implying this may not be exact. In LED 6.2, there is more acute peak splitting, with two central peaks (including that of the substrate itself). This is likely from a slight lattice mismatch in the growth of the $Al_{0.9}Ga_{0.1}As_ySb_{1-y}$ layers with one layer having y ~ 7.2 % as opposed to the 7.6 % required for lattice matching shown by the XRD model.

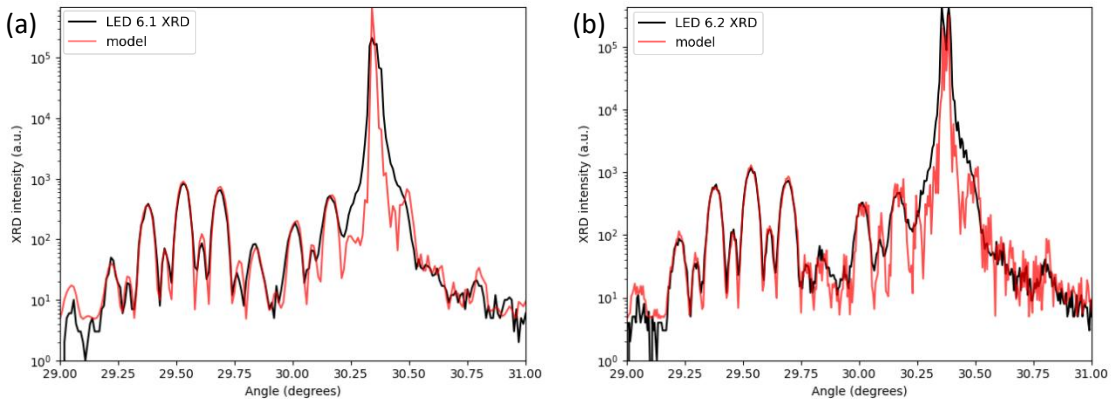

Figure 6.14: XRD scan and corresponding models for (a) LED 6.1 and (b) LED 6.2.

The satellite peaks which can be seen ~ 29.5° correspond to the strained QWs. These are less sharp than those seen in the PL samples in Figure 6.9. This is due to there being fewer QWs in the LED structure (three) in comparison to the PL structure (five), meaning there is less destructive interference between angles, causing broader peaks. Accounting for this, the peaks are well defined, meaning that the sample has good QW formation which should lead to high quality optical performance.

Sample	**$In_xGa_{1-x}As_ySb_{1-y}$**		**QW width / nm**
	x	**y**	
LED 6.1	0.41	0.183	13.2
LED 6.2	0.41	0.175	13.0

Table 6.3: the alloy contents of the type-I QW of the active region of the LEDs LED 6.1 and LED 6.2.

6.1.3.3 Fabrication

The two samples – LED 6.1 and LED 6.2 – were fabricated into 800 µm mesa structures using photolithography and wet-etching, the processes of which is outlined in section 3.4. The etchant which was used is shown in Table 3.3 with its corresponding etch rate. Thermal evaporation was used to apply Ti/Au contacts to the sample for a top-bottom contacting configuration. Part of each sample underwent thermal rapid annealing to see the effect on electrical performance of the device. Once all contacts were applied, the sample was cleaved and mounted onto headers which the top contact was wire bonded to, the final device structure can be seen in Figure 3.8 (b). The complete fabrication process can be seen in Figure 3.7.

6.1.3.4 Electrical testing

Once devices had been fully fabricated then mounted and bonded to TO headers, their electrical properties were tested; this was done for both annealed and unannealed devices. First, the current was measured as a function of forward and reverse bias of the device, the IV curves that this produced are shown in Figure 6.15 (a) and (b) for LED 6.1 and LED 6.2 respectively. The data shows two fully bonded devices for both annealed and unannealed samples. This data was taken using the methodology described in section Figure 3.8. From these curves, it is clear that LED 6.2 shows better electrical performance than LED 6.1 because under the same forward bias, a larger current is produced. Under a forward bias of +2 V, the current in LED 6.1 is ~ 10^{-2} A, whereas for LED 6.2, under the same bias, the current is ~10^{-1} A – for the annealed devices. This means that more charge carriers are flowing through the device under a similar bias, causing more recombinations for a lower input power. It should be noted that a lower resistance can imply that current is bypassing the active region and is not always a beneficial property. Although the two devices showed differing levels of electrical performance, they do both show good diode-like characteristics with a forward bias giving a current of around 10 to 100 times larger than that under reverse bias. It is assumed that there was no structural degradation during the annealing process because the annealing temperature was < 300 °C, which has been shown to not cause structural changes in GaSb based materials [202].

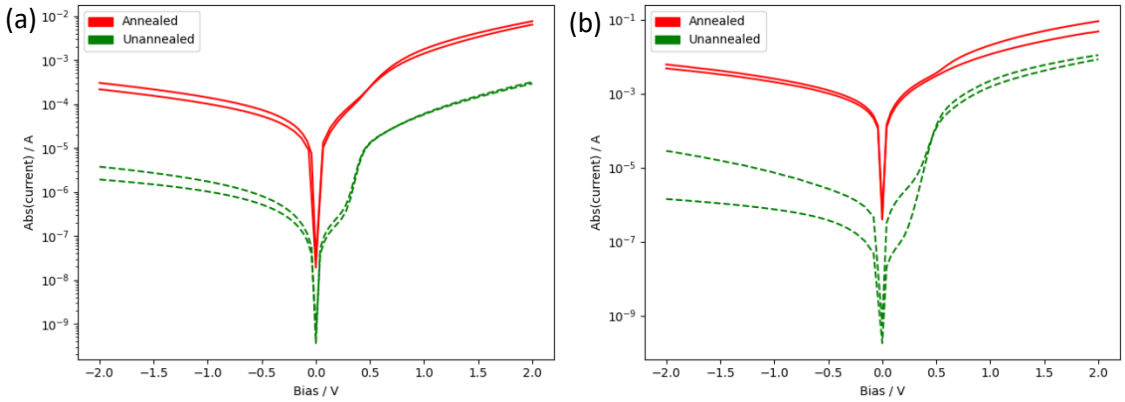

Figure 6.15: The current of two annealed and two unannealed bonded devices of (a) LED 6.1 and (b) LED 6.2 as a function of bias (IV curves).

Moreover, from Figure 6.15 it is also clear that when annealed, the current flowing through the device under a particular bias increases, this can be seen in the difference between the red and green lines on the graph. When considering the forward bias of the devices, annealing increased the current by a factor of ~ 100 for LED 6.1 and ~ 10 for LED 6.2. This process does however

increase the current achieved under reverse bias by a factor greater than when considering the forward bias, this leads to the device having worse diode-like characteristics.

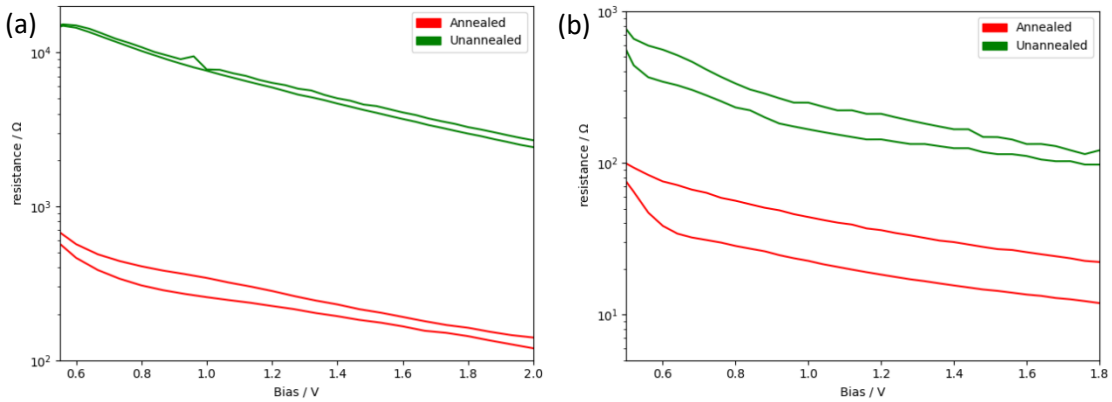

Figure 6.16: The resistance under forward bias (resistance) of the full fabricated and bonded devices (a) LED 6.1 and (b) LED 6.2.

The data shown in Figure 6.15 was analysed as outlined in section 3.5.2 to give the resistance of the device under forward bias. The resistance as a function of forward bias is shown in Figure 6.16 (a) and (b) for LED 6.1 and LED 6.2 respectively. As expected, this shows that as the forward bias is increased, the resistance decreases, this is due to the changing position of the energy bands in p-type and n-type doped regions with respect to one another, allowing charge carriers to move more freely. Furthermore, it is apparent that LED 6.2 has a lower resistance than LED 6.1 at a bias of ~ + 1.8 V. A resistance of around 10 Ω is achieved by LED 6.2, whereas LED 6.1 has a resistance of ~ 100 Ω – for annealed samples. The annealing process itself appears to decrease the resistance under forward bias by a factor of 10 as can be seen in the difference in the red and green like for annealed and unannealed devices respectively.

6.1.3.5 Electroluminescence

The temperature dependant electroluminescence was measured for both LED 6.1 and LED 6.2. The lower resistance – assuming the same output power – will increase the external efficiency of the device significantly so the devices from each sample with the lowest resistance was taken. EL spectra were taken at temperatures from 5 – 300 K for LED 6.2 using the EL setup descried in section 3.6, using an AC frequency of 1 kHz and a duty cycle of 10 % to avoid Joule heating. The spectra obtained can be seen in Figure 6.18 (a) and the corresponding bandgap – temperature relationship can be seen in Figure 6.18 (b) with a Varshni fit.

Power dependant spectra were also taken at low temperature (5 K) to verify the current recombination mechanisms, as discussed in section 2.2.2. The power dependant spectra can be seen in Figure 6.17 (a) and show the expected result of intensity increasing with driving current.

These stops increasing around 100 mA as Joule heating affects begin occurring, limiting the output intensity. No observable blue shift is seen in the low temperature current dependant spectrum, this is typical of type-I active regions.

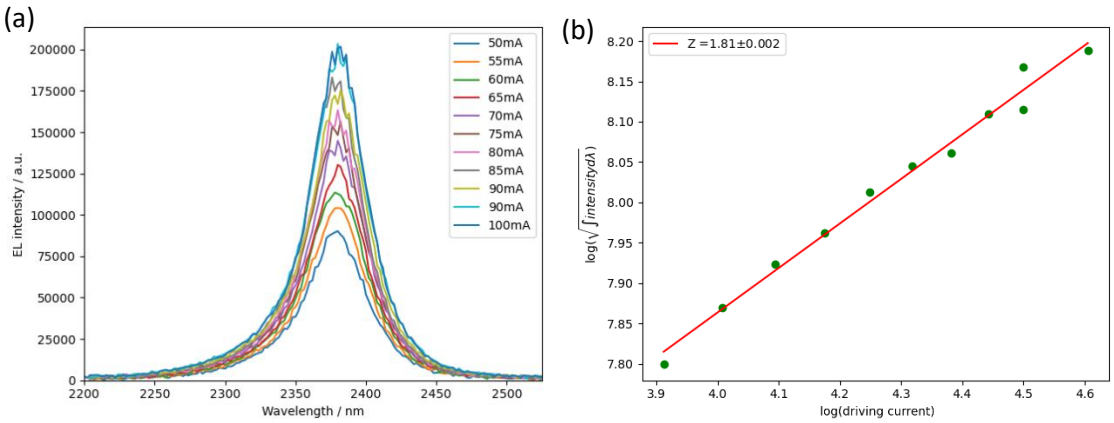

Figure 6.17: (a) the power dependent EL spectra at 5 K, with driving currents ranging from 50 - 100 mA with a driving current of 10 % and (b) the log(laser power) as a function of integrated emission spectra, with a linear fit which was used to calculate the Z-value.

The linear fit shown in Figure 6.17 (b), has a gradient of 1.81, shown as a Z value in the graph. This implies that the recombinations are dominated by radiative at this temperature, as would be expected. The non-radiative recombination current comes from SRH recombination, which is shown due to Z < 2. SRH recombination at low temperature would be expected because it is caused by trap states. Auger recombination is largely supressed at low temperature.

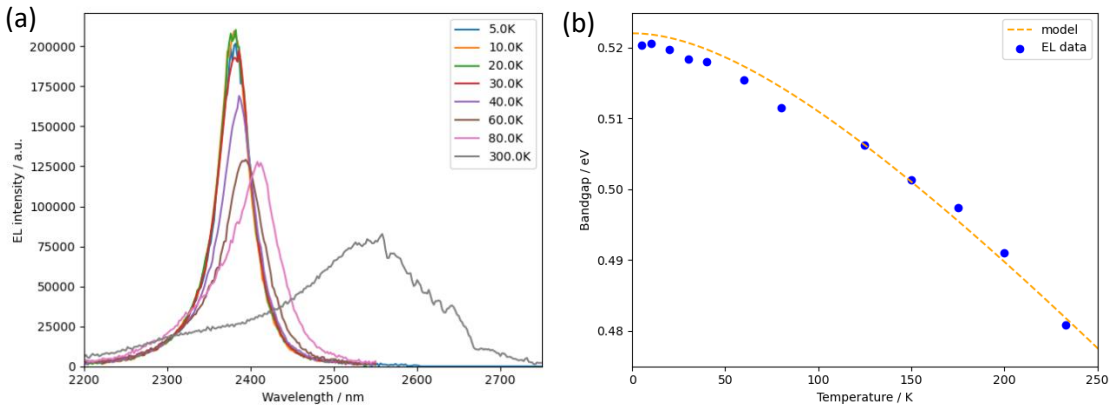

Figure 6.18: (a) the EL spectra of LED 6.2 at temperatures ranging from 5 - 300 K and (b) the bandgaps that this corresponds to at the range of temperatures with a Varshni fit with fitting values of $E_g(0)$ = 0.522±0.001 eV, α = (3.0±0.9)×10^{-4} eV/K and β = 170±90 K.

The temperature dependant spectra act as expected at low temperatures, this can be seen from the 5 – 60 K spectra, with relatively Gaussian peak shapes when accounting for noise. However,

the spectra at 80 K appears to be around the same intensity as that at 60 K but with a smaller bandgap – longer output wavelength. The bandgap obeyed the Varshni model from 4 – 300 K, this can be seen in the plot in Figure 6.18 (b), with the plot of bandgap as a function of the Varshni equation. The data was fitted using the SciPy "curve_fit" function with a user defined Varshni equation. A comparison of this curve fitted data and the interpolation of the given alloy can be seen in Table 6.4, showing that the β value fits within the error, however, the α value fits outside 1.5 times the given error. An interpolation of the bandgaps given in Vurgaftman is not given because that is for bulk materials, whereas here we have a quantum well. The mismatch in the interpolation and the data may also come from how the bandgap of a quantum well changes in comparison to the bulk.

	$E_g(0)$ / eV	α / eV K^{-1}	β / K
Extrapolation from EL data	0.522±0.001	$(3.0\pm0.9)\times10^{-4}$	172±90
Vurgaftman interpolation	N/A	4.53	157

Table 6.4: A comparison of the Varshni parameters from the extrapolation of the EL data and an interpolation of the parameters given in Vurgaftman [21].

Once at room temperature, the electroluminescence spectra of both devices were measured with driving currents between 50 – 105 mA. These spectra can be seen in Figure 6.19 (a) and (b) for LED 6.1 and LED 6.2 respectively. The wavelength of these devices is shorter than the PL samples which the active region was based on. This could be due to a drop-in arsenic and/or indium, an increase in the QW width, despite being grown with the same group-III base and tip temperatures and the same group-V bulk temperatures and valve positions. The peak wavelengths of both devices appear to be around 2700 nm for LED 6.2 and LED 6.1 respectively, with LED 6.1 having a slightly longer wavelength. The difference in wavelength between the devices is most probably due to the difference in active region, with LED 6.1 having a wider QW and higher As content in the InGaAsSb alloy. Both of these factors contribute to a narrowing of the bandgap, hence a longer emission. However, there is peak obfuscation due to the atmospheric absorption bands around ~2750 nm and ~2650 nm, along with the low intensity of the spectra, both of these make peak identification difficult. The actual peak wavelength could be higher than those shown here, but some of the spectra is not visible due to the aforementioned absorption bands. However, this can still be used to find a Z-value because an approximately equal amount of each spectrum is absorbed.

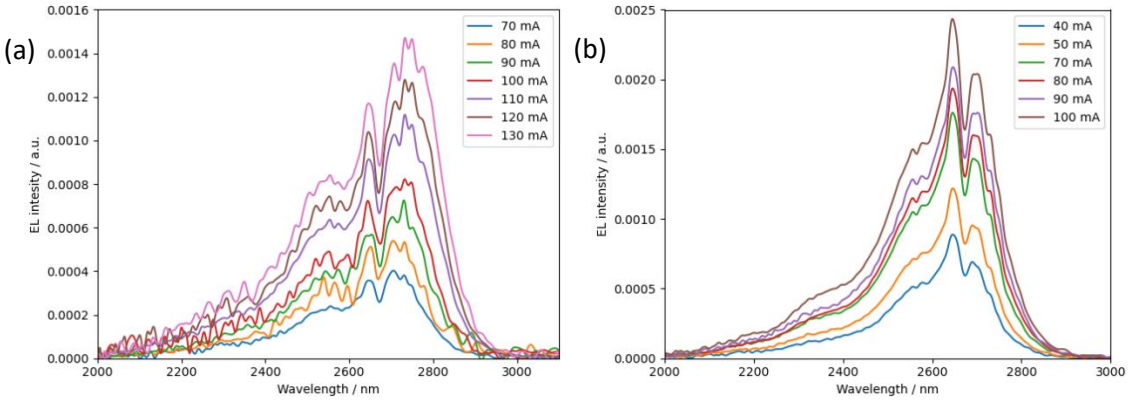

Figure 6.19: the driving current dependant EL spectra of (a) LED 6.1 and (b) LED 6.2, this was taken using a duty cycle of 10 % and AC frequency of 1 kHz.

Figure 6.19 (a) and (b) also shows that the peak intensity of LED 6.2 is almost twice that of LED 6.1, this can be seen when comparing the peaks of (a) and (b). This is likely due to the improved electrical performance of LED 6.2, allowing charge carriers to be injected into the active region with greater ease. When calculating the Z value from the power dependant spectra – as is shown in Figure 6.20 (a) and (b) – the Z values for LED 6.1 and LED 6.2 are 0.98 and 1.65 respectively.

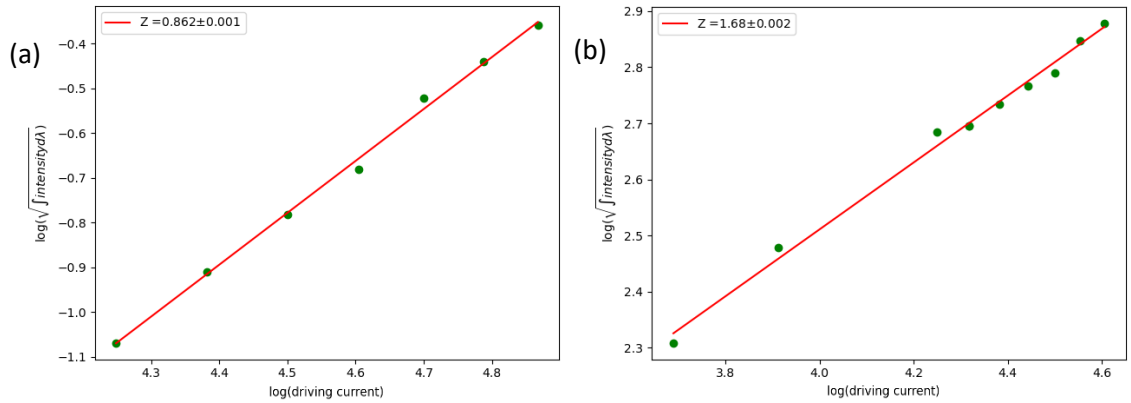

Figure 6.20: plot of the log of the driving current as a function of the log of the square root of the integrated intensity, with a linear fit to determine the Z value, for dominant recombination mechanisms for (a) LED 6.1 and (b) LED 6.2.

An increase in non-radiative recombination is expected at room temperature. This is confirmed by Figure 6.20 (b), which shows that at room temperature, the dominant recombination mechanism of the device is SRH, whereas at low temperatures it was radiative recombination – as was shown in Figure 6.17 (b). Further investigation would be required due to the input current range being less than an order of magnitude, it implies that there could be a trap state somewhere in the bandgap which is present at low and room temperature.

6.2. InGaAsSb/GaSb type-I structures

In order to further increase the room temperature peak wavelength of these type-I devices, the bandgap of the QW alloy must further be decreased. One way of doing this is to increase the indium and arsenic content in the QW. Moreover, to further increase the ease of integration into a resonant cavity structure, the use of GaSb barriers instead of AlGaAsSb barriers is investigated. GaSb can be used as a barrier when the indium and arsenic contents of the alloy are sufficiently high because the band edges are well contained within those of GaSb, creating the desired type-I structure. An example of this InGaAsSb/GaSb type-I band alignment can be seen in Figure 6.21 (a), simulated in Nextnano. This negates the need for the Aluminium and Arsenic cells during the barrier growth. The growth of this structure was previously studied by Sifferman et al. and their results are discussed in section 4.2.2. The GaSb provides less valence band confinement than the quaternary barriers discussed in section 6.1.2. This is compensated for by increasing the amount of indium in the well, which is further beneficial as it decreases the bandgap, allowing access to longer wavelength emission. In this, by decreasing the substrate temperature from 410°C to 350°C, they noticed an increase in the PL intensity of their samples, due to an increase in the miscibility of the material due to the addition of Indium.

6.2.1. Design

When designing the active region, one thing that must be considered is the decreased confinement when using GaSb as a barrier as opposed to $Al_xGa_{1-x}As_{1-y}Sb_y$. The decreased barrier potential means that there is a lower charge carrier confinement in the QW, because of this, it is preferable that $In_xGa_{1-x}As_{1-y}Sb_y$ alloy has a low bandgap. High indium content contributes to a smaller bandgap, as seen in Figure 6.4, as well as increasing the position of the valence band in relation to that of GaSb, therefore increasing the hole confinement potential. However, as seen in Figure 6.2, increasing indium in the $In_xGa_{1-x}As_{1-y}Sb_y$ alloy also decreases the critical layer thickness. Because of this decrease in critical layer thickness, the QW cannot be grown as thick as those demonstrated in LED 6.1 and LED 6.2, even with the addition of arsenic. Therefore, the intended active region would be 20 nm of GaSb followed by a 9 nm $In_xGa_{1-x}As_{1-y}Sb_y$ QW with x ~ 0.55 and y ~ 0.2, a schematic of this can be seen in Figure 6.21 (b). The values of strain that are produced by varying x and y in this system can be found in Figure 6.1 (b) with the corresponding critical layer thicknesses in Figure 6.2. The arsenic content is increased in comparison to the previous active regions to decrease the bandgap and increase the critical layer thickness. The alloy content and QW thickness would be tailored based on optical characterisation via

photoluminescence to optimise PL intensity and wavelength, with a desired output wavelength of ~ 3.3 µm.

6.2.2. Growth

MQW samples were grown on n-GaSb using the same initial outgassing and deoxidation processes as outlined in section 6.1.2.1 for the InGaAsSb/AlGaAsSb samples and in accordance with the MBE processes outlined in section 3.1. However, when growing these samples, rather than growing AlGaAsSb buffer regions, a 167 nm GaSb buffer was grown, followed by a 50 nm $Al_{0.9}Ga_{0.1}Sb$ barrier. This was grown to act as a partial reflective barrier when conducting photoluminescence to increase carrier collection in the active region. Following this, a further 333 nm of GaSb buffer was grown. This growth was done with a substrate temperature of 500 °C. All of this growth, and the following active region was grown at a rate of 1 µm h^{-1}.

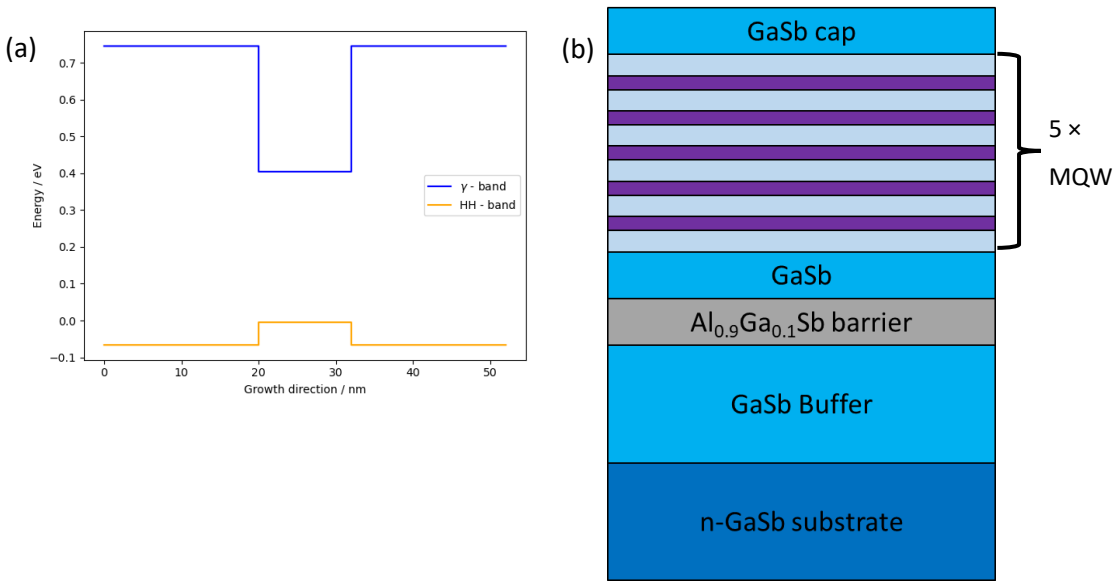

Figure 6.21: (a) A nextnano simulation of the γ-band and HH-band of a GaSb/$In_{0.55}Ga_{0.45}As_{0.165}Sb_{0.835}$ type-I quantum well and (b) a schematic for the GaSb/InGaAsSb MQW calibration/PL samples.

Once the growth of the buffer layer was complete, the growth of the active region could begin. Because the growth of $In_{0.55}Ga_{0.45}As_{0.2}Sb_{0.8}$ is around the miscibility gap of the alloy as previously discussed, the substrate temperature required to create a high quality, uniform alloy is lower than that of GaSb. This requires the substrate temperature to be reduced from the buffer growth, to grow both the GaSb barriers and the QW. Three different substrate temperatures were used when growing the system, these were: 400, 380 and 350 °C. The structural quality of the alloy would be analysed by the characterisation through XRD and optical performance through room temperature PL.

Once an initial 20 nm GaSb barrier had been grown, five repeats of the InGaAsSb QW and GaSb barrier are grown. To grow the GaSb barrier, the base temperature of the Gallium cell was ~900 °C, during the alloy growth this is reduced to ~850 °C. The QW was then grown using a reduced valve setting on the Sb cell to decrease the flux, compared to the growth of GaSb and with an additional As flux. The Gallium cell is then returned to the temperature required for the growth of GaSb and the next part of the barrier is grown. Once five QWs had been grown, a 50 nm GaSb cap is grown before the system is bought back down to temperature and the sample removed. The cell temperatures of Gallium and Indium are based on the growth rate calibrations accounting for the strain in the system too. Throughout the growth run, it is assumed that these group-III cell temperatures give constant group-III mixes in the alloy. Group-V mixes were based on an initial flux, mediated by the cell temperature and valve position, the alloy content that this resulted in would be determined by the XRD scan and modelling done after the growth. If this did not give the desired group-V mix, then the valve position of the cell would be changed. Generally, as these alloys were Sb rich, the Sb cell was kept at a constant valve position and the As cell would then have its valve position changed to increase or decrease the As flux as required for the desired alloy content.

To see the effect of substrate temperature on the miscibility of the InGaAsSb alloy, it was required that the same alloy be grown using different substrate temperatures. There are various challenges in doing this, largely relating to changing the substrate temperature affecting the rate at which group-V materials evaporate off of the substrate surface, varying the group-V incorporation in the alloy at different substrate temperatures. For constant group-III mixtures, as the substrate temperature is increased, the arsenic incorporation in the system also increases. This is due to antimony evaporating at higher temperatures and at a higher rate than arsenic. This did not seem to follow a linear relationship between As valve position and As incorporation over a variety of different substrate temperatures, with a constant As bulk temperature. In order to combat this, different As valve positions were used to compensate for the evaporation rate differences between As and Sb at different temperatures. Over the growth, the indium incorporation was also changed, this was done by changing the temperatures of the indium and gallium cells, to change the fluxes, but to keep the overall growth rate constant. Constant growth rate allowed QWs of approximately the same widths to be grown by keeping the growth time the same. Having a variety of QW widths would add another variable when characterising the material via XRD, meaning it would be more difficult to characterise the alloy content. Moreover, increasing the growth rate would likely decrease material quality which should be avoided.

6.2.3. Characterisation

Once the samples had been grown, they were first characterised via XRD and then by photoluminescence, in the same way which the previous AlGaAsSb/InGaAsSb samples were. This is to confirm the structure and emission of the samples, comparing the results to what was initially targeted.

6.2.3.1 Structural characterisation

The structural characterisation was carried out on the samples using XRD, this was to confirm that satellite peaks were present to check QW formation had occurred. Also, to confirm the alloy content and thickness of the various layers. XRD scans and their models of the samples grown can be seen in Figure 6.22 (a) – (f), the corresponding alloy contents are shown in Table 6.5, the QWs in this growth are around 9 nm.

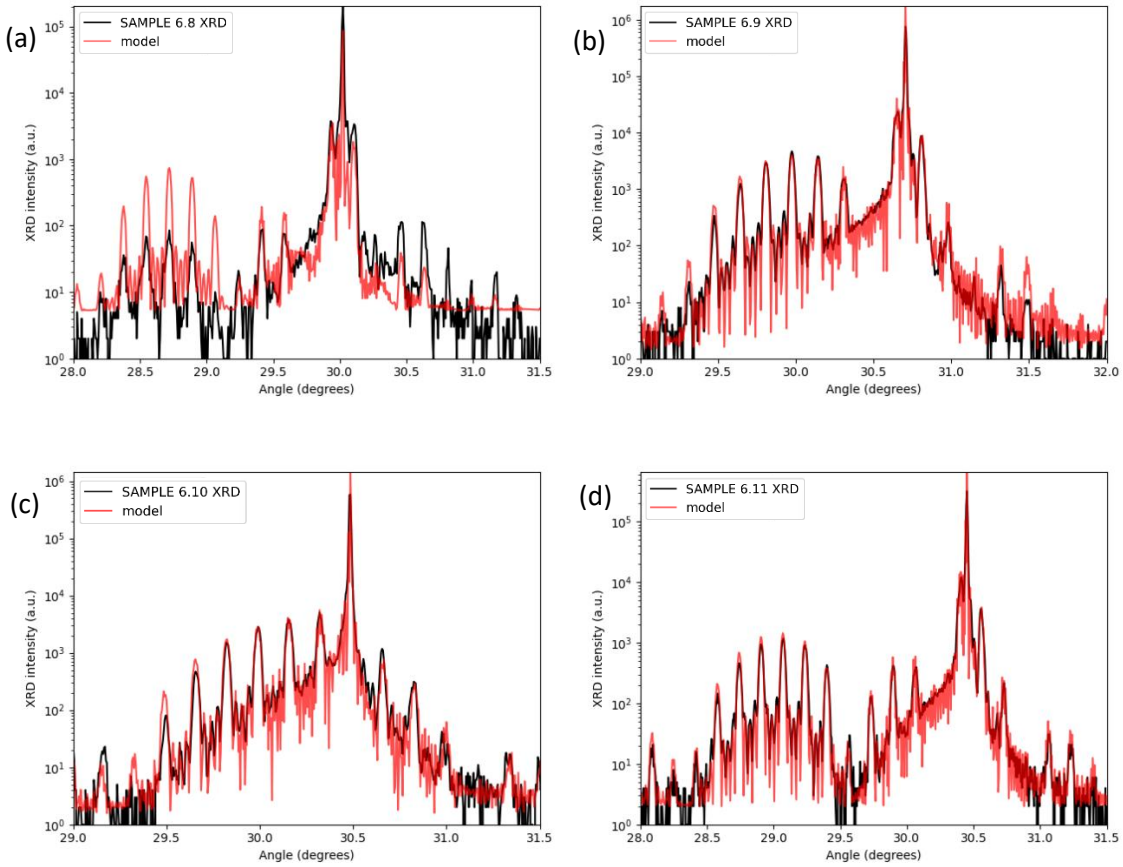

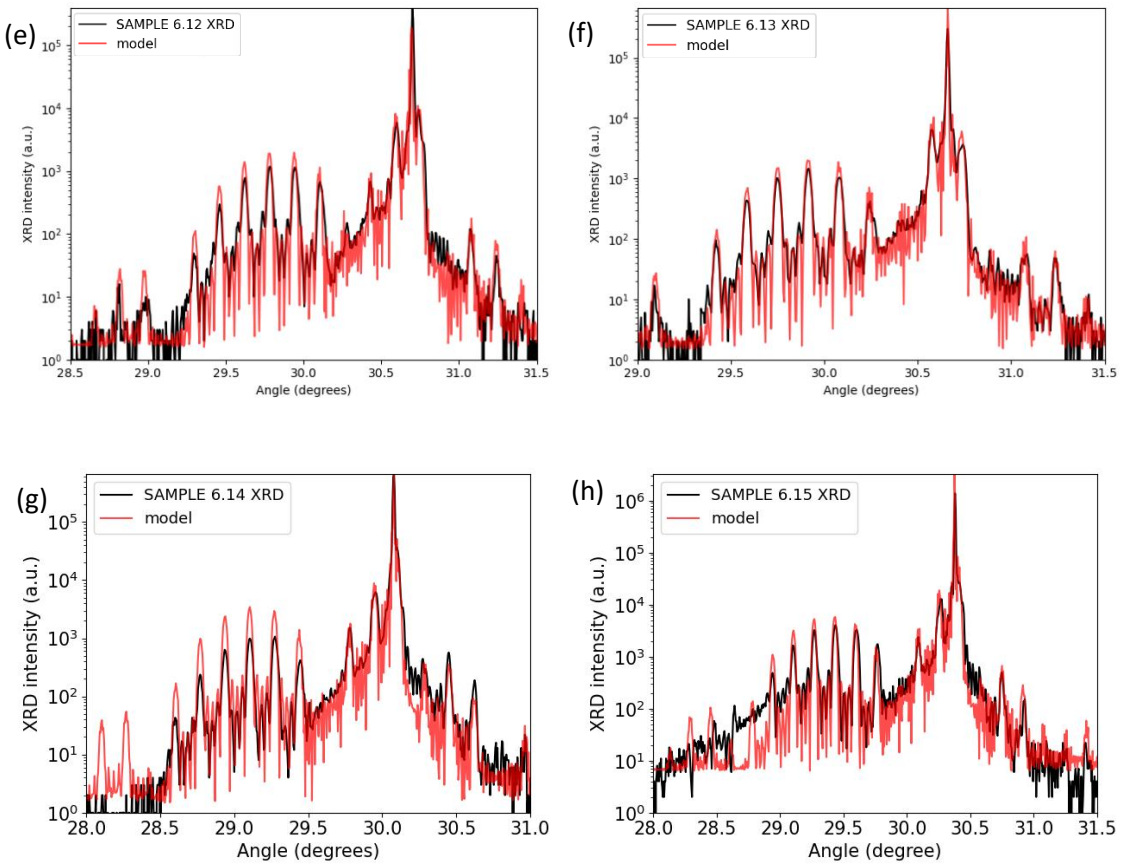

Figure 6.22: XRD scans and corresponding models for (a) SAMPLE 6.8, (b) SAMPLE 6.9, (c) SAMPLE 6.10, (d) SAMPLE 6.11, (e) SAMPLE 6.12, (f) SAMPLE 6.13, (g) SAMPLE 6.14 and (h) SAMPLE 6.15.

Table 6.5 shows that only samples grown using a substrate temperature of 400 and 380 °C had their room temperature PL analysed. This is because all of the samples grown at 350 °C have very poor-quality satellite peaks and did not display room temperature PL emission, implying that QW formation did not properly occur. The poorer quality of XRD can be seen in Figure 6.22 (g) and (h) which shows the scan and model of samples 6.14 and 6.15, both of which were grown with a substrate temperature of 350 °C, this is likely due to a mis-aiming of Arsenic, leading to growing non-optimally in the miscibility gap. Growing at 350 °C should have given better PL signal for a sample, as was shown by Sifferman [83]. Over the range of substrate temperatures, despite the calibration of As and Sb valve positions, it was not possible to grow the exact same alloy contents of the QWs at the different temperatures. However, upon inspection, the satellite peaks of the samples which were grown are well defined, implying good quality QWs with abrupt barriers. The indium content of the QWs was varied between 0.500 – 0.584 and the antimony between 0.835 – 0.693. Despite the growth of a 50 nm $Al_{0.9}Ga_{0.1}Sb$ layer below the active region – which is not lattice matched to GaSb – there does not appear to be any significant extra peaks

from this layer. This implies that this layer is grown close enough to lattice matched that it will not cause any relaxation in the sample.

Sample	$In_xGa_{1-x}As_{1-y}Sb_y$		Substrate temperature / °C
	x	y	
SAMPLE 6.8	0.540	0.835	380
SAMPLE 6.9	0.500	0.742	380
SAMPLE 6.10	0.500	0.682	400
SAMPLE 6.11	0.500	0.884	380
SAMPLE 6.12	0.584	0.693	380
SAMPLE 6.13	0.584	0.660	400
SAMPLE 6.14	0.584	0.757	350
SAMPLE 6.15	0.584	0.729	350

Table 6.5: the alloy contents of samples: SAMPLE 6.8, SAMPLE 6.9, SAMPLE 6.10, SAMPLE 6.11, SAMPLE 6.12, SAMPLE 6.13, SAMPLE 6.14 and SAMPLE 6.15, this is according to the modelling of the XRD scans shown in Figure 1.23.

6.2.3.2 Photoluminescence

Once the samples had been characterised via XRD and had their structures modelled, they had their room temperature PL spectra taken. Room temperature PL was measured using the experimental setup described in section 3.3. The normalised spectra for the samples described in Table 6.5 can be seen in Figure 6.23 (a). Showing that the samples have emission peaks ranging from ~ 2500 – 3400 nm, with SAMPLE 6.11 having the shortest wavelength emission and SAMPLE 6.13 having the longest. The data for SAMPLE 6.9 and SAMPLE 6.10 is obfuscated by the water vapour peak from ~ 2650 – 2850 nm which is highlighted in red on the figure, there is a further absorption peak ~ 2600 nm, causing a slight dip in the spectra.

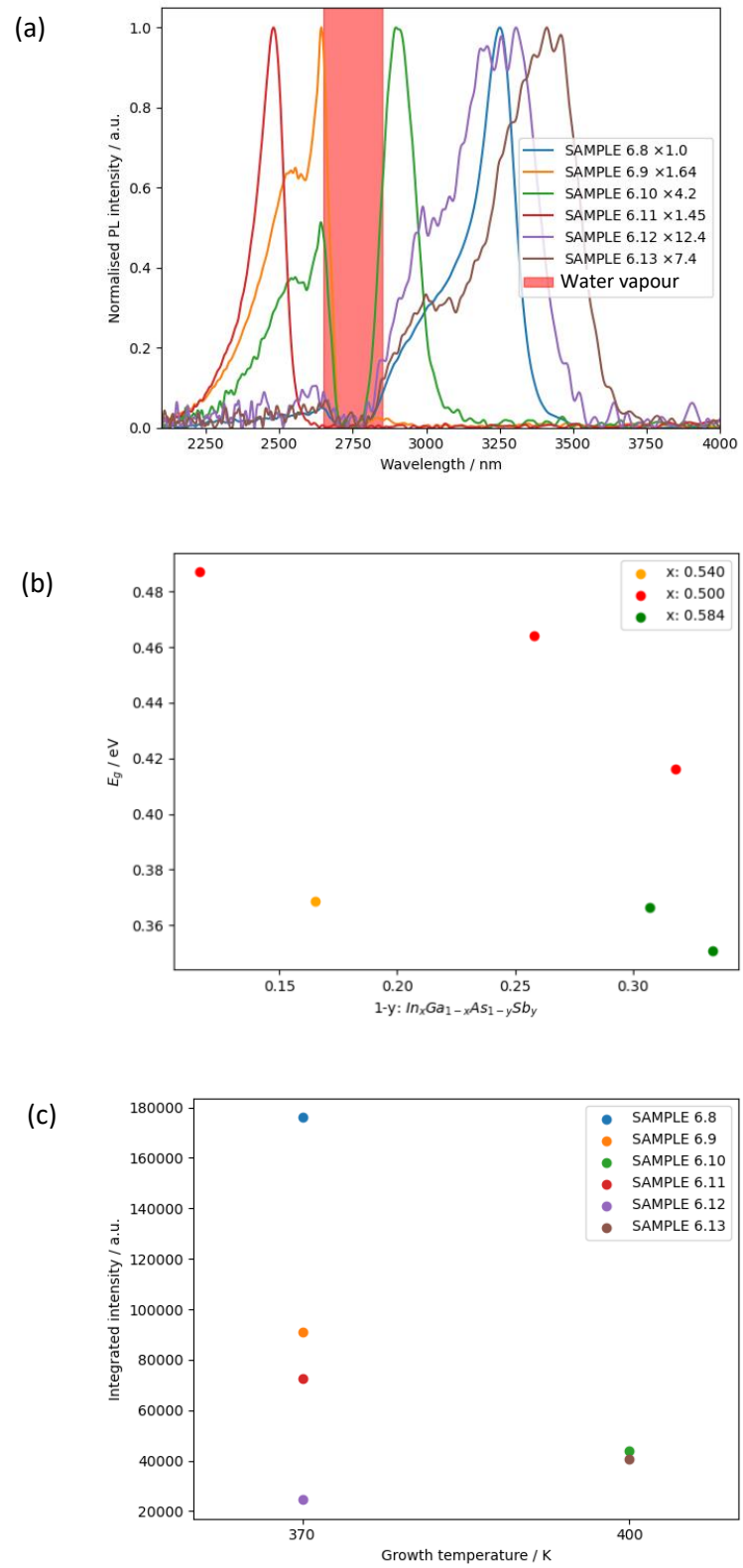

Figure 6.23: (a) the normalised room temperature PL spectra of the InGaAsSb/GaSb samples grown and displayed in Table 6.5, the CO_2 absorption peak is also highlighted to make the peaks clearer; (b) the corresponding bandgaps as a function of alloy content and (c) the integrated intensity of samples as a function of their growth temperature.

The bandgaps corresponding to the PL peaks shown in Figure 6.23 (a) are plotted as functions of their alloy content in Figure 6.23 (b). This shows that as a general trend, when the As content of the alloy is increased whilst holding all other variables constant, this decreases the bandgap, shown for In contents of 0.500 and 0.584. It also shows that as the indium is increased, the bandgap decreases. This is also an expected result which has been shown in simulations and with other samples described in this chapter.

However, because the bandgap of SAMPLE 6.8 is around the same as those with much higher indium and arsenic contents, it implies that there could be a fault in its structural characterisation. The QW of this device could be thicker than those of the other ones, i.e. greater than 9 nm. The trends shown in this graph do however imply that it is possible to obtain emissions around 3300 nm using this material system, which is required for the detection of C-H bonds in plastics. With samples: SAMPLE 6.8, SAMPLE 6.12 and SAMPLE 6.13 falling within this wavelength range. Comparing the relative PL intensities in Figure 6.23 (a) to the substrate temperatures during the active region growth, it is clear that those which were grown at 370°C display a greater PL intensity that those grown at 400°C. This can also be seen in Figure 6.23 (c), which the integrated intensity of those samples grown at 370°C in comparison to those grown at 400°C. However, as well as the XRD of those grown at 350°C having poor satellite peaks, there was also no PL observable at room temperature. The lack of PL at 350°C is likely due to an increase in the As content of the QW as discussed in section 6.2.2 rather than the temperature negatively affecting the miscibility of the intended QW alloy. Although SAMPLE 6.12 and SAMPLE 6.13 give spectra which is in the desired wavelength range the spectra are about five times weaker when not normalised compared to the other samples. This could be due to the alloy being at a point in the miscibility gap, causing non-uniform alloy, which often gives poorer quality emission as experienced by these in comparison to other samples.

As was done in section 6.1.2.3, the power dependant PL spectra of the brightest samples were analysed to determine the dominant recombination mechanisms of MQW systems of this type, using the same analytical method.

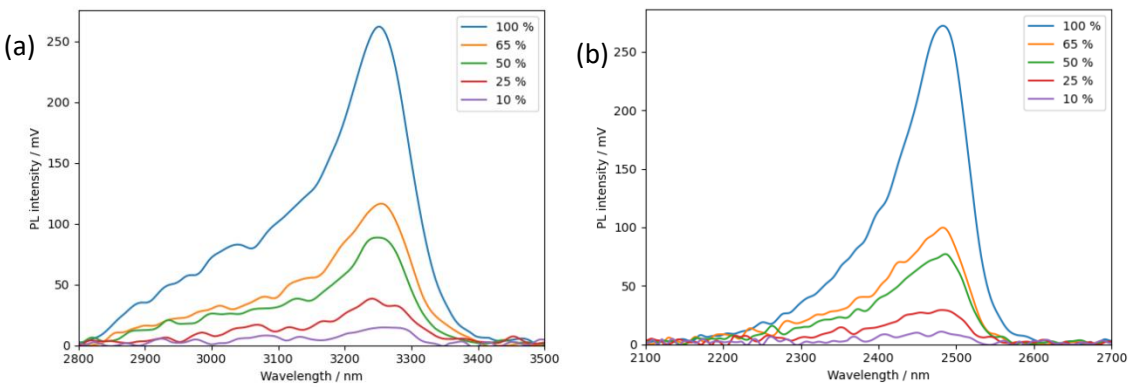

Figure 6.24: room temperature power dependant photoluminescence spectra, using laser powers of 100 %, 65 %, 50 %, 25 % and 10 % for (a) SAMPLE 6.8 and (b) SAMPLE 6.11.

The power dependant room temperature PL can be seen in Figure 6.24 (a) and (b) for samples SAMPLE 6.8 and SAMPLE 6.11 respectively. It should further be noted that SAMPLE 6.8 gave some of the brightest PL emission of a sample grown at Lancaster. This can be seen in the power dependant PL as it is brighter than SAMPLE 6.11 which has a smaller bandgap – this should increase the output power, as shown in Figure 4.15. This shows the expected trend for both samples, with decreasing laser power giving spectra of decreasing intensity. The high energy "tails" of the spectra are larger in these samples than in those with AlGaAsSb barriers. This could be due to a smaller valence band confinement energy, which is exacerbated at higher temperatures.

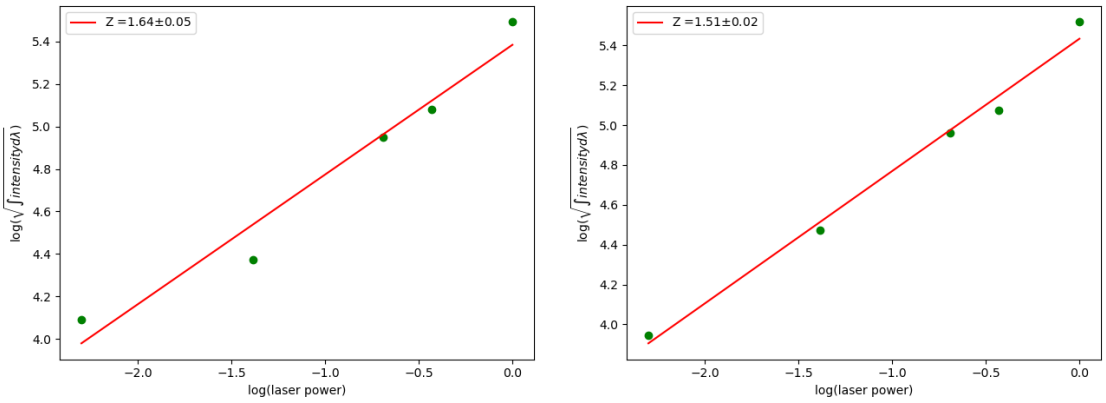

Figure 6.25: the log input laser power as a function of the log of square root of integrated spectral intensity with a linear fit which has its gradient shown as Z for (a) SAMPLE 6.8 and (b) SAMPLE 6.11.

Moreover, no noticeable blue shift can be seen with increasing laser power, which is characteristic of type-I devices, confirming the structures of samples both have the expected bandgap alignment. This is important because with certain InGaAsSb alloys with high In and As, a type-II alignment can be created with GaSb. When considering the dominant recombination

mechanisms, Figure 6.25 (a) and (b) show that SAMPLE 6.8 and SAMPLE 6.11 have Z values of 1.64 and 1.51 respectively. This implies that they both have radiative recombinations as their dominant recombination mechanisms. But whereas samples with AlGaAsSb barriers had very little non-radiative recombination rates, the samples with GaSb barriers seem to cause higher rates of SRH recombination at room temperature, as Z < 2. Suggesting that the difference in barrier material causes trap/defect states in the active region. Another contributing factor to this could also be the QW material, as if defects occur – which is more likely because of the growth in the miscibility gap – this could contribute to SRH recombinations. It should be noted that the data points from 100 – 10 % laser power do not show a perfectly linear relationship as was modelled to obtain the Z-values. This is somewhat due to the increased noise of the PL signal as the laser power is decreased, these points were included in the final analysis as they allow for the data to be analysed over one-order of magnitude of input laser power. The decreased accuracy of the measurement still allows for better analysis than using data over less than an order of magnitude.

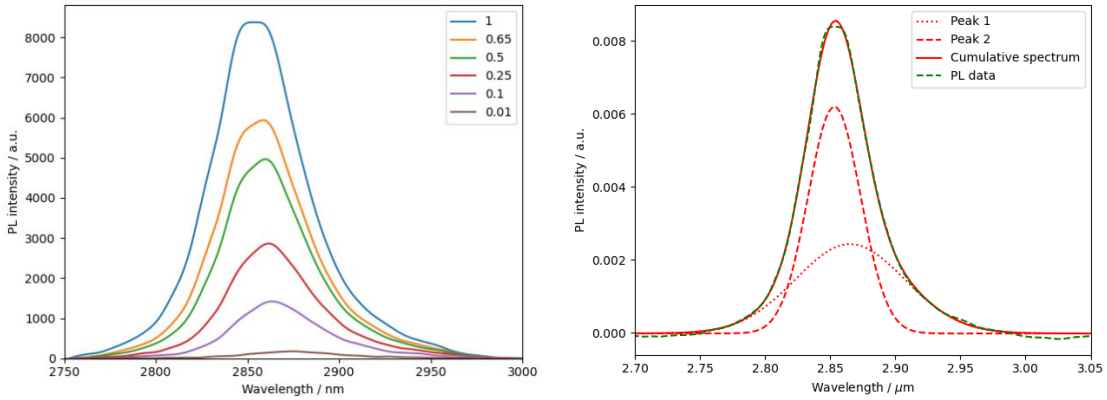

Figure 6.26: (a) the power dependant PL spectra of SAMPLE 6.8 taken at 4 K using various laser powers, shown in the legend and (b) a deconvolution of the PL spectra using laser power of 65% showing two clear peaks.

The PL spectrum for SAMPLE 6.8 was also taken at 4 K using the same set-up, and with a liquid helium cooled cryostat as described in section 3.3. The spectra were obtained using laser power ranged from 100 % - 1 % using neutral density filters; the results are displayed in Figure 6.26 (a). Unlike the spectra at room temperature, which show one central peak, with some high energy peak with a much lower intensity. At low temperature, it seems that there is one single peak which appears to be made up of several Gaussian peaks. This implies that the spectrum is caused by several different charge carrier recombinations from different energy levels, as opposed to just one at room temperature.

Figure 6.26 (b) shows the deconvolution of the peaks, this was done using Origin's multipeak analysis tool, showing that there are two recombinations which cause the PL spectra. The centre of these spectra are at 0.434 eV for peak 1 and 0.432 eV for peaks 2. Because the holes are confined in the heavy-hole band, which has minimal confinement, confirmed by Nextnano simulation, there cannot be a hh_2 energy level. This can be seen in Figure 6.27, whereby the two electrons are confined in the gamma band, then the lowest energy level hole is confined in the heavy-hole and the second lowest is confined in the light hole band, which is type-II.

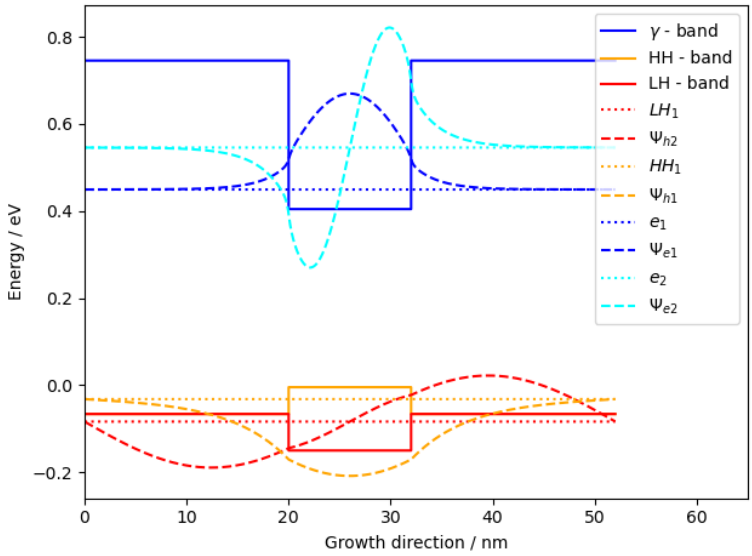

Figure 6.27: Nextnano simulation of the energy levels in the InGaAsSb/GaSb MQW showing the two electrons confined in the conduction band, one hole in the heavy-hole and another hole in the light-hole band.

Moreover, due to band splitting because of the strain on the system, the light-hole energy level (lh_1) is confined in the GaSb barriers, leading to a type-II confinement. The type-II transition in this material systems is highly unlikely due to the strong confinement of the electrons in the InGaAsSb region leading to a very low wavefunction overlap. Because of this, it is evident that one of the transitions responsible for the two peaks come from e_1-hh_1, and the second coming from an unidentified transition corresponding to 0.342 eV. The sample's spectrum is still much brighter at low temperatures in comparison to room temperature. This implies that although at points, non-radiative recombination mechanisms are the almost the dominant recombination path, there is still high rates of radiative recombinations occurring to create a bright spectrum. The samples grown with a substrate temperature of 380°C were shown to have the brightest PL intensity of the InGaAsSb/GaSb MQW structure, in comparison to those grown at 400°C. This is in-line with the findings of Sifferman et al [83]. Samples grown at 350°C were not grown with QW formation good enough to see room temperature photoluminescence. This likely is due to

the As incorporation being too high, confirmed by XRD scans and poor satellite peak quality as previously discussed.

6.3. Summary

In this chapter, the use of $Al_zGa_{1-z}As_wSb_{1-w}/In_xGa_{1-x}As_{1-y}Sb_y$ type-I MQW systems for the active region of a LED was investigated. Through simulating lattice constant of alloy contents of $In_xGa_{1-x}As_{1-y}Sb_y$ it was possible to find a map of the strain available by varying x and y, showing that strains between -0.03 and 0.03 are available for $0.00 < x < 0.60$ and $0.65 < y < 1.00$. Furthermore, the Matthews-Blakeslee and People-Bean critical thickness equation were utilised to see the maximum thickness at which the alloy could be grown before relaxation occurs. Showing that the alloy can be grown anywhere from 1 – 100 nm thick without relaxation occurring depending upon the alloy content. Nextnano was utilised to show that as x is increased in the $In_xGa_{1-x}As_{1-y}Sb_y$ alloy, the bandgap becomes smaller and as y is decreased, the same effect occurs, for a QW of set width. Moreover, it was shown how the width of the QW can reduce the size of the bandgap by around a third by going from a 5 nm to 15 nm QW. Finally, Nextnano was used to demonstrate that decreasing z in $Al_zGa_{1-z}As_wSb_{1-w}$ whilst keeping the alloy lattice matched to GaSb can decrease the bandgap slightly.

Through the growth of $Al_zGa_{1-z}As_wSb_{1-w}/In_xGa_{1-x}As_{1-y}Sb_y$ type-I MQW samples on n-GaSb substrates with $z = 0.35$, $w = 0.034$, $x = 0.34$ and $0.032 < y < 0.112$ with a 9 nm QW, the emission wavelength through PL can be varied between $2.2\ \mu m < \lambda < 2.7\ \mu m$. Then, by increasing x to 0.4, y to 0.124 and increasing the QW thickness to 15 nm, emission of ~ 2.8 µm can be obtained. This was displayed in section 6.1.2.3 through samples: SAMPLE 6.1, SAMPLE 6.2, SAMPLE 6.3, SAMPLE 6.4 and SAMPLE 6.5. By using $z = 0.25$ with $w = 0.02$ for lattice matched barriers, with $x = 0.4$ and $y > 0.12$, room temperature emissions around 3.0 µm can be obtained by using QW thicknesses ~ 14 nm, as displayed in section 6.2 with SAMPLE 6.6 and SAMPLE 6.7. These samples have high rates of radiative recombination at room temperature, evident by Z ~ 2 which was calculated from power dependant PL analysis. However, this is not conclusive due to the range of input laser powers which were used and the level of noise in the spectra taken with lower laser input powers. These active regions were utilised in LEDs which gave good electrical performance, and room temperature electroluminescence spectra with peaks around 2700nm, as shown by LED 6.1 and LED 6.2 in section 6.1.3. However, electrical pumping of the devices gives poorer spectra than optical pumping of the PL samples, with higher rates of non-radiative recombination at room temperatures.

This was developed upon, to create active regions for MQW samples with GaSb barriers. Utilising higher As flux during growth to increase the As incorporation in the alloy. Several MQW samples were grown with $0.50 < x < 0.59$ and $0.65 < y < 0.85$ with 9 nm QWs, as shown in section 6.2.3.1. These samples gave room temperature emissions with bandgaps varying from $2.5\ \mu m < \lambda < 3.4\ \mu m$ with sample SAMPLE 6.8 giving some of the brightest PL of a sample grown at Lancaster. It was found that substrate temperatures between 380 – 400 °C were best for growing uniform alloys, this reduction in temperature helps growing this alloy in its "miscibility gap". Although these longer wavelengths were achieved, they showed poorer rates of radiative recombination, whereas the samples with AlGaAsSb barriers were dominated by radiative recombination at room temperature, the introduction of GaSb barriers appeared to increase the prevalence of SRH recombination.

These GaSb-InGaAsSb MQW systems were then integrated into LEDs. Although the MQW themselves gave room temperature photoluminescence, they were not successfully integrated into LEDs. This was due to complications in the growth regarding Arsenic incorporation in the AlGaAsSb graded cladding. Despite this, the room temperature photoluminescence of these samples shows that in future, they could be integrated into a device using a different structure, such as stepped instead of graded cladding or into an RCLED.

7. Type-II InAs/$InAs_{1-x}Sb_x$ Strain Balanced Superlattices

Type-II InAs/$InAs_{1-x}Sb_x$ structures have been studied extensively in the past. This is due to their tuneable bandgap, as well as their SRH and Auger quenching mechanisms, giving them a high proportion of radiative recombinations in comparison to other structures. In this chapter, strain-balanced InAs/$InAs_{1-x}Sb_x$ superlattices grown on GaSb and their implementation into light emitting diodes is investigated, targeting ~ 4 µm, for the application of CO_2 detection. In previous literature, high Sb superlattice systems have been studied, as well as lower Sb MQW, as discussed in section 4.2.3. High Sb superlattices have shown the ability to emit ~ 5 µm at room temperature. However, studies have not been conducted in the lower Sb region for the strain balanced system. Lower Sb would correspond to a shorter wavelength, so studying this material system would allow the low wavelength limit to be realised, which would open up new applications to the system. This would allow for a shorter wavelength room temperature LED to be created with the benefits which come with the InAs/InAsSb material system. The design of the superlattice will be discussed, including bandgap modelling and the conditions which were used for strain balancing. Samples grown for strain-balancing calibration were analysed using low temperature (4 K) PL, this allowed the dominant recombination mechanism to be identified. Finally, the implementation of the strain-balanced superlattices into a light emitting diode will be discussed, as well as an analysis of the low and room temperature EL spectra.

7.1. Design

In order to obtain strain balancing, a model must be created which accounts for the strain provided by the epitaxial InAs and $InAs_{1-x}Sb_x$ layers on the GaSb substrate. The lattice constants of GaSb, InAs and InSb are shown in Table 7.1.

Material	Lattice constant / Å
GaSb	6.0959
InAs	6.0583
InSb	6.4794

Table 7.1: the lattice constants of GaSb, InAs and InSb. Data from Vurgaftman (2001) [21].

Because InAs has a smaller lattice constant than GaSb, it provides tensile strain on the structure, as discussed in section 2.3.2. According to Vegard's law – discussed in section 2.3.1 – $InAs_{1-x}Sb_x$ will be lattice matched to GaSb when x = 8.93 %. Then, as InSb has a higher lattice constant than GaSb, when x > 8.93 % InAsSb will provide compressive strain on the system – creating strain in the system opposite to that which is caused by InAs. Each monolayer of epitaxial material will then provide this strain, so a multiple of the number of monolayers of each material, with the strain provided should be balanced on each side. The relation which balances these strains is shown in equation 7.1, where ϵ is the strain of the material on a GaSb substrate and ML_A is the number of monolayers of material A. If this equation is satisfied, then the system is strain balanced.

$$\epsilon_{InAsSb_x} \times ML_{InAsSb_x} = \epsilon_{InAs} \times ML_{InAs} \qquad 7.1$$

If the system is strain balanced, this gives the advantage of being able to grow an active region with no net strain, meaning that relaxations will not occur in the material, making it free of defects of this nature. The problem of relaxation in active regions with relatively high level of Sb has been reported before in MQW structures, due to the net strain causing relaxation due to the thickness exceeding that of the material system, strain balancing is a way to combat this.

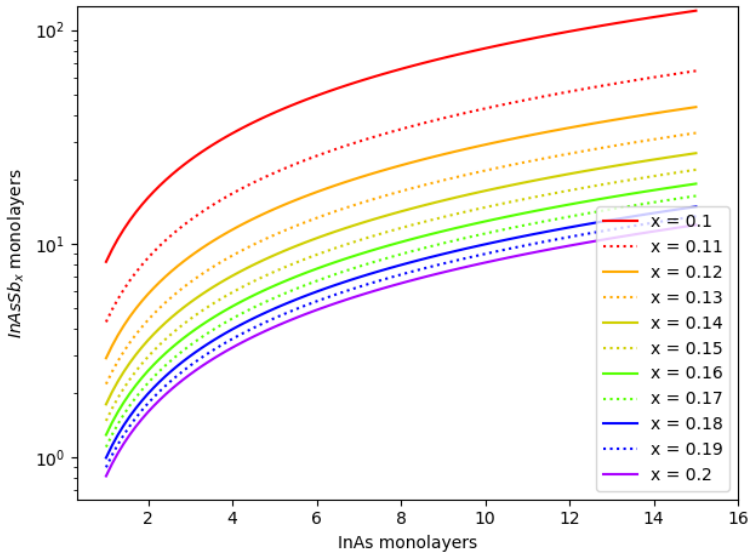

Figure 7.1: The number of InAsSb monolayers for given Sb contents (x) as a function of the number of InAs monolayers in an InAs/InAsSb structure grown on GaSb substrate.

Equation 7.1 was used to simulate the number of InAsSb monolayers which are required to be grown for a given number of InAs monolayers for Sb contents from 10 – 20 % to create the strain balanced conditions. The results of simulating this equation can be seen in Figure 7.1, showing

the strain balancing relation of the material system. As the Sb in the InAsSb increases, fewer InAsSb monolayers are required to create a strain balanced system. This is because each layer provides more strain to counteract the opposite strain of the InAs due to them having a larger lattice constant. The Python 3.0 script used to simulate equation 7.1 and generate Figure 7.1 can be found in the GitHub link in section 9.3.

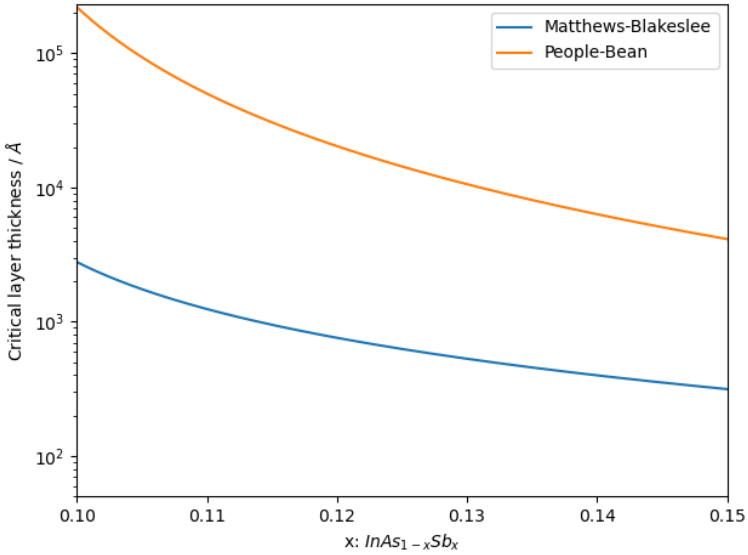

Figure 7.2: The critical layer thickness of $InAs_{1-x}Sb_x$ grown non-strain balanced on GaSb according to the Matthews-Blakeslee and People-Bean models (blue and orange lines respectively).

When growing $InAs_{1-x}Sb_x$ on GaSb, one concern was that before the system is fully formed, it is not strain balanced, so defects could occur due to relaxation from layers being grown over the critical layer thickness. Figure 7.2 shows the critical layer thickness of $InAs_{1-x}Sb_x$ with $0.10 < x < 0.15$ according to the Matthews-Blakeslee and People-Bean models. This shows that even the lowest estimates put the critical layer thickness of InAsSb with 12 % Sb at ~ 100 nm, which is much thicker than epitaxial layers which would be grown as part of a superlattice. Because of this, critical layer thickness of InAsSb will not affect the performance of a SLS from the growth process.

When considering low Sb InAsSb, the structure should contain around 11 % Sb. Using this initial design characteristic, it is possible to find the structures which could be grown strain balanced, as well as checking the strain balancing of the structures which are grown. This is extremely useful when creating an initial design to be grown, as it is possible to see how thick as layer of InAsSb is required to create the correct ratio of InAs to InAsSb in the SLS for a specific Sb content.

7.2. Band-structure modelling

In order to properly tailor the bandedges and bandgap characteristics of InAs/InAsSb strained layer superlattices, it is important to have a working bandgap simulation of the superlattices. To do this, the bandedges were simulated using the Krijn model as discussed in section 2.3 with input parameters taken primarily from Vurgaftman's summation of the literature [21]. Bowing parameters for the conduction and valence bands of InAsSb were taken from the simulations based on InAs/InAsSb MQWs grown on InAs substrates by Keen et. al. [203]. The charge carrier energy levels and wavefunctions were approximated using the k·p 8-band method as described in section 2.5. This simulation is carried out in Nextnano, which applies all of the above methods to give a simulation which outputs bandedges, charge carrier energy levels and charge carrier wavefunction.

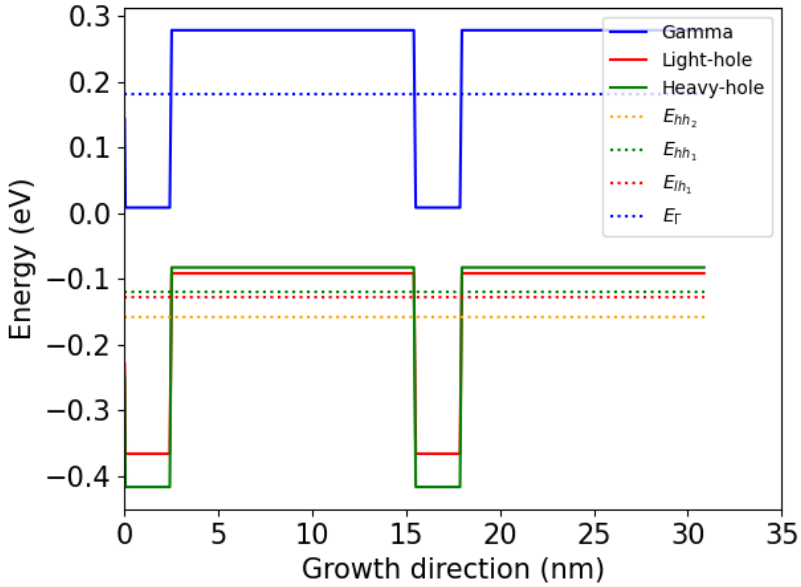

Figure 7.3: An example of the bandstructure simulated using Nextnano as described above showing the three highest energy hole state energy levels in the valence band and the electron energy level in the conduction band at low temperature (10K).

The simulated band structure and energy levels for the electron, heavy-holes and light-holes can be seen in Figure 7.3. This is a simulation for a strain balanced system with InAs layer thickness of 2.46 nm and Sb content in the InAsSb layer of 0.106. Here, three hole states were calculated and on electron state, which can be seen in the dotted lines in Figure 7.3. The three hole states in ascending order of energy from the valence band edges are: first-order heavy-hole (hh_1), first-order light-hole (lh_1) and second order heavy-hole (hh_2). The light-hole and heavy-hole state being very close together is caused by the slight splitting of the bands due to the strain in the system. As discussed in section 2.3.2, strain causes the hole level in the valence band to split,

this is seen acutely in strained type-I QWs where the systems are strained ~ 1 %. However, in this system, the strain on each layer is much lower, so when the band splitting occurs, so the splitting between the light and heavy holes is less acute.

As mentioned above in section 7.1, when InAs/InAsSb structures are grown on GaSb, it is most beneficial to grow them strain balanced – as described in equation 7.1 – to prevent the formation of defects in the structure. Using this condition, the bandgap of the material system at 10 K has been simulated for InAs thicknesses between 2 – 4 nm and x in $InAs_{1-x}Sb_x$ from 0.1 – 0.13. The bandgap is defined as the recombination between e_1-hh_1 as the closest charge carrier energy levels to the bandedges.

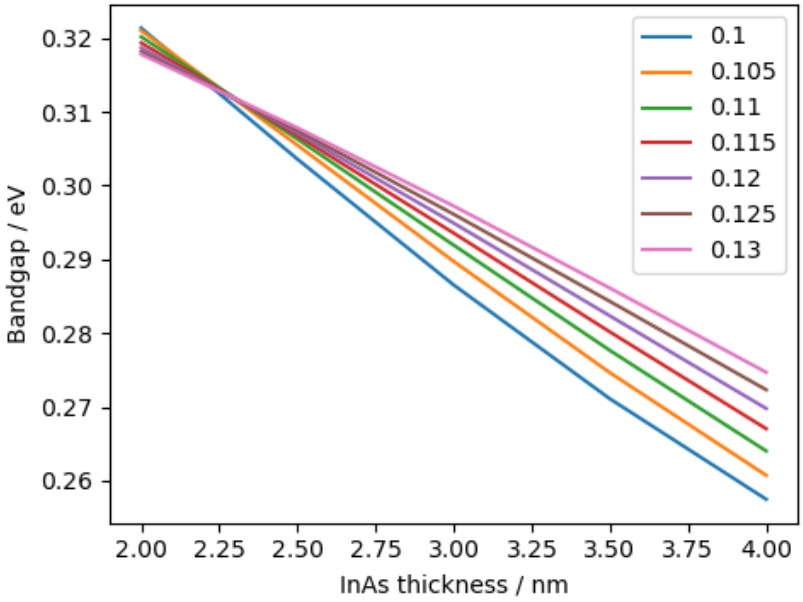

Figure 7.4: The bandgap (e-hh1 transition) of a strain balanced InAs/InAsSb SLS system with InAs layer ranging from 2 - 4 nm and Sb content ranging from 0.1 - 0.13.

This shows that as the thickness of the InAs QW increases – and thus the InAsSb also increases – the bandgap decreases. Moreover, it shows that as the antimony content of the InAsSb is increased, the bandgap decreases, when the InAs thickness is greater than ~2.3 nm. This is due to the absolute energy level of the InAsSb electron and hole level increasing – InSb has a much higher valence band offset than InAs. Because of this, the energy at which the holes are confined is increased as the energy at which the electrons are confined stays the same, resulting in a smaller bandgap. The opposite effect is seen when InAs thickness < 2.3 nm because of the conduction and valence band bowing parameters. When considering the information in Figure 7.4, this must be taken in accordance with how thick the InAsSb layer would be based on the strain balancing equation. When the layer gets to a certain thickness, the electrons would stop

acting in a quantum manner and act as classical particles, giving the layer bulk properties. Acting in a classical manner, which would negate the superlattice effects of the superlattice so should be avoided. This means that some of these bandgaps would not be achievable in practicality.

Because changing the antimony content of the InAsSb QW changes the valence band minima of the SLS system, it is implied that the confinement energy of the holes in the hh_1 band will also change the hole confinement energy.

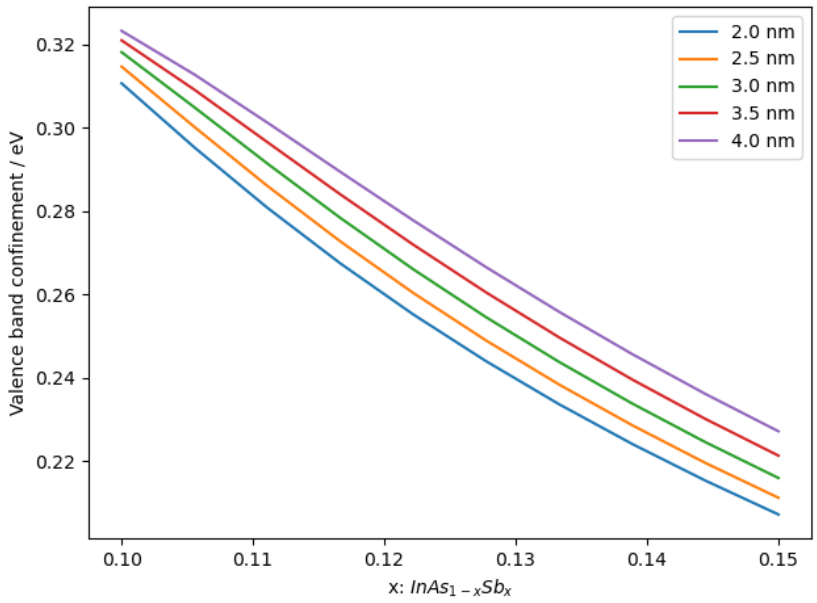

Figure 7.5: The valence band offset, from hh_1 to the valence band minima for strain balanced InAs/InAsSb SLSs with InAs thicknesses ranging from 2 - 4 nm and Sb content of InAsSb from 0.10 - 0.15.

To quantify this confinement energy as a function of InAs layer thickness as well as antimony content for a strain balanced system, simulations were conducted on Nextnano. The valence band confinement energy is shown in Figure 7.5, this shows that as the width of the InAs QW increases, the valence band confinement energy also increases. This is expected as a thicker QW causes the hh_1 energy level to lie closer to the valence band maxima. Moreover, lower antimony InAsSb alloys have a valence band minimum closer to the minimum of the InAs valence band, meaning that the total confinement energy of the QW is lower. This has the effect of decreasing the confinement energy of the hole in this band. The simulation however shows that across this range of variables for the superlattice, there is a relatively large quantum confinement for the holes, this is important for maintaining the charge carrier in the QW.

7.3. Strain-balancing calibration

Before the growth of light emitting diode devices, undoped superlattices were grown. This was to ensure there was good material quality, with abrupt InAs-InAsSb interfaces and that the conditions for strain balancing were met. As well as checking material quality and strain-balancing conditions, undoped superlattice samples can have their bandgaps characterised using photoluminescence spectroscopy. For superlattices, this has to be done at low temperature.

7.3.1. Growth

These samples were grown via molecular beam epitaxy on n-GaSb substrates, the growth process is described in section 3.1. Once the outgassing and in-situ deoxidation process has been completed, a 500 nm GaSb buffer layer was grown at a rate of 1 ML s^{-1} with a substrate temperature of 500 °C. After this, the substrate is cooled down to 430 °C under Sb flux; this is the temperature that InAs/InAsSb superlattices can be optimally grown at. The substrate is kept under Sb flux to prevent Sb evaporation which would cause metallisation of the substrate. Once the substrate is at the correct temperature, the superlattice growth begins.

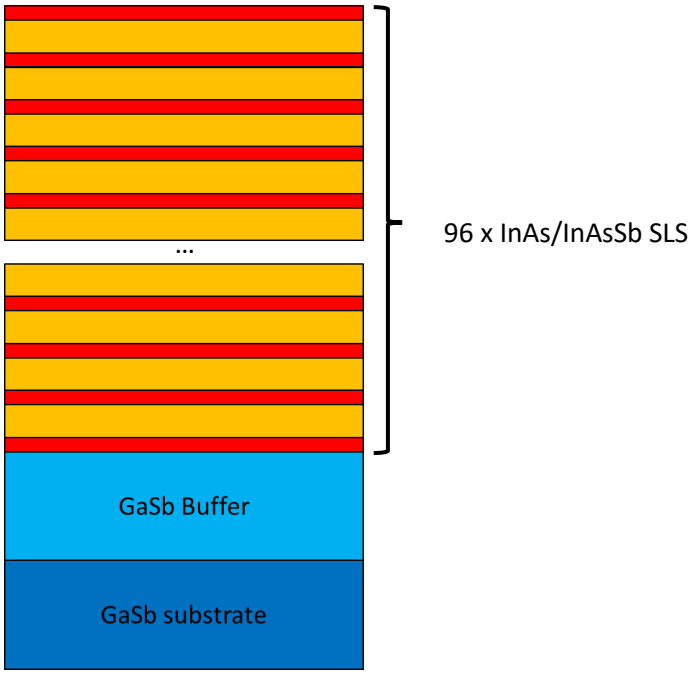

Figure 7.6: Schematic of the InAs/InAsSb strain balanced superlattices grown for calibration.

To grow 1 µm of superlattice, 96 repeats of the InAs/InAsSb alloys were grown, the cell shutter configuration was optimised such that high-quality QWs with abrupt interfaces are formed. The schematic of the grown samples can be seen in Figure 7.6.

7.3.2. Samples

For calibration, four samples were grown. One of these was a bulk InAsSb sample, this was grown to compare the superlattice and bulk emission. After this, six superlattices of varying lattice matched conditions were grown, the alloy content and layer thicknesses of these samples are outlined in Table 7.2. To characterise how strain balanced a superlattice system is, the metric of effective strain (ε_{eff}) is used. For a superlattice structure of InAs/InAsSb$_x$ with *y* monolayer of InAs and *z* monolayers of InAsSb, the effective strain is defined by equation 7.2.

$$\varepsilon_{eff} = \frac{(y\epsilon_{InAs}) + (z\varepsilon_{InAsSb})}{y + z} \qquad 7.2$$

Here: ε_{InAs} is the strain of the InAs and ε_{InAsSb} is the strain of the InAsSb on GaSb. A perfectly strain balanced system would have an effective strain of 0, so the further the effective strain deviates from this, the less strain balanced the system is.

Sample	Structure	Strain balanced condition / nm	Layer thicknesses / nm	ε_{eff}/ %
SAMPLE 7.1	$InAs_{0.902}Sb_{0.098}$	-	-	-
SAMPLE 7.2	$InAs/InAs_{0.907}Sb_{0.093}$	2.39/54.5	2.39/8.32	0.122
SAMPLE 7.3	$InAs/InAs_{0.894}Sb_{0.106}$	2.46/13.0	2.46/8.57	0.0482
SAMPLE 7.4	$InAs/InAs_{0.894}Sb_{0.106}$	2.46/12.7	2.46/13.7	0.00421
SAMPLE 7.5	$InAs/InAs_{0.878}Sb_{0.123}$	2.49/6.65	2.49/7.23	0.0122
SAMPLE 7.6	$InAs/InAs_{0.878}Sb_{0.123}$	3.03/8.22	3.03/8.80	0.0136
SAMPLE 7.7	$InAs/InAs_{0.892}Sb_{0.108}$	2.96/14.2	2.96/12.7	0.0151

Table 7.2: The strain balancing conditions of the SLS strain balancing given the InAs layer thickness as a constant for the calibration samples along with the actual layer thicknesses of the samples, determined by XRD.

Comparing the strain balanced conditions to what was actually grown, it can be seen that sample SAMPLE 7.2 was far off the strain balancing conditions. This is because the Sb content is very low, under these conditions the InAsSb layers provides very little strain. This would then require a very large layer to provide the amount of strain required to counteract the strain provided by the InAs layers. The strain balancing conditions used in this model are confirmed by the XRD scans which was discussed in section 7.1. Because the actual layer thickness was so far from the

strain balanced condition this implies poor material quality, with possible relaxation in the superlattice. To compensate for this, the Sb valve position was increased to raise the flux, this should result in greater Sb incorporation in the InAsSb alloy. SAMPLE 7.3 and SAMPLE 7.4 were grown using a higher Sb valve position, this resulted in both of them having alloy contents and layer thicknesses much closer to that of the strain balanced conditions. SAMPLE 7.7 was grown to compare the performance of superlattices with Sb contents ~ 0.1 when the width of the QWs are increased. This sample was grown around with around 0.0151% effective strain, as calculated using equation 7.2.

7.3.3. Structural characterisation

Once the samples were grown, they had their structures characterised using ω-2θ XRD scans as described in section 3.2. XRD scans can then be used to find the alloy composition and layer thicknesses of the superlattices using modelling software, the XRD scans of the calibration samples along with their respective models can be seen in Figure 7.7 (a) – (g). The corresponding alloy contents and layer thicknesses are displayed in Table 7.2 along with the alloy contents which were required for strain balancing of the system. Figure 7.7 (a) shows the bulk InAsSb sample which was grown to compare the photoluminescence emission spectra of the superlattices. This was grown slightly off lattice matched resulting in a 0.06 % tensile strained system, this lattice mismatch can be seen due to the GaSb and InAsSb peaks occurring at slightly different angles. The InAsSb in the bulk sample is ~ 1000 nm thick, which is lower than the critical thickness of the system according to the People and Bean model.

The XRD scans of the superlattices can be seen in Figure 7.7 (b) – (e). As well as using the extrapolated alloy content and layer thickness based on the model in equation 7.1, the XRD scans can be used to see the quality of the strain balancing independently of the model. When a system is not strain balanced, the main peak of the scan will split, as can be seen in the least strain balanced of all the samples, SAMPLE 7.2, shown in Figure 7.7 (b). A perfectly strain balanced system will have peaks from the InAs and InAsSb layers lining up with one another and the GaSb substrate perfectly and the satellite peaks perfectly match up with one another.

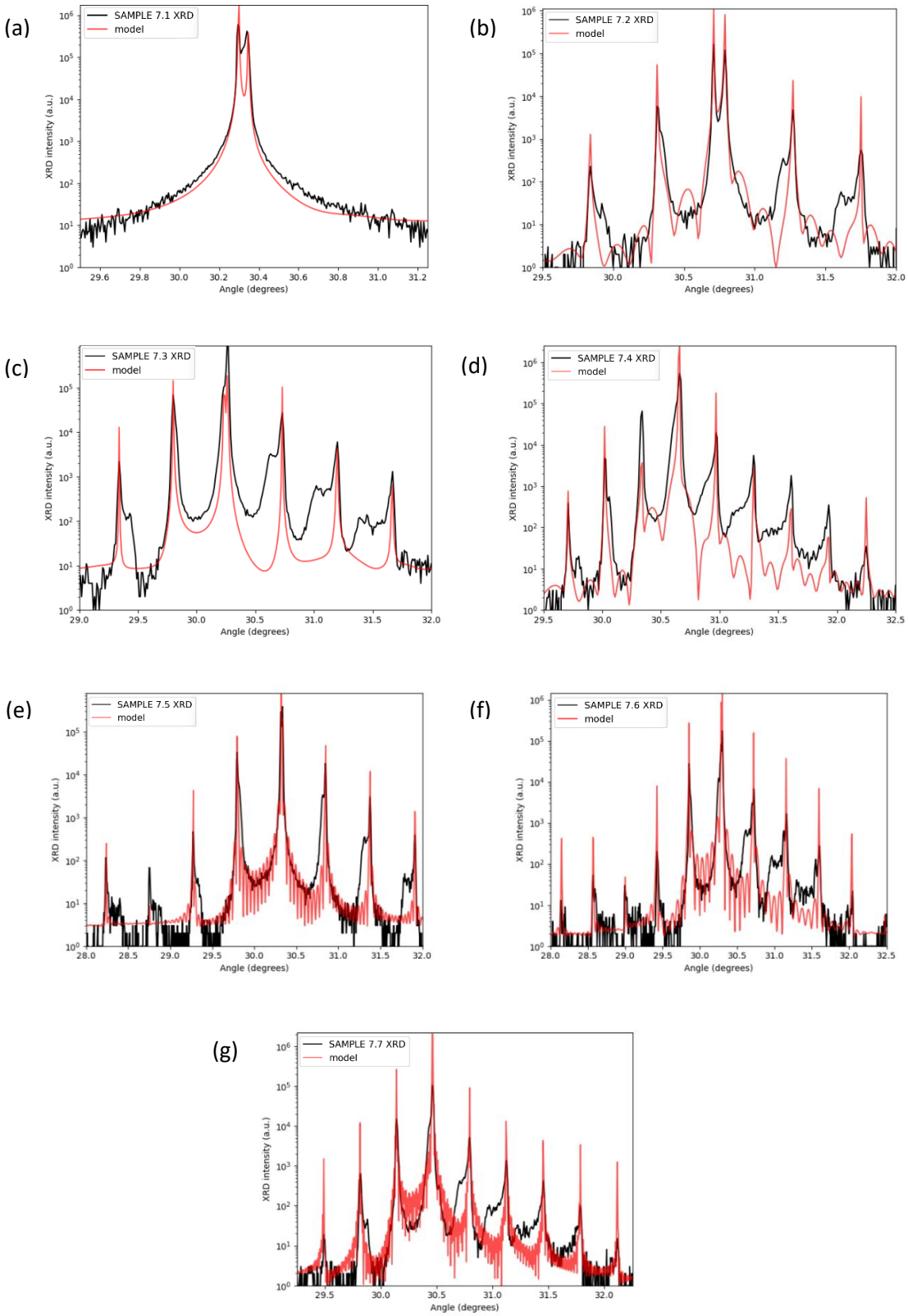

Figure 7.7: The ω-2ϑ scans and corresponding models for (a) SAMPLE 7.1, (b) SAMPLE 7.2, (c) SAMPLE 7.3 (d) SAMPLE 7.4, (e) SAMPLE 7.5, (f) SAMPLE 7.6 and (g) SAMPLE 7.7 which are InAsSb bulk and SLS of various strain balanced conditions respectively.

If this criterion is not met, the result is that “shoulders” appear around the satellite peaks. This can be seen to varying extents in Figure 7.7 (c), (d) and (e), where just to the side of each satellite peak, a smaller peak can be seen, around 10 times weaker in intensity – known as a “shoulder”. As these shoulders get closer to the satellite peak itself, it is possible to qualitatively say that the system is closer to strain balanced. Using this, it is possible to show that SAMPLE 7.4 AND SAMPLE 7.7 are the closest to strain balanced, followed by SAMPLE 7.3 then SAMPLE 7.2, this is further confirmed by the model and effective strain.

7.3.4. Photoluminescence

The samples from Table 7.2 were tested for photoluminescence at 4 K. However, SAMPLE 7.2 was excluded from the testing, this is because its alloy content and layer thicknesses were so far off being strain balanced that little useful information could be obtained from it for the scope of this study. The spectra of SAMPLE 7.5 and SAMPLE 7.6 are also excluded because of their low intensity meaning very little useful information can be obtained by visual inspection of the spectra. To obtain low temperature, a liquid helium cooled cryostat was used, the process of which is outlined in section 3.3. The PL spectra was measured using a monochromator which is also described in section 3.3.

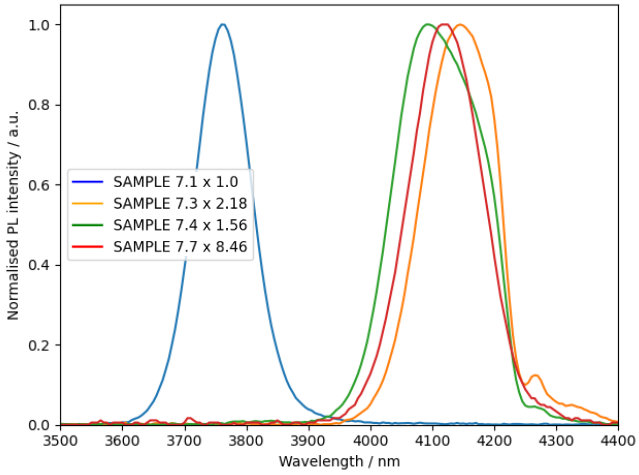

Figure 7.8: Low temperature (4K) normalised photoluminescence comparisons of SAMPLE 7.1 (bulk InAsSb), SAMPLE 7.3 (SLS sample), SAMPLE 7.4 (SLS sample) and SAMPLE 7.7 (SLS samples). The multiplication factor of each spectrum is also shown for the normalisation relative to one-another.

The 4K normalised PL spectra of SAMPLE 7.1, SAMPLE 7.3, SAMPLE 7.4 and SAMPLE 7.7 can be seen in Figure 7.8, this was done using a red laser emitting at a power of 140 mW – maximum output power for this system. Some of the SLSs’ spectra was obscured by the CO_2 absorption peak at around 4250 nm, causing some distortion. When not normalised, the bulk sample (SAMPLE 7.1) has a higher spectral intensity than the SLS samples. However, it should be

considered that the bulk sample also has a larger bandgap than the SLS samples. This could result in higher output power, due to higher energy photons being emitted, meaning a more intense spectrum will be obtained. Moreover, the InAsSb bulk sample produces a narrower spectrum than the SLS samples SAMPLE 7.3, SAMPLE 7.4 and SAMPLE 7.7, with a single Gaussian peak, resulting from one band-to-band recombination. In comparison, despite the obfuscation by the CO_2 absorption peak, it appears that there are two energy transitions which are contributing to the spectra of the SLSs – samples SAMPLE 7.3 and SAMPLE 7.4, this causes a wider spectrum. However, the sample SAMPLE 7.7 does display one Gaussian like peak which is slightly obfuscated by the absorption peak. The single peak in this sample could be due to the sample being better strain balanced compared with the others. As mentioned above, SAMPLE 7.5 and SAMPLE 7.6 had spectra which were around 100 times weaker than those of the other samples. The only difference in this growth is the antimony content in the QW, being ~ 0.12 in comparison to ~0.11 for the other samples. This implies that there is some sort of limiting factor in the structure when using this alloy content, as good LT PL spectra are shown using $InAs_{0.89}Sb_{0.11}$ in the superlattice, and they have also been shown to give strong emission with higher antimony content – shown in section 4.2.3.

Power dependant PL spectra using laser power in the range of 40 – 140 mW can be seen in Figure 7.9 (a) – (d) for the samples outlined in Table 7.2. From this, it is again clear that the InAsSb bulk sample has one peak across all input laser powers, which is from the band-to-band recombination. Furthermore, the spectra suggest that it is two transitions which cause the spectra in for SAMPLE 7.3 and SAMPLE 7.4 (Figure 7.9 (b) and (c)), this is most evident in the low power (40 mW) spectra. In the low power spectra of the superlattice samples, the two peaks can be clearly seen ~ 100 nm apart, this is apparent as the spectral shape is non-Gaussian with two distinct peaks appearing in SAMPLE 7.4. However, over the entire range of laser input powers, the spectrum of SAMPLE 7.7 remains single peak, from e-hh_1 recombination. All of the samples display clear blue shift with increasing laser power. This is characteristic of bulk, as well as type-II recombinations due to band filling and band bending respectively [204]. The sample with the largest extent of blue shift is SAMPLE 7.1, the bulk sample, with all of the SLS structures displaying the effect but to a lesser extent.

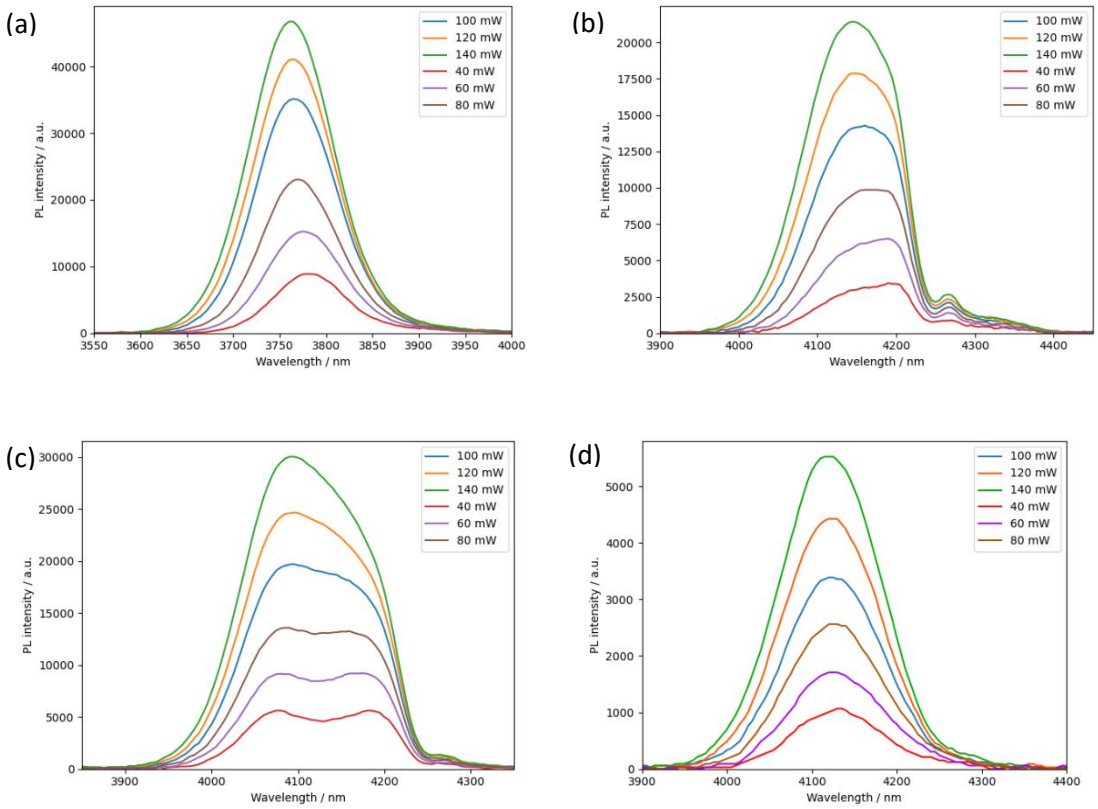

Figure 7.9: Low temperature (4 K), power dependant photoluminescence spectra with laser power from 40 - 140 mW of: (a) SAMPLE 7.1, (b) SAMPLE 7.3 (c) SAMPLE 7.4 and (d) SAMPLE 7.7.

In order to determine the constituent recombinations which make up the spectra of SAMPLE 7.3 and SAMPLE 7.4, multi-peak analysis was conducted on the spectra. This process fits a summation of two Gaussian peaks to the spectra, which allows the spectral information of each peak to be determined. This process was ineffective with the spectra of SAMPLE 7.3 because one of the peaks is highly obfuscated by the CO_2 absorption peak at ~4200 nm which can be seen in Figure 7.9 (b). However, this process could be carried out on SAMPLE 7.4, shown in Figure 7.9 (c), although it may not be completely accurate as some of the spectra is still obscured by the CO_2 absorption peak. Despite the feature obfuscation, it is still clear that all of the samples experience blue shift as the laser power is increased. This can be seen clearly in Figure 7.10, with all peaks showing blue shift with increasing laser power, there is only one peak displayed for SAMPLE 7.7 as the PL spectrum only displayed one peak.

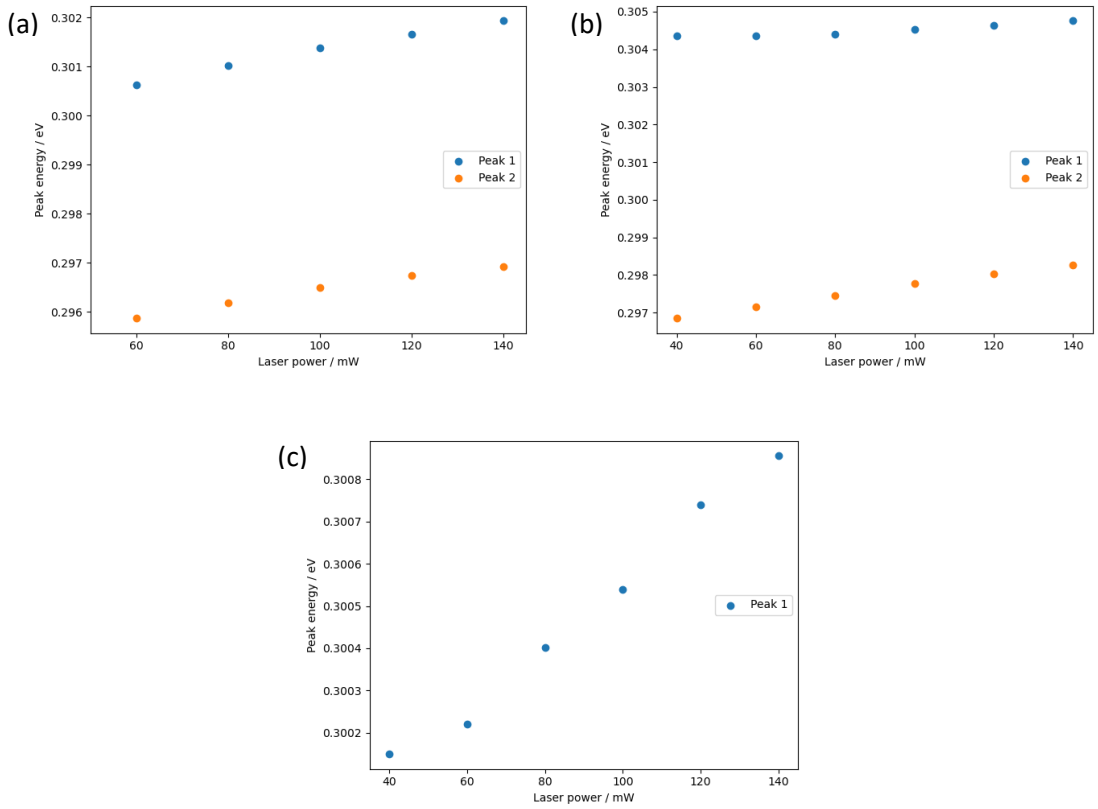

Figure 7.10: plots of peak energy of single or multiple peak as a function of input laser power for the SLS samples (a) SAMPLE 7.3, (b) SAMPLE 7.4 and (c) SAMPLE 7.7.

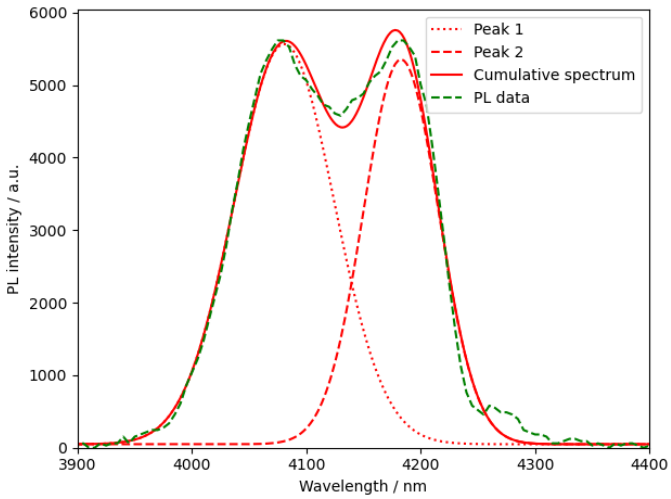

Figure 7.11: The low temperature PL spectra for SAMPLE 7.4 with a laser input power of 40 mW as seen in Figure 7.9. Multi-peak analysis is included showing the two constituent Gaussian peaks which make up the cumulative peak, these peaks are shown as 1 and 2 at 4180 nm and 4080 nm respectively.

The spectra in which there is most clearly two peaks is in SAMPLE 7.4 with a laser input power of 40 mW – this can be seen in Figure 7.9 (c) in the pink line. Figure 7.11 shows this spectrum with multi-peak analysis conducted on it. This shows that there are two constituent Gaussian peaks to the spectra, with peak wavelengths of 4180 nm (0.297 eV) and 4080 nm (0.303 eV). Bandgap analysis, as discussed in section 7.2, shows that peaks 1 and 2 are due to e-hh_1 and e-lh_1 transitions respectively. It is expected that the more probable transition (e-hh_1) would cause a peak of higher intensity, however, this is not the case, it appears that peak 1 increases at a lower rate than peak 2 as laser input power is increased. However, this could be caused by part of the spectrum being obscured by CO_2 absorption. The e-hh_2 transition can be disregarded, as the hh_2 level is below lh_1, according to the bandgap modelling shown in Figure 7.3, this would result in a transition with energy corresponding to an emission wavelength of < 4000 nm. No peaks for the SAMPLE 7.3 or SAMPLE 7.4 spectra can be seen which correspond to this energy, implying that the higher energy transition is due to the e-lh_1 transition.

The power dependant spectra were analysed as outlined in section 2.2.2 to find the dominant recombination mechanisms during PL. The linear fit to the $\log_{10}$ of input laser power as a function of $\log_{10}$ of the square root of integrated intensity can be seen in Figure 7.12 (a) – (d) for SAMPLE 7.1, SAMPLE 7.3, SAMPLE 7.4 and SAMPLE 7.7. The Z values extrapolated from this data are 1.4, 1.39, 1.58 and 1.48 for the samples respectively, the error is taken from the sum of the squared errors in Python 3.0 Numpy Polyfit.

These Z values imply that the recombinations are due to a mix of SRH and radiative recombinations. If $1< Z < 1.5$ this implies SRH is dominant, and if $2 > Z > 1.5$ this implies that radiative is dominant. All of the samples are ~ 1.5 implying a similar mix of each type of recombination. This data could however be affected by how little Auger recombination there is in the system, associated with Z = 3. Auger recombination is diminished in this analysis due to the system being at low temperature, this means that the majority of recombinations occurring will result in SRH or radiative. Although other SLS systems may have Z ~ 2, this could be due to radiative recombinations, as well as equal amount of SRH and Auger.

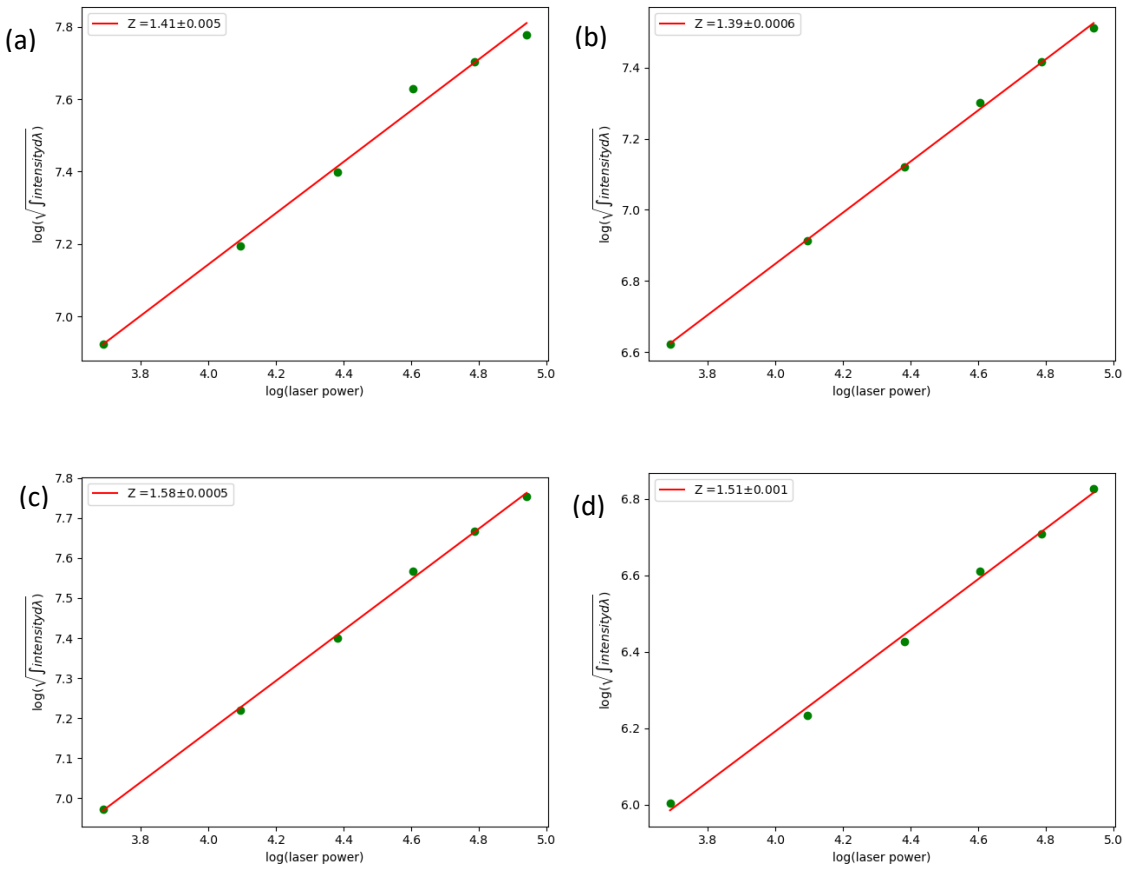

Figure 7.12: $\log_{10}$ of the input laser power as a function of $\log_{10}$ of the square root of the integrated intensity of the spectra, with a linear fit to find the Z value, for (a) SAMPLE 7.1, (b) SAMPLE 7.3, (c) SAMPLE 7.4 and (d) SAMPLE 7.7.

The Ga-free system is meant to reduce the SRH recombination which does not appear to entirely be the case in this system as SRH is present. It does appear that the bulk sample, as well as the worse strain balanced SAMPLE 7.3 systems do have a greater amount of non-radiative recombinations in comparison to the better strain balanced SAMPLE 7.4 and SAMPLE 7.7. It should however be noted that the range of laser powers was from 40 – 140 mW which is less than an order of magnitude so may not be entirely accurate. In order to obtain a more accurate value, in future, a neutral density filter could be used, allowing for a greater range of laser input powers.

7.4. Light emitting diodes

When the cell set points were found for the optimal growth of the SLS active region, this was used to create the active region for a LED. Initially, three different LEDs were grown, each slightly changing the characteristics of the active region. The design, growth, fabrication and characterisation of which will be outlined.

7.4.1. Growth

The devices were grown on (001) n-GaSb substrates, before growth they go through an outgassing process as well as an in-situ deoxidation process using a substrate temperature of 600 °C. Once this is done, the substrate is cooled down and the growth of an n-GaSb region begins at 500 °C, this is doped with Te with a concentration of 2×10^{18} cm^{-3}. Approximately 500 nm of n-GaSb is grown at a growth rate of 1 ML s^{-1}, this is followed by 50 nm of undoped GaSb, to minimise any Te entering the superlattice (intrinsic region). A growth rate of 1 ML s^{-1} was used for the rest of the growths of the LED samples, including the SLS structure as well as the electron blocking layer. The growth of the superlattice follows once the substrate has cooled to the correct temperature, the process of this is exactly the same as that described in section 7.3.2.

The superlattice in the device can be seen in the schematic in Figure 7.13, in two different devices the number of superlattice repeats (x) was varied to see the effect on device performance. The number of repeats in the three different superlattice devices can be seen in Table 7.3. After the superlattice has been grown, the substrate is heated to the growth temperature of GaSb a 50 nm cap of undoped GaSb is grown. This is followed by 50 nm of p-$Al_{0.9}Ga_{0.1}As_{0.07}Sb_{0.93}$ doped with Be. This is an electron blocking layer, so that electrons do not leak out of the superlattice. Lower electron leakage causes more recombinations to occur in the superlattice itself rather than in any of the other regions, this has been shown in several previous devices in the literature [32, 205]. The triple layer calibration was used to find the set points to grow the electron blocking barrier as outlined in section 3.1.2.

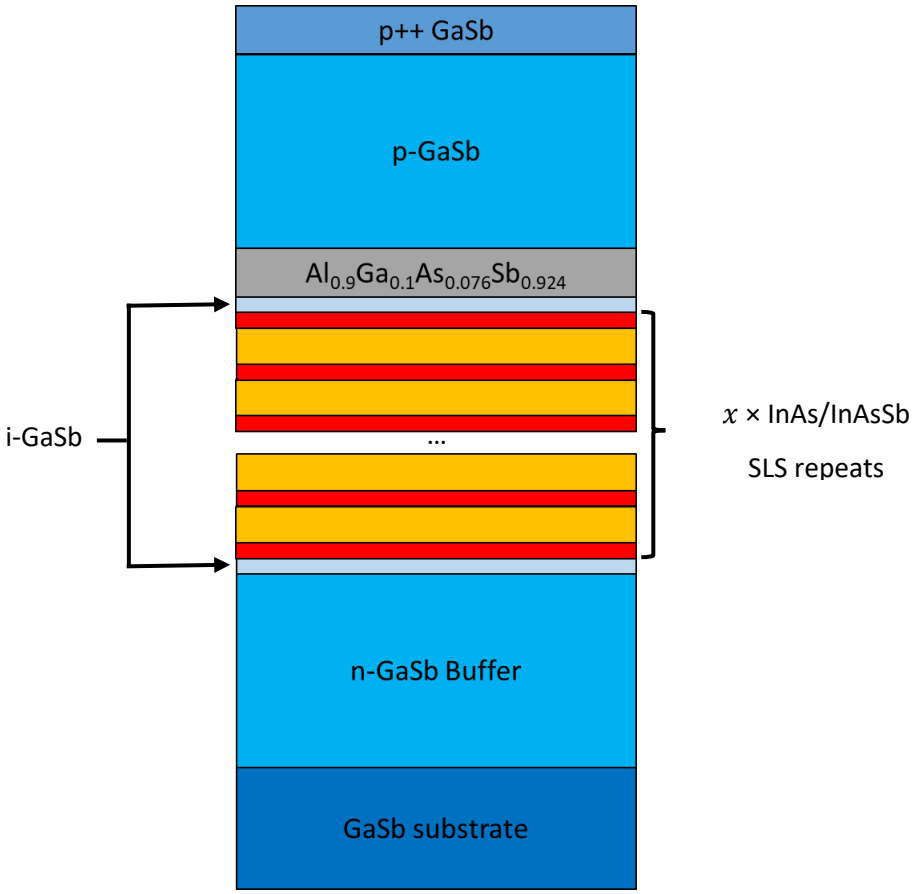

Figure 7.13: the structure of the LEDs containing strain balanced superlattices.

After the electron barrier, 500 nm of p-GaSb is grown, doped with Be with a concentration of 2×10^{18} cm^{-3}. The structure is capped with a 50 nm p++ GaSb contacting layer with a dopant concentration of 1×10^{19} cm^{-3}. The doping in the contact layer is increased by increasing the base temperature of the Be cell from 870 °C to 877 °C, this was based on calibration growths with the doping concentrations measured using Hall effect measurements. A schematic of the complete LED structure can be seen in Figure 7.13 and the band structure is shown in Figure 7.14.

7.4.2. Band structure

For the SLS system to be integrated into an LED to obtain electroluminescence and create a useable device, it is important to put the active region previously discussed into a p-i-n structure. The structure utilised for this used the SLS active region discussed in section 7.3.2, this was put in between n-GaSb and p-GaSb, the bandedges of this structure were simulated at 4 K and can be seen in Figure 7.14 (a). Figure 7.14 (b) shows the superlattice region, showing the band-bending which occurs as a result of the mismatch in band positions in the respective regions.

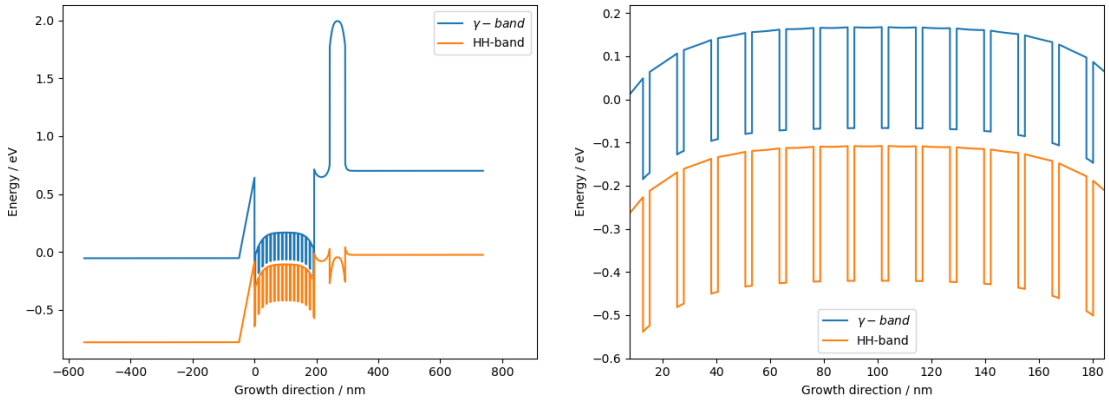

Figure 7.14: (a) the bandstructure of the active region and electron blocking layer in between n and p-doped GaSb regions for use as an LED and (b) closer look at the band structure of the superlattice region.

The bandstructure of this device does pose some challenges to the electrical and optical performance. First, the active region, which can be seen between ~ 550 – 850 nm in the growth direction in Figure 7.14, has a significantly different conduction and valence band offset than the GaSb doped regions. This results in there being large discontinuities in the conduction and valence band from the GaSb regions into the InAs based active region. The significant discontinuity causes potential barriers for charge carriers to be injected into the active region. This can require higher voltages being needed to inject charge carriers into the active region or charge carriers only being able to enter via tunnelling. In turn, this causes poor electrical performance of the device and lowers the probability that charge carriers will recombine in the active region. However, the $Al_{0.9}Ga_{0.1}As_{0.07}Sb_{0.93}$ electron blocking barrier – which can be seen at ~ 1000 nm does not appear to cause any band bowing or discontinuity problems with the bandstructure in the valence band.

7.4.3. Structural characterisation

Much like the samples for strain balancing calibration and PL, the devices' structures were characterised by XRD with modelling to confirm that the strain balancing criteria were still being met. As well as this, XRD is used to check that the electron blocking layer was grown lattice matched. If this criterion is not met, it could cause defects to occur in the structure which is detrimental to electrical performance.

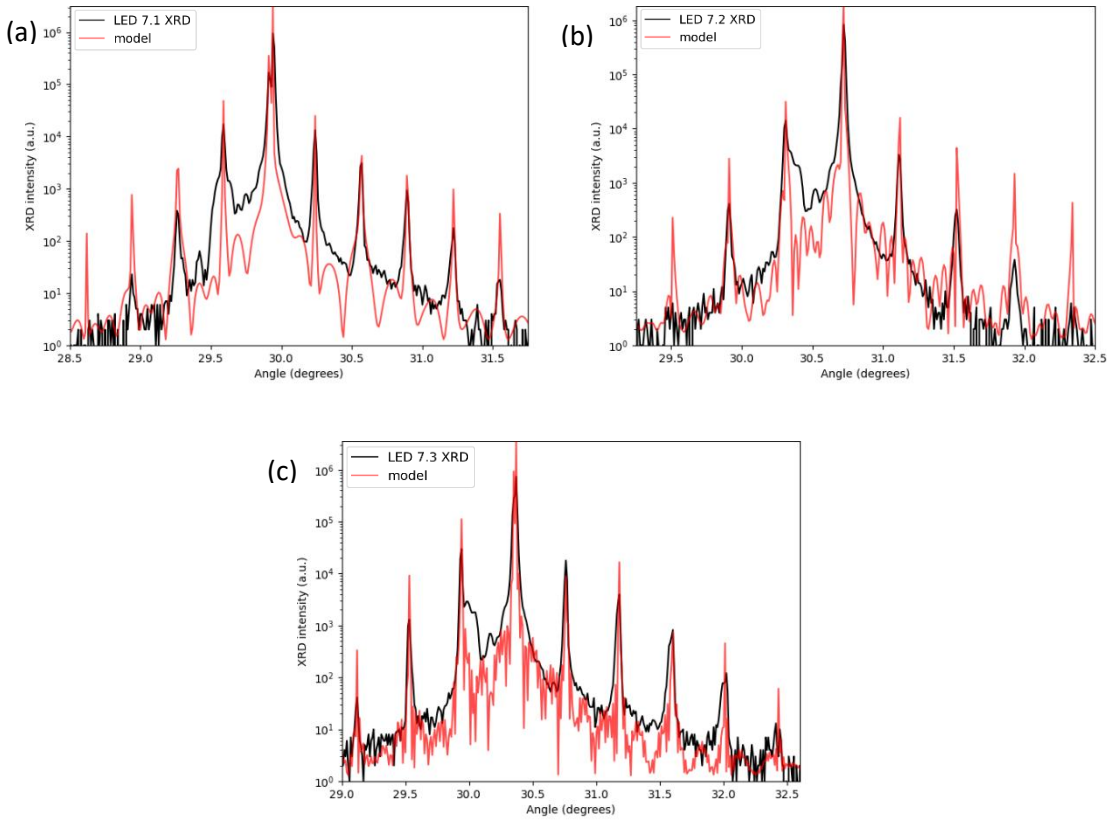

Figure 7.15: XRD ω-2ϑ scans of the strain balanced superlattice LEDs for samples: (a) LED 7.1, (b) LED 7.2 and (c) LED 7.3.

The XRD scans that were conducted on the three devices with the design shown in Figure 7.15. The ω-2θ scans along with the corresponding models can be seen in Figure 7.15 (a), (b) and (c) for LED 7.1, LED 7.2 and LED 7.3 respectively. The superlattice region information in each device which was extracted from the XRD model can be seen in Table 7.3 along with the strain balancing conditions based on the model in equation 7.1. From all of the scans shown in Figure 7.15, it is clear that the AlGaAsSb electron blocking layer for each device is lattice matched to GaSb as no additional peak can be seen, implying that it is in line with the substrate peak.

Sample	Sb content (aim)	Sb content (actual)	QW thickness (aim) / nm	QW thickness (actual) / nm	Strain balanced conditions / nm	Superlattice repeats
LED 7.1	0.110	0.111	2.5/9.8	2.40/13.3	2.40/9.98	32
LED 7.2	0.111	0.112	2.4/10	2.49/10.2	2.49/9.75	32
LED 7.3	0.112	0.115	2.5/9.8	2.44/9.98	2.44/8.45	64

Table 7.3: the Sb content and QW thicknesses of the three strain balanced superlattice LEDs grown, corresponding to the XRD scans shown in Figure 7.15: XRD ω-2ϑ scans of the strain balanced superlattice LEDs for samples: (a) LED 7.1, (b) LED 7.2 and (c) LED 7.3.

When analysing the scans in Figure 7.15 to see if the structures are strain balanced, it appears that they are, although LED 7.1 (Figure 7.15 (a)) does show some minor peak splitting implying that the strain balancing is not perfect. The other two devices (LED 7.2 and LED 7.3) appear to have no peak splitting in the main GaSb peak or in any of the satellite peaks. This is further confirmed by the information presented in Table 7.3, where LED 7.1 has a much thicker layer of InAsSb than is required to create strain balanced conditions. But LED 7.2 and LED 7.3 are both very close to the strain balanced conditions, with LED 7.2 being the closest.

7.4.4. Device fabrication

The LED devices were all fabricated into mixed area mesa diodes with top-bottom contact configuration via standard photolithographic techniques as described in section 3.4. Before they were cleaved, they were probed to characterise current normalised by area and perimeter current, as will be described in the next section. Once this initial electrical characterisation had been completed, the sample was scribed and wire bonded to 800 µm mesa structures.

7.4.5. Electrical characterisation

7.4.5.1 Probing

Once the devices had the relevant contacts applied and had been etched into mesa structures, the initial electrical characterisation via probing – as described in section 3.5.1.1 – was conducted. During fabrication, three mesa structures of different diameters were created: 800, 400 and 200 µm. This makes it possible to check the current flow properties of the devices,

whether the current is recombining in the bulk (superlattice) or if it is flowing around the surface of the mesa structure and recombining elsewhere.

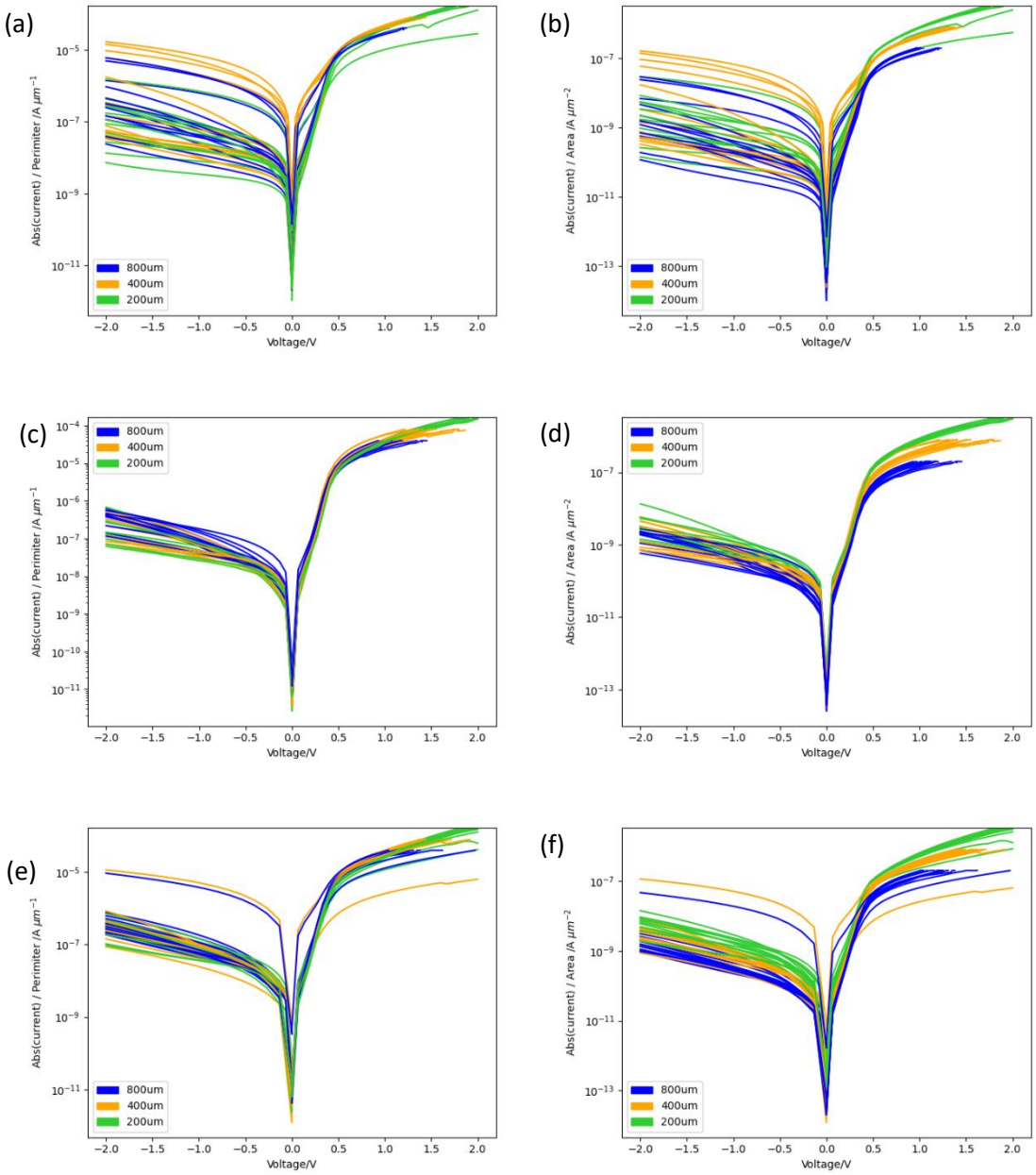

Figure 7.16: Probed IVs normalised for mesa area and perimeter of 800, 400 and 200 µm mesa structures for LED 7.1, LED 7.2 and LED 7.3, which are: (a) perimeter normalised LED 7.1, (b) area normalised LED 7.1, (c) perimeter normalised LED 7.2, (d) area normalised LED 7.2, (e) perimeter normalised LED 7.3 and (f) area normalised LED 7.3.

The IV curves for LED 7.1, LED 7.2 and LED 7.3 normalised for perimeter and area can be seen in Figure 7.16 (a) – (f). The shape of these curves show diode like characteristics, implying that the devices are working as they should. When considering the grouping together of the curves when normalised around perimeter rather than area, this implies that the current is flowing along the surface of the mesa, as opposed to going through the mesa in the superlattice. This is an adverse

electrical property of the device as it implies that the recombinations are not occurring in the superlattice at room temperature.

7.4.5.2 Bonded devices

Once the devices had been probed, they were cleaved, mounted and wire bonded, as described in 3.4.5 to create a working device. The devices were bonded in the top-bottom contact configuration with the 800 µm mesas being used for the top contact. The current-voltage (IV) characteristics of these devices were tested from bias ranges of -1.0 V to +1.0V, this was done according to the method laid out in section 3.5.1 and the results are shown in Figure 7.17 (a), (c) and (e).

The IV curves of LED 7.1, LED 7.2 and LED 7.3 show good diode-like characteristics. LED 7.1 devices show reverse bias with ~ 100 times lower current than that of forward bias; LED 7.2 and LED 7.3 devices showing ~ 1000 times lower current in reverse bias, there are however a few defective devices showing a large reverse bias current.

Along with the IV characteristics, Figure 7.17 (b), (d) and (f) show the corresponding resistances as a function of forward bias for various devices from LED 7.1, LED 7.2 and LED 7.3. They show that as the forward bias increases, the resistance decreases, which agrees with the change in the energy band positions charge transport easier. All of the devices show slightly different resistance-voltage characteristics, but at a forward bias of +0.8 V, the resistance of the best performing devices are ~ 10 Ω. A low resistance decreases the amount of power required to put through a device to allow it to operate, which is a beneficial electrical characteristic, especially in an LED where low operational power is a defining characteristic. However, it can also be an indicator that current is going around the active region rather than through it, causing lower levels of efficiency, as charge carriers are not undergoing radiative recombination.

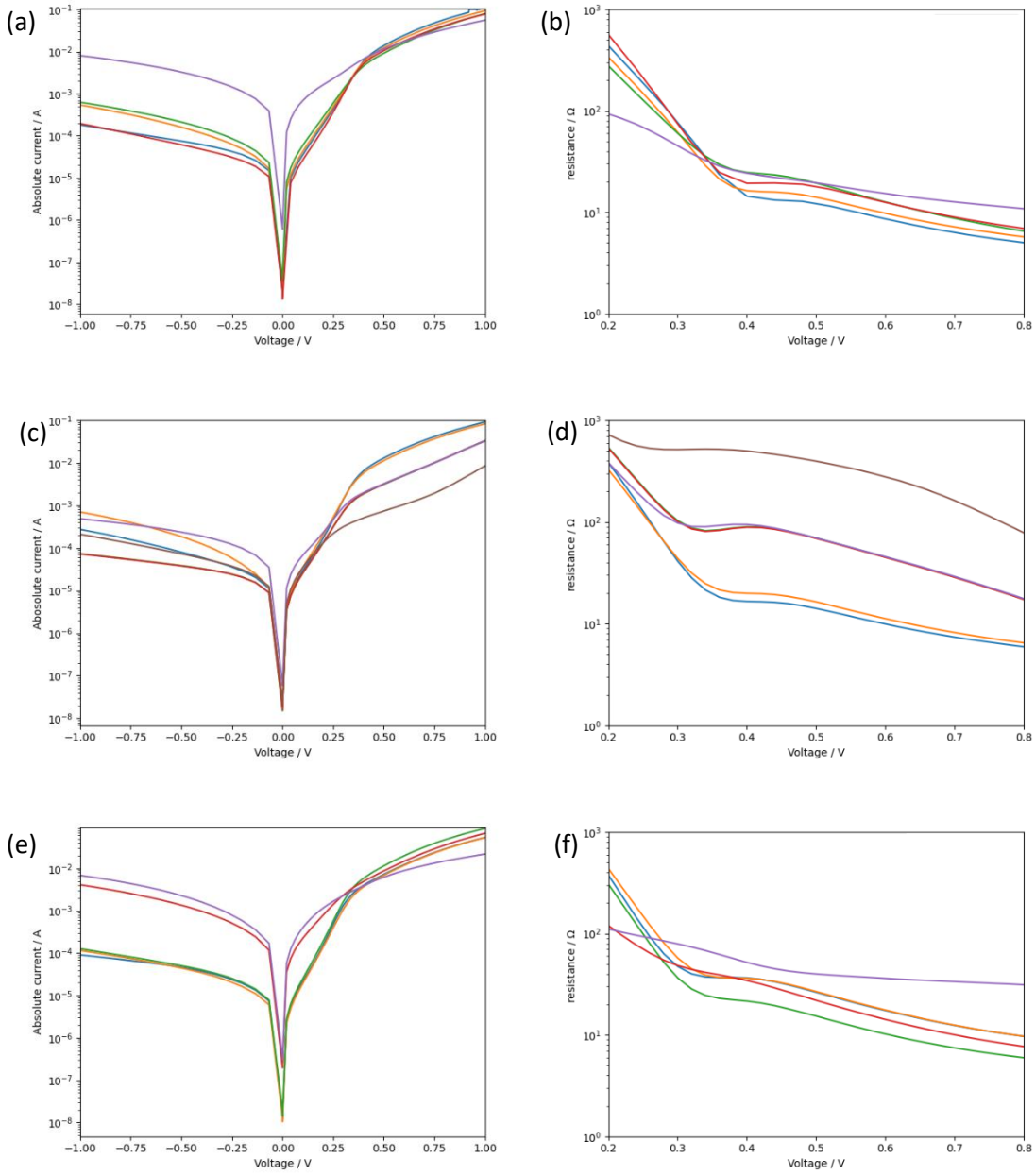

Figure 7.17: the IV curves and corresponding resistances or several devices fabricated from: (a) LED 7.1 IV curve, (b) LED 7.1 resistance, (c) LED 7.2 IV curve, (d) LED 7.2 resistance, (e) LED 7.3 IV curve and LED 7.3 resistance.

7.4.6. Electroluminescence

The devices which showed the best electrical characteristics – lowest resistance at a bias of ~ +1.0 V – had their electroluminescence tested. All of the devices (LED 7.1, LED 7.2 and LED 7.3) were tested at room temperature using a duty cycle of 10 % with a current of up to 200 mA using the methodology outlined in section 3.6. None of the devices gave electroluminescence spectra at room temperature, leading to low temperature testing being carried out. This was done using a cryogenic gas-free cryostat to bring the sample down to 4 K then using a heater to increase the temperature to find the effect of temperature on emission. The use of a cryogenic

gas-free cryostat is outlined in section 3.6. LED 7.1 and LED 7.3 did not give electroluminescence spectra, even at low temperatures. LED 7.2 gave low temperature electroluminescence, the spectrum from 1500 – 4800 nm can be seen in Figure 7.18. This spectrum shows two clear peaks, one at 1650 nm (0.752 eV) and 4120 nm (0.301 eV). The peak at 0.752 eV is in good agreement with photoluminescence of bulk GaSb, grown on GaSb substrates reported by Chidley et. al. [206], this implies that this peak is due to recombinations occurring in the bulk GaSb. Recombinations in the GaSb are expected due to the high surface current as shown by the normalisation of probed IV curves around mesa perimeter in section 7.4.5.1. This is because the SLS region is bypassed and the recombinations either happen on the surface in the GaSb in the active region or around the GaSb on the surface below the mesa. This means that charge carriers are travelling around the active region to combine elsewhere rather than in the active region. As discussed in section 7.2, this could be due to the discontinuities in the bandstructure causing problems with charge carrier injection from the GaSb into the active region. If recombinations are not occurring in the active region, the next place they are most likely to occur is in the GaSb bulk structure. However, recombinants are still occurring in the superlattice region, this can be seen by the peak at 4 120 nm. This is in good agreement with both the PL samples, which were almost identical to the active region in the LED and to the results of bandgap simulations. Although the CO_2 absorption peak was slightly obscuring the spectrum, the peak was still visible, allowing the peak wavelength to be found.

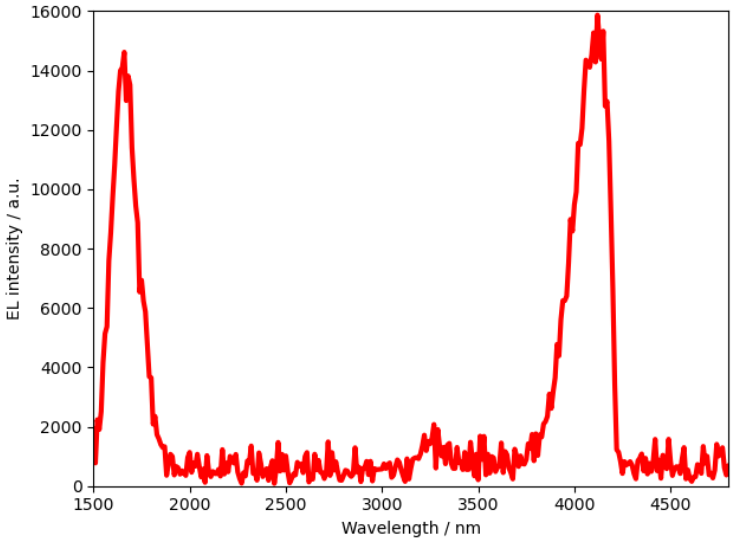

Figure 7.18: the electroluminescence of LED 7.2 at 7 K with an input current of 85 mA and duty cycle of 15 %, using a 1000 Hz A.C. source.

The peak coinciding with recombination in the superlattice at 7 K can be seen in Figure 7.19 (a) with driving currents varying from 55 – 100 mA. The spectra show increasing intensity up until

around 90 mA, above 90 mA heating effects in the device limit the radiative recombinations. The spectra do not appear to have a gaussian-like shape as would be expected of emission at low temperature in quantum structures, this is due to the CO_2 absorption band at 4200 nm which is obscuring the lower energy section of the spectrum. These spectra also only show one peak, as opposed to the PL samples which displayed two, this corresponds to the e-hh_1 transition which is the expected most likely transition.

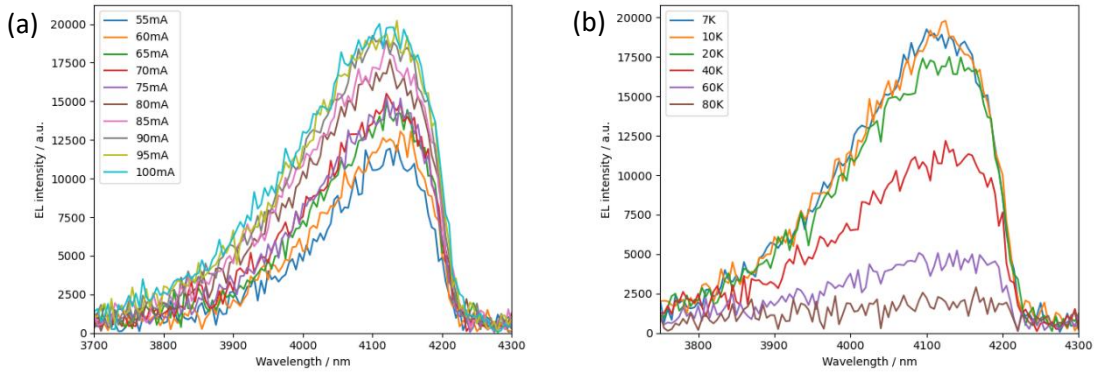

Figure 7.19: Electroluminescence spectra of LED 7.2 for (a) current variation from 55 - 100 mA and (b) temperature dependence from 7 - 80 K with a driving current of 90 mA.

The temperature dependant spectra from 7 – 80 K can be seen in Figure 7.19 (b), this was measured with a device driving current of 90 mA. As is expected, the intensity of the spectra decreases as the temperature rises, and the peak appears to red shift as the bandgap decreases with temperature. However, it is difficult to characterise the precise shift in bandgap as temperature increases due to the proximity of the peak to the CO_2 absorption band making it difficult to quantify. Furthermore, this device only emitted light up to around 80 K, which limits its potential for a commercialisation. This is probably due to the problems caused by bandstructure and injecting charge carriers into the active region.

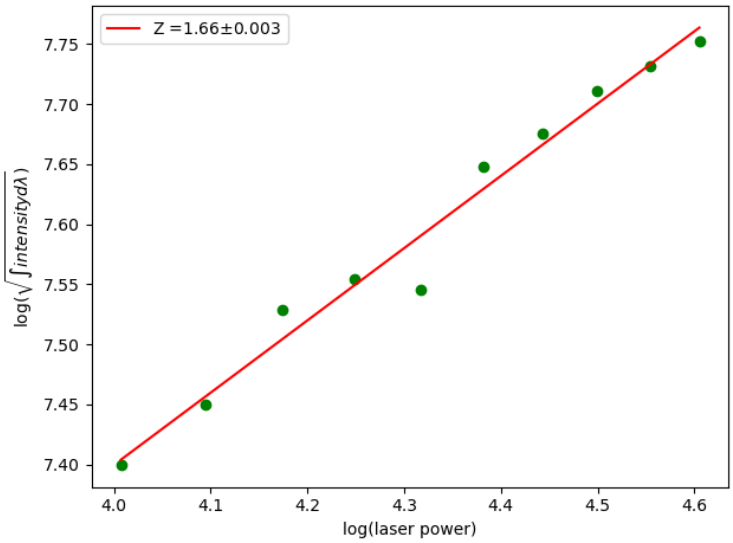

Figure 7.20: plot of the natural logarithm of the driving current as a function of the natural logarithm of the square rooted integrated intensity of the spectra of LED 7.2 as seen in Figure 7.19 (a). The red line shows the linear interpolation of this data with a gradient (Z-value) of 1.62.

As discussed in section 2.2.3, it is possible to find the dominant charge carrier recombination mechanism of a device from its integrated emission spectra at varying injection currents. This analysis was carried out on the spectra shown in Figure 7.19 (a) with driving currents from 50 – 90 mA, spectral data from driving currents above 90 mA were not used in this analysis because electrical heating limited emission. The graph in Figure 7.20 shows the logarithm of the driving current as a function of the logarithm of the square root of the integrated intensity. The red line corresponds to a linear interpolation of the data, showing that the gradient of this data corresponds to a Z value of 1.66 ± 0.003. This implies that the recombination mechanisms of the device are a mixture of SRH and radiative recombination, with Z = 1 corresponding to SRH and Z = 2 corresponding to radiative. This is expected, as at low temperature, Auger recombination is lower due to it being $\propto T^3$. As well as this, type-II bandgap alignment suppresses Auger recombination as explained in section 2.2. The presence of SRH recombination is unexpected due to the Ga-free nature of the superlattice, however, this could be caused by other native defects in the structure.

LED 7.2 was the best performing device of all of the ones grown, as the other ones did not work. LED 7.1 and LED 7.2 both had equal numbers of repeats for their active region and the rest of the structure was the same. This implies that LED 7.1 did not emit light due to the strain balancing conditions being too far from strain balanced, this could have caused relaxation to occur in the superlattice. LED 7.3 however, had almost the same strain balancing as LED 7.2, implying that it was not relaxation in the system which stopped the emission. This can further

be seen in the XRD scan, the strain balancing conditions are very close to perfect with little to no peak splitting. This implies that it was the doubling of repeats which caused the lack of light being emitted, a thicker intrinsic region will increase the resistance across it, causing further problems regarding the injection of charge carriers.

7.5. Room-temperature light emitting diode

In order to create an LED emitting at room temperature, the factors which limited the device reported at 4K in section 7.4 were changed. These were: injection of electrons from GaSb into the InAs based superlattice and the resistance of the devices due to the thickness of the depletion region. A device was designed which had a ~330 nm active region and a 500 nm n-InAsSb region below the active region. The thinner active region decreases the resistance across the depletion region, allowing for carriers to be injected more easily. The InAsSb has its conduction bandedge closer to the mini-band created by the SLS, meaning that there is less of a gap to breach compared to GaSb into the InAs/InAsSb SLS mini-band. Moreover, the electron blocking barrier was changed from a lattice matched $Al_{0.9}Ga_{0.1}AsSb$ layer, to an $AlAs_{1-x}Sb_x$ layer. This is because it was simpler to grow, requiring less calibration due to the less complex structure. A schematic of the new structure can be seen in Figure 7.21.

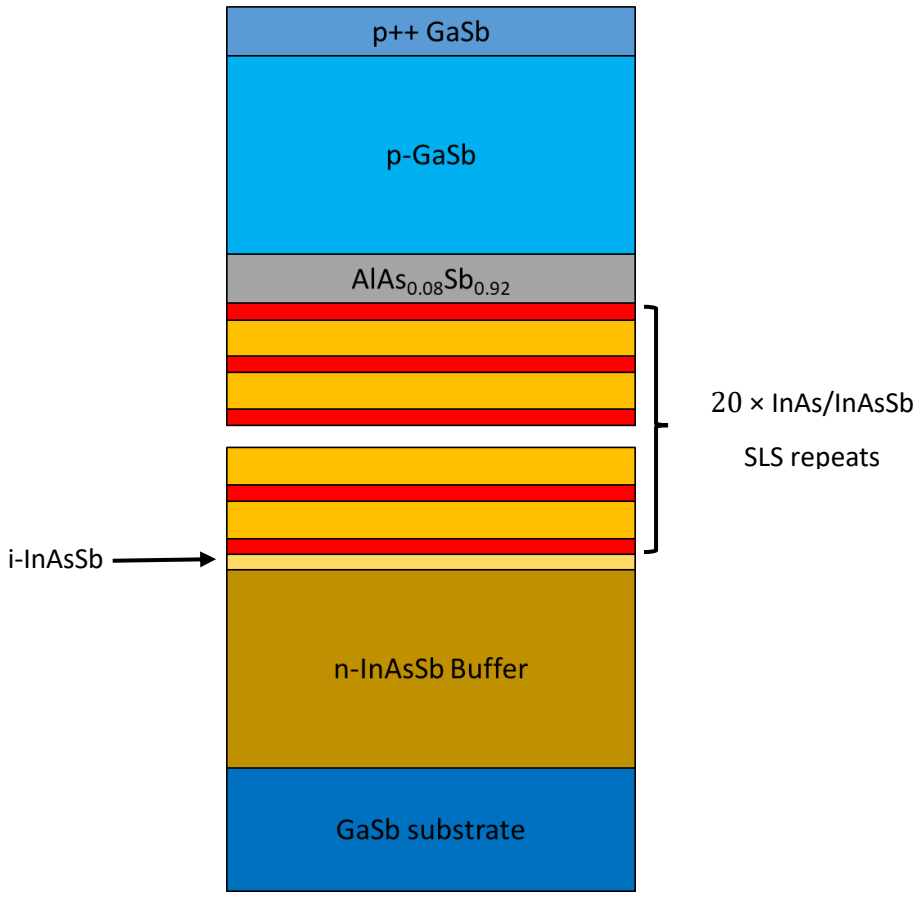

Figure 7.21: A schematic of the LED with an n-InAsSb buffer region grown on n-GaSb substrate.

7.5.1. Band structure

The bandedges of the improved device design can be seen in Figure 7.22. Comparing it to the bandstructure in Figure 7.14, where GaSb was used as the n-doped region before the active region. There is a gradual increase in energy from the n-buffer to the SLS active region, making it easier for charge carriers to be injected. The AlAsSb electron blocking layer also still provides a sufficient potential barrier with the removal of Gallium from the alloy.

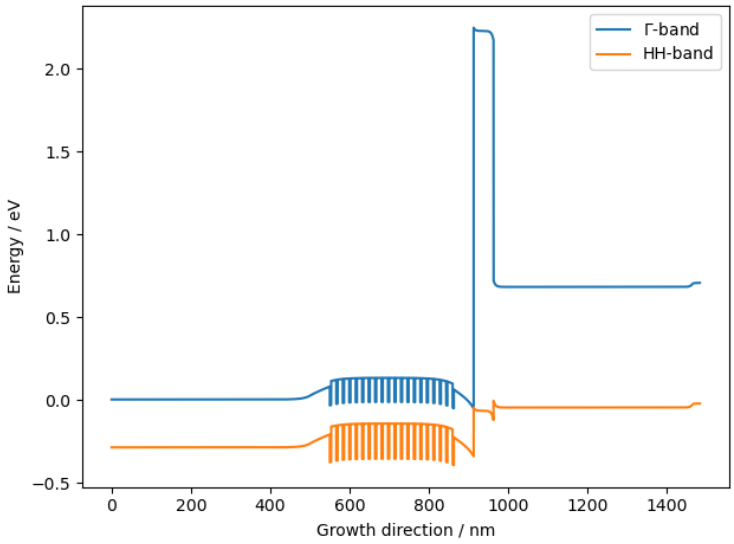

Figure 7.22: The band structure of the Gamma and heavy-hole bands of the LED structure with an n-InAsSb buffer region simulated in Nextnano.

7.5.2. Growth

The growth of the structure follows that described for the previous LED sample in section 7.4.1. The differences in growth only come from the n-InAsSb buffer region, the i-InAsSb region before the SLS and the AlAsSb replacing the AlGaAsSb. The n-InAsSb region was grown at a rate of 1 ML/s at 420°C, doped using Te to a concentration of 2×10^{18} cm^{-3}. The Te was shut off to grow the 50 nm i-InAsSb layer just before the SLS, this was to eliminate dopants entering the active region. The p-electron blocking region was grown directly after the superlattice as well, this was done at the same growth rate, using the same substrate temperature as the previous device.

The cell temperature set-points for the growth of the superlattice region, as outlined in section 7.3.1, were used to grow strain balanced quantum wells of a specific InAsSb alloy content and well thicknesses. The antimony valve set point for the superlattice was changed so that it would create lattice matched InAsSb to GaSb for the buffer region. Furthermore, to grow a 50 nm AlAsSb electron blocking barrier with a critical thickness > 50 nm, an approximate As cell valve position was chosen to try and obtain the correct flux to create a sufficiently lattice matched alloy for this layer. Based on modelling of the XRD scan of each specific growth, the As valve position was changed to obtain an alloy content which had a critical layer thickness of > 50 nm, thus, would have no relaxation. This was based on the Matthew-Blakeslee model as a more conservative estimate.

7.5.3. Structural characterisation

To confirm the structure of the devices which were grown, XRD was used. Three samples were grown: LED 7.4, LED 7.5 and LED 7.6, their XRD scans can be seen in Figure 7.23 (a), (b) and (c) respectively. The superlattice active region characteristics as well as the electron blocking barrier alloy content can be found in Table 7.4.

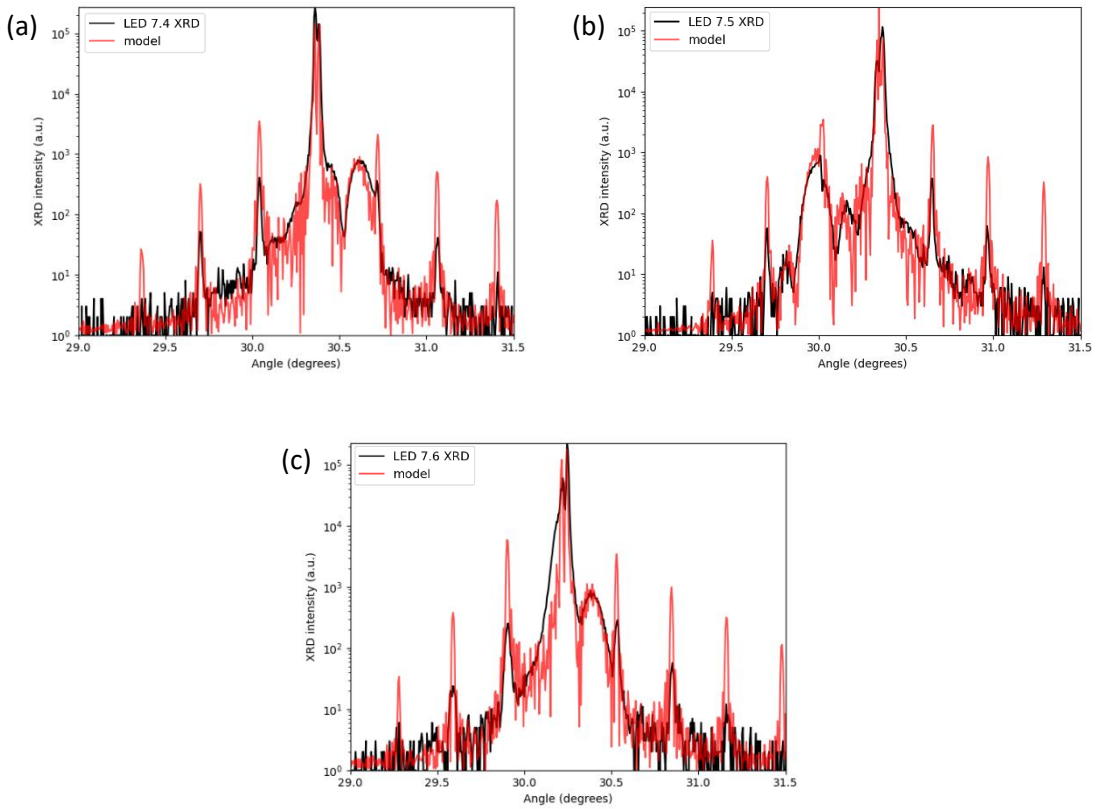

Figure 7.23: XRD and corresponding models for (a) LED 7.4, (b) LED 7.5 and (c) LED 7.6.

Each of the different device samples have a SLS active region which is approximately the same as that of the PL sample SAMPLE 7.7, described in Table 7.2. Moreover, it is clear that although the InAsSb bulk layer is not perfectly lattice matched, it is close enough to the GaSb peak that it would not cause relaxation, 500 nm would be within its critical layer thickness according to the People and Bean model [40] as modelled using the script available in section 9.3. The only non-superlattice satellite peak observable from the scans is that of the AlAsSb layer, the relatively broad peak shifting to the left and right of the substrate peak between scans. This is due to miscalibration of the As valve position. The As content in the AlAsSb alloy to make it close to lattice matched with GaSb is very small, however a high As bulk temperature is required to grow the InAs based alloys in the superlattice. It would be detrimental to the repeatability of the group-III incorporations to change the bulk temperature of the As cell mid growth. This means

that a small As valve position is required to create the correct flux for the alloy, at small valve positions, the As flux varies significantly which is why several growths were needed to achieve the correct AlAsSb alloy. With the valve positions for LED 7.4, LED 7.5 and LED 7.6 being 30, 15 and 22 respectively.

Sample	$AlAs_xSb_{1-x}$	Critical layer thickness / nm		InAs / nm	$InAs_{1-x}Sb_x$	
		Matthews-Blakeslee	People-Bean		Width / nm	x
LED 7.4	0.135	34.0	49.0	2.85	12.2	0.103
LED 7.5	0.010	21.4	20.8	3.05	13.1	0.111
LED 7.6	0.116	62.3	1430	3.08	13.2	0.116

Table 7.4: The critical layer thicknesses of the 50 nm AlAsSb alloys grown as the electron barrier in the SLS LED samples. As well as the alloy content and thickness of the SLS active region.

The critical layer thicknesses of the AlAsSb alloys grown as the electron blocking barrier of each of the devices is shown in Table 7.4. From this, it is clear that only LED 7.6 has an electron barrier which is an alloy which will not have caused relaxations in the material grown on GaSb. LED 7.4 and LED 7.5 both have electron barriers which exceed the critical layer thickness for the alloys grown in both the Matthews-Blakeslee and People-Bean models, this could cause relaxations in the material, which will negatively impact the crystalline properties of the p-GaSb grown above it.

7.5.4. Device fabrication

The devices were fabricated in the same way that they were for the previous LED device, as outlined in section 7.4.4, in line with the methodology laid out in section 3.4. Devices had top-bottom contacting configurations with 800, 400 and 200 µm mesa structures.

7.5.5. Electrical characterisation

Once the samples had been fully fabricated, they were mounted onto TO headers and wire bonded. They first had their IV characteristics tested, as was done for the previous LED samples in section 7.4.5.2. The IV curves for the three fabricated devices are shown in Figure 7.24 (a), (c) and (e); the corresponding resistances are shown in Figure 7.24 (b), (d) and (f) for LED 7.4, LED 7.5 and LED 7.6 respectively.

All of the IV curves show that the devices have diode-like characteristics, implying that the dopants had properly incorporated into the system and there was good contacting. Moreover, the resistance being ~ 10 Ω when the devices have a forward bias of ~ 1.5 V shows good electrical characteristics of the device, this was similar to other devices shown throughout this thesis which have successfully operated at room temperature. This implies that there isn't a problem with moving charge carriers through the device.

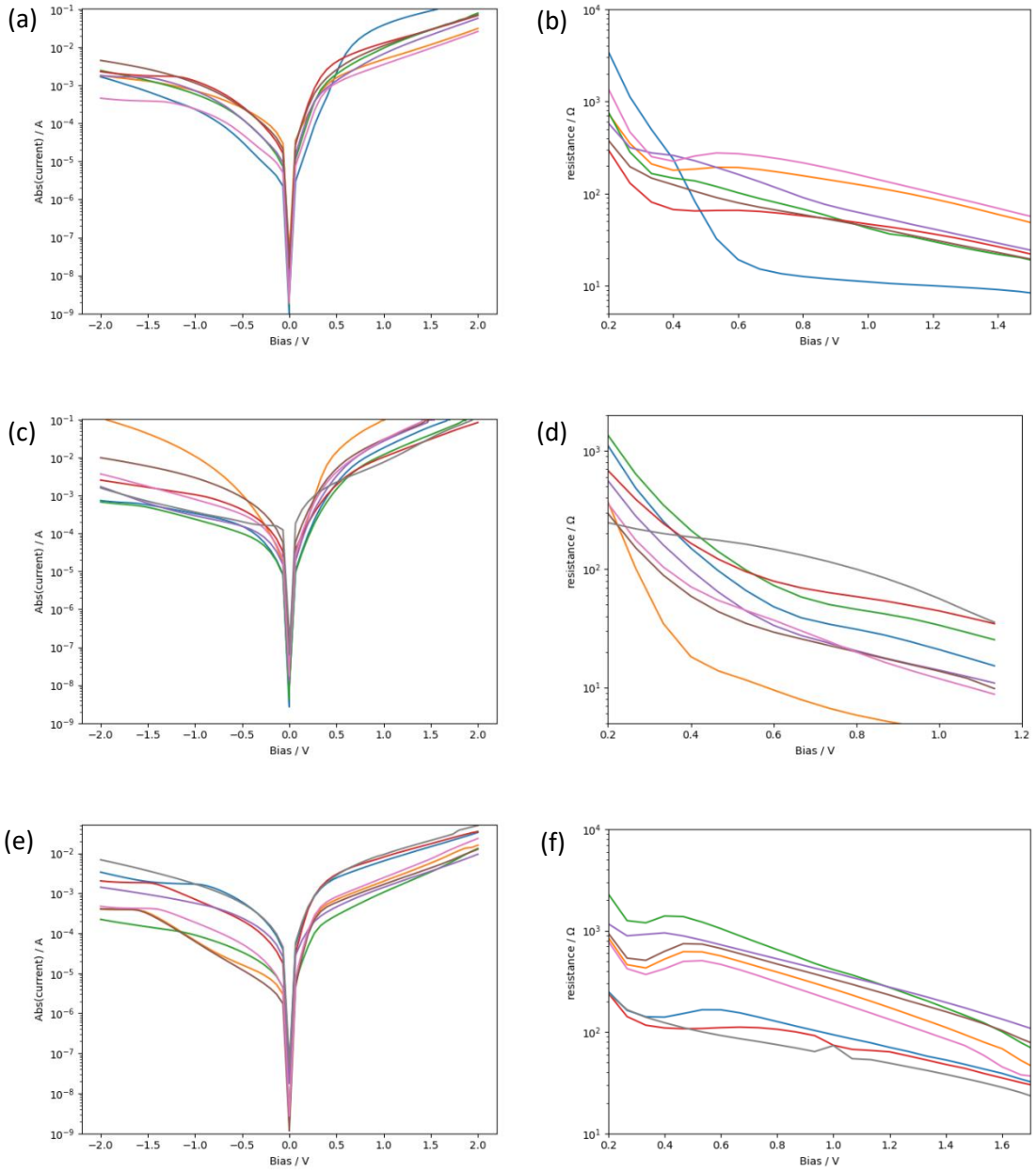

Figure 7.24: The IV curves and corresponding resistances of several devices fabricated from: (a) and (b), LED 7.4; (c) and (d), LED 7.5; and (e) and (f) LED 7.6.

7.5.6. Electroluminescence

The optical properties of LED 7.6 were tested; the others were not due to the thickness of the electron blocking barrier exceeding its critical layer thickness. The optical testing of LED 7.6 was conducted from 4 – 300 K using the set-up described in section 3.6, using an AC source of 1kHz and a duty cycle of 10 % to reduce Joule heating. The current dependant EL spectra measured at 4K can be seen in Figure 7.25 (a), the peak is around 3900 nm and blue shifts as the driving current is increased. This blue shift is characteristic of type-II devices, so this confirms the nature of the emission coming from the type-II superlattice structure [204].

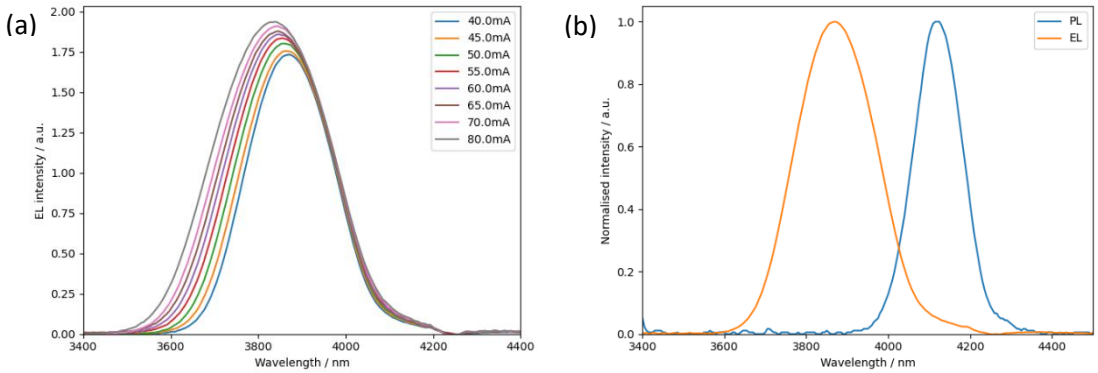

Figure 7.25: (a) 4K current dependent electroluminescence of LED 7.6 from 40 - 80 mA, after which heating effects quenched the increase in EL intensity and (b) a comparison between the EL and PL sample at 4K.

A comparison of the EL and PL at 4 K can be seen in Figure 7.25 (b), this shows that the EL has blue shifted by 23.3 meV with respect to the PL. This is expected in a device due to band filling, which does not occur in PL samples. Moreover, as the number of QW repeats increases, the charge carrier confinement offset decreases as the mini-band forms. Because of this, the PL samples will have a smaller bandgap, as they have a 1 µm active region, whereas the active region in the device is ~300 nm thick. This is a further attribute to the reduction in emission wavelength of the device compared with the PL sample.

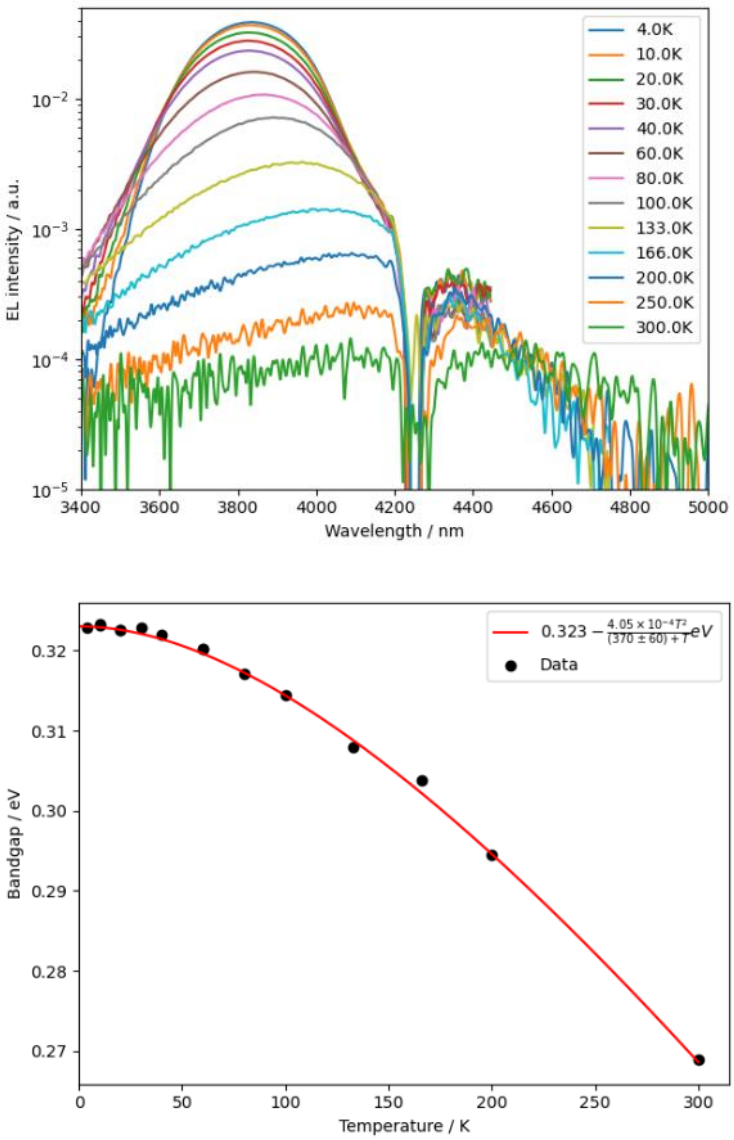

Figure 7.26: (a) the EL spectra driven with an AC of frequency 1.00kHz, duty cycle 10 % and driving current 80mA from 4 - 300 K and (b) the corresponding bandgap dependence with a fitted Varshni plot.

The temperature dependant spectrum of LED 7.6 from 4 – 300 K can be seen in Figure 7.26 (a). From this, it is clear that the sample acts as expected, with the wavelength increasing as temperature is increased. The bandgap dependence can be seen in Figure 7.26 (b), being fitted with the Varshni fit of parameters: $E_g(0)$ = 0.323 eV, α = 0.405 meV K^{-1} and β = 370 ± 60. Using bandgap values from Vurgaftman [21], the value of α obtained here is identical to two significant figures as that displayed in the paper. However, the Debye temperature (β) is different, with the linear interpolation for $InAs_{0.884}Sb_{0.116}$ being 161 K. The discrepancy in the Debye temperature could be due to the effects that quantum confinement has on the bandgap and how that shifts with temperature. The intensity of the low temperature spectrum is very high, however, as the temperature is increased to 300 K (RT), the intensity of the spectrum undergoes strong quenching of a factor > 100. Implying that the increase in temperature has a profound effect on

the radiative recombination. The CO_2 absorption peak can clearly be seen in the room temperature spectrum, this means that this structure has the possibility of being used in the detection of CO_2.

The data from Figure 7.26 (a) was also analysed by plotting the EL intensity normalised to intensity at 0 K as a function of $1/k_BT$, with T being the temperature the EL was measured at. A plot of this can be seen in Figure 7.27, with a fit showing the non-radiative recombination activation energy, given by equation 7.3. Where $E_{A_1}(T)$ is the temperature dependant activation energy; with the non-radiative coefficient C_1 and E_{A_2} is the non-temperature dependant non-radiative activation energy, with the coefficient of C_2. This was fitted to the Arrhenius plot using data fitting in Python 3.0 and can be seen as the red line on Figure 7.27.

$$I = \frac{I_0}{1 + C_1 \exp\left(-\frac{E_{A_1}(T)}{k_B T}\right) + C_2 \exp\left(-\frac{E_{A_2}}{k_B T}\right)} \tag{7.3}$$

This gives a non-radiative activation energy E_{A_2} = 3±1 meV, it is implied that this would correspond to the defect mediated SRH activation energy as it does not correspond with any activation energies relating to band structure calculations, such as the Auger mechanisms [207]. Regarding the temperature dependant activation energy, $E_{A_1}(T)$, this is dependent on the bandgap as described by the Varshni equation and often corresponds to Auger recombination processes, shown in 7.4. This is obtained by combining equations 2.1 and 2.18.

$$E_{A_1}(T) = \frac{m_C}{m_C + m_{HH}}\left[E_g(0) - \frac{\alpha T^2}{T + \beta}\right] \tag{7.4}$$

Find the activation energy, the coefficient before the bandgap was found using the data fitting code. Different Auger mechanisms have different coefficients, as discussed in section 2.2.2.3. The coefficient found by the data fitting was in accordance with $\frac{m_c}{m_c+m_{HH}}$ for the specific material system, because of this, it was evident that the CHCC Auger process is dominant for the non-radiative recombination mechanisms at room temperature.

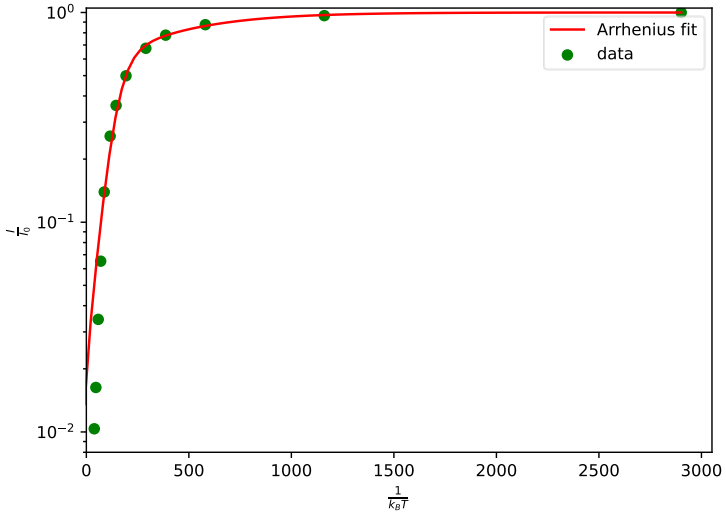

Figure 7.27: plot of EL intensity normalised to intensity at T = 0 K as a function of $1/k_BT$ with an Arrhenius plot fitted.

The value for the effective mass ratio of the experimental data is $(7\pm1)10^{-2}$, whereas the linearly extrapolated data from Vurgaftman et. al. shows a ratio of $6.35x10^{-2}$. The data for the Varshni equation was taken directly from a fitting of the Varshni parameters to the experimental data shown in Figure 7.26 (b). This implies that the main cause of non-radiative in this system is the CHCC process as the activation energy calculated from Figure 7.27 corresponds within experimental error from low temperature up to room temperature. It should however be noted that the fit is worse at higher temperatures, however, this could be due to a decrease in accuracy in measuring the EL spectra as the intensity decreases.

7.6. Summary

In this chapter, the conditions of strain balancing InAs with $InAs_{1-x}Sb_x$ alloys grown as a superlattice on n-GaSb substrates have been discussed and simulated. The benefits of growing strain balanced samples were discussed and a map of possible strain balanced growths was given. The bandstructure of the type-II active region was shown, and a k·p 8-band simulation via Nextnano was conducted. This showed the possible states for the electrons in the conduction bands and the three lowest valence band states which were hh_1, lh_1 and hh_2. As well as the active region itself, a simulation of the active region inside a LED structure was conducted, which showed band-bowing between the GaSb doped regions and the active region.

Strain-balancing calibration samples with x = ~10.5 % were then grown and had photoluminescence spectra measured at 4 K. The emission spectra, with peaks at ~ 4100 nm corresponded to the bandgap simulations, with e_1-hh_1 and e_1-lh_1 recombinations being

measured. Moreover, it was shown that when the antimony fraction is increased from ~ 0.11 to ~ 0.12, that there is a significant decrease in the intensity of the spectra. It has been shown in previous literature that SLS structures and strain balanced structures work for InAsSb alloys with Sb contents of > 0.13. The several structures grown with Sb ~ 0.12 which did not give PL signal at ~ 4 K implies that there could be something innate about this Sb incorporation which supresses radiative recombination, but this would require further investigation. This is not a material relaxation problem, because the layer thickness of the InAsSb layer was less than that of the critical layer thicknesses of both the Matthews-Blakeslee and People-Bean model.

These strain-balanced SLS active regions were also placed into LED structures and fabricated into 800 µm mesa diode devices. Of the three devices grown, only LED 7.2 gave electroluminescence from 7 – 80 K, with the low temperature recombination mechanisms being SRH and radiative. The fact that this device does not produce emission above 80 K is likely to be due to the band bowing between the GaSb and InAsSb based active region, giving high potential barriers for the charge carriers to cross. Based on this, more LEDs with the n-GaSb buffer before the active region replaced with an n-InAsSb buffer and a thinner active region were grown and characterised. These device gave room temperature emission with a clear spectrum, with the peak wavelength being ~ 4500 nm. Showing that this material system is suitable for integration into devices for room temperature emission. However, the material system is limited by non-radiative modes including the CHCC Auger process and SRH recombination.

Further research into this material system could include creating thinner QWs in the SLS active region to see how this affects emission. In terms of both intensity and wavelength, it could be possible to bring the room temperature emission down to < 4000 nm leading to more applications for the material system. This could possibly lead to applications in sensing carbon black pigmented plastics, as referred to in section 5.4.3.1.

8. Conclusion

- First report of a strain-balanced InAs/$InAs_{1-x}Sb_x$ strained layer superlattice LED with dilute Sb grown on GaSb. The device gave bright emission up to room temperature with a peak wavelength of ~4.5 µm, making it an ideal candidate for devices sensing CO_2.
- A comprehensive study into the fundamental physical properties of the InAs/$InAs_{1-x}Sb_x$ material system was also conducted, showing the dominant recombination mechanisms as well as the emission limiting factors from 4K to room temperature.
- Investigation into the optimal growth temperature of high-In type-I InGaAsSb/GaSb MQWs. Showing that a decreased growth temperature increases the miscibility of the high-In alloy, resulting in bright room temperature PL samples.
- An extensive review of existing plastic sorting technologies was conducted showing the possibility for black plastics to be integrated into a circular economy using existing infrastructure with new technologies.
- Distinct mid-infrared fingerprints for polypropylene, polyethylene and polyvinylchloride were found in the 3 – 4 µm region for regular and carbon-black pigmented samples. Showing that it is possible to detect them using existing mid-infrared emitter/detector technology.

8.1. Optical solutions to sorting black plastics

The current industrial technologies' inability to sort plastic containing the carbon black pigment by polymer type via NIR spectroscopy has led them to being non-recyclable on a mass scale. This is a problem as it contributes to the linearity of the current economic model, which requires greater amount of virgin resources to be extracted and processed into new plastics. However, the climate crisis and related pollution crises show that this linear model of the economy is insufficient in providing for humanity in a sustainable way, a move to a circular economy is vital. Being able to recycle as many different types of plastic as possible is a vital part of a circular economy. A case was argued as to why rather than banning black plastics, it would be more beneficial to find technologies which are able to recycle them.

There currently exist several methods which can be used to sort black plastics by polymer type, including laser induced breakdown spectroscopy (LIBS) and mid-infrared spectroscopy. However, both of these methods are highly energy intensive, largely due to them relying on a laser source. However, using mid-infrared spectroscopy, conducted using Fourier-transform Infrared (FTIR) spectroscopy, it was shown that commonly used plastics: polypropylene (PP), polyethylene (PE) and polyvinylchloride (PVC) show absorption characteristics in the 3.3 – 3.6 µm range. These absorption peaks are caused by CH_2 and CH_3 symmetrical and asymmetrical rotational bonds in the polymer, they are detectable in plastics both with and without carbon-black pigment. This shows that MIR spectroscopy in the 3 – 4 µm range has the possibility of being suitable for identifying plastics containing carbon black pigment. Moreover, this shows that there is a possibility that these absorption peaks may be identifiable in different plastics by using MIR LEDs with peak wavelengths corresponding to the absorption lines for each different type of plastic. This would allow an array of LEDs to be able to be used to identify black plastics by polymer type. LEDs would give the advantage over other light sources due to them having a lower power consumption and being portable, meaning the sorting technology would have a lower power usage and could have hand-held sensing applications.

8.2. Type-I InGaAsSb/AlGaAsSb MQWs

A study of the strained, type-I InGaAsSb MQW systems grown on n-GaSb substrates was conducted with lattice matched $Al_wGa_{1-w}AsSb$ barriers with varying Al content, this was in the range $0 < w < 0.35$. Moreover, a range of Indium and Antimony contents in the QWs was studied to find a plethora of available bandgaps and emission ranges in this material.

Simulations of the InGaAsSb alloy's critical layer thicknesses when grown on a GaSb substrate were carried out using the Matthews-Blakeslee and People-Bean models. Both models give slightly different absolute values for the critical thicknesses of the alloy, this is due to the considerations that they give for the cause of dislocations. However, both models show that it is possible to obtain InGaAsSb QWs with thicknesses greater than 10 nm with Indium levels greater than 0.3 by increasing the As content in the QW relative to the amount needed with lower levels of Indium. Bandgap simulations were conducted using Nextnano, k·p 8-band simulations at room temperature on the type-I QW with varying group-III and group-V mixtures. This shows that it is possible to get a wide variety of bandgaps from 0.7 eV to 0.35 eV using 10 nm QWs at room temperature, it was further possible to engineer bandgaps by changing the thickness of the QW, by varying the QW from 5 nm to 15 nm the bandgap of a set alloy could be changed from 0.6 eV to 0.45 eV.

Samples were grown via MBE, structurally characterised via XRD and devices fabricated using standard photolithographic techniques. With an $In_{0.34}Ga_{0.66}As_ySb_{1-y}$/ $Al_{0.35}Ga_{0.65}As_{0.034}Sb_{0.966}$ type-I active region five samples were grown, it was shown that with a 9.3 nm QW, by increasing the As content (y) from 0.032 to 0.112 the RT PL emission energy decreases from 0.56 eV to 0.50 eV, increasing the QW width to 14.5 nm further decreases the emission energy to 0.48 eV. When the structure was changed to $In_{0.4}Ga_{0.6}As_{0.15}Sb_{0.85}/Al_{0.25}Ga_{0.75}As_{0.02}Sb_{0.98}$, the PL peak energy further decreased to 0.41 eV, around 3µm with high rates of radiative recombination. One contributing factor to the high rates of radiative recombination is the suppression of certain Auger recombination mechanisms due to strain in the QW. However, when integrated into an LED structure, this gave room temperature emission around 2.7 µm with an increased rate of non-radiative recombinations.

To see the effects of removing Al from the barriers, InGaAsSb/GaSb type-I samples were grown on n-GaSb substrates. To obtain the desired wavelength of ~ 3.3 µm, the Indium concentration in the QW's alloy was grown with a range of 0.5 – 0.55 with varying As concentrations from 0.15 – 0.3. This gave a range of samples with PL peak wavelengths spanning from 2.5 – 3.4 µm. Moreover, it was found that a lower substrate temperature of 380 °C yielded samples which had better quality QWs with more intense PL spectra when compared to those grown with a substrate temperature of 400 °C. The difficulties in growing the alloy with a substrate temperature of 350 °C were shown due to the increase in the Arsenic incorporation in the alloy. These findings are significant because the growth of this InGaAsSb alloy is in the miscibility gap, meaning it is more difficult to form a uniform alloy. So, growing the alloy in this alloy range allows for a wider range of alloys to be accessed for future devices. Finding ideal growth temperatures for the different alloy mixtures in the miscibility gap is vital in creating high-quality type-I QWs which can be integrated into LEDs for emission at 3.3 µm at room temperature.

8.3. Type-II InAs/InAsSb strain balanced superlattice

Type-II InAs/InAsSb strain balanced superlattices grown on n-GaSb superlattices were studied, with the Sb content being varied between 0.10 – 0.12 and the thickness of the QWs altered whilst maintaining strain balanced conditions. Simulations of the strain balanced conditions were carried out, showing the different systems which could be grown strain balanced, which is critical in order to prevent the formation of defects in the structure. Moreover, band-structure simulations were carried out in Nextnano, showing that increasing the thickness of the InAs layer and decreasing the amount of Sb in the InAsSb alloy whilst maintaining strain balancing conditions both decrease the bandgap, and thus increase the wavelength. At 4K, the bandgap

energy ranges from 0.32 – 0.26 eV for 0.10 < Sb < 0.13 and the thickness of the InAs layer from 2 – 4 nm, this is a wavelength range of 3.88 – 4.77 µm.

The strain balance calibration samples showed bright PL spectra at low temperature, with samples being grown with InAs thicknesses between 2.5 – 3.0 µm and Sb contents between 0.106 – 0.123. The low temperature PL spectra of these samples were between 4.1 – 4.2 µm as expected based on the simulations which were carried out. Low temperature PL has a Z-value of ~1.5, this implies that the recombination mechanisms at low temperature are around equal parts radiative and SRH, this is in comparison to Z-values of ~2 obtained for samples with higher Sb contents. This implies that dilute Sb in this system causes an SRH contribution to the recombinations, which is not seen in samples with higher Sb, as shown in previous work at Lancaster University. Moreover, it was shown that when Sb > 0.12, for strain balanced samples, the PL is extremely dim. This implies that there could be a possible limiting factor which occurs when in this system at Sb ~ 0.12.

The superlattices grown for these strain balance calibrations were then integrated into two LEDs as the active region. Both grown on n-GaSb substrates with p-GaSb top layers and a lattice matched p-$Al_{0.9}Ga_{0.1}As_{1-y}Sb_y$ electron blocking layer, but one had an n-GaSb layer before the SLS and the other had an n-InAsSb one. Both devices gave spectra at low temperature, but the device with an n-GaSb buffer ceased emitting at 80 K due to problems injecting charge carriers into the active region because of the mismatch in conduction band-edges. Whereas the device with an n-InAsSb buffer emitted up to room temperature, with a peak wavelength ~ 4.5 µm. This means that this is a viable structure for devices used in the detection of CO_2.

8.4. Future work

To further the research conducted in this thesis, the study of the spectral fingerprint of more plastic types in the 3 – 4 µm range should be conducted using FTIR spectroscopy. This could include but is not limited to: polyethylene terephthalate (PET), polystyrene (PS) and styrene butadiene rubber – commonly used in the production of automotive tyres. Moreover, LED spectra around 3.3 – 3.6 µm could be tested when being reflected from the surface of plastics, this would show if it is possible to discern these spectral characteristics using LEDs, as opposed to a multimode laser as in FTIR spectroscopy. Furthermore, given that the aforementioned research yielded positive results, a simple spectrometer could be created using an LED with a tailored linewidth and an array of very spectrally pure resonant cavity detectors which could be used to detect which plastics had which absorption bands and thus discriminate between the different polymer types.

The research on type-I devices and active regions could be furthered by growing a larger number of samples with AlGaAsSb lattice matched barriers and increasing the wavelength from ~ 3 µm to the intended 3.3 µm for use in polymer detection. This could be done by increasing the indium as well as the arsenic contents in the alloy. Further growths should also be conducted with a substrate temperature of 350 °C with a lower Arsenic content to see how its emission compares to those which were grown using a higher substrate temperature. Also, a greater selection of alloys could be grown for the InGaAsSb/GaSb material system emitting at 3.3 µm. The combination of both of these would allow for a comparison between the materials systems, seeing which is more suitable for integration into high performing LEDs. The integration of the InGaAsSb/GaSb material system into RCLEDs would also be beneficial, as the negation of the AlGaAsSb barriers could make cavity growth as well as charge transportation through the cavity much easier.

For the development of the InAs/InAsSb material system, it would be beneficial to conduct further investigations on the cause of the poor rates of radiative recombinations in SLS structures with Sb ~ 0.12. This could include growing SLS structures with thinner repeats, as this somewhat increases the intensity of the samples shown here, this could allow for Z-values to be calculated to see what mechanisms is limiting the emission. Moreover, a set-up allowing a wider range of laser input powers for PL should be used, over at least one order of magnitude to more accurately calculate the Z value. As well as this, using the material system, which was successfully integrated into an LED structure, the effect of thinning the QW in line with the strain balancing conditions could be investigated. This would show the possible spectral range which this material system can cover. Finally, the system could be integrated into RCLEDs, this would be important if it were to be used for the detection of CO_2 or CO.

9. Appendix

9.1. Mid-infrared light emitting diodes from literature review

Active region	Peak wavelength / µm		Output power / µW	Date	Citation
GaSb bulk	1.7			1971	[57]
$In_{0.94}GaAs$ bulk	3.3			1992	[59]
InAsSbP bulk	4.7			1992	[59]
$InAsSb_x$ bulk	x = 0	3.3		1993	[58]
	x = 0.06	3.5			
	x = 0.15	4.2			
GaInAsSb/ AlGaAsSb bulk	4.37		3 700	1997	[62]
InAsSb/ InAsSbP bulk	4.5		50	1999	[60]
InGaAsSb/ AlGaAsSb bulk	4.37		20	2013	[64]
AlInSb bulk	3.9 – 7.6			2018	[65]
InAsSb bulk	4.5		6	2019	[9]
GaInSb/ GaSb SQW	x = 0.26	1.9		1996	[68]
	x = 0.35	2.2			
$InAs/InAsSb_x$ type-II QW	x = 0.16	5	50	1998	[69]
	x = 0.25	8	24		
GaSb/InAs type-II QW	3.3			2019	[71]
$GaIn_{0.9}As$/ AlGaAs type-I QW	2.4		1.85	1996	[84]

$Al_{0.25}GaAs_{0.02}Sb$/ $In_{0.16}Ga_{0.84}AsSb$ type-II MQW	2.0			1996	[73]
$Al_{0.25}GaAs_{0.02}Sb$/ $In_{0.40}GaAs_{0.14}Sb$ type-I MQW	2.8			2004	[72]
$Al_{0.25}GaAs_{0.02}Sb$/ $In_{0.30}GaAs_{0.096}Sb$ type-I MQW	2.24			2004	[76]
AlGaInAsSb/ InGaAsSb type-I MQW	2		2 800	2010	[78]
	3		140		
AlGaInAsSb/ $In_{0.55}GaAs_{0.22}Sb$ type-I MQW	3.0 – 3.5		700	2008	[79]
AlGaInSb/GaInSb type-I MQW	4.2			2016	[80]
$In_{0.55}GaAsSb$/ GaSb type-I MQW	3.4			2015	[83]
$InAs_{0.915}Sb$/ $Al_{0.12}InAs$ type-I MQW	3.4		80	2022	[10]
InAs/$InAsSb_{0.08}$ type-II SLS	4.2		100	1999	[94]
InAs/$InAsSb_{0.13}$ type-II MQW	4.0		1.4	2006	[95]
InAs/$InAsSb_{0.08}$ type-II MQW	4.2		12	2009	[32]
InAs/$InAsSb_x$ type-II MQW	x = 6	4.4	8.2	2018	[96]
	x = 8	4.7	3.3		
InAs/InAsSb RCLED	3.96			2004	[110]
InGaAsSb/ AlGaAsSb RCLED	2.3		400	2008	[111]
InAsSb RCLED	4.2		5.5	2019	[200]
InAsSb/AlInAs RCLED	4.5			2020	[113]

InAs/GaAsSb RCLED	4.6		2023	[114]
InAs/GaSb ICLED	4	900	2008	[100]
InAs/GaSb ICLED	8.6	600		[101]
InAs/GaSb ICLED	3.81		2015	[102]
InAs/GaSb RC-ICLED	3.3	30	2020	[104]
InAs/GaInSb W-QW ICLED	3.1	2 900	2018	[106]

Table 9.1: a summary of the mid-infrared devices in the literature as discussed in this chapter including the active region type, their peak wavelength emission and the output power where it was disclosed.

9.2. Sample and LED MBE codes

Sample name	**MBE code**
Sample 6.1	XMB2179
Sample 6.2	XMB2181
Sample 6.3	XMB2182
Sample 6.4	XMB2184
Sample 6.5	XMB2185
Sample 6.6	XPB2295
Sample 6.7	XPB2296
LED 6.1	XPB2299
LED 6.2	XPB2300
Sampe 6.8	XPB2395
Sample 6.9	XPB2416
Sample 6.10	XPB2417
Sample 6.11	XPB2418
Sample 6.12	XPB2421
Sample 6.13	XPB2423
Sample 6.14	XPB2419
Sample 6.15	XPB2422
Sample 7.1	XPB2360
Sample 7.2	XPB2361

Sample 7.3	XPB2362
Sample 7.4	XPB2363
Sample 7.5	XPB2484
Sample 7.6	XPB2485
Sample 7.7	XPB2486
LED 7.1	XPB2366
LED 7.2	XPB2367
LED 7.3	XPB2368
LED 7.4	XPB2491
LED 7.5	XPB2492
LED 7.6	XPB2493

Table 9.2: Samples and LEDs as named in their thesis and their corresponding MBE codes as per Lancaster University nomenclature.

9.3. Python scripts

The Python 3.0 scripts used for simulations in this thesis are available at: https://github.com/bondpw/Thesis-scripts.git.

The script used to calculate the strain balancing conditions for InAs/$InAs_{1-x}Sb_x$ strain layered superlattices grown on GaSb substrates is “Strain balancing.py”. The scripts which are used to calculate the critical layer thickness of $In_xGa_{1-x}As_{1-y}Sb_y$ and $Al_xGa_{1-x}As_{1-y}Sb_y$ on GaSb substrates are “Critical thickness – InGaAsSb.py” and “Critical thickness – AlGaAsSb.py” respectively. Both scripts can be used to find the critical layer thickness according to the Matthews-Blakeslee or People-Bean equation, this is defined by the user.

Bibliography

1. Bauer, C., et al., *A Mid-infrared QEPAS sensor device for TATP detection.* Journal of Physics: Conference Series, 2009. **157**: p. 012002.
2. Peng, Q., et al., *Lasers in medicine.* Reports on Progress in Physics, 2008. **71**(5): p. 056701.
3. Willer, U., et al., *Near- and mid-infrared laser monitoring of industrial processes, environment and security applications.* Optics and Lasers in Engineering, 2006. **44**(7): p. 699-710.
4. Popa, D. and F. Udrea, *Towards Integrated Mid-Infrared Gas Sensors.* Sensors, 2019. **19**(9): p. 2076.
5. Vainio, M. and L. Halonen, *Mid-infrared optical parametric oscillators and frequency combs for molecular spectroscopy.* Physical Chemistry Chemical Physics, 2016. **18**(6): p. 4266-4294.
6. Signoret, C., et al., *MIR spectral characterization of plastic to enable discrimination in an industrial recycling context: II. Specific case of polyolefins.* Waste Management, 2019. **98**: p. 160-172.
7. Becker, W. and N. Eisenreich, *Using spectroscopic methods for identification of technical plastics from E&E and ELV sector*, in *CARE*. 2006: Vienna. p. 1 - 15.
8. Becker, W. and N. Eisenreich, *Identification of black polymers in the mid-infrared spectral region with an FTIR-spectrometer*, in *CARE*. 1998: Vienna.
9. Delli, E., et al., *Heteroepitaxial Integration of Mid-Infrared InAsSb Light Emitting Diodes on Silicon.* IEEE Photonics Journal, 2019. **11**(3): p. 1-8.
10. Altayar, A.R., et al., *Electroluminescence characterization of mid-infrared InAsSb/AlInAs multi-quantum well light emitting diodes heteroepitaxially integrated on GaAs and silicon wafers.* Journal of Crystal Growth, 2022. **586**: p. 126627.
11. Sifferman, S.D., *Mid-infrared type-I diode lasers design using molecular beam epitaxy*, in *Electrical and computer engineering*. 2020, The University of Texas at Austin: Texas. p. 118.
12. Tournié, E., et al., *Mid-infrared III–V semiconductor lasers epitaxially grown on Si substrates.* Light: Science & Applications, 2022. **11**(1): p. 165.
13. Delli, E., et al., *Mid-Infrared InAs/InAsSb Superlattice nBn Photodetector Monolithically Integrated onto Silicon.* ACS Photonics, 2019. **6**.
14. Ryu, G., et al., *Comparative study of metamorphic InAs layers grown on GaAs and Si for mid-infrared photodetectors.* Solid-State Electronics, 2021. **176**: p. 107942.
15. *Material Social Futures*. 2025 [cited 2025 10th April]; Available from: https://www.lancaster.ac.uk/material-social-futures/.
16. Geyer, R., J.R. Jambeck, and K.L. Law, *Production, use, and fate of all plastics ever made.* Science Advances, 2017. **3**(7): p. e1700782.
17. Rosen, C. *Decomposition Rates - How long does it take to decompose?* [Organisation web page] 2020 [cited 2022 20th July]; Available from: https://www.openwildingproject.org/post/decomposition-rates-how-long-does-it-take-to-decompose.

18. Young, H. and R. Freedman, *Molecules and condensed matter*, in *University Physics with Modern Physics, Global Edition*. 2019, Pearson Education, Limited: Harlow, UNITED KINGDOM.

19. Coldren, L.A., S.W. Corzine, and M.L. Mashanovitch, *Diode Lasers and Photonic Integrated Circuits*. 2012, Newark, UNITED STATES: John Wiley & Sons, Incorporated.

20. Varshni, Y.P., *Temperature dependence of the energy gap in semiconductors.* Physica, 1967. **34**(1): p. 149-154.

21. Vurgaftman, I., J.R. Meyer, and L.R. Ram-Mohan, *Band parameters for III–V compound semiconductors and their alloys.* Journal of Applied Physics, 2001. **89**(11): p. 5815-5875.

22. Dixit, V.K., et al., *A versatile phenomenological model for the S-shaped temperature dependence of photoluminescence energy for an accurate determination of the exciton localization energy in bulk and quantum well structures.* Journal of Physics D: Applied Physics, 2014. **47**(6): p. 065103.

23. Wilson, J. and J. Hawkes, *Elements of solid state physics*, in *Optoelectronics: an introduction*. 1998, Prentice Hall Europe: Hertfordshire. p. 37 - 89.

24. Young, H. and R. Freedman, *Particles behaving as waves*, in *University Physics with Modern Physics, Global Edition*. 2019, Pearson Education, Limited: Harlow, UNITED KINGDOM.

25. Schubert, E.F., *3. Theory of Radiative Recombination*, in *Light-Emitting Diodes (2nd Edition)*. 2006, Cambridge University Press.

26. Schubert, E.F., *LED Basics: Optical Properties*, in *Light-Emitting Diodes* 2006, Cambridge University Press.

27. Schubert, E.F., *Radiative and non-radiative recombination*, in *Light-Emitting Diodes* 2006, Cambridge University Press.

28. Eales, T.D., et al., *The Nature of Auger Recombination in Type-I Quantum Well Lasers Operating in the Mid-Infrared.* IEEE Journal of Selected Topics in Quantum Electronics, 2022. **28**(1: Semiconductor Lasers): p. 1-11.

29. Lindle, J.R., et al., *Auger lifetime in InAs, InAsSb, and InAsSb-InAlAsSb quantum wells.* Applied Physics Letters, 1995. **67**(21): p. 3153-3155.

30. Gadedjisso-Tossou, K.S., et al., *Recombination channels in 2.4–3.2 µm GaInAsSb quantum-well lasers.* Semiconductor Science and Technology, 2013. **28**(1): p. 015015.

31. Sweeney, S.J., *Novel Experimental Techniques for Semiconductor Laser Characterisation and Optimisation.* Physica Scripta, 2004. **2004**(T114): p. 152.

32. Carrington, P.J., et al., *Temperature dependence of mid-infrared electroluminescence in type II InAsSb/InAs multi-quantum well light-emitting diodes.* Semiconductor Science and Technology, 2009. **24**(7): p. 075001.

33. Bett, A.W., et al., *III-V compounds for solar cell applications.* Applied Physics A: Materials Science & Processing, 1999. **69**(2): p. 119-129.

34. Vegard, L., *Die Konstitution der Mischkristalle und die Raumfüllung der Atome.* Zeitschrift für Physik, 1921. **5**(1): p. 17-26.

35. Krijn, M.P.C.M., *Heterojunction band offsets and effective masses in III-V quaternary alloys.* Semiconductor Science and Technology, 1991. **6**(1): p. 27-31.

36. O'Reilley, E.P., *Valence band engineering in strained-layer structures* Semiconductor Science Technology, 1989. **4**(121): p. 121-137.

37. Thijs, P.J.A., et al., *High-performance /spl lambda/=1.3 /spl mu/m InGaAsP-InP strained-layer quantum well lasers.* Journal of Lightwave Technology, 1994. **12**(1): p. 28-37.

38. Hjalmarson, H.P. and S.R. Kurtz, *Electron Auger processes in mid-infrared InAsSb/InGaAs heterostructures.* Applied Physics Letters, 1996. **69**(7): p. 949-951.

39. Matthews, J.W. and A.E. Blakeslee, *Defects in epitaxial multilayers: I. Misfit dislocations.* Journal of Crystal Growth, 1974. **27**: p. 118-125.

40. People, R. and J.C. Bean, *Calculation of critical layer thickness versus lattice mismatch for GexSi1−x/Si strained-layer heterostructures.* Applied Physics Letters, 1985. **47**(3): p. 322-324.

41. Hu, S.M., *Misfit dislocations and critical thickness of heteroepitaxy.* Journal of Applied Physics, 1991. **69**(11): p. 7901-7903.

42. *Applications of Molecular Spectroscopy to Current Research in the Chemical and Biological Sciences*. 2016: IntechOpen.

43. Burrows, A., et al., *Molecular spectroscopy*, in *Chrmistry*[3]. 2009, Oxford University Press: Oxford. p. 444 - 507.

44. Dudley Williams, I.F., *Infrared spectra*, in *Spectroscopic methods in organic chemistry*. 2008, McGraw-Hill Education: Berkshire. p. 27 - 61.

45. Birner, S., et al., *nextnano: General Purpose 3-D Simulations.* IEEE Transactions on Electron Devices, 2007. **54**(9): p. 2137-2142.

46. Deen, M.J. and Basu, *Appendix A: k.p Method*, in *Silicon Photonics*. 2012. p. 403-420.

47. Farrow, R.F.C., *Molecular Beam Epitaxy*. 2014, New York, UNITED STATES: Elsevier Science & Technology.

48. Bracker, A.S., et al., *Surface reconstruction phase diagrams for InAs, AlSb, and GaSb.* Journal of Crystal Growth, 2000. **220**(4): p. 384-392.

49. Young, H. and R. Freedman, *University Physics with Modern Physics, Global Edition*. 2019, Harlow, UNITED KINGDOM: Pearson Education, Limited.

50. Harrington, G.F. and J. Santiso, *Back-to-Basics tutorial: X-ray diffraction of thin films.* Journal of Electroceramics, 2021. **47**(4): p. 141-163.

51. Tkachenko, N.V., *Optical Spectroscopy : Methods and Instrumentations*. 2006, San Diego, NETHERLANDS, THE: Elsevier Science & Technology.

52. Liu, Z., et al., *Advanced technologies in InGaN micro-LED fabrication to mitigate the sidewall effect.* Light: Science & Applications, 2025. **14**(1): p. 64.

53. Harris, C.R., et al., *Array programming with NumPy.* Nature, 2020. **585**(7825): p. 357-362.

54. Larkin, P., *Infrared and Raman Spectroscopy : Principles and Spectral Interpretation*. 2011, San Diego, UNITED STATES: Elsevier.

55. Hall, R.N., et al., *Coherent Light Emission From GaAs Junctions.* Physical Review Letters, 1962. **9**: p. 366-368.

56. Melngailis, I. and R.H. Rediker, *Properties of InAs Lasers.* Journal of Applied Physics, 1966. **37**(2): p. 899-911.

57. Blom, G.M., *Electroluminescence in Liquid-Phase Epitaxial GaSb Diodes.* Journal of Applied Physics, 1971. **42**(3): p. 1057-1062.

58. Dobbelaere, W., et al., *InAsSb light emitting diodes and their applications to infra-red gas sensors.* Electronics Letters, 1993. **29**: p. 890-891.

59. Zotova, N., et al., *Optoelectronic sensors based on narrowband A3B5 alloys*. OE Fiber. Vol. 1587. 1992: SPIE.

60. Gao, H.H., et al., *InAsSb/InAsSbP light emitting diodes for the detection of CO and CO2 at room temperature.* Journal of Physics D: Applied Physics, 1999. **32**(15): p. 1768.

61. Cherng, M.J., et al., *MOVPE growth of GaInAsSb.* Journal of Crystal Growth, 1986. **77**(1): p. 408-417.

62. Popov, A.A., V.V. Sherstnev, and Y.P. Yakovlev, *1.94-μm light-emitting diodes for moisture-content measurements.* Technical Physics Letters, 1997. **23**(10): p. 783-785.

63. Krier, A., et al., *Room temperature midinfrared electroluminescence from GaInAsSbP light emitting diodes.* Applied Physics Letters, 2007. **90**(21).

64. Petukhov, A.A., et al., *High-temperature luminescence in an n-GaSb/n-InGaAsSb/p-AlGaAsSb light-emitting heterostructure with a high potential barrier.* Semiconductors, 2013. **47**(9): p. 1258-1263.

65. Fujita, H., et al., *AlInSb Mid-Infrared LEDs of High Luminous Efficiency for Gas Sensors.* physica status solidi (a), 2018. **215**(8): p. 1700449.

66. Meriggi, L., et al., *Enhanced emission from mid-infrared AlInSb light-emitting diodes with p-type contact grid geometry.* Journal of Applied Physics, 2015. **117**(6).

67. Ding, Y., et al. *Investigation of mid-infrared AlInSb LEDs with an n-i-p structure*. in *2014 Conference on Optoelectronic and Microelectronic Materials & Devices*. 2014.

68. Baranov, A.N., et al., *Electroluminescence of GaInSb/GaSb strained single quantum well structures grown by molecular beam epitaxy.* Semiconductor Science and Technology, 1996. **11**(8): p. 1185.

69. Tang, P.J.P., et al., *Efficient 300 K light-emitting diodes at λ∼5 and ∼8 μm from InAs/In(As1−xSbx) single quantum wells.* Applied Physics Letters, 1998. **72**(26): p. 3473-3475.

70. Yu, Z., *Molecular beam epitaxy growth of InGaSb/AlGaAsSb strained quantum well diode lasers.* Journal of Semiconductors, 2011. **32**(10): p. 103002.

71. Mikhailova, M.P., et al., *Electroluminescence in n-GaSb/InAs/p-GaSb Heterostructures with a Single Quantum Well Grown by MOVPE.* Semiconductors, 2019. **53**(1): p. 46-50.

72. Li, W., et al., *Strain-compensated InGaAsSb/AlGaAsSb mid-infrared quantum-well lasers.* Applied Physics Letters, 2004. **84**(12): p. 2016-2018.

73. Garbuzov, D., et al., *AlGaAsSb/InGaAsSb/GaSb quantum well lasers with separate confinement heterostructures for 2-um operation*. Photonics West '96. Vol. 2682. 1996: SPIE.

74. Newell, T., et al., *The effect of increased valence band offset on the operation of 2 μm GaInAsSb-AlGaAsSb lasers.* IEEE Photonics Technology Letters, 1999. **11**(1): p. 30-32.

75. Kim, J.G., et al., *Room-temperature 2.5 μm InGaAsSb/AlGaAsSb diode lasers emitting 1 W continuous waves.* Applied Physics Letters, 2002. **81**(17): p. 3146-3148.

76. Lin, C., et al., *Low threshold room-temperature continuous-wave operation of 2.24–3.04 μm GaInAsSb/AlGaAsSb quantum-well lasers.* Applied Physics Letters, 2004. **84**(25): p. 5088-5090.

77. Lu, Q., A. Marshall, and A. Krier, *Metamorphic Integration of GaInAsSb Material on GaAs Substrates for Light Emitting Device Applications.* Materials, 2019. **12**(11): p. 1743.

78. Jung, S., et al., *Dual wavelength GaSb based type I quantum well mid-infrared light emitting diodes.* Applied Physics Letters, 2010. **96**(19): p. 191102.

79. Suchalkin, S., et al., *GaSb based light emitting diodes with strained InGaAsSb type I quantum well active regions.* Applied Physics Letters, 2008. **93**(8): p. 081107.

80. Ding, Y., et al., *Design, Simulations, and Optimizations of Mid-infrared Multiple Quantum Well LEDs.* Procedia Engineering, 2016. **140**: p. 36-42.

81. Chen, Y., et al., *High-Power, High-Efficiency GaSb-Based Laser with Compositionally Linearly Graded AlGaAsSb Layer.* Applied Sciences, 2023. **13**(9): p. 5506.

82. Jung, S., et al., *High dimensional addressable LED arrays based on type I GaInAsSb quantum wells with quinternary AlGaInAsSb barriers.* Semiconductor Science and Technology, 2011. **26**(8): p. 085022.

83. Sifferman, S.D., et al., *Highly Strained Mid-Infrared Type-I Diode Lasers on GaSb.* IEEE Journal of Selected Topics in Quantum Electronics, 2015. **21**(6): p. 1-10.

84. Grietens, B., et al., *Growth and characterization of mid-infrared InGaAs/InAlAs strained triple-quantum-well light-emitting diodes grown on lattice-mismatched GaAs substrates.* Journal of Applied Physics, 1996. **80**(7): p. 4177-4181.

85. Grein, C.H., P.M. Young, and H. Ehrenreich, *Minority carrier lifetimes in ideal InGaSb/InAs superlattices.* Applied Physics Letters, 1992. **61**(24): p. 2905-2907.

86. Meyer, J.R., et al., *Comparison of Auger coefficients in type I and type II quantum well midwave infrared lasers.* IEEE Journal of Quantum Electronics, 2021. **57**(5): p. 1-10.

87. Zegrya, G.G. and A.D. Andreev, *Mechanism of suppression of Auger recombination processes in type-II heterostructures.* Applied Physics Letters, 1995. **67**(18): p. 2681-2683.

88. Hoffman, C., et al., *Type-II quantum-well lasers for the mid-wavelength infrared.* Applied Physics Letters, 1995. **67**: p. 757-759.

89. Moiseev, K.D., et al., *Electroluminescence of quantum-well structures on type-II InAs/GaSb heterojunctions.* Technical Physics Letters, 1998. **24**(6): p. 477-479.

90. Hoffman, D., et al., *Electroluminescence of InAs-GaSb heterodiodes.* IEEE Journal of Quantum Electronics, 2006. **42**(2): p. 126-130.

91. Khoshakhlagh, A., et al., *Long-Wave InAs/GaSb Superlattice Detectors Based on nBn and Pin Designs.* IEEE Journal of Quantum Electronics, 2010. **46**(6): p. 959-964.

92. Craig, A.P., et al., *InAsSb-based detectors on GaSb for near-room-temperature operation in the mid-wave infrared.* Applied Physics Letters, 2021. **118**(25).

93. Ting, D.Z., et al., *Long and Very Long Wavelength InAs/InAsSb Superlattice Complementary Barrier Infrared Detectors.* Journal of Electronic Materials, 2022. **51**(9): p. 4666-4674.

94. Pullin, M.J., et al., *Room-temperature InAsSb strained-layer superlattice light-emitting diodes at λ=4.2 μm with AlSb barriers for improved carrier confinement.* Applied Physics Letters, 1999. **74**(16): p. 2384-2386.

95. Krier, A., et al., *Mid-infrared electroluminescence at room temperature from InAsSb multi-quantum-well light-emitting diodes.* Applied Physics Letters, 2006. **89**(9): p. 091110.

96. Keen, J.A., et al., *Electroluminescence and photoluminescence of type-II InAs/InAsSb strained-layer superlattices in the mid-infrared.* Infrared Physics & Technology, 2018. **93**: p. 375-380.

97. Delli, E., et al., *Mid-infrared type-II InAs/InAsSb quantum wells integrated on silicon.* Applied Physics Letters, 2020. **117**(13): p. 131103.

98. Yang, R.Q., *Infrared laser based on intersubband transitions in quantum wells.* Superlattices and Microstructures, 1995. **17**(1): p. 77-83.

99. Meyer, J.R., et al., *The Interband Cascade Laser.* Photonics, 2020. **7**(3): p. 75.

100. Koerperick, E.J., et al., *Active Region Cascading for Improved Performance in InAs–GaSb Superlattice LEDs.* IEEE Journal of Quantum Electronics, 2008. **44**(12): p. 1242-1247.

101. Koerperick, E.J., et al., *Cascaded Superlattice InAs/GaSb Light-Emitting Diodes for Operation in the Long-Wave Infrared.* IEEE Journal of Quantum Electronics, 2011. **47**(1): p. 50-54.

102. Ricker, R.J., et al., *Dual-Color InAs/GaSb Cascaded Superlattice Light-Emitting Diodes.* IEEE Journal of Quantum Electronics, 2015. **51**(12): p. 1-6.

103. Zhou, Y., et al., *InAs/GaSb superlattice interband cascade light emitting diodes with high output power and high wall-plug efficiency.* Applied Physics Letters, 2019. **114**(25): p. 253507.

104. Díaz-Thomas, D.A., et al., *3.3 µm interband-cascade resonant-cavity light-emitting diode with narrow spectral emission linewidth.* Semiconductor Science and Technology, 2020. **35**(12): p. 125029.

105. Díaz-Thomas, D.A., et al., *Single mode, distributed feedback interband cascade lasers grown on Si for gas sensing.* Applied Physics Letters, 2025. **126**(3).

106. Kim, C.S., et al., *Improved mid-infrared interband cascade light-emitting devices.* Optical Engineering, 2018. **57**: p. 1.

107. Canedy, C.L., et al., *High-power and high-efficiency midwave-infrared interband cascade lasers.* Applied Physics Letters, 2006. **88**(16).

108. Schubert, E.F., et al., *Resonant cavity light-emitting diode.* Applied Physics Letters, 1992. **60**(8): p. 921-923.

109. Bainbridge, A., et al., *Resonant Cavity–Enhanced Photodiodes for Spectroscopy of C□H Bonds.* physica status solidi (a), 2021. **218**(17): p. 2100056.

110. Green, A.M., et al., *Resonant-cavity-enhanced photodetectors and LEDs in the mid-infrared.* Physica E: Low-dimensional Systems and Nanostructures, 2004. **20**(3): p. 531-535.

111. Ducanchez, A., et al., *Fabrication and Characterization of GaSb-Based Monolithic Resonant-Cavity Light-Emitting Diodes Emitting Around 2.3 µm and Including a Tunnel Junction.* IEEE Journal of Selected Topics in Quantum Electronics, 2008. **14**(4): p. 1014-1021.

112. Meriggi, L., *Antimonide-based mid-infrared light-emitting diodes for low-power optical gas sensors*. 2015, University of Glasgow.

113. Al-Saymari, F.A., et al., *Mid-infrared resonant cavity light emitting diodes operating at 4.2 µm.* Optics express, 2020. **28 16**: p. 23338-23353.

114. Al-Saymari, F.A., et al., *Resonant cavity enhanced InAs/GaAsSb SLS LEDs with a narrow spectral linewidth and a high-spectral intensity operating at 4.6 µm.* Applied Physics Letters, 2023. **123**(20).

115. Davison, N.B., et al., *Development and optimisation of a near-infrared spectroscopic system for glucose quantification in aqueous and intralipid-based samples.* Engineering Research Express, 2024. **6**(2): p. 025340.

116. Bainbridge, A., et al., *Resonant cavity-enhanced photodiode array for miniaturised spectroscopic sensing.* Optics Express, 2022. **30**(3): p. 3230-3237.

117. Brolis. *Brolis - Herdline*. 2024 [cited 2024 29/08/2024]; Available from: https://brolisherdline.com/.

118. Antanaitis, R., et al., *In-Line Registered Milk Fat-to-Protein Ratio for the Assessment of Metabolic Status in Dairy Cows.* Animals, 2023. **13**(20): p. 3293.

119. Antanaitis, R., et al., *The Relation between Milk Lactose Concentration and the Rumination, Feeding, and Locomotion Behavior of Early-Lactation Dairy Cows.* Animals, 2024. **14**(6): p. 836.

120. Milla, M.J., et al., *Localized surface plasmon resonance frequency tuning in highly doped InAsSb/GaSb one-dimensional nanostructures.* Nanotechnology, 2016. **27**(42): p. 425201.

121. *Monomers & polymers*. 2020 [cited 2023 19th June]; Available from: https://www.plasticsoupfoundation.org/en/plastic-problem/what-is-plastic/monomers-and-polymers/.

122. Knight, L. *A brief history of plastics, natural and synthetic*. 2014 [cited 2023 19th June]; Available from: https://www.bbc.co.uk/news/magazine-27442625.

123. *History of plastics*. 2019 [cited 2023 19th June]; Available from: https://www.plasticsindustry.org/history-plastics.

124. *Plasatics - the facts 2022*. 2022, Plastics europe.

125. Bucknall, D., G., *Plastics as a material system in a circular economy.* Phil. Trans. R. Soc. A, 2020(378).

126. Sastri, V., *Materials used in medical devices*, in *Plastics in medical devices: properties requirements and applications*. 2022, Elsevier: Oxford.

127. Steinmetz, Z., et al., *Plastic mulching in agriculture. Trading short-term agronomic benefits for long-term soil degradation?* Science of The Total Environment, 2016. **550**: p. 690-705.

128. Beghetto, V., et al., *Recent Advancements in Plastic Packaging Recycling: A Mini-Review.* Materials, 2021. **14**(17): p. 4782.

129. *The lifecycle of plastics*. 2021 [cited 2023 19th June]; Available from: https://wwf.org.au/blogs/the-lifecycle-of-plastics/.

130. McDonough, W. and M. Braungart, *Cradle to cradle : remaking the way we make things*. 2009, London: Vintage.

131. Smil, V., d. Ieee Xplore, and p. Mit Press, *Energy and civilization : a history*. 2017, Cambridge, Massachusetts.

132. Britannica, T.e.o.E. *Crude oil*. 2023 [cited 2023; Available from: https://www.britannica.com/science/crude-oil.

133. Ochoa-Estopier, L.M., M. Jobson, and R. Smith, *The use of reduced models for design and optimisation of heat-integrated crude oil distillation systems.* Energy, 2014. **75**: p. 5-13.

134. Bryce, E. *How do we turn oil into plastics?* 2021 [cited 2023 5th July]; Available from: https://www.livescience.com/how-oil-is-turned-into-plastic.html.

135. *Plastic applications database*. 2005, Knovel.

136. Baheti, P. *How is plastic made? A simple step-by-step explanation*. 2023 [cited 2023 5th July]; Available from: https://www.bpf.co.uk/plastipedia/how-is-plastic-made.aspx.

137. Edward Kosior, J.M., *Current idustry position on plastic production and recycling*, in *Plastic waste and recycling*. 2020, Elsevier. p. 133-162.

138. Locke, J., *Some considerations of the consequences of lowering the interest and raising the value of money (Letter to a member of Parliament. 1691.) Short observations on a printed paper entitled,'For encouraging the coining silver money in England'... Further considerations concerning raising the value of money. Two treatises of government*. Vol. 4. 1824: C. and J. Rivington.

139. Steffen, W., et al., *The Anthropocene: conceptual and historical perspectives.* Philosophical Transactions of the Royal Society A: Mathematical, Physical and Engineering Sciences, 2011. **369**(1938): p. 842-867.

140. Thompson, M. and J.O. Reno, *Rubbish Theory : The Creation and Destruction of Value - New Edition*. 2017, London, UNITED KINGDOM: Pluto Press.

141. Venugopal, V. *Shining a light on the microplastics mess in our oceans*. Technology 2023 [cited 2023 4th July]; Available from: https://spie.org/news/photonics-focus/julyaugust-2023/shining-light-on-ocean-microplastics.

142. *What is the linear economy?* 2020 [cited 2023 5th July]; Available from: https://ellenmacarthurfoundation.org/what-is-the-linear-economy.

143. OECD, *Global Plastics Outlook*. 2022.

144. *What is a circular economy?* 2022 [cited 2022 20th July]; Available from: https://ellenmacarthurfoundation.org/topics/circular-economy-introduction/overview.

145. Alexander, A., S. Pascucci, and F. Charnley, *Handbook of the Circular Economy : Transitions and Transformation*. 2023, Berlin/Boston, GERMANY: Walter de Gruyter GmbH.

146. *Reduce Reuse Recycle*. 2023 [cited 2023 27th July]; Available from: https://reducereuserecycle.co.uk/.

147. Smithers, R. *Use of plastic bags in England drops by 59% in a year*. 2020 [cited 2023 27th July]; Available from: https://www.theguardian.com/environment/2020/jul/30/use-of-plastic-bags-in-england-drops-by-59-in-a-year.

148. Hussain, A., et al., *Impact of single use polyethylene shopping bags on environmental pollution, a comprehensive review.* 2020.

149. Muposhi, A., M. Mpinganjira, and M. Wait, *Considerations, benefits and unintended consequences of banning plastic shopping bags for environmental sustainability: A systematic literature review.* Waste Management & Research, 2022. **40**(3): p. 248-261.

150. Britannica, E. *Recycling*. 2023 [cited 2023 27th June]; Available from: https://www.britannica.com/science/recycling.

151. Jia, C., et al., *Deconstruction of high-density polyethylene into liquid hydrocarbon fuels and lubricants by hydrogenolysis over Ru catalyst.* Chem Catalysis, 2021. **1**(2): p. 437-455.

152. O.Berk. *What is the downcycling process of plastic?* 2018 [cited 2023 21st August]; Available from: https://www.oberk.com/packaging-crash-course/downcycling-temp.

153. Europe, P. *Collecting and sorting of plastics waste*. 2022 [cited 2023 21st August]; Available from: https://plasticseurope.org/sustainability/circularity/waste-management-prevention/collection-sorting/.

154. Biffa. *Plastic recycling at Biffa Polymers*. 2023 [cited 2023 21st August]; Available from: https://www.biffa.co.uk/waste-services-and-products/recycling-recovery-processes/plastic-recycling.

155. Merrington, A., *9 - Recycling of Plastics*, in *Applied Plastics Engineering Handbook (Second Edition)*, M. Kutz, Editor. 2017, William Andrew Publishing. p. 167-189.

156. MacLeod, M., et al., *The global threat from plastic pollution.* Science, 2021. **373**(6550): p. 61-65.

157. Lancen, L. *How much energy does it take to recycle one ton of plastic and what are the benefits?* 2023 [cited 2023 22nd June]; Available from: https://www.climateofourfuture.org/how-much-energy-does-it-take-to-recycle-one-ton-of-plastic-and-what-are-the-benefits/.

158. Galve, J.E., et al., *Life Cycle Assessment of a Plastic Part Injected with Recycled Polypropylene: A Comparison with Alternative Virgin Materials.* International Journal of Precision Engineering and Manufacturing-Green Technology, 2022. **9**(3): p. 919-932.

159. ISO, *Environmental management — Life cycle assessment — Principles and framework*, ISO, Editor. 2006, ISO.

160. Schyns, Z.O.G. and M.P. Shaver, *Mechanical Recycling of Packaging Plastics: A Review.* Macromolecular Rapid Communications, 2021. **42**(3): p. 2000415.

161. Zeller, M., et al., *Chemical Recycling of Mixed Plastic Wastes by Pyrolysis – Pilot Scale Investigations.* Chemie Ingenieur Technik, 2021. **93**(11): p. 1763-1770.

162. Jiang, J., et al., *From plastic waste to wealth using chemical recycling: A review.* Journal of Environmental Chemical Engineering, 2022. **10**(1): p. 106867.

163. Quicker, P., M. Seitz, and J. Vogel, *Chemical recycling: A critical assessment of potential process approaches.* Waste Management & Research, 2022. **40**(10): p. 1494-1504.

164. Serranti, S. and G. Bonifazi, *2 - Techniques for separation of plastic wastes*, in *Use of Recycled Plastics in Eco-efficient Concrete*, F. Pacheco-Torgal, et al., Editors. 2019, Woodhead Publishing. p. 9-37.

165. Neo, E.R.K., et al., *A review on chemometric techniques with infrared, Raman and laser-induced breakdown spectroscopy for sorting plastic waste in the recycling industry.* Resources, Conservation and Recycling, 2022. **180**: p. 106217.

166. Masoumi, H., S.M. Safavi, and Z. Khani, *Identification and classification of plastic resins using near infrared reflectance spectroscopy.* International Journal of Mechanical and Industrial Engineering, 2012. **6**: p. 213-220.

167. Kusenberg, M., et al., *Towards high-quality petrochemical feedstocks from mixed plastic packaging waste via advanced recycling: The past, present and future.* Fuel Processing Technology, 2022. **238**: p. 107474.

168. Li, H., et al., *An improved classification method of waste smartphone plastics based on near-infrared spectroscopy.* Journal of Material Cycles and Waste Management, 2023.

169. Araujo-Andrade, C., et al., *Review on the photonic techniques suitable for automatic monitoring of the composition of multi-materials wastes in view of their posterior recycling.* Waste Management & Research, 2021. **39**(5): p. 631-651.

170. Rozenstein, O., E. Puckrin, and J. Adamowski, *Development of a new approach based on midwave infrared spectroscopy for post-consumer black plastic waste sorting in the recycling industry.* Waste Manag, 2017. **68**: p. 38-44.

171. Adarsh, U.K., et al., *Spectroscopy: A promising tool for plastic waste management.* TrAC Trends in Analytical Chemistry, 2022. **149**: p. 116534.

172. Paul East, K.B. *Black plastic packaging forum: options for improving the recycling of black plastic packaging - 2020 update*. 2020.

173. Turner, A., *Black plastics: Linear and circular economies, hazardous additives and marine pollution.* Environment International, 2018. **117**: p. 308-318.

174. Fleck, J.E.T., *Carbon black recycled from car tires*. 2021, Fraunhofer.

175. Cardona-Uribe, N., M. Betancur, and J.D. Martínez, *Towards the chemical upgrading of the recovered carbon black derived from pyrolysis of end-of-life tires.* Sustainable Materials and Technologies, 2021. **28**: p. e00287.

176. Holait, A., *Recovered carbon black as a more sustainable feedstock*. 2023, Lawrence industries.

177. *Plastic food packaging waste*. 2019, Parliamentary office of Science and Technology: London.

178. Gove, M., *25 Year ENvironmental Plan*, F.a.R.A. Environment, Editor. 2018, Westminster Parliament: London.

179. *Waste Management Plan for England*, F.a.R.A. Environment, Editor. 2020, Westminster Parliament: London.

180. *Net Zero Strategy: Build Back Greener*, E.S.a.N. Zero and E.a.I.S. Business, Editors. 2021, HM Government: London.

181. *UK Net Zero Research and Innovation Framework: Delivery Plan 2022 to 2025*, E.S.a.N. Zero, Editor. 2023, HM Government: London.

182. *Recources and waste strategy for England*, F.a.R.A. Environment, Editor. 2018, HM Government: London.

183. Hunter, A., *Black plastics: what's the problem?*, in *Greenpeace*. 2018, Greenpeace.

184. Farrell, S. and I. Quinn, *Are brands doing enough to eliminate black plastic?*, in *The Grocer*. 2019, William Reed.

185. Nsubuga, J., *Black plastics to be banned from supermarkets by Christmas*, in *Metro*. 2019, DMG media.

186. Oka, R. and T. Masui, *Synthesis and characterization of black pigments based on calcium manganese oxides for high near-infrared (NIR) reflectance.* RSC Advances, 2016. **6**(93): p. 90952-90957.

187. Dvorak, R., E. Kosior, and L. Moody, *In-market trial to prove recycling process for black CPET trays*. 2011, WRAP: Banbury.

188. Dvorak, R., E. Kosior, and L. Moody, *Masking strength of NIR detectable black colourants*. 2013, WRAP: Banbury.

189. *Unisort Black*. NIR sorting systems 2024 [cited 2024 25th January]; Available from: https://steinertglobal.com/magnets-sensor-sorting-units/sensor-sorting/nir-sorting-systems/unisort-black/.

190. *Detection of black and inert objects*. 2019 [cited 2024 25th January]; Available from: https://www.pellencst.com/profile-detection/.

191. *Technologies*. 2024 [cited 2024 January 25th]; Available from: https://www.tomra.com/en/waste-metal-recycling/products/technologies.

192. Palleschi, V., *Laser-induced breakdown spectroscopy: principles of the technique and future trends.* ChemTexts, 2020. **6**(2): p. 18.

193. Roh, S.-B., et al., *Development of intelligent sorting system realized with the aid of laser-induced breakdown spectroscopy and hybrid preprocessing algorithm-based radial basis function neural networks for recycling black plastic wastes.* Journal of Material Cycles and Waste Management, 2018. **20**(4): p. 1934-1949.

194. Kim, E. and W.Z. Choi, *Real-time identification of plastics by types using laser-induced breakdown spectroscopy.* Journal of Material Cycles and Waste Management, 2019. **21**(1): p. 176-180.

195. Signoret, C., et al., *Alterations of plastics spectra in MIR and the potential impacts on identification towards recycling.* Resources, Conservation and Recycling, 2020. **161**: p. 104980.

196. Carrera, B., et al., *A machine learning based classification models for plastic recycling using different wavelength range spectrums.* Journal of Cleaner Production, 2022. **374**: p. 133883.

197. Smith, B.C., *The infrared spectra of polymers II: polyethylene.* Spectroscopy, 2021. **36**(9): p. 24 - 29.

198. Ul-Hamid, A., et al., *Failure investigation of an underground low voltage XLPE insulated cable.* Anti-Corrosion Methods and Materials, 2015. **62**: p. 281-287.

199. Smith, B.C., *The infrared spectra of polymers III: hydrocarbon polymers.* Spectroscopy, 2021. **36**(11): p. 22 - 25.

200. Al-Saymari, F.A., et al., *Electroluminescence enhancement in mid-infrared InAsSb resonant cavity light emitting diodes for CO2 detection.* Applied Physics Letters, 2019. **114**(17): p. 171103.

201. Bachmann, K.J., F.A. Thiel, and H. Schreiber, *Melt and solution growth of bulk single crystals of quaternary III–V alloys.* Progress in Crystal Growth and Characterization, 1979. **2**: p. 171-206.

202. Liu, Z.Y., B. Hawkins, and T.F. Kuech, *Chemical and structural characterization of GaSb(100) surfaces treated by HCl-based solutions and annealed in vacuum.* Journal of Vacuum Science & Technology B: Microelectronics and Nanometer Structures Processing, Measurement, and Phenomena, 2002. **21**(1): p. 71-77.

203. Letka, V., et al., *Modelling and measurement of bandgap behaviour in MWIR InAs/InAs(0.815)Sb(0.185) strained-layer superlattices*. SPIE Security + Defence. Vol. 10433. 2017: SPIE.

204. Hodgson, P.D., et al., *Blueshifts of the emission energy in type-II quantum dot and quantum ring nanostructures.* Journal of Applied Physics, 2013. **114**(7).

205. Keen, J.A., et al., *InAs/InAsSb type-II strained-layer superlattices for mid-infrared LEDs.* Journal of Physics D: Applied Physics, 2018. **51**(7): p. 075103.

206. Chidley, E.T.R., et al., *Photoluminescence of GaSb grown by metal-organic vapour phase epitaxy.* Semiconductor Science and Technology, 1991. **6**(1): p. 45.

207. Olson, B.V., et al., *Identification of dominant recombination mechanisms in narrow-bandgap InAs/InAsSb type-II superlattices and InAsSb alloys.* Applied Physics Letters, 2013. **103**(5): p. 052106.